



Dipl.-Ing. Merit Bodner, BSc

# Degradation Phenomena in Polymer Electrolyte Fuel Cells

## DOCTORAL THESIS

to achieve the university degree of  
Doktorin der technischen Wissenschaften  
submitted to

**Graz University of Technology**

Supervisor

Assoc.Prof. Dipl.-Ing. Dr.techn. Viktor Hacker

Institute of Chemical Engineering and Environmental Technology

Graz, March 2017

## **AFFIDAVIT**

I declare that I have authored this thesis independently, that I have not used other than the declared sources/resources, and that I have explicitly indicated all material which has been quoted either literally or by content from the sources used. The text document uploaded to TUGRAZonline is identical to the present doctoral thesis.

---

Date

---

Signature



# Kurzfassung

Polymerelektrolytmembranbrennstoffzellen wandeln die in Wasserstoff gespeicherte chemische Energie mit hoher Effizienz in elektrische Energie um. Um die Brennstoffzelle kommerziell in mobilen, stationären oder portablen Anwendungen zu etablieren, ist neben der hohen Effizienz und der Wasserstoffinfrastruktur auch eine hohe Lebensdauer notwendig.

Degradation von Brennstoffzellen lässt sich in die chemische Zersetzung und die mechanische Schädigung der Elektrolytmembran, die Oxidation, Agglomeration oder Vergiftung des Platinkatalysators und die Kohlenstoffkorrosion unterteilen. Nur auf Basis eines grundlegenden Verständnisses dieser Effekte können die eingesetzten Materialien, die Brennstoffzellenkomponenten und die Betriebsmodi weiterentwickelt werden.

In der vorliegenden Arbeit wurden die wesentlichen Degradationsmechanismen in Einzelzellversuchen charakterisiert. Dazu wurden 25 cm<sup>2</sup> Zellen mit segmentierten Stromabnehmerplatten verwendet. Durch die orts aufgelöste Messung von Strom und Temperatur ist es möglich, Gradienten und andere lokale Effekte zu identifizieren und mit den Betriebsparametern in Verbindung zu setzen. Mit Hilfe beschleunigter Alterungsprotokolle wurden die unterschiedlichen Degradationsmechanismen hervorgerufen.

Die untersuchten Phänomene sind stark überlappend und beeinflussen sich gegenseitig. Durch Kombination der orts aufgelösten Messung und der beschleunigten Degradationstests mit einer sehr holistischen Herangehensweise an das Thema wurden Parameter wie die Wasserstoffpermeation und lokale Temperatureffekte als wesentliche Einflussfaktoren auf die Degradationsrate identifiziert und experimentell untersucht.

# Abstract

Polymer electrolyte fuel cells are capable of converting the chemical energy of hydrogen into electrical energy at high efficiencies. Therefore, there is a growing interest in their application in automotive powertrains as well as stationary and mobile applications. In order to establish fuel cells commercially, beside high efficiency and hydrogen infrastructure, a long lifetime is required.

Degradation is subdivided into chemical decomposition and mechanical damage of the polymer electrolyte membrane; oxidation, agglomeration and poisoning of the platinum electrocatalyst and carbon corrosion. Only with a profound understanding of the respective effects, the materials, fuel cell components and operation modes can be improved accordingly.

The most severe degradation phenomena were investigated in a single cell setup. The segmented single cell with an active area of 25 cm<sup>2</sup> was utilised. Measurement of the spatial distribution of current and temperature enables the identification of gradients and other local effects in respect to the operation parameters. With the aid of accelerated stress tests (ASTs), different degradation phenomena were induced. The different mechanisms have proven to strongly overlap and influence each other.

By combining segmented cell measurements with accelerated stress tests in a holistic approach to the subject of degradation, most of the lifetime limiting effects could be classified and investigated experimentally. Thereby, hydrogen crossover and local temperature effects were identified as the most severe in terms of accelerated degradation.

# Acknowledgement

First, I want to express my deep gratitude and appreciation to my supervisor Prof. Viktor Hacker. Only with his strong support and highly skilled knowledge, I was able to complete this thesis.

I want to thank the entire team of the Fuel Cells System Group at Graz University of Technology; it's prosperous environment allows achieving a high scientific standard. Amongst all, I especially thank Roman Teuffenbach, Mija Rami and Philipp Schopp, whose master theses I supervised in my time as a part of the team. Dr. Stephan Nestl and Dipl.-Ing. Bernhard Marius both supported me during parts of the experiments and were crucial for the success thereof. Special appreciation also goes to Dr. Alexander Schenk, whose support was priceless for me throughout the years.

I thank Prof. Hansjörg Weber and Dipl.-Ing. Dietmar Salaberger for providing ex-situ measurements.

My gratitude also goes to all of the project partners of each of the projects to which I contributed to. From the Second Act project, I want to especially emphasise the fruitful discussions I have had with Dr. Thor Aarhaug (SINTEF) and Prof. Andrea Casalegno (POLIMI) and their entire teams as well as the great cooperation with Dr. Laila Grahl-Madsen (EWII) regarding the materials tested within this thesis. I thank Dr. Sylvie Escribano (CEA), who in the role as coordinator has enabled this project to be so successful. My appreciation also goes to the other partners from DLR (ex-situ measurements), JRC (harmonisation protocols), ICI and Nedstack. I am grateful that I was able to work in such a scientifically rich environment.

From the FC Diamond project, I want to express my appreciation for the cooperation with Dr. Reinhard Tatschl (AVL) and his group, Dipl.-Ing. Sönke Gößling (ZBT) and Dr. Larisa Karpenko (IPTC). From the PEMREX S project, I want to thank the AVL Fuel Cell group and all involved partners from ElringKlinger.

Each and every one has helped me grow and gain confidence to continue to work in this complex and yet amazing field of fuel cell research. During the completion of this thesis my interest for the subject has only been ever-growing.

# Preface

This thesis was conducted at Graz University of Technology at the Institute of Chemical Engineering and Environmental Technology within the Fuel Cell Systems group.

All presented data were obtained within the scope of the Second Act project, which received funding from the European Union's Seventh Framework Programme (FP7/2007-2013) for the Fuel Cells and Hydrogen Joint Technology Initiative under grant agreement n° 621216.

As a major share of my results have been published in peer-reviewed journals [1-4] previously, this thesis summarises both those as well as additional, unpublished results.



*Euer Geist und eure Tugend dienen dem Sinn der Erde, meine Brüder: und aller Dinge Wert werde neu von euch gesetzt! Darum sollt ihr Kämpfende sein! Darum sollt ihr Schaffende sein!*

*F. Nietzsche*



# Content

1.	Introduction .....	1
1.1.	Cost Reduction and Commercial Competitiveness .....	2
1.2.	Scope of the Thesis .....	3
2.	Fuel Cell Theory .....	4
2.1.	Operation Characteristics .....	5
2.2.	Fuel Cell Efficiency.....	7
3.	Membrane Electrode Assembly.....	8
3.1.	Membrane .....	8
3.2.	Catalyst Layer.....	10
3.3.	Microporous Layer .....	10
3.4.	Gas Diffusion Layer.....	11
4.	Single Cell Design .....	12
4.1.	In-house Segmented Single Cell.....	12
4.2.	Standardised Layout .....	12
4.2.1.	Single Serpentine Layout .....	13
4.2.2.	Three Channel Serpentine Layout .....	14
4.3.	Reference Electrode.....	14
5.	Characterisation Methods .....	16
5.1.	Electrochemical Characterisation .....	16
5.1.1.	Polarisation Curves .....	16
5.1.2.	Electrochemical Impedance Spectroscopy .....	16
5.1.3.	Hydrogen Diffusion Measurements / Linear Sweep Voltammetry .	17
5.1.4.	Cyclic Voltammetry .....	18
5.2.	Additional Characterisation .....	19
5.2.1.	Off-Gas Analysis .....	19
5.2.2.	Fluoride Selective Electrode.....	20
5.2.3.	<sup>19</sup> F-NMR.....	20
5.2.4.	Computed Tomography .....	20
6.	Fuel Cell Degradation.....	22

6.1.	Membrane Degradation .....	23
6.2.	Carbon Corrosion .....	24
6.3.	Catalyst Degradation .....	25
6.4.	Degradation in Real Systems .....	25
6.4.1.	Automotive .....	26
6.4.2.	Stationary.....	26
6.4.3.	Beneficial Effects from Ageing .....	27
7.	Accelerated Stress Tests .....	28
7.1.	ASTs for Specific Component Testing .....	28
7.1.1.	OCV Hold Tests.....	29
7.1.2.	Voltage Cycling.....	29
7.2.	Multi-component Testing .....	31
7.2.1.	Reactant Starvation .....	31
7.2.2.	Startup-shutdown Cycles .....	32
7.2.3.	Specific Tests for Mobile Applications.....	34
7.2.4.	Specific Tests for Stationary Applications .....	35
8.	Experimental .....	37
8.1.	Determining the Total Fluorine Emission Rate .....	37
8.1.1.	Theory.....	37
8.1.2.	Experimental Setup.....	37
8.1.3.	Results and Discussion .....	38
8.1.4.	Conclusion .....	41
8.2.	Chemical Membrane Degradation by OCV Hold Testing.....	41
8.2.1.	Theory.....	42
8.2.2.	Experimental Setup.....	42
8.2.3.	Results and Discussion .....	42
8.2.4.	Conclusion .....	45
8.3.	Humidity induced Platinum Agglomeration .....	45
8.3.1.	Theory.....	45
8.3.2.	Experimental Setup.....	46
8.3.3.	Results and Discussion .....	47

8.3.4.	Conclusion .....	54
9.	Conclusion.....	56
10.	List of Tables.....	59
11.	List of Figures.....	60
12.	List of Abbreviations.....	63
13.	List of Variables .....	65
14.	References.....	66
15.	List of Publications .....	ii
15.1.	Journal Articles .....	ii
15.2.	Book Chapters .....	iii
15.3.	Reports .....	iii
15.4.	Lectures and Publications .....	iv
15.5.	Conference Contributions .....	v
15.6.	Poster .....	viii
16.	Selected Peer Reviewed Publications .....	xi
16.1.	H <sub>2</sub> Generation from Alkaline Electrolyzer. ....	xi
16.2.	The Effect of Platinum Electrocatalyst on Membrane Degradation in Polymer Electrolyte Fuel Cells. ....	xxix
16.3.	Effect of Pinhole Location on Degradation in Polymer Electrolyte Fuel Cells. ....	xlv
16.4.	Air Starvation induced Degradation in Polymer Electrolyte Fuel Cells. ....	lix

# 1. Introduction

With an increasing global energy demand, the world is struggling to reach the goal of limiting global warming to 2 °C above the pre-industrial level. Therefore, it was agreed upon in the Paris Agreement to reduce greenhouse gas (GHG, Figure 1) emissions significantly. In detail, this would further require a reduction of the European Union’s emissions by 40% by 2030 [5]. By 2050, this would, however, require a reduction by 85% globally. These goals are only achievable with a significant increase of the share of renewable energy. Sunlight, wind, tidal and waves are, however, time dependent and strongly fluctuating. Energy from these sources therefore needs to be stored in incomparable quantities [6].

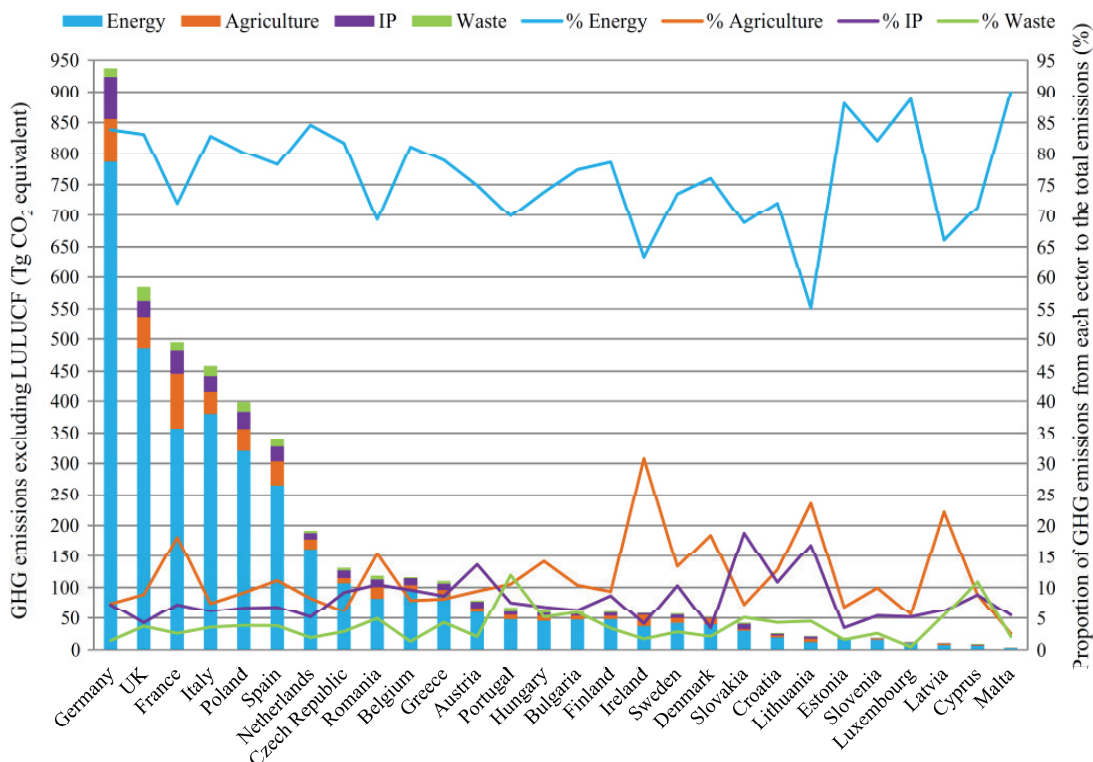


**Figure 1:** National GHG emissions with contributions listed according to the different sectors for the EU28 countries in 2012 [7].

With its high abundance, bound in water or hydrocarbons, hydrogen is a suitable energy carrier for a sustainable future energy market. Surplus electrical energy can be converted into hydrogen by electrolysis at a satisfying efficiency and high purity [1].

The only reaction product from the combustion of hydrogen is water. Fuel cells are able to convert the compound's chemical energy into electrical energy at a high efficiency of 60% or more. When the thermal energy is used as well, as it is the case in combined heat and power (CHP) units, the overall efficiency can be increased to 90%. Stationary and automobile applications are of major interest in this regard, as energy supply by hydrogen powered fuel cells is a potentially carbon-free, sustainable approach, leading to no local emissions [6,8–10].

Within the transport sector, passenger vehicles account for up to 70% of the GHG emissions. Due to that, alternative technologies in road transport are of special interest. In a well-to-wheel (WTW) study by Yazdanie et al. [11], it was found that fuel cell electric vehicles (FCEVs) were the only approach to reduce the WTW energy demand, the GHG emissions and the costs at the same time, if hydrogen is produced from methane steam reforming. With hydrogen from renewable production pathways, the GHG emission reduction was the highest for fuel cell electric vehicles in the respective study.

However, fuel cells face lifetime limitations, as they do not respond well to changing operation conditions. Sudden load changes, fluctuating humidity, contamination, fuel and air starvation can all lead to irreversible degradation [12]. This is especially severe in automotive applications, but can affect stationary systems as well. Changing load conditions, startup/shutdown (SU-SD) and freeze/thaw cycles cannot be avoided completely and thus strategies for degradation mitigation are required [13]. Therefore, it is of utmost importance to fully understand the underlying mechanisms. Only with an extended lifetime and reduced costs at a level comparable to conventional systems, the fuel cell can be established as a truly competitive alternative.

### 1.1. Cost Reduction and Commercial Competitiveness

Despite recent advances, the costs are high for polymer electrolyte fuel cells (PEFCs). In 2013, the U.S. Department of Energy (DoE) estimated the system costs to be \$55 kW<sup>-1</sup>, with the aim to reduce the costs to \$30 kW<sup>-1</sup>. In order to meet the requirements for a competitive product, a variety of approaches is possible. Beside an expected cost reduction by mass manufacturing, the used components are to be optimised in order to accomplish this task. Possible approaches to lower fuel cell costs are for example the reduction of the platinum loading either by enhancing the distribution or by alloying it with cheaper metals, such as Pd, Ru, Co or Ag [14–16]. The bipolar plates (BP) are another critical factor, determining not only the costs, but also volume and weight of the stack.

By introducing coated metal bipolar plates, all three can be significantly reduced [17].

## 1.2. Scope of the Thesis

This thesis aims to provide a fundamental understanding of the most detrimental degradation phenomena affecting polymer electrolyte fuel cells. All aspects were evaluated and those considered the most severe were selected for further investigation. With a holistic approach to the subject as a whole a detailed understanding of each of the important mechanisms was obtained.

Within this thesis, the principles and composition of polymer electrolyte fuel cells are explained, followed by a detailed description of the different degradation mechanisms known from literature. In this regard, available accelerated stress test (AST) protocols are discussed and listed by their respective aim. Some of these tests were selected for experiment, which are partially featured in the experimental section. Published data [1–4] are, however, not included, but added in the appendix, along with a complete list of publications.

## 2. Fuel Cell Theory

Ever since the initial discovery of their fundamental principles in 1839 by Sir William Grove and the first development of a fuel cell system by Francis Bacon a century later, fuel cells have seen fluctuating scientific attention. The initial systems were based on liquid alkaline electrolytes and were used in pioneering projects at that time, such as the Apollo programme. Over the time, however, various other types of fuel cells based on different types of electrolytes emerged. Amongst those, the phosphoric acid fuel cell (PAFC) was one of the first acidic fuel cells and was the first one to be considered commercially viable for mainstream power production [18].

However, with the invention of the solid polymer electrolyte, another acidic fuel cell, the proton exchange fuel cell or polymer electrolyte fuel cell has been able to make a leap towards becoming a commercially attractive alternative to conventional energy converters in the past years. With this development, a simpler and lighter setup can be achieved, enabling the operation at lower temperatures and making these systems more attractive for various applications, such as automotive and stationary [18].

Within a polymer electrolyte fuel cell, hydrogen is converted to protons and electrons in the hydrogen oxidation reaction (HOR) on the anode. Protons travel through the polymer electrolyte membrane (PEM) and electrons through an external circuit towards the cathode. Thus, the electrical energy becomes directly usable. At the cathode, oxygen is reduced in the presence of protons and electrons in the oxygen reduction reaction (ORR), forming water (Figure 2), which exits the fuel cell with the cathode off-gas [19].

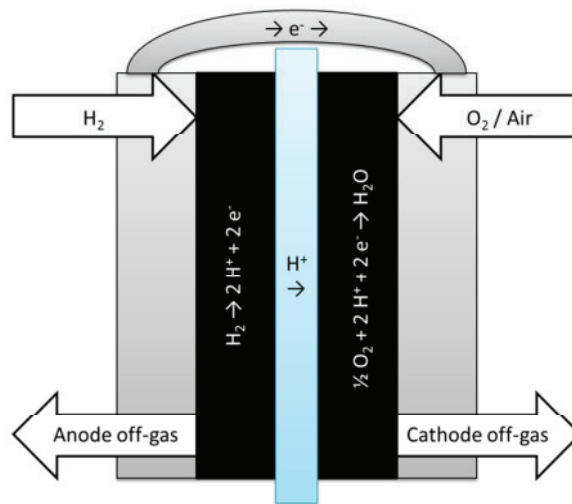


**Figure 2:** Principle of a polymer electrolyte fuel cell.

### 2.1. Operation Characteristics

The theoretic voltage of a fuel cell is defined by the electrochemical reactions on anode and cathode, respectively. The equilibrium between hydrogen and protons is the reference in the galvanic series, i.e. 0.000 V. Therefore, the theoretical maximum cell voltage ( $V_0$ ) in a polymer electrolyte fuel cell is defined by the oxygen reduction reaction and given as 1.229 V. A real fuel cell will, however, never reach such a high value. Depending on the operation temperature and whether or not the formed water is condensed, the ideal voltage drops. Additionally, in real cells, other factors contribute to an even lower value. Reactant crossover through the membrane leads to mixed potentials on the respective electrodes and therefore lowers the overall open circuit voltage (OCV) [18,20].

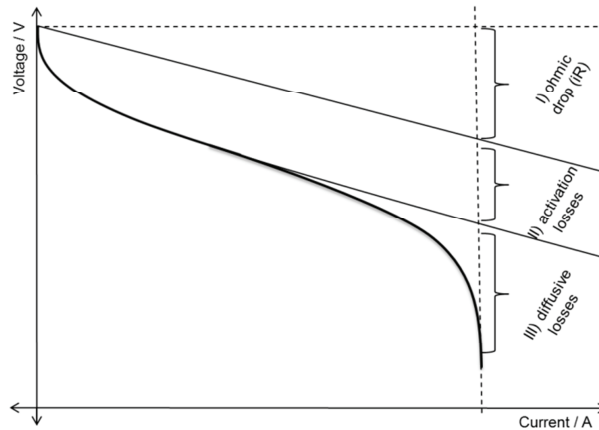


**Figure 3:** Polarisation curve with different losses [19].

Whereas the ideal current-voltage-characteristics show as little decline with increasing current density ( $i$ ) as possible, three different areas can be distinguished in real curves (Figure 3). At low current densities, the voltage ( $V$ ) declines, following a logarithmic behaviour according to the Tafel law. This is partially caused by the irreversibility of the oxygen reduction reaction. With a further increasing current density, the polarisation curve eventually exhibits a linear behaviour in the ohmic region (according to Equation 1). This is caused by the resistance ( $R_{\Omega}$ ), which mainly derives from the membranes resistance towards proton transport in this region. At high current densities, the voltage drops sharply in the diffusion limited region of the curve [20].

### Equation 1

$$V = iR_{\Omega}$$

The polarisation curve can be described by Equation 2.  $R$  is the ideal gas constant and  $F$  the Faraday constant. The kinetic and mass transport losses are included, as well as the ohmic losses [20].

### Equation 2

$$V = V_0 - \frac{RT}{F} \cdot \ln \left( \frac{i}{1 - \frac{i}{i_l}} \right) - R_{\Omega}i$$

This equation is, however, only applicable for a pre-determined position within the fuel cell. The behaviour of the full cell is better described by Equation 3, as it reflects local variations.  $a_1$  (V) and  $a_2$  ( $\text{cm}^2 \text{A}^{-1}$ ) are parameters [20].

**Equation 3**

$$V = V_0 - \frac{RT}{F} \ln(i) - R_{\Omega}i - a_1 \exp(a_2i)$$

The power density (P) of a fuel cell is defined by Equation 4 and of fundamental importance for system manufacturing [20].

**Equation 4**

$$P = iV$$

2.2. Fuel Cell Efficiency

The theoretical maximum efficiency (Equation 5) is defined by the reactions' thermodynamics. At standard conditions, this equals a maximum efficiency ( $\eta_{max}$ ) of 83%. However, this value is impossible to achieve within a real fuel cell system due to voltage losses ( $\eta_{Voltage}$ , Equation 6) caused by the kinetics and a limited fuel efficiency ( $\eta_{Fuel}$ , Equation 7) [18,20].

**Equation 5**

$$\eta_{max} = \frac{\Delta G}{\Delta H}$$

**Equation 6**

$$\eta_{Voltage} = \frac{V}{V_{Nernst}}$$

Any stoichiometry higher than 1 results in a fuel efficiency lower than 100%. In real operation, this is, however, necessary to prevent starvation, ensure proper mass transport for the removal of water and contaminants as well as a homogeneous reactant distribution over the surface area of a fuel cell [21,22].

**Equation 7**

$$\eta_{Fuel} = \frac{1}{\lambda}$$

### 3. Membrane Electrode Assembly

The very core of a polymer electrolyte fuel cell is the membrane electrode assembly (MEA, Figure 4), as the electrochemical reactions take place within it. It consists of a polymer electrolyte membrane, sandwiched between two electrodes. Each electrode consists of a gas diffusion layer (GDL), a microporous layer (MPL) and a catalyst layer (CL). The latter is in direct contact with the PEM, whereas the other two layers are responsible to assure a proper reactant distribution, water management and enable electric and thermal conductivity. The right choice of properties is therefore fundamental in order to ascertain proper fuel cell operation.



**Figure 4:** Scheme of a membrane electrode assembly.

#### 3.1. Membrane

Even though electrolytes used to be liquid in initial fuel cell development, the benefits of solid electrolytes have become apparent and have almost completely displaced previous materials. By the use of ionomers, which are defined as ion conductive polymers, a simpler cell setup is possible, outdating the necessity of pumps and complex sealing [18]. The ideal membrane would possess the following qualities [23]:

- High proton conductivity
- Insoluble in water under the given conditions
- Impermeable for gases, including hydrogen and oxygen
- Electric isolator
- Mechanical, chemical and electrochemical stability
- Adequate water management
- High tolerance towards contamination

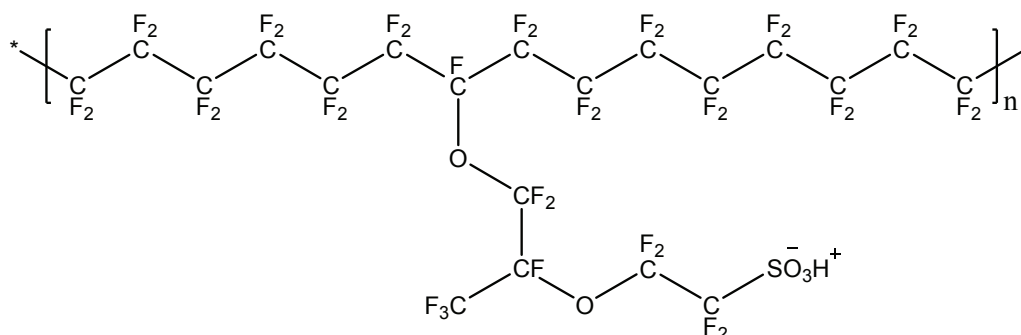


**Figure 5:** Chemical structure of Nafion® according to Chen and Schmidt-Rohr [24].

Polymer electrolyte membranes, as used in PEFCs, are usually perfluorinated ionomers, but other materials are possible as well. The most common PEM in fuel cells is Nafion®, which is a thin film of a perfluorosulphonic acid (PFSA) polymer. The polymer consists of a hydrophobic polytetrafluoroethylene (PTFE) backbone, with functional vinyl ether linked sidechains, terminated by hydrophilic sulphonic acid groups (Figure 5). The latter form clusters and channels, which enable the ionic conductivity of the ionomer. Proper humidification is crucial for both the channel formation and the ion mobility, as the acid groups have to be dissociated. This also limits the fuel cell operation temperature to below 100°C [25]. As the network forms in the presence of water, the membrane also swells [26]. When soaked with water, an unreinforced membrane can swell up to 140% [23] with typical membrane thicknesses in the range of 25 – 175 µm [25]. In order to minimise the mechanical stress, most available membranes are reinforced. This can be accomplished by implementing different materials into the membrane network. With non-conductive materials, such as zirconium phosphate or expanded PTFE sheets, the swelling of the ionomer itself is not altered, but the overall expansion of the membrane is reduced. However, a compromise between enhanced mechanical properties and the ionic conductivity has to be found [26,27].

PFSA membranes exhibit a high chemical stability in fuel cell environment, a high mechanical stability and a high ionic conductivity if humidified properly. With this type of membrane, stable operation has been reported for over 50,000 h [25].

### 3.2. Catalyst Layer

The electrochemical reactions take place within the catalyst layer. Therefore, the properties are of utmost importance. The catalyst layer has to provide the following properties [23]:

- Electrocatalytic activity towards the respective reaction
- Large electrochemically active surface area (ECSA)
- Excellent ionic and electric conductivity
- Efficient water and reactant gas transport – enabled by a high porosity with small pore sizes
- High chemical and electrochemical long term stability in the respective environment
- High tolerance towards contamination

Therefore, the CL is required to contain the catalyst, which is usually supported by an electrically conductive material such as carbon and ionomer to provide the necessary ionic conductivity and also to function as a binder [25]. Most common fuel cell catalysts are based on platinum nanoparticles on carbon support, but also various other types of alloys are possible [23]. For fuel cells with platinum electrocatalysts, metal loading in the range of  $0.2 \text{ mg cm}^{-2}$  with 30wt% Nafion® content have achieved high power densities [28]. When manufactured with pore formers, a porosity of up to 65% can be achieved with a typical pore size in the range of 0.01 to 0.5  $\mu\text{m}$ . The total CL thickness is, in dependence on the preparation method, in the range of 10 to 30  $\mu\text{m}$  [23].

### 3.3. Microporous Layer

The microporous layer is typically applied onto the GDL and has a similar porosity as the catalyst layer. The MPL has an evening effect on the gas diffusion layer and thus ensures an improved distribution of the catalyst layer. With its hydrophobic character, it aids the water transport, provides electrical conductivity and enhances the reactant gas transport. As is the case for the CL

composition, the right ratio between the binder (typically PTFE) and carbon is fundamental for optimised fuel cell operation [25]. A typical thickness is in the range of 30 to 60  $\mu\text{m}$  [23].

### 3.4. Gas Diffusion Layer

The gas diffusion layer with a thickness in the range of 200 – 400  $\mu\text{m}$  is typically made of carbon paper or cloth with pore sizes in the range of 10 to 30  $\mu\text{m}$ , treated with 5 – 10wt% PTFE to ensure hydrophobicity for optimised water management. This is necessary to ensure the following properties [23]:

- Electric and thermal conductivity
- Mechanical stability and support for the entire MEA
- Suitable mass transport properties regarding water and reactant gas transport

The pore size has to be adapted accordingly in order to ensure optimal mass transport and inhibit the accumulation of condensed water. This is especially important on the cathode, as it is necessary to remove excessive amounts of product water in relation to the current density [25].

## 4. Single Cell Design

### 4.1. In-house Segmented Single Cell

For the experiments conducted during the completion of this thesis, an in-house built cell with a segmented cathode was used (Figure 6) [3,29]. The current was detected in  $3 \times 10$  segments over a rectangular surface area of  $25 \text{ cm}^2$ , using shunt resistors. However, this layout is unique and thus incomparable with vast parts of the literature. Thus, for further research, a different design was chosen.

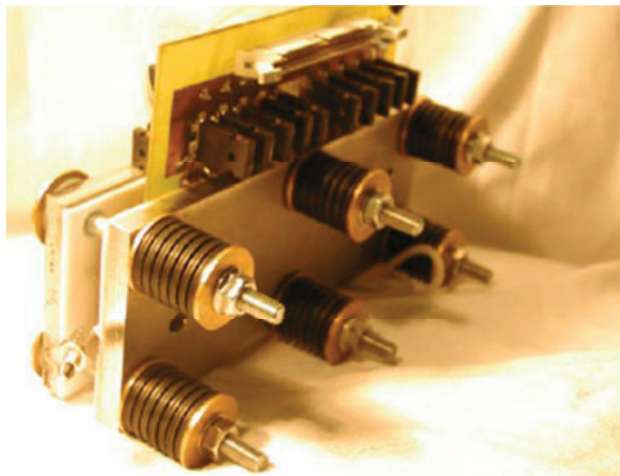


**Figure 6:** In-house built segmented single cell [29].

### 4.2. Standardised Layout

Various layouts are available for the PEFC. The flow field pattern strongly influences mass transport properties, water management and current density distribution and it is usually necessary to compromise.

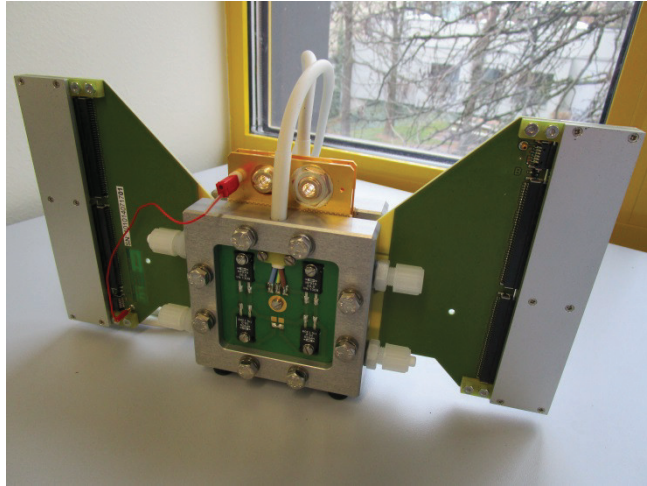


**Figure 7:** Commercial segmented single cell (S++ Simulation Services, Germany).

For the sake of comparability, a new 5\*5 cm<sup>2</sup> single cell (S++ Simulation Services, Germany, Figure 7) was purchased.

A single cell with a segmented cathode current collector with 10\*10 segments and 5\*5 segments for temperature measurement was used. Graphite plate and carbon paper were not segmented.

With a 2.5 mm graphite plate, the error by transverse current was given as approximately 5% by the manufacturer under normal operation (R. Kraume, personal communication, 16.4.2014). Two different types of flow fields were realised.

#### *4.2.1. Single Serpentine Layout*

Similar to the JARI - the Japanese standard test cell [30,31], a single serpentine layout with 1 mm channel width, depth and rib width was chosen (Figure 8). A single serpentine layout possesses a relatively long channel and a high pressure drop between inlet and outlet. This can be used for simulating a larger cell or stack.

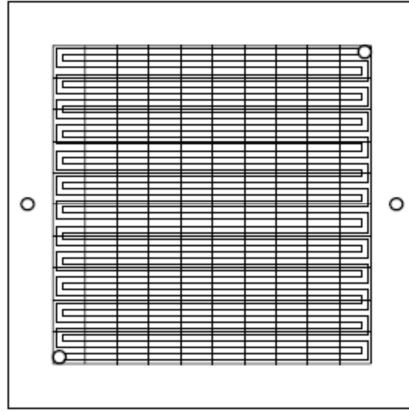


**Figure 8:** Single serpentine layout with segments.

#### 4.2.2. Three Channel Serpentine Layout

The second most common layout is the 3 channel serpentine flow field [31,32]. The channel width was chosen to be 0.8 mm, with a rib width of 0.8 or 1 mm for every third rib, respectively. The channel depth was chosen to be 1 mm (Figure 9). The pressure drop is smaller in this type of cell and the channel length is reduced compared to the single serpentine layout. It does, however, provide a better utilisation of the segments.

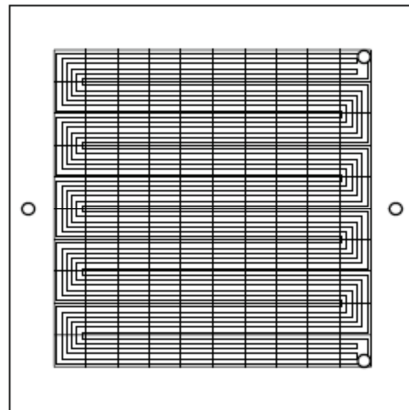


**Figure 9:** Three channel serpentine layout with segments.

#### 4.3. Reference Electrode

During planning of the single cell experiments, the possibility of characterisation with a reference electrode was included. The ability to determine the respective anode and cathode potential separately represents an immense gain of information. Therefore, a platinum wire with a diameter of 0.5 mm was implemented in the anode flow field as reference electrode. A schematic drawing is shown in Figure 10.

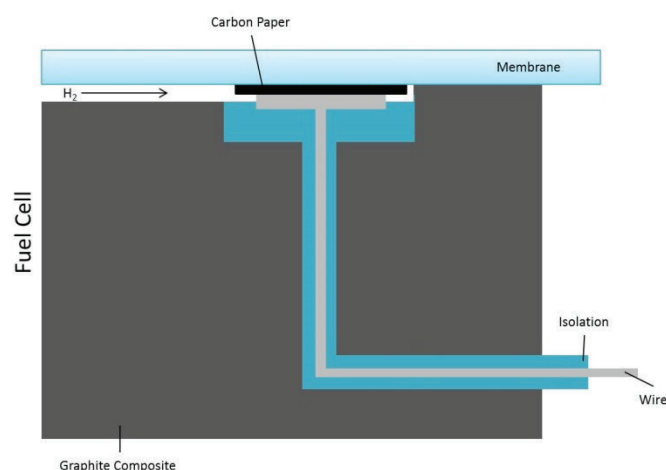


**Figure 10:** Scheme of a platinum wire reference electrode.

The detailed set up of the reference electrode is shown in Figure 11. Above the platinum wire, a carbon paper piece with a diameter of 2 mm was placed to ensure contact with the membrane.

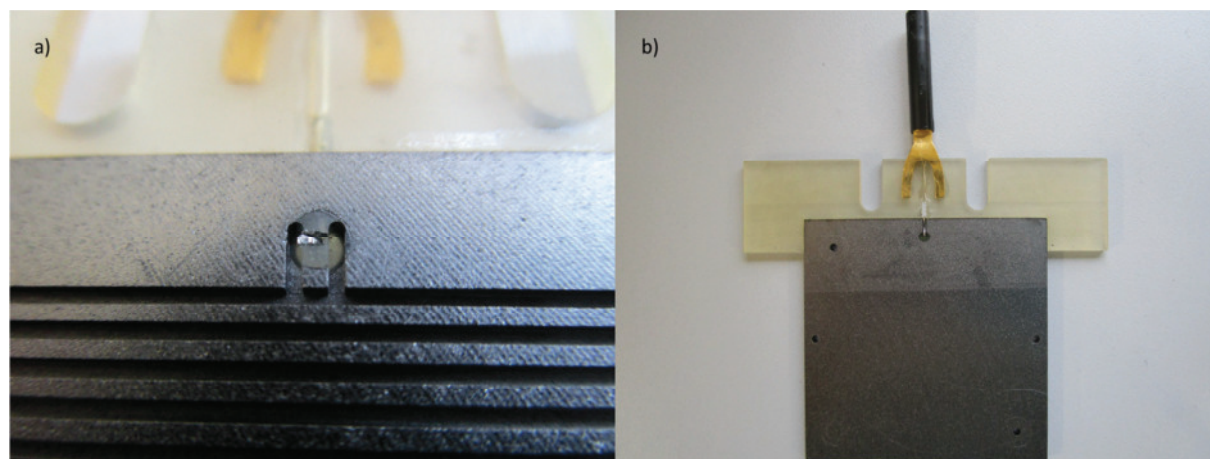


**Figure 11:** Reference electrode a) as implemented in the flow field and b) as implemented in the graphite plate.

*Note:* The connection was highly instable. Replacing the carbon paper piece with a piece of membrane in identical dimensions resulted in a slightly more stable connection. However, measurement was still not reliable and thus the reference electrode experiments were not extended for the sake of other, more promising approaches.

## 5. Characterisation Methods

Multiple different characterisation methods were applied in order to obtain a deeper understanding of the fuel cell characteristics, operational parameters as well as the degradation mechanisms.

### 5.1. Electrochemical Characterisation

Electrochemical characterisation was conducted in-situ in all cases. The single cell was operated at the conditions described individually for each experiment.

#### *5.1.1. Polarisation Curves*

Steady state polarisation curves are recorded galvanostatically, whilst the cell voltage is obtained. Each current step is held for two minutes or more, of which only the last minute is used for calculation (Figure 12).

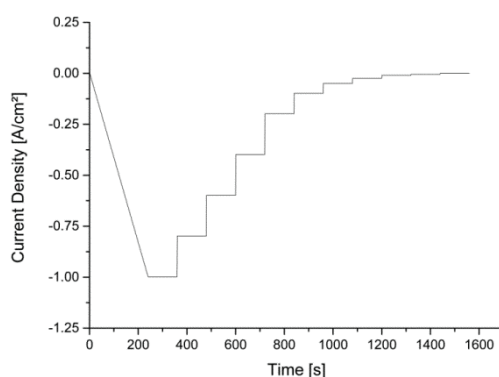


**Figure 12:** Example of the current density characteristics over time for a polarisation curve.

If not stated otherwise in the experiments, the gas flow is adapted to maintain a steady stoichiometry until the minimum of the mass flow controllers is reached.

#### *5.1.2. Electrochemical Impedance Spectroscopy*

Impedance is defined as the resistance towards alternating current. Figure 13 shows the equivalent circuit of a half-cell with the double layer capacity  $C_{dl}$ , the charge transfer resistance  $R_{t,M}$  and the electrolyte resistance  $R_e$  [33].

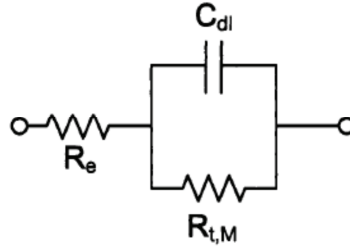


**Figure 13:** Electrical circuit of the impedance of a single electrochemical reaction [33].

For fuel cell characterisation, the electrochemical impedance spectroscopy (EIS) is recorded by forcing a sinusoidal current or voltage signal on the cell at a steady operation point. The respective response is recorded for a frequency spectrum and depicted in a Nyquist plot (Figure 14) [34].

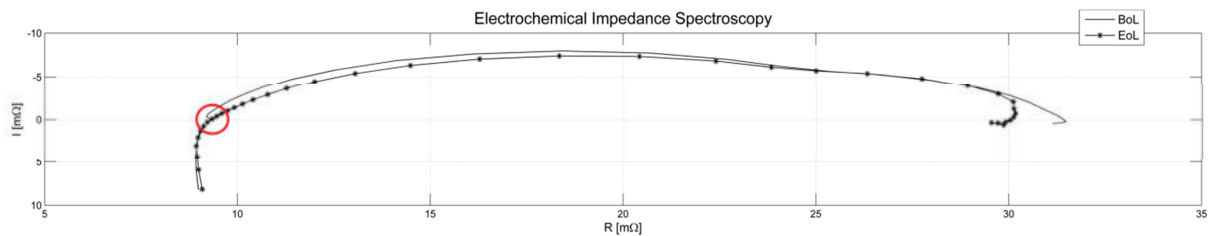


**Figure 14:** Nyquist plot of an MEA before and after AST testing in [2] at a current density of  $0.2 \text{ A cm}^{-2}$ .

The real part (depicted as  $R$ ) can be described by Equation 8 with  $\omega$  being the frequency. If the frequency  $\omega \rightarrow \infty$ , the real part equals the high frequency or electrolyte resistance and can be read from the Nyquist plot, as indicated in Figure 14 [33,34].

### Equation 8

$$R = R_e + \frac{R_{t,M}}{1 + \omega^2 R_{t,M}^2 C_{dl}^2}$$

#### 5.1.3. Hydrogen Diffusion Measurements / Linear Sweep Voltammetry

Ahead of every hydrogen diffusion measurement, the cathode is purged with nitrogen until the voltage drops to below 90 mV. The anode gas flow is pure hydrogen with a flow rate of  $87 \text{ ml min}^{-1}$  and  $413 \text{ ml min}^{-1}$  of nitrogen on the cathode side during experiment, if not stated otherwise. Temperature and humidification are not altered.

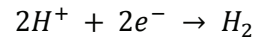
A voltage of 430 mV is held for one hour and the responding current is recorded. Thereby, all hydrogen, crossing through the membrane is oxidised at the

cathode. The given protons travel back to the anode side, where they are reduced.

Reaction at the cathode:



Reaction at the anode:



During linear sweep voltammetry (LSV), identical reactions take place as during hydrogen diffusion measurements. However, in this experimental mode, instead of keeping the voltage constant, it is changed over time, as the name indicates. The upper voltage limit was set to be 450 mV with a sweep rate of  $1 \text{ mV s}^{-1}$ .

High current values are an indicator for increased hydrogen crossover due to membrane thinning or even pinhole formation.

In this regard, anode and cathode refers to the respective electrodes during normal fuel cell operation.

#### 5.1.4. Cyclic Voltammetry

Cyclic voltammetry (CV) measurements are conducted straight after the hydrogen diffusion measurement and the same settings are used. Therefore, the cathode is already sufficiently purged with nitrogen. The order is reversed for some of the test series.

The voltage is cycled between a higher and a lower voltage (Figure 15). Typical values would be e.g. a sweep rate of  $50 \text{ mV s}^{-1}$  with 600 mV as the upper and 90 mV for the lower voltage limit.

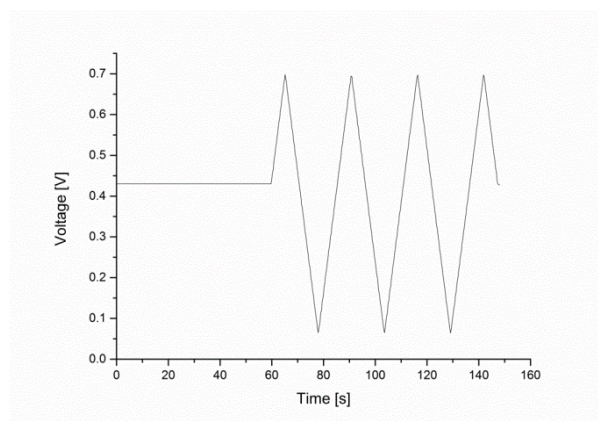


**Figure 15:** Voltage profile of cyclic voltammetry cycles.

From the hydrogen desorption peak ( $Q_{des}$ , Figure 16) the cathode catalyst surface area ( $A_{Pt}$ ,  $m^2 g^{-1}$ ) can be calculated according to Equation 9 after subtraction of the double layer (dashed line, Figure 16) and with knowledge of the electrode loading ( $L_{CA}$ ,  $mg cm^{-2}$ ) and the geometric area of the electrode ( $A_g$ ,  $cm^2$ ) [35].

### Equation 9

$$A_{Pt} = \frac{Q}{210\mu Ccm_{Pt}^{-2}(L_{CA}A_g)}$$

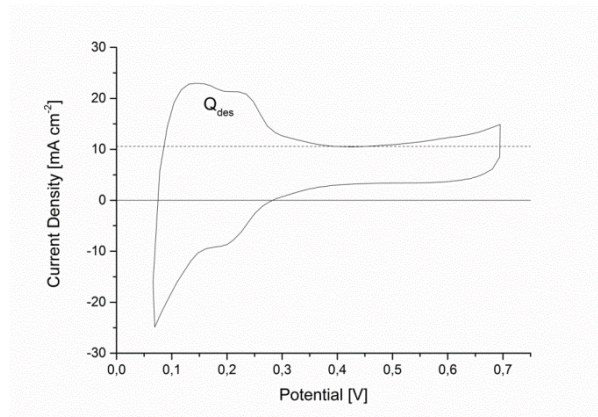


**Figure 16:** Example of a CV-curve including the hydrogen desorption peak ( $Q_{des}$ ) and the double layer (dashed line).

## 5.2. Additional Characterisation

In addition to the electrochemical characterisation, various methods of non-electrochemical characterisation were applied in order to fully understand degradation. Whilst off-gas and waste water analysis are non-destructive and, at least the first, in-situ; further analysis of the MEA is inevitably ex-situ and often destructive.

### 5.2.1. *Off-Gas Analysis*

Simultaneously with the electrochemical characterisation, the off-gas on either the anode or the cathode side is analysed with an online gas analyser (ABB). The concentrations of CO and CO<sub>2</sub> are analysed with two units set for different concentration ranges (Uras 14) by infrared spectroscopy. Hydrogen is quantified with a Caldos 17 unit by conductometry and oxygen with a Magnos 106 unit by using the paramagnetic properties of oxygen in a magnetic field.

### *5.2.2. Fluoride Selective Electrode*

The off-gases of anode and cathode pass through two separate condensation traps. The condensed water is quantified and samples are mixed with total ionic strength adjustment buffer II (TISAB II), as received from Thermo Scientific, at a ratio of 50:50. Thereby, all free metal ion contaminants are bound as metal complexes, thus do not reduce the fluoride activity. In order to determine the fluoride emission rate (FER) the solution is analysed in regards of fluoride ion content with a 9609BNWP fluoride ion selective electrode (F-ISE) from Thermo Scientific.

### *5.2.3. <sup>19</sup>F-NMR*

Nuclear magnetic resonance (NMR) is based on the relaxation of a nucleus with a certain spin in a magnetic field. <sup>19</sup>F is the only naturally abundant fluorine isotope and has, as well as <sup>1</sup>H, a nuclear spin of ½ and is thus NMR active [36]. Therefore, <sup>19</sup>F-NMR provides an excellent possibility to investigate the structure of Nafion® [24,37]. The results from NMR measurements were, however, not included in this thesis, but can be found in the master thesis of Mija Rami [38].

### *5.2.4. Computed Tomography*

Low energy X-ray imaging ( $E < 25$  keV) can be used to identify inhomogeneity in fuel cell electrodes, visualise spray pattern and millimetre-scale features on the surface of 5\*5 cm<sup>2</sup> electrodes [39].

X-ray beams with intensity in the range of 7 – 16 keV have a high sensitivity towards liquid water. Below 7 keV, almost all of the X-ray beam is absorbed by thicker water or electrolyte clusters and above 16 keV, the sensitivity towards smaller water agglomerations is lost [40].

With soft X-ray computed tomography (CT) with energy below 10 keV, morphological changes can be detected in the MEA without the destruction of it. This method allows a 3 dimensional visualisation of the MEA structure [41]. Various investigations were performed, utilising synchrotron radiation and X-ray diffraction to visualise water distribution [42].

### *Fuel Cell Degradation due to X-ray Exposure*

Degradation effects in fuel cells during in-situ characterisation by X-ray CT went unnoticed for a long time, since only a small part of the active fuel cell area was exposed. Yet, when exposing a major part of the membrane electrode assembly to X-rays, a noticeable damage occurs [43]. Performance loss due to radiation used for X-ray tomography (XTM) depends on the duration of exposure. The effects observed are known from common accelerated durability tests, yet failure

occurs faster. Degradation of the binding ionomer in the catalyst layer leads to delamination and thus decreased catalyst utilisation. Therefore, synchrotron radiation, as used for XTM imaging, interferes with fuel cell operation and causes irreversible degradation. With a beam energy of 13.5 keV, exposure time has to be limited to 100 s in order to avoid the measurement of artefacts [44].

Up to a beam intensity value of  $1.0 \text{ J cm}^{-2}$ , the performance degradation was found to be a function of the X-ray dose and independent of the intensity. The fuel cell is more prone to performance degradation when exposed to X-rays at a higher temperature and high relative humidity. The altered performance of the fuel cell causes additional heat load and affects the liquid water distribution. Impedance data show a higher membrane humidification with increasing X-ray dose and even catalyst layer flooding was indicated, caused by a reduced water contact angle [45]. The decrease of water surface tension and the decomposition of PTFE cause increased wetting and potential flooding, affecting the cathode more than the anode. It has been shown that the open circuit voltage can be restored after the irradiation beam is switched off. Though during consecutive operation, a serious performance decrease was noted, indicating severe and irreversible degradation of the fuel cell materials [42].

Also, the loss of sulphuric acid groups reduces the membrane conductivity [42]. Increased levels of sulphate that were identified in the product water might lead to reversible poisoning of the catalyst [45]. Additionally to the poisoning of the catalyst by sulphur compounds, the decomposition of the polymer electrolyte also leads to the release of  $\text{CO}_2$  as well as  $\text{CO}$ , with the latter being a strong catalyst poison as well [42].

The exact dose limit, however, highly depends on the cell design, orientation, operating conditions and the entire setup in general [46].

## 6. Fuel Cell Degradation

The individual fuel cell components are all exposed to different, but harsh conditions, often strongly changing with fluctuating and dynamic load requirements in a fuel cell system. These conditions induce mechanical and chemical failure. Thus, degradation of the individual components is a limiting factor for the system's overall lifetime. The most critical parameters for degradation are:

- Reactant crossover
- Low pH value
- High or fluctuating temperatures
- High, low or fluctuating humidity
- High cell voltage or cell reversal

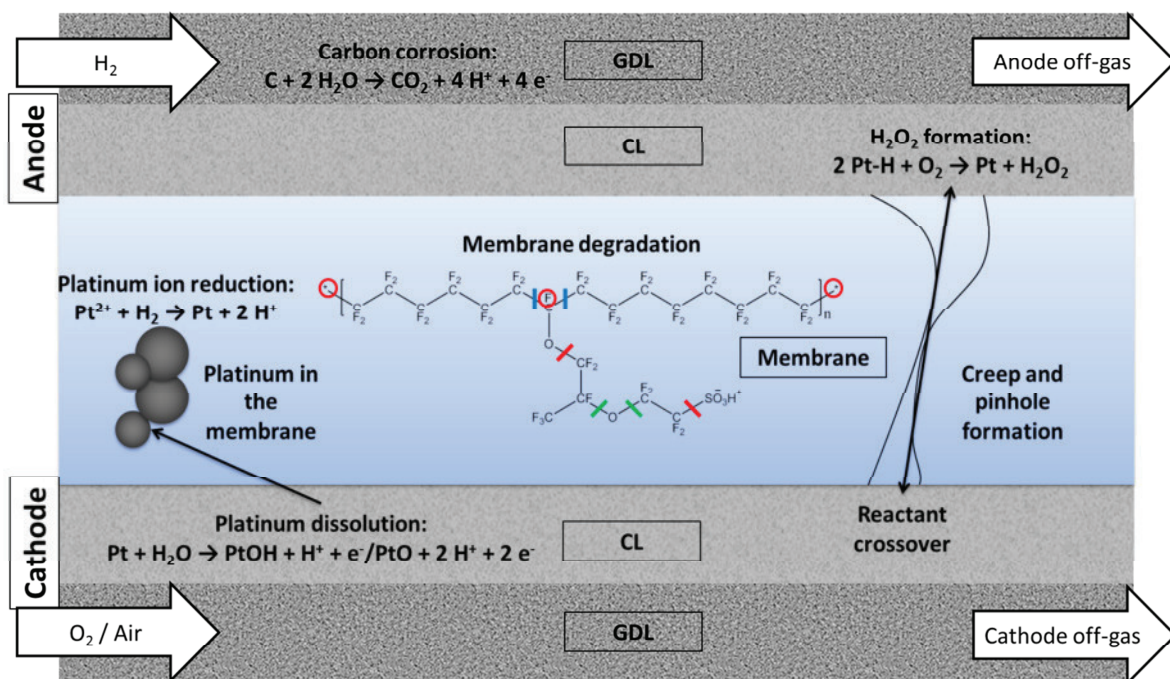


**Figure 17:** Overview of the different dominant degradation mechanisms in polymer electrolyte fuel cells

The affected components are mainly the gas diffusion layer, the catalyst layer and the membrane (Figure 17). Within the GDL, carbon corrosion is a major issue as carbon support material is lost due to oxidation, negatively affecting the

porous, electronic and hydrophobic properties of the electrodes. In the CL, the carbon catalyst support can also undergo oxidation. However, platinum electrocatalyst oxidation on the cathode is more fundamental. Platinum ions are either washed out or reduced, leading to platinum agglomeration or the formation of a platinum band within the membrane. Membrane degradation is either accelerated by mechanical stress, leading to creep and pinhole formation or by chemical degradation. The latter is caused by attack of the centres indicated in Figure 18 by radicals, which are formed from hydrogen peroxide. The different degradation mechanisms have been discussed extensively in multiple own publications [2–4,19,47]. Therefore, they will only be briefly listed, yet with an emphasis on the characteristic phenomena in different operation modes.

### 6.1. Membrane Degradation

For the polymer electrolyte membrane degradation, three different mechanisms can be distinguished.

The harsh environment of a fuel cell can lead to chemical decomposition of the ionomer. This is mainly triggered by the formation of radicals due to elevated gas crossover rates – especially at a high cell voltage – and in the presence of metal ion contamination. Radicals can then attack the polymer backbone as well as other weak bonds within the polymer structure, such as the ether bonds in the side chains (Figure 18). The chemical decomposition of the ionomer leads to the release of backbone and side chain fragments (proposed for the scission at positions indicated in blue and green) as well as hydrofluoric acid (proposed for the scission at positions indicated in red) in case of an unzipping mechanism. The detailed mechanism is well-described elsewhere [2,47–49].

Whereas the fuel cell FER can easily be determined using a fluoride ion selective electrode for effluent water analysis, fluorine bound in fragments is inaccessible for this method. Thus, the decomposition of the oligomeric fragments is necessary in order to fully quantify polymer electrolyte membrane degradation [38,50]. By treating the fuel cell effluent water with alkali at elevated temperatures, the remaining fluorine bonds are broken and all fluorine becomes accessible for analysis. Untreated samples give the fluoride emission rate and the treated samples the total fluorine emission rate (tFER), the difference of these two values gives the fluorine emission rate (FnER). Thus, FnER represents selectively the emission of oligomeric ionomer fragments, which allows

elucidating the respective underlying degradation mechanism. This is discussed in chapter 8.1 of the present thesis.

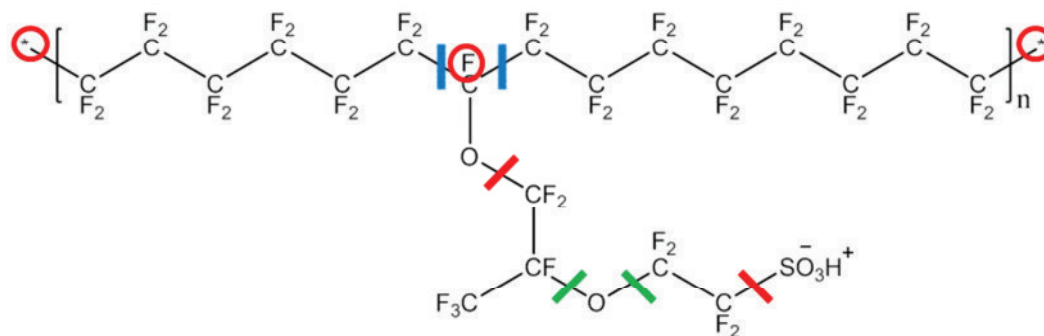


**Figure 18:** Centres prone to radical attack in the Nafion® ionomer according to Coms [49] (red and blue) and Ghassemzadeh and Holdcroft [51] (green).

PFSA membranes can also undergo thermal degradation. Up to 275 °C, the membrane has been reported to only lose water. At temperatures in the range of 275 to 450 °C, the sulphonic acid groups and side chains are decomposed, releasing SO<sub>2</sub> and HF, respectively. Eventually, at 550 °C the complete polymer decomposition was reported [52]. However, such temperatures are highly unlikely to be seen in normal fuel cell operation and would indicate much worse effects regarding fuel cell degradation. The glass transition temperature of Nafion® is, however, in the range of 120 - 130 °C. This is utilised for the MEA manufacturing process [23,27], but obviously has to be avoided during normal operation to mitigate harmful deformation of the membrane.

The membrane swells during water uptake, as has been discussed previously, and shrinks if dried. Within the membrane electrode assembly this causes strain and can result in the formation of cracks and pinholes. Since this is neither caused by chemical nor thermal effects, this degradation mechanism is referred to as mechanical degradation [2,47,53].

Although these different mechanisms can be well distinguished in theory, they strongly overlap in reality [53].

## 6.2. Carbon Corrosion

As carbon based support is used as GDL, within the MPL and as catalyst support, carbon degradation has a significant impact on the stability and duration of fuel cell operation. Amongst different effects contributing to it, one of the most obvious factors is fuel starvation on the anode. If the anode is depleted from

hydrogen and the cell voltage left uncontrolled, the voltage drops and carbon is oxidised instead of the intended fuel. This results – in dependence on the potential – in the emission of CO and CO<sub>2</sub>, respectively [54]. As carbon is lost irreversibly, the structure of the electrodes is altered. This affects the water management, the gas distribution properties, heat management and even the electric conductivity. If the carbon support of the catalyst is degraded, platinum nanoparticles are isolated and can no longer contribute to the catalytic reaction. Thus, carbon support corrosion has a significant impact on fuel cell operation. Hydrogen starvation is one of the most obvious causes, but can be avoided fairly easy. Other failure modes, such as radical formation, however, are more complex to mitigate [3,47].

### 6.3. Catalyst Degradation

Most polymer electrolyte fuel cell catalysts are based on platinum nanoparticles on carbon support, as discussed above. However, the large surface area equals also an extensive surface energy and thus agglomeration is one of the fundamental issues as all systems thrive towards an energetic minimum. This is partially, but not solely, driven by oxidation and dissolution of platinum metal and appears more detrimental on the cathode. Metal ions can be washed out of the fuel cell and reduced by crossover hydrogen, forming a platinum band within the membrane or redeposit within the electrode. The first two modes result in an irreversible loss of platinum, but all mechanisms result in a reduction of the catalytically active surface area [3,47].

### 6.4. Degradation in Real Systems

Degradation is strongly influenced by the respective operation conditions and thus, beside material properties, the operation mode determines the type of failure, eventually causing the end of life (EoL). Fuel cells for automotive applications have become of ever-growing interest, as they are a suitable substitute for internal combustion engines (ICE), operating at a high efficiency and without the loss of customer convenience. In battery electric vehicles (BEV) for example, long charging times are an obstacle for commercialisation. However, fuel cells suffer from degradation in the case of strongly changing power demand and the corresponding instable operation point. This can be mitigated to a certain degree by the implementation of back-up batteries or

capacitors to cover load peaks. However, undesirable effects cannot be completely avoided. Also, fuel cells for automotive applications undergo various SU-SD cycles and strongly varying temperatures over their lifetime. All this contributes to a shortening of their durability and only the avoidance of degradation enables a broad commercialisation of fuel cells [12,55].

Stationary systems, on the other hand, benefit from very stable operation conditions with only few SU-SD cycles over their lifetime. A change of energy demand is limited to different residential requirements and depending on the respective season and time of the day; both being more predictable than any automotive condition. A very high efficiency is possible, as the thermal energy can be utilised as well [10,55].

#### *6.4.1. Automotive*

Dynamically changing load conditions affect fuel cell materials in various ways, as multiple harmful conditions overlap. The two dominant issues due to the changing load conditions in automotive applications are water management and the dynamic response of the control system. At peak current density values, extensive amounts of product water can condense and accumulate within the electrode porous structure, leading to flooding. The pores are blocked and the concentration overpotential increases. On the other hand, in case of a sudden load increase, the system will respond by adapting the flow rate, resulting in water drag out and thus dehydration of the membrane. The membrane resistance and thus the ohmic drop increases and membrane degradation is accelerated. Additionally, late response to increased load conditions results in reactant starvation and thus carbon corrosion and the corresponding loss of electrochemically active surface area [55].

#### *6.4.2. Stationary*

In order to assess degradation in stationary systems, two stacks with a power range of 1.5 - 2 kW with 55 cells each were operated for 12,860 h at a current density of 0.26 A cm<sup>-2</sup> and at 60 - 65 °C by De Moor et al. [56]. During operation, the system underwent approximately 250 SU-SD cycles and had to be shut down due to low cell voltage in some cells. The respective cells displayed higher gas leakage, detected at random locations in the cell, but preferentially cells near the stack anode inlet were affected. This is due to the strong gradient in humidification, as hydrogen is fed dry, whereas air is humidified and the cell operated in counter flow. Examination of the membrane shows that the polymer electrolyte degrades at a higher rate on the anode than on the cathode. Degradation is for both electrodes more extensive near the anode inlet than

further down the channel. Extensive anode polymer electrolyte degradation accelerates the degradation of the cathode polymer electrolyte by enabling gas crossover and thus radical formation. Membrane reinforcement, however, guarantees electric isolation and prevents short circuit.

#### *6.4.3. Beneficial Effects from Ageing*

For normally operated fuel cell stacks held at a steady state current, an improvement of the mechanical adhesion between electrodes and membrane over the time in service was documented. The adhesion is stronger on the anode than on the cathode, probably due to the presence of native defects or the difference in thicknesses. During ageing, the binding agent, i.e. Nafion®, undergoes chemical degradation and a more organised phase is formed within the catalyst layer, with a higher probability of crystallisation. The binding agent is redistributed and thereby may cause the improvement of the mechanical properties [57].

A positive effect on fuel cell durability due to the formation of a platinum band within the membrane was documented in aged MEAs. This has been speculated to inhibit membrane degradation by catalysing the decomposition of hydrogen peroxide into non-harmful species [2,58].

## 7. Accelerated Stress Tests

With duration targets of 5,000 and 40,000 hours in operation for transportation and stationary applications [59], respectively, full lifetime testing is barely feasible for real systems. Therefore, accelerated stress tests need to be developed in order to identify potentially critical degradation modes, compare different systems and, ultimately, predict the durability.

Even though various attempts have been made in the past, a reliable lifetime prediction based on AST data is still difficult, as the failure modes vary and follow complex and non-linear pattern [60].

### 7.1. ASTs for Specific Component Testing

Both the U.S. American Department of Energy (Table 1) and the European Commission's Joint Research Centre (JRC) recommend specific test protocols for harmonised material durability validation [61,62].

**Table 1:** Operation parameters suggested by the DoE [61].

		<b>Electrocatalyst cycle</b>	<b>Catalyst support cycle</b>	<b>Chemical membrane degradation</b>
<b>Operation parameters</b>				
<b>Cell</b>	Cell temperature /°C	80	80	90
	Pressure /bara	atm.	atm.	1.5
	Relative humidity	100% / 100%	100% / 100%	30% / 30%
<b>Anode</b>	Gas type	H <sub>2</sub>	H <sub>2</sub>	H <sub>2</sub>
	Stoichiometry	-	n.d.	10**
	Gas flow rate /ml min <sup>-1</sup>	200*	n.d.	-
<b>Cathode</b>	Gas type	N <sub>2</sub>	N <sub>2</sub>	Air
	Stoichiometry	-	n.d.	10**
	Gas flow rate /ml min <sup>-1</sup>	75*	n.d.	-
<b>AST parameters</b>				

Type	Triangle sweep	Triangle sweep	Steady state
Voltage /V	0.6 - 1.0	1.0 - 1.5	OCV
Sweep rate /mV s <sup>-1</sup>	50	500	-
Cycle duration /s	16	2	-
Number of cycles	30,000	5,000	-
Total duration /h	133.33	400.00	500.00
	* for a 50 cm <sup>2</sup> cell		** at a reference current of 0.2 A cm <sup>-2</sup>

### 7.1.1. OCV Hold Tests

As maintaining the fuel cell under OCV conditions provokes hydrogen peroxide formation, this is utilised as accelerated stress test specifically for membrane degradation. Experiments have shown that the performance as well as the voltage decay rate and the ohmic resistance are depending on the gas flow rates under OCV conditions. The trend of the fluoride emission rate is, however, more complex, as the initial FER reflects the proportionality of the flow rates well, but declines in the investigated cases at different speeds. This is opposed to what would be expected [63].

The DoE proposed an OCV hold protocol for selective membrane degradation in which a single cell is held at open circuit conditions for a total of 500 h at a temperature of 90 °C, relative humidity of 30% and gas flow rates according to a stoichiometry of 10 at a current density of 0.2 A cm<sup>-2</sup> on both anode and cathode (Table 1). Fluoride release rate, hydrogen diffusion current and high frequency resistance are recorded every 24 h [61].

### 7.1.2. Voltage Cycling

Since the oxidation state of Pt is depending on the potential, voltage cycling can be utilised to selectively enforce catalyst degradation. Therefore, the potential ranges are set to be 0.6 and 1.0 V for the dissolution of platinum, avoiding contributions from other degradation modes. Below 0.6 V, platinum may redeposit and beyond 1.0 V, the platinum catalyst degradation overlaps with carbon corrosion. The latter effect is targeted by another AST for selective carbon support degradation through cycling the potential above 1.0 V [64]. The Pt dissolution rate increases with increasing potential in the range between 0.65 to 1.1 V. Above 1.1 V, however, a decreasing Pt ion concentration was found due

to the formation of a protective Pt-O layer, inhibiting dissolution [65]. Beside the voltage range, the wave form, gas flow rates on anode and cathode as well as the temperature also have a strong impact on Pt-loss and have been studied previously [64].

At a potential of 0.207 V vs. the reversible hydrogen electrode (RHE), carbon corrosion can theoretically set in. Carbon surface oxides have, however been found to form at electrode potentials above 0.8 V and an acceleration of carbon oxidation was found to occur at potentials exceeding 1.2 V. Thus, potential cycling in the range of 1.2 V is best suited to induce carbon support corrosion, as is already mentioned above. The choice of the upper potential limit might also affect the fuel cell degradation. 1.4 V is close to the potential the cathode reaches during reversed current and local fuel starvation. It is also the potential above which the oxygen evolution reaction starts, which would also affect the degradation mode due to mechanical effects [65].

Dhanushkodi et al. [65] applied five different ASTs in a single cell experiment with three MEA types with different cathode catalyst loadings. In all cases, an empirical exponent expression correlation between the performance loss and carbon emission was found. This is, however, restricted to each type of MEA, but can be utilised as a helpful tool to predict performance loss in drive cycle tests using the carbon emission data.

In a study by Bi and Fuller [66], the potential was cycled between 0.87 and 1.2 V in a square wave pattern with dwell times of 30 s at each potential. The AST was performed at 40, 60 and 80 °C in order to determine the effect of the temperature on the fuel cell behaviour. It was noted that a higher temperature resulted in an increased fluoride emission rate, yet the FER was still low in comparison to ASTs designed for membrane degradation testing. The dissolution rate of platinum and thus the loss of ECSA also increased with the temperature and a Pt band was formed in the membrane with its size depending on the operation temperature. Higher temperatures led to more platinum, deposited in the membrane and the remaining cathode catalyst particles exhibited an increased average particle size. At a temperature of 80 °C, significant carbon corrosion occurred on the cathode due to the high potentials.

### Catalyst Ageing Protocols

In the Fuel Cell Technical Team (FCTT) Roadmap, a triangle sweep test with 30,000 cycles and a ramp of 50 mV s<sup>-1</sup> in the range of 0.6 and 1.0 V (Table 1) for single cells with 25 – 50 cm<sup>2</sup> was proposed in 2013 with conditions last revised 2010 [61]. In these protocols, a single cell is fed with hydrogen on the anode and nitrogen on the cathode with a relative humidity of 100% on both, at

atmospheric pressure and a cell temperature of 80 °C. For a 50 cm<sup>2</sup> fuel cell, the hydrogen feed rate is 200 ml min<sup>-1</sup> and 75 ml min<sup>-1</sup> of nitrogen, respectively. Dhanushkodi et al. [64] proposed an accelerated stress test under similar conditions, but with air on the cathode and a square-wave voltage signal with dwell times of 3 s for each voltage step instead, as a higher rate of performance losses had been reported under these conditions. Three different temperature set points were chosen at 40, 60 and 80 °C. At a higher temperature, higher rates of open circuit voltage drop were recorded and also higher voltage decay rates at low and high current densities were noted. The temperature also affected the formation of a platinum band within the membrane. At higher cell temperatures, the band was more intense and at a larger distance to the cathode, from where it originated. Performance loss and loss of electrochemically active catalyst surface area increase with temperature and correlate, yet not linearly at 80 °C. This could be due to a change of more fundamental properties, since also the speed, at which the characteristics change, changes as more cycles are conducted. In general, at 40 and 60 °C, Pt loss was the predominant factor in MEA degradation. At 80 °C, however, changes in both catalyst and membrane were noted.

#### Carbon Support Ageing Protocols

Similar to the catalyst ageing protocol, the Fuel Cell Technical Team Roadmap also proposed a voltage cycling test for carbon corrosion [61]. With a sweep rate of 500 mV s<sup>-1</sup>, the voltage is cycled between 1.0 and 1.5 V for a total of 5,000 cycles (Table 1). The conditions are chosen as for the catalyst ageing protocol. Thereby, the carbon support is expected to be oxidised selectively, limiting the effect on other degradation modes.

## 7.2. Multi-component Testing

Whereas the above-mentioned testing protocols are aimed to provoke degradation of selected components, real system failure induces multiple degradation modes at once. As they often correlate and interact, multi-component testing is a necessary addition in order to fully understand real life fuel cell failure.

### *7.2.1. Reactant Starvation*

Reactant starvation, especially on the anode, is one of the obvious and most detrimental issues in fuel cell operation. Dynamic load changes require a fast adaption of the respective gas flow rates. This is a major issue in system design

and manufacturing, as sudden increases in energy demand are barely predictable [67–69].

In the case of hydrogen undersupply, the cell voltage drops and carbon is oxidised instead of the fuel, as has been discussed above and in the corresponding literature [3,47].

Other than fuel starvation, an undersupply of oxygen merely leads to a voltage drop slightly below zero. The critical reversal air stoichiometry depends on the load. With a higher load, the voltage drops at a higher stoichiometry value. Tests have shown an increased temperature near the cathode inlet and a reduced temperature near the outlet. Thus, degradation is most likely caused by the temperature gradient [4,21].

### *7.2.2. Startup-shutdown Cycles*

Startup-shutdown cycling affects both mobile and stationary applications, but due to the operational mode, mobile or automotive applications face these conditions at a much higher frequency [70].

Prior to the fuel cell startup, the anode and cathode compartment are both filled with air and as hydrogen is fed to the anode side, the potential drops from that of oxygen and water on Pt ( $\sim 1$  V) to that of the reversible hydrogen electrode (0 V). However, near the anode outlet the potential is still high, as air is still present until purged out completely. This leads to a mixed overall potential on the anode with a strong gradient between inlet and outlet. With the high electric conductivity, given by the gas diffusion layer and the catalyst layer, the polarisation is strongly depending on the ionic conductivity. As the lateral ohmic drop of the ionomer is high, only a slight polarisation occurs amongst the anode inlet and anode outlet regions. However, protons can be transported towards the cathode, but without an external circuit, no reaction is possible. This leads to the oxidation of water, carbon support and platinum on the cathode in the area near the anode outlet. The potential rises in order to provide electrons for the oxygen reduction reaction on the cathode near the anode inlet and protons for the ORR on the anode side near its outlet, respectively (Figure 19). During shutdown, the reverse process occurs. Thereby, the fuel cell faces transient potentials on the electrodes due to the hydrogen/air front on the anode, resulting in corrosion of the cathode carbon catalyst support during SU-SD cycling. This can lead to a significant loss of performance due to a reduction of the active catalyst surface area. The topography and duration of these phenomena strongly depend on the gas flow rates, the load, the humidification and the flow field layout [70].

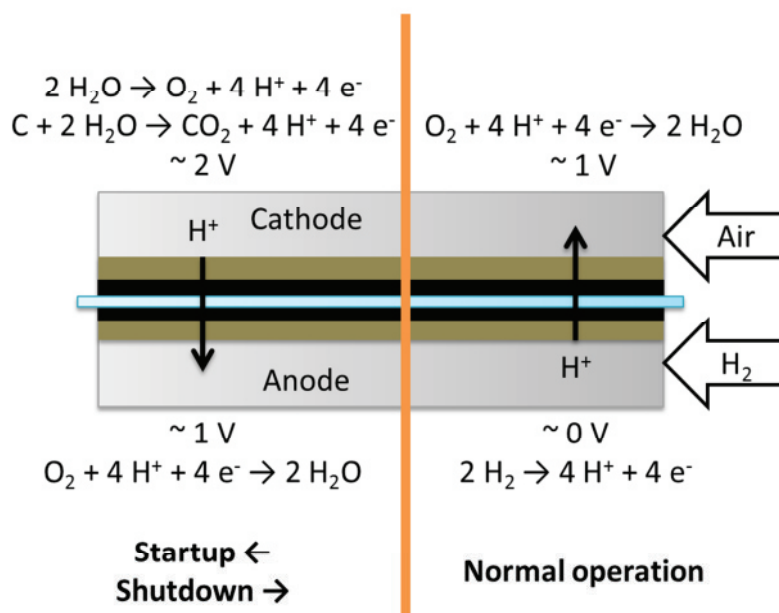


**Figure 19:** Fuel cell operation under normal conditions (right) and during SU-SD conditions (whole).

In experiments using a national physical laboratory (NPL) reference electrode [70], it has been shown that the fuel cell behaves differently during startup and shutdown. The latter decreases the driving force of the carbon oxidation reaction, as platinum is oxidised and more electrons and protons are generated for the oxygen reduction reaction in the anode compartment. On the other hand, during startup, platinum is reduced on the anode side at potential around 0.7 V, increasing the trend towards carbon oxidation. This results in a higher CO<sub>2</sub> content during startup than during shutdown, also correlating with a lower maximum potential on the cathode during shutdown. The CO<sub>2</sub> content also decreases with increasing humidity, as the total volume of the gas is higher due to the additional mass of water. This increases the total flow and consequently reduces the dwell time and minimises the area of exchange due to flooding [70]. Mitigation strategies may involve engineering solutions, such as inert gas purging, use of high flow rates to minimise the dwell time or applying an external load to avoid cathode polarisation. In experiments, it was shown that the external circuit has a stronger mitigating effect during shutdown than during startup due to hydrogen being consumed on the anode during purging, accelerating the purging of the anode. Alternatively, material based solutions are possible, such as reducing the anode platinum loading to avoid the ORR taking place on the anode, changing the cathode carbon support material or voluntarily

promoting the oxygen evolution reaction by adding catalyst to the cathode CL, catalysing the water oxidation over carbon oxidation [70].

### 7.2.3. Specific Tests for Mobile Applications

Fuel cells in automotive applications are required to withstand various dynamically changing load cycles. Therefore, a standardised test protocol is required as is available for internal combustion engines. The European commission therefore issued a protocol, which features a fuel cell dynamic load cycle (FC-DLC, Figure 20) in accordance to the load conditions, portrayed by the New European Driving Cycle (NEDC).

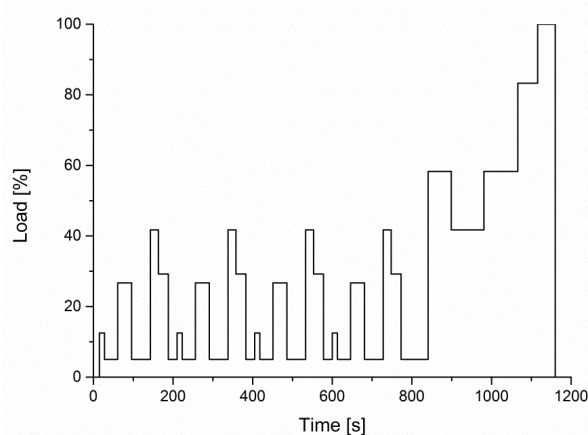


**Figure 20:** Fuel cell dynamic load cycle according to Tsoitridis et al. [62].

Enz et al. [12] used an adapted AST to investigate the effect of the NEDC on a fuel cell for automotive applications. They conducted the tests with various forerun times to induce either cathode or anode starvation or both at the same time. The chemical oxidation of carbon is favoured at electrode potentials close to 0 V on the cathode. Therefore, a higher carbon dioxide emission was noted in the case of critical operation with no forerun time prior to the load change, as this leads to oxygen starvation and thus a cathode potential drop. On the anode, the carbon corrosion is clearly related to fuel starvation, as carbon support is oxidised instead. Thus, the anode carbon emission rate is in general higher than on the cathode.

In a joined study by Argonne National Laboratory (Argonne) and the European Commission's Joint Research Centre by Bloom et al. [71], different testing protocols, all optimised in regards to transportation, were conducted on two different stacks and compared. The tests were performed according to the protocol by the DoE and the US Fuel Cell Council for a dynamic stress test (DST). The one used in the International Electro-technical Commission and the

FCTestNet (IEC), one for the New European Driving Cycle (European Commission for Europe (ECE)), as well as the wet protocol from the US Driving Research and Innovation for Vehicle Efficiency and Energy Sustainability Fuel Cell Technical Team were conducted. The trend in the performance decay rates correlated with the duration time at full power, thus indicating a connection between degradation and water produced during testing, as the same trend was documented in two different stacks.

Diloyan et al. [72] studied the effect of vibrations, as they might occur during normal driving cycles, on the Pt agglomeration and particle growth in polymer electrolyte fuel cells by combining an accelerated stress test designed for catalyst degradation with a mechanical vibration protocol. The average particle size was reported to be 10% smaller for the samples that had been exposed to vibration than those that were operated without vibration. However, the most dominant factor for catalyst agglomeration was time in this particular study.

#### *7.2.4. Specific Tests for Stationary Applications*

Stationary operation is defined by a constant load point in which the fuel cell or fuel cell stack is operated. Thus, since the MEA does not undergo such rapidly changing operation conditions as in a mobile application, many degradation modes do not occur and fuel cell lifetime is extended. However, the DoE goal of 50,000 h of stationary operation is still an obstacle. Therefore, Dubau et al. [73] applied a broad spectrum of analytical methods on selected MEAs withdrawn from a real life stationary fuel cell stack, which had been operated for 12,860 h in counter-flow at a current density of  $0.26 \text{ A cm}^{-2}$ , and compared their properties with those of a pristine MEA. They chose one MEA from the centre of the stack, which had shown only minor performance loss and one which exhibited a vast decay. Infrared thermography was used to detect pinholes in all membrane electrode assemblies. It was shown that the air outlet region of the cells was the most prone to the formation of holes in the polymer electrolyte membrane. Small holes were however found to not affect the fuel cell stack behaviour significantly and were even found in the pristine MEA. Those MEAs with larger defective areas caused a significant reduction of the global cell voltage. The selected MEAs were characterised using a segmented single cell as well as scattered electron microscopy (SEM) and transmitted electron microscopy (TEM). Thereby, it was shown that the less performing segments correlated with the areas of extensive cathode catalyst layer and GDL thinning. However, in these areas a substantial amount of platinum was still detected. The performance decay can thus be assigned to a loss of porosity and Pt agglomeration and

detachment, but not a loss of the platinum catalyst itself. Cathode thinning was more extensive for areas close to pinholes.

## 8. Experimental

Major parts of this thesis are available in peer-reviewed journals and can be found in the Appendix along with a complete list of my publications [1–4]. In this chapter, results, which are to a larger part unpublished, will be discussed in detail.

In addition to my previously published results, experiments have been performed with the aim to obtain a deeper understanding regarding Nafion® decomposition by determining the total fluorine emission rate. Experiments were also conducted according to the DoE protocol for chemical membrane degradation and according to the DoE protocol for electrocatalyst agglomeration [61]. The latter was adapted in order to understand the effect of water within the fuel cell on the degradation rate.

### 8.1. Determining the Total Fluorine Emission Rate

The practical work on fluorine analysis was performed by Mija Rami during completion of her Master thesis [38]. Therefore, the chapter dedicated to these results will be kept short, as the details can be found in her work. However, this is partially considered relevant in regard to the present thesis and thus is discussed as well.

#### *8.1.1. Theory*

As has been discussed above and in the literature [47,48], the decomposition of the polymer electrolyte results in the release of HF, which can be quantified by the use of a F-ISE. However, polymer fragments can be released in significant quantities as well and thus the fluoride emission rate is an insufficient parameter to quantify electrolyte degradation. Therefore, a method to determine the total fluorine emission rate is developed. The thermal decomposition of the ionomer is made use of and by adding different alkalis, released fluoride is captured.

#### *8.1.2. Experimental Setup*

A procedure that had been developed for Nafion® decomposition was adjusted to suit the requirements of effluent water samples in order to evaluate the tFER [38].

The accelerated stress tests were conducted in a 25 cm<sup>2</sup> single cell. The segmented cell was equipped with a membrane electrode assembly for stationary applications (IRD A/S, Odense, Denmark) and operated at 65 °C with a relative humidity of 80% at a reference current of 0.5 A cm<sup>-2</sup> and stoichiometries of 1.5 and 2 on anode and cathode, respectively. Each AST consisted of 100 cycles, during which the cathode stoichiometry was reduced either to 0.9, 0.7 or 0.0 once an hour for 10 seconds. In-between testing, the fuel cell was stored under nitrogen atmosphere at room temperature overnight [74].

The anode off-gas was washed by bubbling through a 1 M aqueous KOH solution to gather the effluent water and capture any volatile compound in the gas stream. The solution was changed and effluent water samples were taken every 100 hours of testing and after complete shutdown of the fuel cell, including the characterisation and purging.

From the solution, 100 ml samples are heated until dry, followed by thermal treatment at 500 °C for 7 h in lidded Ni-crucibles. After treatment, the samples were dissolved in deionised water, the pH adjusted to 7 with concentrated HCl and mixed with TISAB II in a ratio of 1:1. In untreated samples, the pH was also adjusted to 7 and mixed with TISAB II for F-ISE measurements [38,48].

### *8.1.3. Results and Discussion*

As is shown in Figure 21 a, the total fluorine emission rate vastly exceeds the fluoride emission rate without previous treatment. This is very much expected from the literature [38,48,50].

Subtracting the FER from the tFER gives the fluorine emission rate alone (Figure 21 b). This represents a better visualisation of the emission of oligomeric fragments from the ionomer. The distinction of the different fluorine sources is fundamental for assessing the underlying degradation mechanism.

It can be seen that the trend of the tFER becomes more distinguished for the FnER.

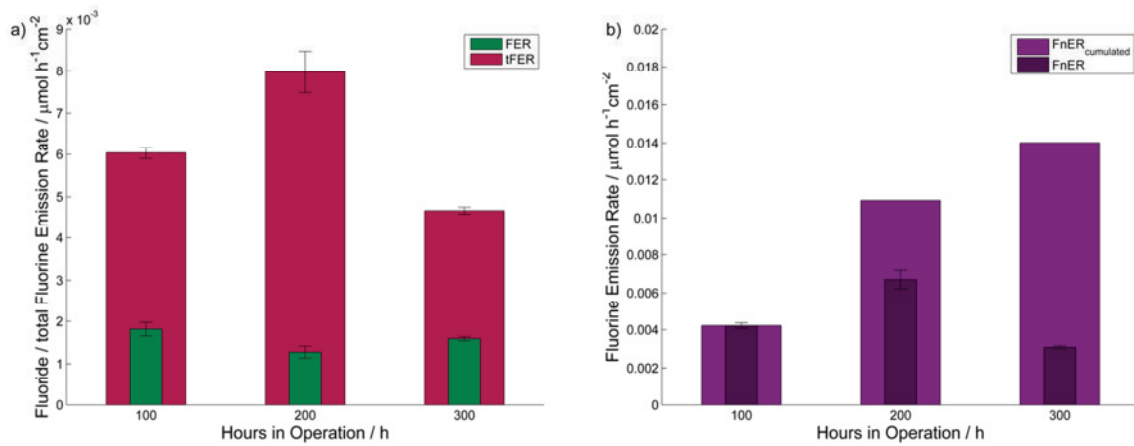


**Figure 21:** The respective emission rates of a) fluoride and total fluorine and b) of the fluorine emission rate without fluoride.

Figure 22 gives a comparison of the respective emission rates with the high frequency resistance (HFR). The latter is an inversely proportional characteristic of the membrane's ion conductivity, as has been discussed above. The values for beginning of testing (BoT) and end of testing (EoT) mark the respective values before and after a test. As the fuel cell was safely stored overnight, the BoT value for the respective hours in operation marks the HFR after the next startup and prior to the following 100 h of testing.

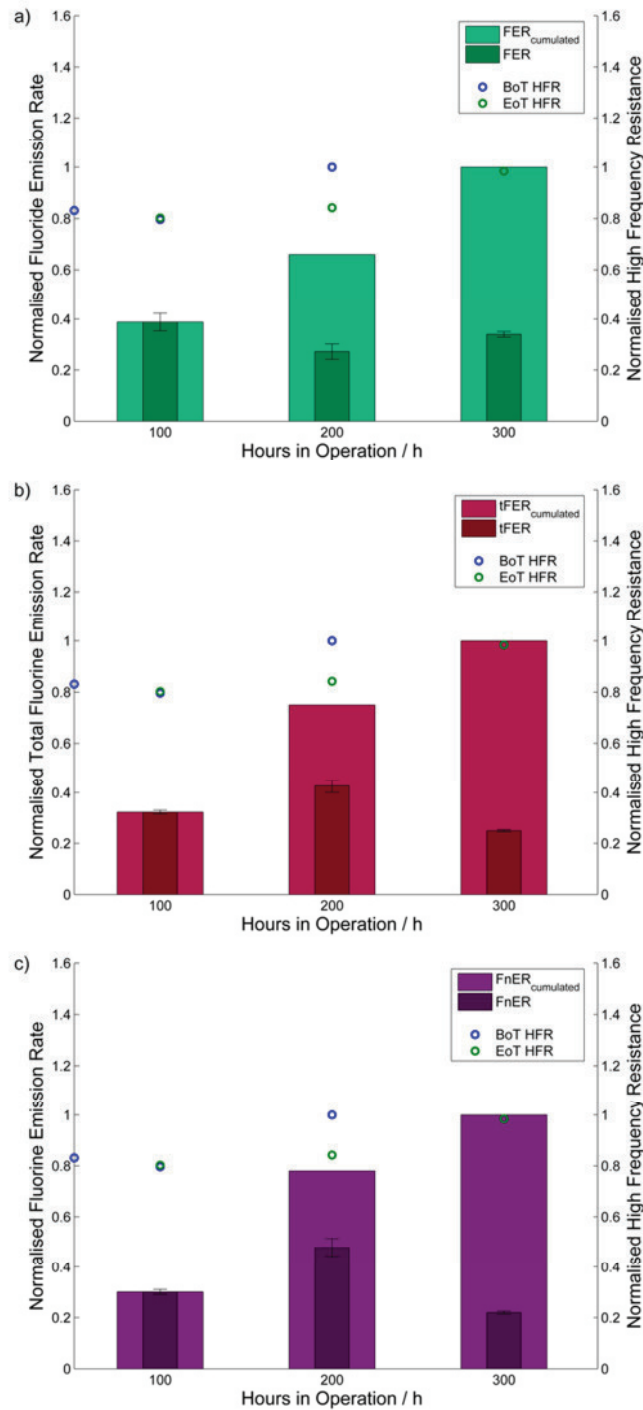


**Figure 22:** The normalised high frequency resistance in comparison to a) the normalised and cumulated normalised fluoride, b) the normalised and cumulated normalised total fluorine emission rate and c) the normalised and cumulated normalised fluoride emission rate without fluoride.

The HFR in Figure 22 a) does not correlate with the fluoride emission rate. No elevated FER is recorded as the HFR indicates after the startup and prior to the final test. Any emitted fluoride would be included in the 200 hours' sample. A

fairly better comparability can be found for the total fluorine emission rate (Figure 22 b), as the tFER value after completion of the 200 h test including shutdown exhibits a peak value. This value is even more distinct for the FnER (Figure 22 c).

It should also be noted that the membrane resistance at the end of testing of the 200 h test is not increased. After shut-down, however, the effluent water samples are collected, exhibiting an increased tFER and FnER. When the fuel cell is again characterised after startup, the HFR is clearly increased. Thus, during shutdown, detrimental conditions must have occurred, resulting in the dissociation of a significant amount of side chains [48]. The oligomeric fragments are released and the membrane conductivity is reduced.

#### *8.1.4. Conclusion*

The fluoride emission rates shown in the presented tests exhibit no correlation with the change in high frequency resistance. This was expected and supports the conclusion that the FER is not suitable for indicating the membrane degradation on its own. Thermal treatment of the samples makes the fluorine, bound in oligomeric residues, accessible for quantification. The thereby determined total fluorine emission rate is a more reliable indicator and correlates with the change of membrane resistance. With the knowledge of both FER and tFER, the fluorine emission rate can be obtained. This represents the emission of polymer fragments only and exhibits the best correlation with the change of membrane properties. Therefore, a more detailed understanding is possible.

The detachment of side chains is expected to directly affect the ion conductivity of the polymer electrolyte. The correlation of HFR and FnER indicates the release of sidechain fragments. In respect to the positions prone to chain scission in Figure 18, the results indicate predominant bond breakage at the centres proposed by Ghassemzadeh and Holdcroft [51], which are marked in green.

However, further experiments would be necessary to confirm this. The decomposition of the polymer backbone tends to lead to an increased HF emission rate. This would not necessarily lead to an immediate change of membrane properties, as was observed after the initial ASTs.

## 8.2. Chemical Membrane Degradation by OCV Hold Testing

Polymer electrolyte membranes are required to withstand a large variety and strongly alternating conditions to enable extended fuel cell durability. This is crucial to position fuel cells as commercially viable products. Only with

fundamental knowledge of the respective dominant degradation mode, it is possible to improve the used materials accordingly.

### *8.2.1. Theory*

The DoE AST aims to accelerate the ionomer decomposition by maintaining a single fuel cell at OCV conditions at an elevated temperature, low relative humidity and with a high gas stoichiometry on both anode and cathode [61]. As has been discussed above, membrane degradation is accelerated by OCV conditions, due to radical formation. This is a result of increased reactant gas crossover.

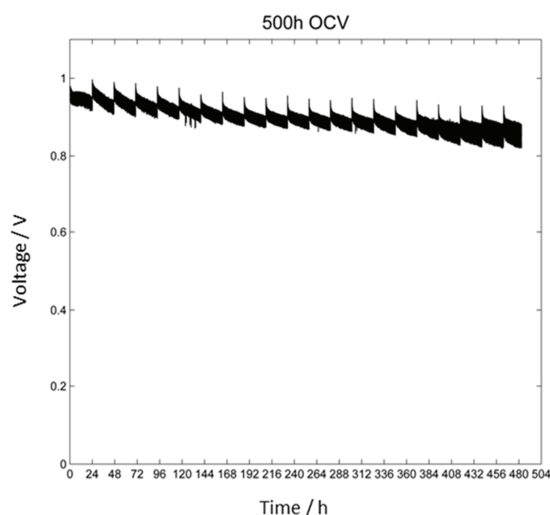
### *8.2.2. Experimental Setup*

A 25 cm<sup>2</sup> single cell with an MEA (IRD A/S, Odense, Denmark) for stationary applications was operated at the conditions according to [61]. The temperature was set to 90 °C with a relative humidity of 30% and a stoichiometry of 10 calculated for a reference current density of 0.2 A cm<sup>-2</sup> for both anode and cathode, respectively. However, as the technical setup did not allow as high pressures as required by the protocol, a pressure of 0.1 bar on anode and cathode was chosen, respectively.

The fuel cell was characterised initially and after 500 hours of testing using the conditions reported previously [3]. The high frequency resistance and the hydrogen diffusion current were recorded every 24 hours along with effluent water samples being taken for FER analysis. This experiment was partially conducted by Dr. Stephan Nestl.

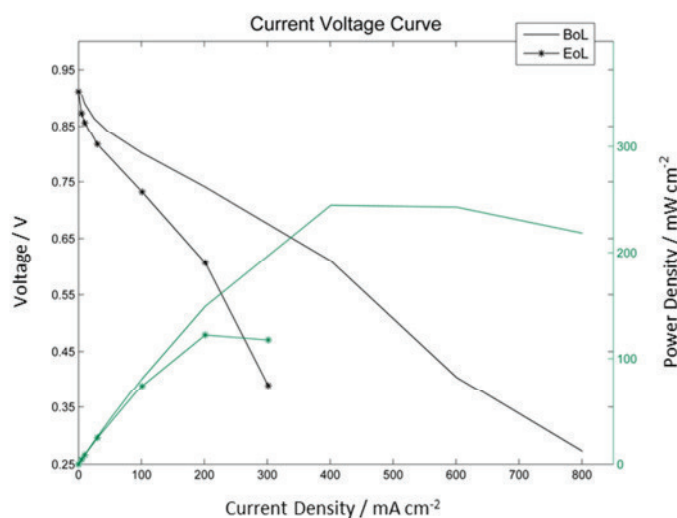
### *8.2.3. Results and Discussion*

The OCV was initially recorded with a value of 970 mV and gradually decreased over the duration of 500 h. Each interruption for testing led to a partial recovery of the voltage. The overall trend, however, exhibited a clear decline (Figure 23).



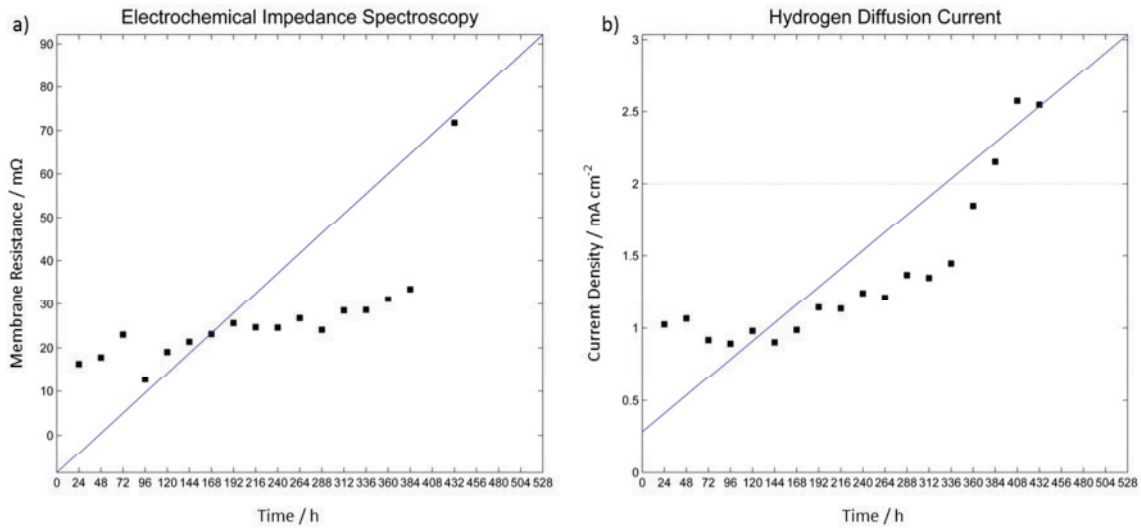
**Figure 23:** Open circuit voltage over the duration of 500 hours under OCV hold conditions.

The polarisation curves (Figure 24) show a clear reduction of the maximum current density and the maximum power density, indicating severe degradation after the test.



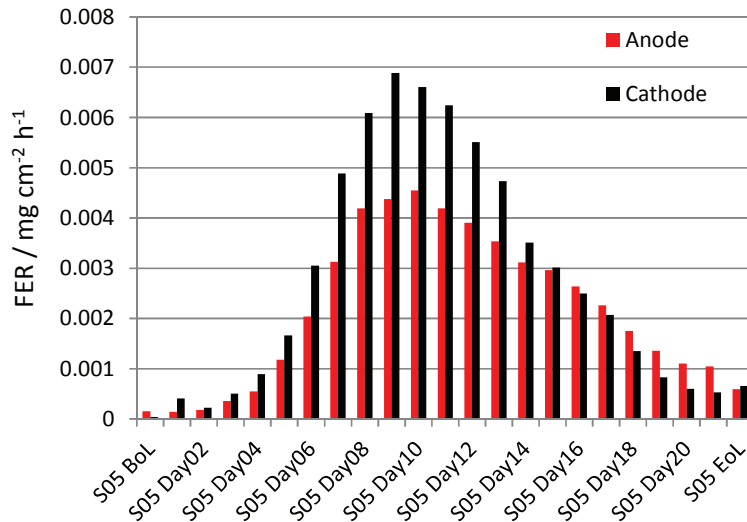
**Figure 24:** Polarisation curve before (BoL) and after (EoL) 500 hours of OCV hold conditions.

Figure 25 a shows the progress of the high frequency resistance over the duration of the test. The membrane conductivity exhibits a rather steady decrease over most of the test, followed by a sharp drop at the final characterisation. The corresponding hydrogen diffusion current shown in Figure 25 b follows a similar pattern. The light red line indicates the target value of a maximum hydrogen diffusion current density of  $2 \text{ mA cm}^{-2}$  given by the test protocol [61] and is exceeded after extensive testing.



**Figure 25:** a) The high frequency resistance and b) the hydrogen diffusion current, measured every 24 hours over the duration of 500 hours of OCV hold testing.

Figure 26 shows the FER measured every 24 hours over the duration of the test for anode and cathode, respectively. The value is significantly higher on the cathode than on the anode in most of the cases. It can also be seen that the values traverse a maximum, after which the fluoride emission rates for the anode starts exceeding the respective FER values of the cathode.



**Figure 26:** Fluoride emission rate, determined every 24 hours over the duration of 500 hours of OCV hold testing.

All results indicate a severe degradation of the polymer electrolyte membrane following multiple mechanisms. The decreased open circuit voltage and the elevated hydrogen diffusion current density indicate membrane thinning and pinhole formation. The increased membrane resistance, however, is the result of a loss of ion conductive moieties. As is known from results that have been discussed previously, these two degradation modes do not necessarily correlate. The conducted AST aims to provoke chemical membrane degradation; mechanical harm appears therefore negligible. This allows the conclusion that chemical degradation can affect the membrane according to different mechanisms. The results indicate both the dissociation of the acidic ion conducting groups as well as the decomposition of the structure giving backbone.

#### *8.2.4. Conclusion*

The results obtained by operating the fuel cell at the conditions given by the DoE [61] support both theories of a chemical attack of the backbone as well as the dissociation of the ion conductive polymer fragments [38,47,48]. Both mechanisms have to take place in parallel to obtain the given results.

### 8.3. Humidity induced Platinum Agglomeration

The presented results were conducted on initiation by Prof. Andrea Casalegno with the aim to compare the results of three different institutions – the Politecnico di Milano (POLIMI), the Joint Research Centre and the Fuel Cell Systems Group at Graz University of Technology. For this thesis, however, only the latter results will be discussed.

#### *8.3.1. Theory*

As has been discussed above, platinum electrocatalyst degradation is mainly due to agglomeration of the catalyst nanoparticles. This is strongly depending on the electrode potential [47]. This fact is utilised by the DoE protocol for fuel cell electrocatalyst degradation [61]. Pt dissolution is, however, also expected to be influenced by humidity and the osmotic drag is able to affect the distribution of redeposited platinum. Therefore, the effect of the potential dependent degradation with different relative humidities on platinum agglomeration was investigated.

### 8.3.2. Experimental Setup

A segmented 25 cm<sup>2</sup> single fuel cell was operated with a reference MEA or an improved MEA (both IRD A/S, Odense, Denmark) for stationary applications. Both membrane electrode assemblies consisted of a Nafion® XL membrane and identical GDLs. The anode catalyst loading was identical and given as 0.2 mg<sub>Pt</sub> cm<sup>-2</sup>. The catalyst type was, however, changed for the improved MEA on both anode and cathode. On the cathode, the catalyst loading was 0.4 for the reference and 0.6 mg<sub>Pt</sub> cm<sup>-2</sup> for the improved MEA (L. Grahl-Madsen, personal communication, 23.11.2016).

The single cells were equipped with triple serpentine flow fields in co-flow mode. In Figure 27 to Figure 32, the inlets are located in the upper corner, whereas the outlets are located on the right. The cells were characterised at the reference conditions described previously [3] as well as at 80 °C with synthetic air or oxygen on the cathode before and after the respective AST (Table 2). The conditions during each of the ASTs are listed in Table 3.

**Table 2:** Operation conditions during characterisation.

Cell Temperature / °C		65	80	80	80
Outlet Pressure		atm.	atm.	atm.	atm.
<b>Anode</b>	Gas	H <sub>2</sub>	H <sub>2</sub>	H <sub>2</sub>	H <sub>2</sub>
	Dew Point / °C	60	80	80	80
	Inlet Temperature / °C	70	85	85	85
	Stoichiometry	1.5		2	
	Gas Flow / ml min <sup>-1</sup>		500		50
<b>Cathode</b>	Gas	air	air	O <sub>2</sub>	N <sub>2</sub>
	Dew Point / °C	60	80	80	80
	Inlet Temperature / °C	70	85	85	85
	Stoichiometry	2		9.52	
	Gas Flow / ml min <sup>-1</sup>		1000		50
<b>Polarisation Curve</b>		✓	✓	✓	
<b>EIS</b>		✓	✓	✓	
<b>LSV</b>					✓
<b>CV</b>					✓

The voltage was cycled between 0.6 and 1 V with a sweep rate of 50 mV s<sup>-1</sup>. Each cycle lasts 16 s, giving total test duration of 133.33 h for 30,000 cycles. Cyclic voltammetry was recorded after 0, 10, 100, 1,000, 5,000, 10,000 and 30,000 cycles. If the testing conditions diverge from the characterisation conditions, an initial and a final CV were measured additionally. During the tests, hydrogen and nitrogen were supplied to anode and cathode, respectively with a

flow rate of 100 ml min<sup>-1</sup> on each side. The inlet temperature was set to be 5 °C above the respective dew point to avoid condensation of water in the gas lining and the outlet pressure was atmospheric.

**Table 3:** Conditions during the respective ASTs.

	Anode Dew Point /°C	Cathode Dew Point /°C	Cell Temperature /°C
Reference AST	80	80	80
AST Gradient	53.2	95	80
AST Condensation	95	95	80

During testing, however, the cell temperature rose uncontrollably for the last test with dew points of 95 °C for both anode and cathode. Therefore, the results of this particular AST will not be regarded further on.

### 8.3.3. Results and Discussion

The change in electrochemical parameters for the reference MEA before and after the reference AST and the AST with a humidity gradient is shown in Table 4 and Table 5.

The single cell analysis exhibited a severe effect of the reference accelerated stress test on the electrochemical parameters. The power density was reduced from 366.6 to 218.4 mW cm<sup>-2</sup> and the electrochemically active surface area changed from 29.5 to 21.5 m<sup>2</sup> g<sup>-1</sup>. The high frequency resistance and the hydrogen diffusion current did, however, not indicate any membrane degradation (Table 4). Therefore, any reduction in performance eventually has to be caused by a loss of the active catalyst surface area.

**Table 4:** Electrochemical parameters before and after the reference AST for the reference MEA.

Reference AST	65 °C, Air		80 °C, O <sub>2</sub>		80 °C, Air	
	BoT	EoT	BoT	EoT	BoT	EoT
<b>Power Density / mW cm<sup>-2</sup></b>	278.9	158.8	625.3	458.4	362.6	218.4
<b>HFR / mΩ @ 1.25A</b>	8.16	11.39	7.60	9.19	7.21	7.04
<b>HFR / mΩ @ 5A</b>	7.85	8.56	8.14	8.84	7.25	7.28
<b>HFR / mΩ @ 12.5A</b>			7.15	8.42	7.11	7.16
<b>HFR / mΩ @ 25A</b>			7.58	7.45		
<b>Hydrogen Diffusion Current / mA cm<sup>-2</sup></b>					0.81	0.65
<b>Electrochemical Surface Area / m<sup>2</sup> g<sup>-1</sup></b>					29.51	21.54

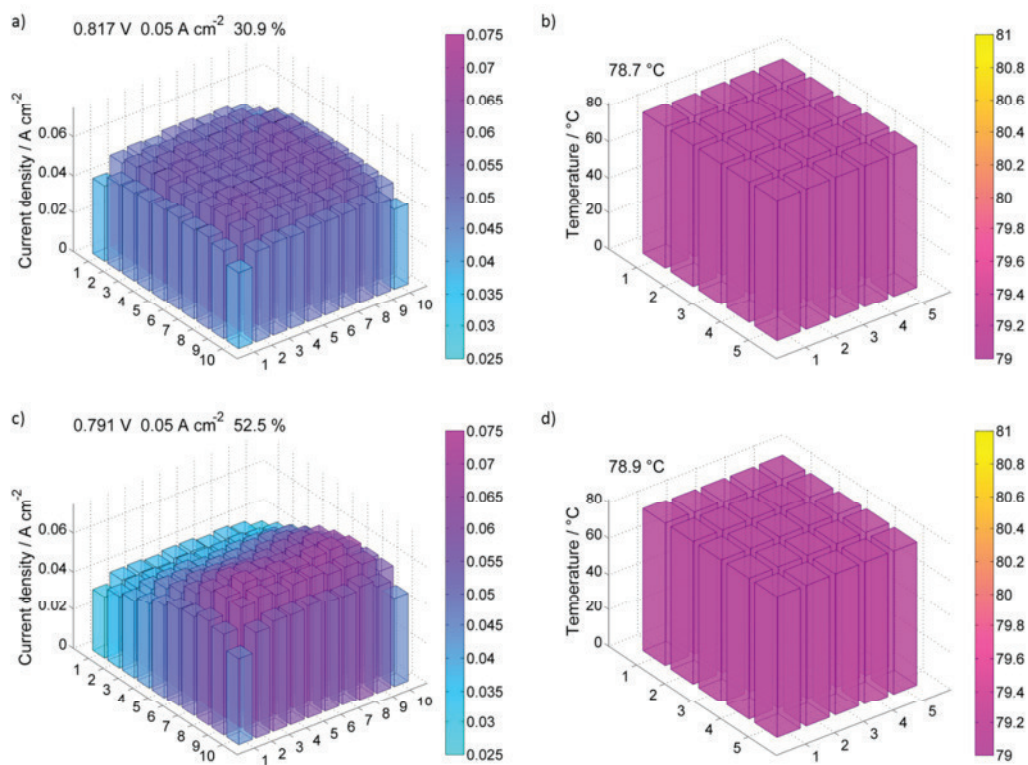


**Figure 27:** Current density (a and c) and temperature (b and d) distribution for the reference MEA before (a and b) and after (c and d) the reference AST at 0.05 A cm<sup>-2</sup>.

The changed local conditions are displayed in Figure 27 and Figure 28 at a current density of 0.05 and 0.5 A cm<sup>-2</sup>, respectively for the reference membrane electrode assembly before and after the reference AST. At both current values it is obvious that the AST induces a gradient in the current density distribution to a similar extend.

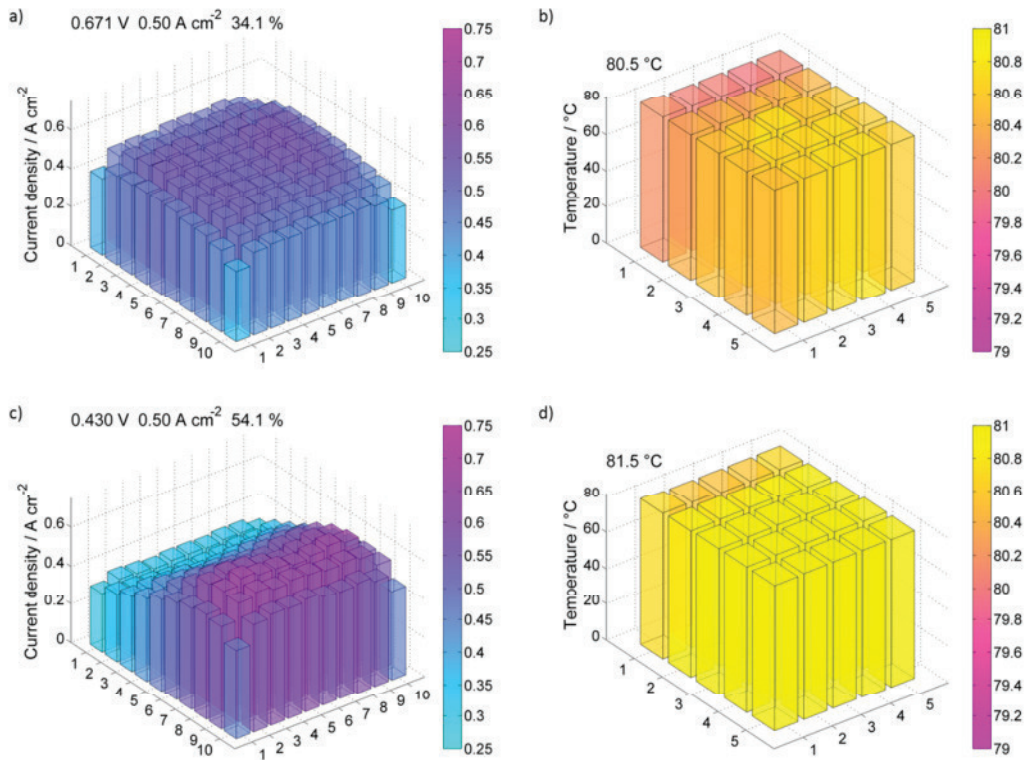
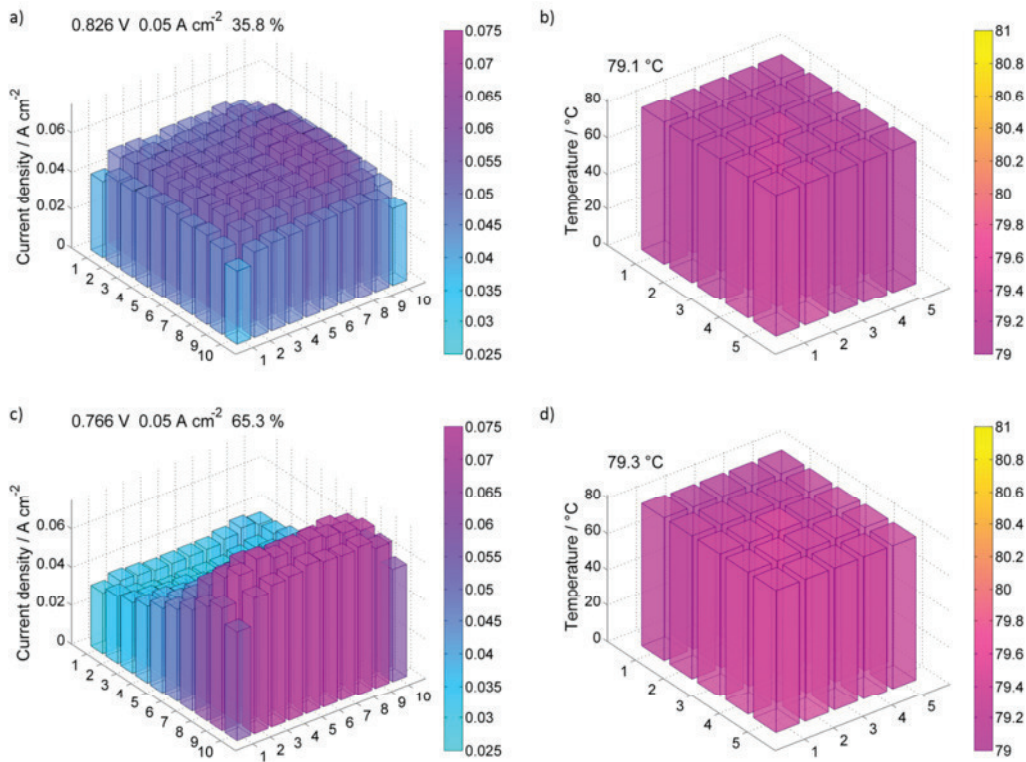


**Figure 28:** Current density (a and c) and temperature (b and d) distribution for the reference MEA before (a and b) and after (c and d) the reference AST at 0.5 A cm<sup>-2</sup>.

For the reference MEA, which underwent the AST with a humidity gradient between anode and cathode, the power density is reduced from 406.9 to 91.3 mW cm<sup>-2</sup> and the electrochemically active surface area changed from 34.2 to 13.6 m<sup>2</sup> g<sup>-1</sup>. Again, the membrane parameters remain unaffected (Table 5). The current density and temperature distribution at 0.05 A cm<sup>-2</sup> (Figure 29) is rather homogeneous initially and exhibits a severe gradient after the AST.

**Table 5:** Electrochemical parameters before and after the AST with a humidity gradient for the reference MEA.

AST Gradient	65 °C, Air		80 °C, O <sub>2</sub>		80 °C, Air	
	BoT	EoT	BoT	EoT	BoT	EoT
<b>Power Density / mW cm<sup>-2</sup></b>	372.1	96.0	667.8	247.8	406.9	91.3
<b>HFR / mΩ @ 1.25A</b>	11.14	19.71	8.29	11.32	7.23	8.93
<b>HFR / mΩ @ 5A</b>	7.51	12.02	8.07	10.33	7.11	8.27
<b>HFR / mΩ @ 12.5A</b>			6.90	10.39		
<b>Hydrogen Diffusion Current / mA cm<sup>-2</sup></b>					0.49	0.40
<b>Electrochemical Surface Area / m<sup>2</sup> g<sup>-1</sup></b>					34.17	13.56



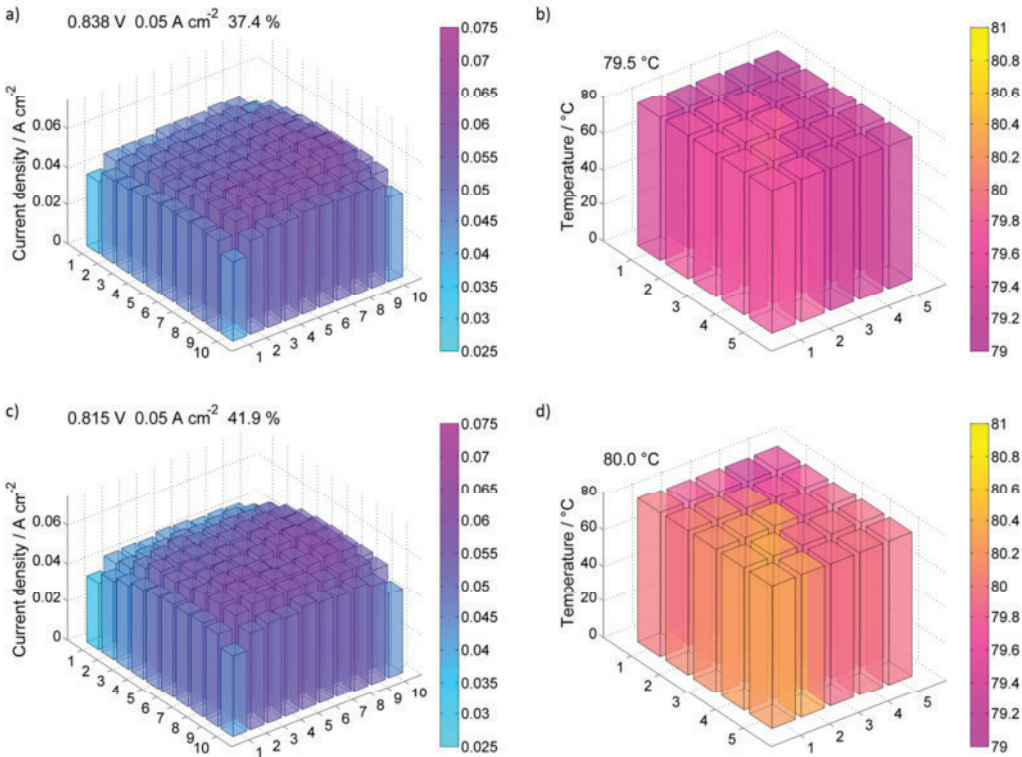
**Figure 29:** Current density (a and c) and temperature (b and d) distribution for the reference MEA before (a and b) and after (c and d) the AST with a humidity gradient at  $0.05 \text{ A cm}^{-2}$ .

Table 6 and Table 7 contain the electrochemical parameters before and after both ASTs for the improved MEA.

**Table 6:** Electrochemical parameters before and after the reference AST for the improved MEA.

Reference AST	65 °C, Air		80 °C, O <sub>2</sub>		80 °C, Air	
	BoT	EoT	BoT	EoT	BoT	EoT
<b>Power Density / mW cm<sup>-2</sup></b>	413.8	319.3	686.9	602.0	441.8	369.5
<b>HFR / mΩ @ 1.25A</b>	9.42	8.71	9.12	9.26	6.96	7.47
<b>HFR / mΩ @ 5A</b>	9.74	9.88	7.59	9.10	6.68	7.20
<b>HFR / mΩ @ 12.5A</b>	8.55	7.69	7.54	11.19	6.81	7.16
<b>HFR / mΩ @ 25A</b>			8.52	7.91		
<b>Hydrogen Diffusion Current / mA cm<sup>-2</sup></b>					0.41	0.86
<b>Electrochemical Surface Area / m<sup>2</sup> g<sup>-1</sup></b>					39.19	19.56

After the reference AST, the power density for the improved MEA is changed from 441.8 to 369.5 mW cm<sup>-2</sup>, whereas the electrochemically active surface area is reduced from 39.2 to 19.6 m<sup>2</sup> g<sup>-1</sup>. The high frequency resistance is again barely altered, but the hydrogen diffusion current increases. However, as the power density shows little change, any degradation appears not to affect the fuel cell operation significantly (Table 6). The current density and temperature distribution at 0.05 (Figure 30) and 0.5 A cm<sup>-2</sup> (Figure 31) shows that after the AST only a minor gradient is induced.



**Figure 30:** Current density (a and c) and temperature (b and d) distribution for the improved MEA before (a and b) and after (c and d) the reference AST at 0.05 A cm<sup>-2</sup>.

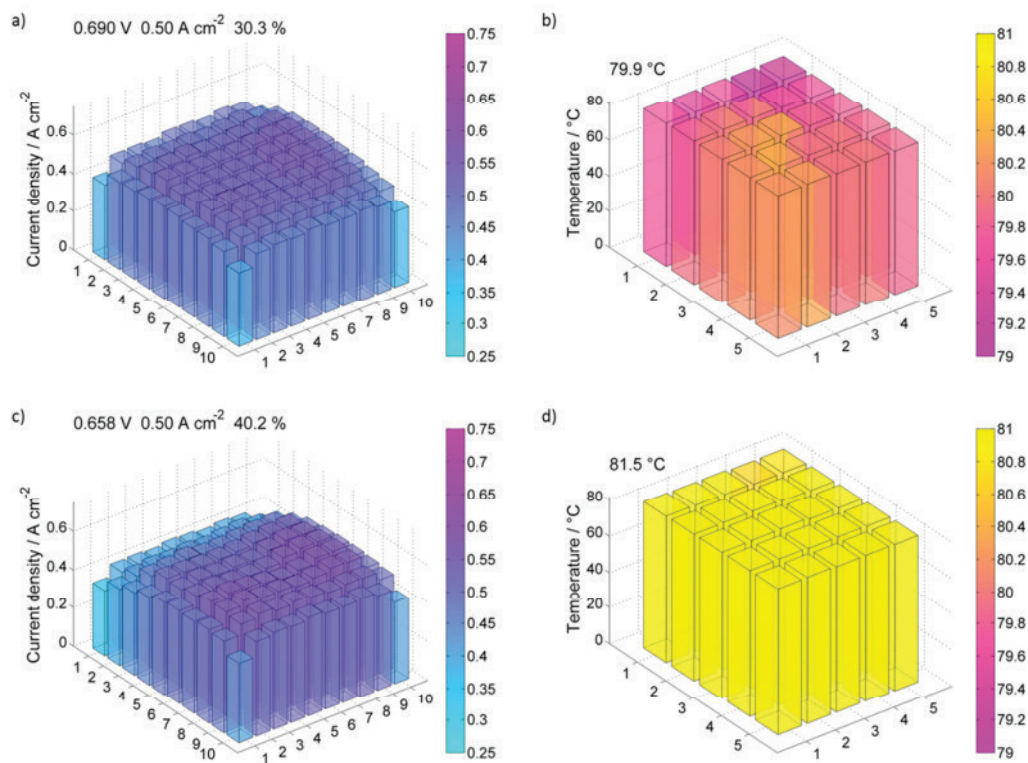


**Figure 31:** Current density (a and c) and temperature (b and d) distribution for the improved MEA before (a and b) and after (c and d) the reference AST at 0.5 A cm<sup>-2</sup>.

The improved MEA is, however, strongly affected by the AST with a higher cathode relative humidity (Table 7). The maximum power density drops from 447.0 down to 34.8 mW cm<sup>-2</sup> and the ECSA is reduced from 42.5 to 15.9 m<sup>2</sup> g<sup>-1</sup>. The high frequency resistance is slightly increased, but the hydrogen diffusion current seems unaffected. Figure 32 shows that the current density and the temperature distribution at 0.05 A cm<sup>-2</sup> are strongly affected by the accelerated stress testing and a gradient is clearly visible after testing.

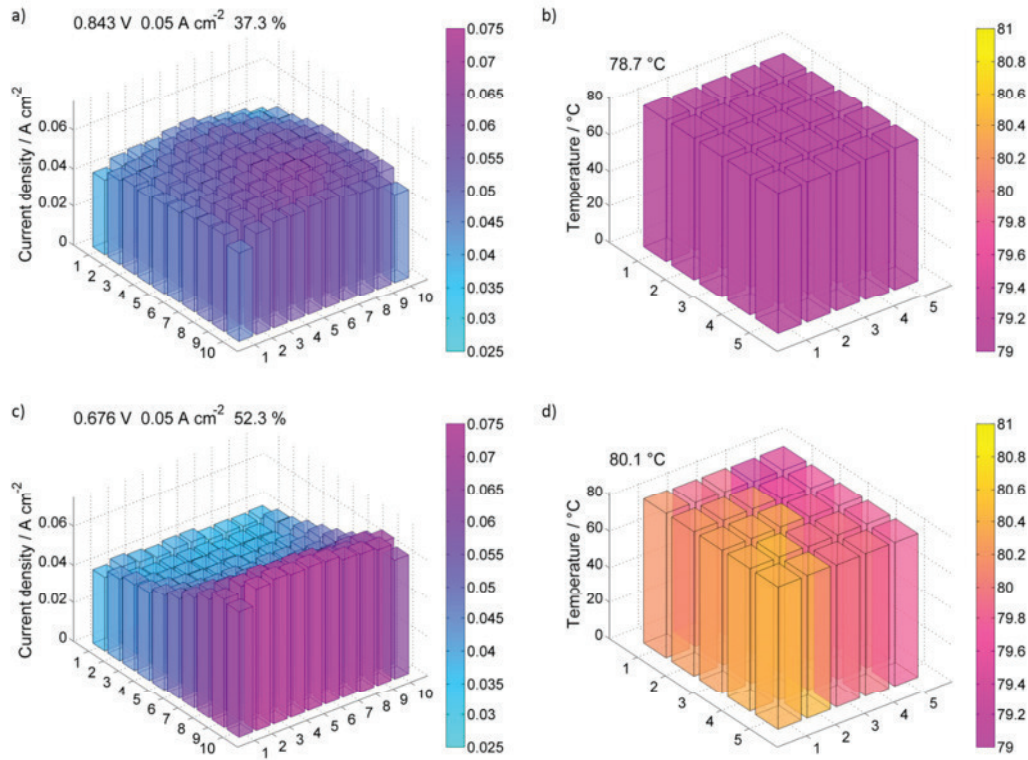


**Figure 32:** Current density (a and c) and temperature (b and d) distribution for the improved MEA before (a and b) and after (c and d) the AST with a humidity gradient at  $0.05 \text{ A cm}^{-2}$ .

**Table 7:** Electrochemical parameters before and after the AST with a humidity gradient for the improved MEA.

AST Gradient	65 °C, Air		80 °C, O <sub>2</sub>		80 °C, Air	
	BoT	EoT	BoT	EoT	BoT	EoT
<b>Power Density / mW cm<sup>-2</sup></b>	414.1	36.7	690.0	136.8	447.0	34.8
<b>HFR / mΩ @ 1.25A</b>	9.20	9.68	8.91	10.72	7.27	7.90
<b>HFR / mΩ @ 5A</b>	8.61	9.68	7.75	11.09	6.88	7.90
<b>HFR / mΩ @ 12.5A</b>	7.83	9.68	7.32	11.09	6.82	7.90
<b>Hydrogen Diffusion Current / mA cm<sup>-2</sup></b>					0.57	0.36
<b>Electrochemical Surface Area / m<sup>2</sup> g<sup>-1</sup></b>					42.46	15.87

From the electrochemical parameters it is obvious that the most severe effect derives from platinum electrocatalyst degradation, as was the primary intention of this particular AST protocol. Figure 33 shows that the ECSA declines for all MEAs and all ASTs. However, the relative effect is more severe for the humidity gradient AST with an oversaturated cathode gas stream with a clear performance

loss in the inlet region. An effect of condensed water is therefore visible for both the overall ECSA and the local current density distribution.

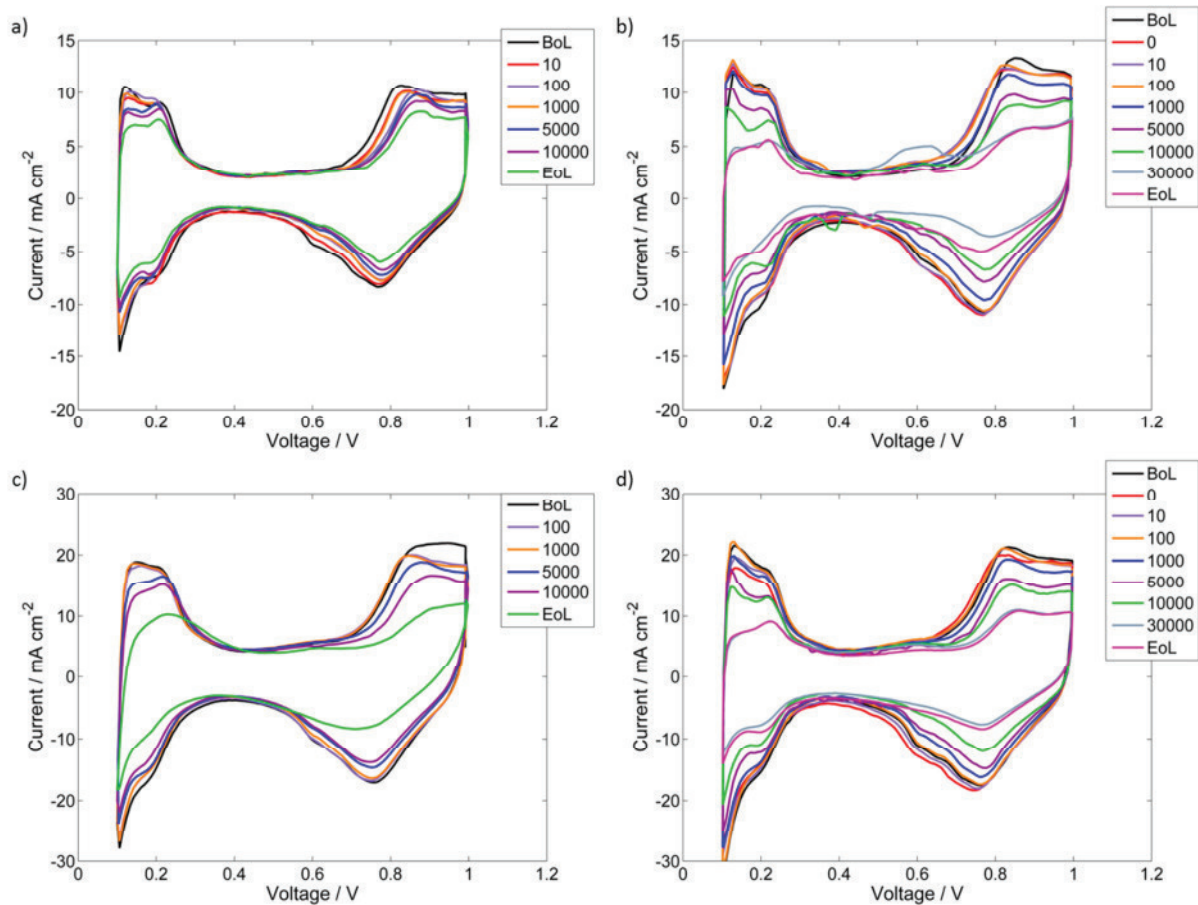


**Figure 33:** Cyclic voltammety curves over the duration of the reference AST (a and c) and the AST with a humidity gradient (b and d) for the reference MEA (a and b) and the improved MEA (c and d).

#### 8.3.4. Conclusion

The initial gradient between the highest and lowest local current density is in the range between 30 and 37%, independent of the total current for all tested MEAs. However, after accelerated stress testing, a more severe gradient in the range of 40.2% to 65.3% is visible for all MEAs.

The reference MEA exhibited a decline in electrochemically active surface area to 73.0% after the reference AST and 39.7% of the respective initial value after the AST with a gradient. The power densities declined to 60.2% and 22.4% for the respective tests.

Only the improved MEA seems unaffected by the reference AST on a local level. Despite the drastic decline of ECSA down to 49.9% of the initial value, the power density still reaches 83.6%. On the other hand, the AST with an oversaturated cathode gas stream exhibits a detrimental effect on the power density, as it

declines to 7.8% and also the current density distribution is significantly altered for the improved MEA, even though the loss of ECSA down to 37.4% of the initial value is comparable for this MEA after both ASTs. Thus, another effect is bound to contribute to the degradation. One possible cause could be a loss of anode catalyst surface area. For clarification, ex-situ characterisation is conducted by the project partners.

Within the work, it was shown that a significant enhancement was possible by changing the catalyst. The improved MEA exhibited a better stability under the DoE testing conditions. However, despite the good results during standardised testing, the catalyst has shown to be more prone to humidity induced degradation.

## 9. Conclusion

The aim of this thesis is to aid the understanding of degradation mechanisms, limiting the durability of polymer electrolyte fuel cells. Initially, the focus was set on membrane degradation and thus, the effect of pinholes on fuel cell operation was investigated. The results, however, indicated a strong interaction and correlation with other degradation mechanism. Subsequently, a more holistic approach was chosen to identify detrimental conditions during fuel cell operation and to obtain a fundamental understanding of the corresponding degradation effects.

The study on the effect of membrane defects, i.e. pinholes, on fuel cell operation [3] pointed out a strong influence by the locally altered temperatures due to the direct combustion of hydrogen with oxygen, enabled by an increased gas crossover in the affected area. Initially, a local increase in current density is evident near the defects. However, the positive effect of the elevated temperature is quickly overshadowed by the negative effects of extensive reactant crossover. Hydrogen starvation was induced by load cycling during constant gas flow conditions. Cell reversal during starvation, loss of cathode ECSA and the increased carbon emission rate exhibited a clear correlation and were all a result of the introduced membrane defects. A more detrimental effect was evident in a fuel cell with defects close to the anode inlet.

In order to provide a better understanding of the degradation mechanisms leading to membrane decompositions and rupture mechanical and chemical stress was induced simultaneously in another study [2]. Therefore, a segmented single cell was operated at OCV conditions, accompanied by relative humidity cycling between 80 and 0% every 24 h. A pristine membrane underwent an identical procedure. The effluent water was collected for each test and the fluoride emission rate was determined. This allows evaluating the effect of the presence of the platinum electrocatalyst on in-situ membrane degradation. A higher FER was evident for the membrane in the absence of Pt, thus allowing the hypothesis that the formation of harmful radicals is mitigated by the presence of a catalyst.

Additionally, as is described in the experimental section of this thesis, the DoE protocol for chemical membrane degradation was conducted in single cell experiment. The open circuit voltage exhibited a vast decline and the target value for the maximum hydrogen diffusion current density was exceeded. The

high frequency resistance remained fairly stable throughout most of the experiment, but a sudden increase was noted during the last hours of testing. The fluoride emission rate was found to be higher on the cathode than on the anode throughout most of the test and traversed a peak value. The results indicate simultaneous backbone decomposition and sidechain dissociation. Both mechanisms have to occur in order to exhibit the given results.

As the decomposition of the ionomer apparently not only leads to the emission of fluoride, but also of oligomeric fragments, a procedure to determine the total fluorine emission rate was developed. The respective experiments were conducted by Mija Rami and are described in her master thesis [38]. From the results of both the fluoride emission rate and the total fluorine emission rate, the emission of fluorine, bound in polymer fragments can be calculated. Therefore, samples were used, deriving from tests described previously [74]. The FnER exhibited the best correlation with the high frequency resistance, indicating a favoured dissociation of the sidechain, containing the ion conductive moieties.

Effluent water samples, used for the determination of the fluorine emission rate, derived from tests in which the cathode stoichiometry was cycled to different extends for a short period of time. In another study, the cathode stoichiometry was cycled for different durations in order to determine, whether cathode starvation is able to induce degradation in polymer electrolyte fuel cells [4]. Short cathode supply interruption exhibited a positive effect on the fuel cell performance due to reduction of oxide species on the Pt surface, resulting in an increased electrochemically active surface area of the cathode catalyst. After extensive cycling, however, a distinct gradient appeared in the current density and temperature distribution. Computed tomography visualised a clearly different catalyst particle size distribution in dependence on the location within the fuel cell. Therefore, oxygen starvation induces a gradient, which leads to inhomogeneous current density and temperature distribution and can thus locally accelerate degradation.

As the platinum electrocatalyst stability is another major issue in fuel cell research, it has been considered in the conducted thesis. It has been discussed above that platinum can be oxidised and dissolved under fuel cell operation conditions. Thus, the DoE proposed a protocol with the aim being the selective acceleration of platinum electrocatalyst agglomeration. This protocol was conducted in its proposed form and extended in order to evaluate the effect of liquid water on the agglomeration rate as well as on the dissolution and distribution of redeposited platinum. As these experiments were conducted in

cooperation with other research institutes, only excerpts of the results are discussed here. The major focus was on evaluating the stability of a reference MEA in comparison with improved materials. The improved membrane electrode assembly exhibited a far better stability during the AST conducted strictly in accordance to the parameters proposed by the DoE. The recorded current density distribution did not exhibit an as strong gradient after testing as for the reference MEA. However, the novel materials appeared to be more prone to degradation when the cathode gas stream was oversaturated with water than the reference MEA and the performance rapidly declined.

Within the completion of this thesis, it was shown that membrane degradation does not necessarily lead to the emission of fluoride ions, but can also result in a loss of oligomeric fragments. The results indicate dissociation of the sidechains, containing the ion conductive moieties.

Also, different accelerated stress tests were conducted in order to determine the effect of different degradation mechanisms, which limit the lifetime of polymer electrolyte fuel cells. Amongst others, hydrogen crossover and locally altered temperatures were identified as the most detrimental factors, accelerating degradation. Inhomogeneous operation conditions are able to induce the latter and must therefore be avoided.

## 10. List of Tables

Table 1: Operation parameters suggested by the DoE [60].	28
Table 2: Operation conditions during characterisation.	46
Table 3: Conditions during the respective ASTs.	47
Table 4: Electrochemical parameters before and after the reference AST for the reference MEA.	47
Table 5: Electrochemical parameters before and after the AST with a humidity gradient for the reference MEA.	49
Table 6: Electrochemical parameters before and after the reference AST for the improved MEA.	50
Table 7: Electrochemical parameters before and after the AST with a humidity gradient for the improved MEA.	53

# 11. List of Figures

Figure 1: National GHG emissions with contributions listed according to the different sectors for the EU28 countries in 2012 [7].....	1
Figure 2: Principle of a polymer electrolyte fuel cell. ....	5
Figure 3: Polarisation curve with different losses [19]. ....	6
Figure 4: Scheme of a membrane electrode assembly.....	8
Figure 5: Chemical structure of Nafion® according to Chen and Schmidt-Rohr [24].....	9
Figure 6: In-house built segmented single cell [29]. ....	12
Figure 7: Commercial segmented single cell (S++ Simulation Services, Germany).....	13
Figure 8: Single serpentine layout with segments.....	14
Figure 9: Three channel serpentine layout with segments.....	14
Figure 10: Scheme of a platinum wire reference electrode.....	15
Figure 11: Reference electrode a) as implemented in the flow field and b) as implemented in the graphite plate. ....	15
Figure 12: Example of the current density characteristics over time for a polarisation curve.....	16
Figure 13: Electrical circuit of the impedance of a single electrochemical reaction [33].....	17
Figure 14: Nyquist plot of an MEA before and after AST testing in [2] at a current density of $0.2 \text{ A cm}^{-2}$ . ....	17
Figure 15: Voltage profile of cyclic voltammetry cycles.....	18
Figure 16: Example of a CV-curve including the hydrogen desorption peak ( $Q_{des}$ ) and the double layer (dashed line). ....	19
Figure 17: Overview of the different dominant degradation mechanisms in polymer electrolyte fuel cells .....	22
Figure 18: Centres prone to radical attack in the Nafion® ionomer according to Coms [49] (red and blue) and Ghassemzadeh and Holdcroft [50] (green). ....	24

Figure 19: Fuel cell operation under normal conditions (right) and during SU-SD conditions (whole).....	33
Figure 20: Fuel cell dynamic load cycle according to Tsoitridis et al. [61]. .....	34
Figure 21: The respective emission rates of a) fluoride and total fluorine and b) of the fluorine emission rate without fluoride. ....	39
Figure 22: The normalised high frequency resistance in comparison to a) the normalised and cumulated normalised fluoride, b) the normalised and cumulated normalised total fluorine emission rate and c) the normalised and cumulated normalised fluorine emission rate without fluoride. ....	40
Figure 23: Open circuit voltage over the duration of 500 hours under OCV hold conditions. ....	43
Figure 24: Polarisation curve before (BoL) and after (EoL) 500 hours of OCV hold conditions. ....	43
Figure 25: a) The high frequency resistance and b) the hydrogen diffusion current, measured every 24 hours over the duration of 500 hours of OCV hold testing. ....	44
Figure 26: Fluoride emission rate, determined every 24 hours over the duration of 500 hours of OCV hold testing.....	44
Figure 27: Current density (a and c) and temperature (b and d) distribution for the reference MEA before (a and b) and after (c and d) the reference AST at 0.05 A cm <sup>-2</sup> .....	48
Figure 28: Current density (a and c) and temperature (b and d) distribution for the reference MEA before (a and b) and after (c and d) the reference AST at 0.5 A cm <sup>-2</sup> .....	49
Figure 29: Current density (a and c) and temperature (b and d) distribution for the reference MEA before (a and b) and after (c and d) the AST with a humidity gradient at 0.05 A cm <sup>-2</sup> . ....	50
Figure 30: Current density (a and c) and temperature (b and d) distribution for the improved MEA before (a and b) and after (c and d) the reference AST at 0.05 A cm <sup>-2</sup> .....	51
Figure 31: Current density (a and c) and temperature (b and d) distribution for the improved MEA before (a and b) and after (c and d) the reference AST at 0.5 A cm <sup>-2</sup> .....	52

Figure 32: Current density (a and c) and temperature (b and d) distribution for the improved MEA before (a and b) and after (c and d) the AST with a humidity gradient at  $0.05 \text{ A cm}^{-2}$ . ..... 53

Figure 33: Cyclic voltammetry curves over the duration of the reference AST (a and c) and the AST with a humidity gradient (b and d) for the reference MEA (a and b) and the improved MEA (c and d). ..... 54

## 12. List of Abbreviations

AST	Accelerated stress test
DoE	(U.S.) Department of energy
BEV	Battery electric vehicle
BoL	Beginning of lifetime
BoT	Beginning of testing
BP	Bipolar plate
CL	Catalyst layer
CHP	Combined heat and power
CT	Computed tomography
CV	Cyclic voltammetry
DST	Dynamic stress test
EIS	Electrochemical impedance spectroscopy
ECSA	Electrochemically active surface area
EoL	End of lifetime
EoT	End of testing
ECE	European commission for Europe
FER	Fluoride emission rate
F-ISE	Fluoride ion selective electrode
F <sub>n</sub> ER	Fluorine emission rate
FCEV	Fuel cell electric vehicle
FCTT	Fuel cell technical team
GDL	Gas diffusion layer
GHG	Greenhouse gas
HFR	High frequency resistance
HOR	Hydrogen oxidation reaction
ICE	Internal combustion engine
IEC	Internal electro-technical commission
JRC	Joint research centre
LSV	Linear sweep voltammetry
MEA	Membrane electrode assembly
MPL	Microporous layer
NPL	National physical laboratory
NEDC	New European driving cycle
NMR	Nuclear magnetic resonance
OCV	Open circuit voltage

ORR	Oxygen reduction reaction
PFSA	Perfluorosulphonic acid
PAFC	Phosphoric acid fuel cell
POLIMI	Politecnico di Milano
PEFC	Polymer electrolyte fuel cell
PEM	Polymer electrolyte membrane
PTFE	Polytetrafluoroethylene
RHE	Reversible hydrogen electrode
SEM	Scattered electron microscopy
SU-SD	Startup-shutdown
tFER	Total fluorine emission rate
TISAB II	Total ionic strength adjustment buffer II
TEM	Transmitted electron microscopy
XTM	X-ray tomography

## 13. List of Variables

Charge transfer resistance	$R_{t,M}$	$\Omega$ or $\Omega\text{cm}^2$
Current or current density	$i$	$\text{A}$ or $\text{A cm}^{-2}$
Double layer capacitance	$C_{dl}$	$\text{F}$ or $\text{F cm}^{-2}$
Electrolyte or ohmic resistance	$R_e$	$\Omega$ or $\Omega\text{cm}^2$
Enthalpy	$\Delta H$	$\text{kJ mol}^{-1}$
Faraday constant	$F$	$\text{C mol}^{-1}$
Frequency	$\omega$	$\text{Hz}$
Fuel efficiency	$\eta_{\text{fuel}}$	$\%$
Gas constant	$R$	$\text{J K}^{-1} \text{mol}^{-1}$
Gibbs free energy	$\Delta G$	$\text{kJ mol}^{-1}$
Imaginary part	$I$	$\Omega$ or $\Omega\text{cm}^2$
Parameter	$a_1$	$\text{V}$
Parameter	$a_2$	$\text{cm}^2 \text{A}^{-1}$
Power or power density	$P$	$\text{W}$ or $\text{W cm}^{-2}$
Real part	$R$	$\Omega$ or $\Omega\text{cm}^2$
Resistance	$R_{\Omega}$	$\Omega$ or $\Omega\text{cm}^2$
Stoichiometric ratio	$\lambda$	
Temperature	$T$	$\text{K}$
Theoretical maximum cell voltage	$V_0$	$\text{V}$
Thermodynamic maximum efficiency	$\eta_{\text{max}}$	$\%$
Voltage	$V$	$\text{V}$
Voltage efficiency	$\eta_{\text{voltage}}$	$\%$

## 14. References

- [1] Bodner M, Hofer A, Hacker V. H<sub>2</sub> generation from alkaline electrolyzer. *Wiley Interdiscip Rev Energy Environ* 2015;4:365–81.
- [2] Bodner M, Cermenek B, Rami M, Hacker V. The Effect of Platinum Electrocatalyst on Membrane Degradation in Polymer Electrolyte Fuel Cells. *Membranes (Basel)* 2015;5:888–902.
- [3] Bodner M, Hochenauer C, Hacker V. Effect of pinhole location on degradation in polymer electrolyte fuel cells. *J Power Sources* 2015;295:336–48.
- [4] Bodner M, Schenk A, Salaberger D, Rami M, Hochenauer C, Hacker V. Air Starvation Induced Degradation in Polymer Electrolyte Fuel Cells. *Fuel Cells* 2017;17:18–26.
- [5] COP21. <http://www.cop21.gouv.fr/en/> 2017.
- [6] IEA. *TECHNOLOGY ROADMAP Hydrogen and Fuel Cells*. Paris: Springer-Verlag; 2015.
- [7] Su M, Pauleit S, Yin X, Zheng Y, Chen S, Xu C. Greenhouse gas emission accounting for EU member states from 1991 to 2012. *Appl Energy* 2016;184:759–68.
- [8] Ammermann H, Hoff P, Atanasiu M, Ayllor J, Kaufmann M, Tisler O. *Advancing Europe’s energy systems: Stationary fuel cells in distributed generation*. Publications Office of the European Union; 2015.
- [9] Martín AJ, Hornés A, Martínez-Arias A, Daza L. Recent Advances in Fuel Cells for Transport and Stationary Applications. *Renew. Hydrog. Technol.*, 2013, p. 361–80.
- [10] Wang Y, Chen KS, Mishler J, Cho SC, Adroher XC. A review of polymer electrolyte membrane fuel cells: Technology, applications, and needs on fundamental research. *Appl Energy* 2011;88:981–1007.
- [11] Yazdanie M, Noembrini F, Heinen S, Espinel A, Boulouchos K. Well-to-wheel costs, primary energy demand, and greenhouse gas emissions for the production and operation of conventional and alternative vehicles. *Transp Res Part D Transp Environ* 2016;48:63–84.
- [12] Enz S, Dao TA, Messerschmidt M, Scholta J. Investigation of degradation effects in polymer electrolyte fuel cells under automotive-related operating conditions. *J Power Sources* 2015;274:521–35.
- [13] Wu J, Yuan XZ, Martin JJ, Wang H, Zhang J, Shen J, et al. A review of PEM fuel cell durability: Degradation mechanisms and mitigation strategies. *J Power Sources* 2008;184:104–19.
- [14] Guerrero Moreno N, Cisneros Molina M, Gervasio D, Pérez Robles JF. Approaches to polymer electrolyte membrane fuel cells (PEMFCs) and their cost. *Renew Sustain Energy Rev* 2015;52:897–906.
- [15] Chen H, Pei P, Song M. Lifetime prediction and the economic lifetime of

- Proton Exchange Membrane fuel cells. *Appl Energy* 2015;142:154–63.
- [16] Schenk A, Grimmer C, Perchthaler M, Weinberger S, Pichler B, Heinzl C, et al. Platinum-cobalt catalysts for the oxygen reduction reaction in high temperature proton exchange membrane fuel cells - Long term behavior under ex-situ and in-situ conditions. *J Power Sources* 2014;266:313–22.
- [17] Taherian R. A review of composite and metallic bipolar plates in proton exchange membrane fuel cell: Materials, fabrication, and material selection. *J Power Sources* 2014;265:370–90.
- [18] Breeze P. *Fuel Cells. Power Gener. Technol.* 2nd ed., Elsevier Ltd.; 2014, p. 129–52.
- [19] Hacker V, Bodner M, Schenk A. Integration of a Membrane Reactor with a Fuel Cell. *Integr. Membr. Syst. Process.*, Oxford, UK: John Wiley & Sons, Ltd; 2016, p. 285–306.
- [20] St-Pierre J. Overview Performance and Operational Conditions. In: Garche J, editor. *Encycl. Electrochem. Power Sources, Vol. 2*, Amsterdam: Elsevier; 2009, p. 901–11.
- [21] Dou M, Hou M, Liang D, Shen Q, Zhang H, Lu W, et al. Behaviors of proton exchange membrane fuel cells under oxidant starvation. *J Power Sources* 2011;196:2759–62.
- [22] Baumgartner WR, Parz P, Fraser SD, Wallnöfer E, Hacker V. Polarization study of a PEMFC with four reference electrodes at hydrogen starvation conditions. *J Power Sources* 2008;182:413–21.
- [23] Ramasamy R. Membrane-Electrode Assemblies. In: Garche J, editor. *Encycl. Electrochem. Power Sources, Vol. 2*, Amsterdam: Elsevier; 2009, p. 787–805.
- [24] Chen Q, Schmidt-Rohr K. Backbone Dynamics of the Nafion Ionomer Studied by  $^{19}\text{F}$  -  $^{13}\text{C}$  Solid-State NMR. *Macromol Chem Phys* 2007;208:2189–203.
- [25] Scott K. *Membrane Electrode Assemblies for Polymer Electrolyte Membrane Fuel Cells.* Woodhead Publishing Limited; 2012.
- [26] Alberti G. Membranes. In: Garche J, editor. *Encycl. Electrochem. Power Sources, Vol. 2*, Amsterdam: Elsevier; 2009, p. 650–66.
- [27] Shi S, Weber AZ, Kusoglu A. Structure / property relationship of Nafion XL composite membranes. *J Memb Sci* 2016;516:123–34.
- [28] Zhang Y, Smirnova A, Verma A, Pitchumani R. Design of a proton exchange membrane (PEM) fuel cell with variable catalyst loading. *J Power Sources* 2015;291:46–57.
- [29] Baumgartner WR. *Charakterisierung von Polymer-Elektrolyt-Membran-Brennstoffzellen.* Graz University of Technology, 2007.
- [30] Hashimasa Y, Numata T, Moriya K, Watanabe S. Study of fuel cell structure and heating method. *J Power Sources* 2006;155:182–9.
- [31] Murakawa H, Ueda T, Yoshida T, Sugimoto K, Asano H, Takenaka N, et al. Effect of water distributions on performances of JARI standard PEFC by

- using neutron radiography. *Nucl Instruments Methods Phys Res Sect A Accel Spectrometers, Detect Assoc Equip* 2009;605:127–30.
- [32] Manso AP, Marzo FF, Barranco J, Garikano X, Garmendia Mujika M. Influence of geometric parameters of the flow fields on the performance of a PEM fuel cell. A review. *Int J Hydrogen Energy* 2012;37:15256–87.
- [33] Orazem ME, Tribollet B. *Electrochemical Impedance Spectroscopy*. Hoboken, NJ, USA: John Wiley & Sons, Inc.; 2008.
- [34] Haman CH, Vielstich W. *Elektrochemie. 4., vollst.* Weinheim: Wiley-VCH Verlag GmbH & Co. KGaA; 2005.
- [35] Gasteiger HA, Gu W, Makharia R, Mathias MF, Sompalli B. Beginnig-of-life MEA performance - Efficiency loss contributions. In: Vielstich W, Lamm A, Gasteiger HA, editors. *Handb. Fuel Cells Fundam. Technol. Appl. Vol. 3*, Chichester, Sussex: John Wiley & Sons Ltd,; 2003, p. 593–610.
- [36] Hesse M, Meier H, Zeeh B. *Spektroskopische Methoden in der organischen Chemie. 7th ed.* Stuttgart: Georg Thieme Verlag; 2005.
- [37] Chen Q, Schmidt-Rohr K.  $^{19}\text{F}$  and  $^{13}\text{C}$  NMR signal assignment and analysis in a perfluorinated ionomer (Nafion) by two-dimensional solid-state NMR. *Macromolecules* 2004;37:5995–6003.
- [38] Rami M. *Effluent Water Analysis in Polymer Electrolyte Fuel Cells*. Graz University of Technology, 2017.
- [39] Holst T, Vassiliev A, Kerr R, Li Q, Steenberg T, Terkelsen C, et al. Determining the platinum loading and distribution of industrial scale polymer electrolyte membrane fuel cell electrodes using low energy X-ray imaging. *J Power Sources* 2014;270:208–12.
- [40] Kuhn R, Scholta J, Krüger P, Hartnig C, Lehnert W, Arlt T, et al. Measuring device for synchrotron X-ray imaging and first results of high temperature polymer electrolyte membrane fuel cells. *J Power Sources* 2011;196:5231–9.
- [41] Deevanhxay P, Sasabe T, Minami K, Tsushima S, Hirai S. Oblique soft X-ray tomography as a non-destructive method for morphology diagnostics in degradation of proton-exchange membrane fuel cell. *Electrochim Acta* 2014;135:67–76.
- [42] Schneider A, Wieser C, Roth J, Helfen L. Impact of synchrotron radiation on fuel cell operation in imaging experiments. *J Power Sources* 2010;195:6349–55.
- [43] Roth J, Eller J, Büchi FN. Effects of Synchrotron Radiation on Fuel Cell Materials. *J Electrochem Soc* 2012;159:F449–55.
- [44] Roth J, Eller J, Büchi FN. Effects of Synchrotron Radiation on Polymer Electrolyte Fuel Cell Materials. *ECS Trans.*, 2011, p. 371–8.
- [45] Eller J, Büchi FN. Polymer electrolyte fuel cell performance degradation at different synchrotron beam intensities. *J Synchrotron Radiat* 2014;21:82–8.
- [46] Eller J, Roth J, Marone F, Stampanoni M, Wokaun A, Büchi FN. Implications of polymer electrolyte fuel cell exposure to synchrotron radiation on gas

- diffusion layer water distribution. *J Power Sources* 2014;245:796–800.
- [47] Bodner M, Senn J, Hacker V. Degradation mechanisms and lifetime. unpublished work.
- [48] Bodner M, Rami M, Marius B, Schenk A, Hacker V. Determining Membrane Degradation in Polymer Electrolyte Fuel Cells by Effluent Water Analysis. *ECS Trans* 2016;75:703–6.
- [49] Coms FD. The Chemistry of Fuel Cell Membrane Chemical Degradation. *ECS Trans.*, vol. 16, ECS; 2008, p. 235–55.
- [50] Aarhaug TA. Assessment of PEMFC Durability by Effluent Analysis. Norwegian University of Science and Technology, 2011.
- [51] Ghassemzadeh L, Holdcroft S. Quantifying the structural changes of perfluorosulfonated acid ionomer upon reaction with hydroxyl radicals. *J Am Chem Soc* 2013;135:8181–4.
- [52] Samms SR. Thermal Stability of Nafion® in Simulated Fuel Cell Environments. *J Electrochem Soc* 1996;143:1498.
- [53] Vengatesan S, Fowler MW, Yuan X-Z, Wang H. Diagnosis of MEA degradation under accelerated relative humidity cycling. *J Power Sources* 2011;196:5045–52.
- [54] Kim J, Lee J, Tak Y. Relationship between carbon corrosion and positive electrode potential in a proton-exchange membrane fuel cell during start/stop operation. *J Power Sources* 2009;192:674–8.
- [55] Pei P, Chen H. Main factors affecting the lifetime of Proton Exchange Membrane fuel cells in vehicle applications: A review. *Appl Energy* 2014;125:60–75.
- [56] De Moor G, Bas C, Charvin N, Dillet J, Maranzana G, Lottin O, et al. Perfluorosulfonic acid membrane degradation in the hydrogen inlet region: A macroscopic approach. *Int J Hydrogen Energy* 2016;41:483–96.
- [57] Danerol AS, Bas C, Flandin L, Claude E, Alberola ND. Influence of ageing in fuel cell on membrane/electrodes interfaces. *J Power Sources* 2011;196:3479–84.
- [58] Macauley N, Wong KH, Watson M, Kjeang E. Favorable effect of in-situ generated platinum in the membrane on fuel cell membrane durability. *J Power Sources* 2015;299:139–48.
- [59] <https://energy.gov/eere/fuelcells/fuel-cells>. Off Energy Effic Renew Energy 2017.
- [60] Bae SJ, Kim S-J, Park JI, Park CW, Lee J-H, Song I, et al. Lifetime prediction of a polymer electrolyte membrane fuel cell via an accelerated startup–shutdown cycle test. *Int J Hydrogen Energy* 2012;37:9775–81.
- [61] Fuel Cell Technical Team Roadmap. 2013.
- [62] Tsotridis G, Pilenga A, Marco G De, Malkow T. EU Harmonised Test Protocols for PEMFC MEA Testing in Single Cell Configuration for Automotive Applications, JRC Science for Policy report. 2015.
- [63] Aarhaug TA, Svensson AM. Degradation Rates of PEM Fuel Cells Running at

- Open Circuit Voltage. ECS Trans., vol. 3, ECS; 2006, p. 775–80.
- [64] Dhanushkodi SR, Kundu S, Fowler MW, Pritzker MD. Study of the effect of temperature on Pt dissolution in polymer electrolyte membrane fuel cells via accelerated stress tests. *J Power Sources* 2014;245:1035–45.
- [65] Dhanushkodi SR, Tam M, Kundu S, Fowler MW, Pritzker MD. Carbon corrosion fingerprint development and de-convolution of performance loss according to degradation mechanism in PEM fuel cells. *J Power Sources* 2013;240:114–21.
- [66] Bi W, Fuller TF. Temperature Effects on PEM Fuel Cells Pt/C Catalyst. *J Electrochem Soc* 2008;155:215–21.
- [67] Qu S, Li X, Hou M, Shao Z, Yi B. The effect of air stoichiometry change on the dynamic behavior of a proton exchange membrane fuel cell. *J Power Sources* 2008;185:302–10.
- [68] Kim B, Cha D, Kim Y. The effects of air stoichiometry and air excess ratio on the transient response of a PEMFC under load change conditions. *Appl Energy* 2015;138:143–9.
- [69] Liang D, Shen Q, Hou M, Shao Z, Yi B. Study of the cell reversal process of large area proton exchange membrane fuel cells under fuel starvation. *J Power Sources* 2009;194:847–53.
- [70] Brightman E, Hinds G. In situ mapping of potential transients during start-up and shut-down of a polymer electrolyte membrane fuel cell. *J Power Sources* 2014;267:160–70.
- [71] Bloom I, Walker LK, Basco JK, Malkow T, Saturnio A, De Marco G, et al. A comparison of Fuel Cell Testing protocols – A case study: Protocols used by the U.S. Department of Energy, European Union, International Electrotechnical Commission/Fuel Cell Testing and Standardization Network, and Fuel Cell Technical Team. *J Power Sources* 2013;243:451–7.
- [72] Diloyan G, Sobel M, Das K, Hutapea P. Effect of mechanical vibration on platinum particle agglomeration and growth in Polymer Electrolyte Membrane Fuel Cell catalyst layers. *J Power Sources* 2012;214:59–67.
- [73] Dubau L, Castanheira L, Chatenet M, Abbou S, Lottin O, De Moor G, et al. Carbon corrosion induced by membrane failure: The weak link of PEMFC long-term performance. *Int J Hydrogen Energy* 2014;39:21902–14.
- [74] Bodner M, Schenk A, Marius B, Rami M, Hacker V. Air Starvation Accelerated Stress Tests in Polymer Electrolyte Fuel Cells. *ECS Trans* 2016;75:769–76.

# Appendix

## 15. List of Publications

Below is a complete list of publications up to the date of the completion of this thesis.

### 15.1. Journal Articles

- 2017 Bodner M, Schenk A, Salaberger D, Rami M, Hochenauer C, Hacker V. Air Starvation Induced Degradation in Polymer Electrolyte Fuel Cells. *Fuel Cells*. 2017 Feb 2;17(1):18-26. Available from, DOI: 10.1002/fuce.201600132
- 2016 Bodner M, Rami M, Marius B, Schenk A, Hacker V. Determining Membrane Degradation in Polymer Electrolyte Fuel Cells by Effluent Water Analysis. *ECS transactions*. 2016 Sep 23;75(14):703-706. Available from, DOI: 10.1149/07514.0703ecst
- Bodner M, Schenk A, Marius B, Rami M, Hacker V. Air Starvation Accelerated Stress Tests in Polymer Electrolyte Fuel Cells. *ECS transactions*. 2016 Sep 23;75(14):769-776. Available from, DOI: 10.1149/07514.0769ecst
- Schenk A, Gamper S, Grimmer C, Pichler BE, Bodner M, Weinberger S et al. Development of Low Cost High-Temperature Polymer Electrolyte Fuel Cell Membrane-Electrode-Assemblies for Combined Heat and Power Plants in Single Family Homes. *ECS transactions*. 2016 Sep 23;75(14):435-441. Available from, DOI: doi:10.1149/07514.0435ecst
- Schenk A, Gamper S, Grimmer C, Bodner M, Weinberger S, Hacker V. Phosphoric Acid Tolerant Oxygen Reduction Reaction Catalysts for High-Temperature Polymer Electrolyte Fuel Cells. *ECS transactions*. 2016 Sep 23;75(14):939-942. Available from, DOI:

doi:10.1149/07514.0939ecst

Feketeföldi B, Cermenek B, Spirk C, Schenk A, Grimmer C, Bodner M et al. Chitosan-Based Anion Exchange Membranes for Direct Ethanol Fuel Cells. *Journal of Membrane Science & Technology*. 2016;6(1):145. Available from: 10.4172/2155-9589.1000145

2015 Bodner M, Hochenauer C, Hacker V. Effect of pinhole location on degradation in polymer electrolyte fuel cells. *Journal of power sources*. 2015;(295):336-348. Available from: doi:10.1016/j.jpowsour.2015.07.021

Bodner M, Hofer A, Hacker V. H<sub>2</sub> generation from alkaline electrolyzer. *Wiley interdisciplinary reviews / Energy and environment [Electr. Res.]*. 2015;(4):365- 381. Available from: 10.1002/wene.150

Bodner M, Cermenek B, Rami M, Hacker V. The Effect of Platinum Electrocatalyst on Membrane Degradation in Polymer Electrolyte Fuel Cells. *Membranes [Electr. Res.]*. 2015;5(4):888-902. Available from: 10.3390/membranes5040888

## 15.2. Book Chapters

2016 Hacker V, Bodner M, Schenk A. Integration of a Membrane Reactor with a Fuel Cell. In *Integrated Membrane Systems and Processes*. 1 ed. John Wiley & Sons. 2016.

## 15.3. Reports

2014 Bodner M, Hofer A, Cermenek B, Hacker V. Green Cell - Neue Materialien für die alkalische Hochleistungs-Direkt-Ethanol-Brennstoffzelle. 2014.

#### 15.4. Lectures and Publications

- 2017 Hacker V, Bodner M. Localisation of Inhomogeneous Degradation Effects in PEFCs. 2017. 7<sup>TH</sup> INTERNATIONAL CONFERENCE on FUNDAMENTALS AND DEVELOPMENT OF FUEL CELLS, Stuttgart, Germany.
- 2016 Bodner M, Schenk A, Marius B, Rami M, Hacker V. Air Starvation Accelerated Stress Tests in Polymer Electrolyte Fuel Cells. 2016. Pacific Rim Meeting on Electrochemical and Solid-State Science 2016, Honolulu, United States.
- Hacker V, Schenk A, Bodner M. Carbon support corrosion and membrane degradation. 2016. 9<sup>th</sup> International Summer School on Advanced Studies of Polymer Electrolyte Fuel Cells, Graz, Austria.
- Schenk A, Grimmer C, Bodner M, Cermenek B, Hacker V. DAFC, DBFC, HTPEM and AFC. 2016. 9<sup>th</sup> International Summer School on Advanced Studies of Polymer Electrolyte Fuel Cells, Graz, Austria.
- Schenk A, Gamper S, Grimmer C, Pichler BE, Bodner M, Weinberger S et al. Development of Low Cost High-Temperature Polymer Electrolyte Fuel Cell Membrane-Electrode-Assemblies for Combined Heat and Power Plants in Single Family Homes. 2016. Pacific Rim Meeting on Electrochemical and Solid-State Science 2016, Honolulu, United States.
- 2015 Bodner M, Hacker V. Degradation of polymer electrolyte fuel cells accelerated by membrane defects. 2015. IEA-IA-AFC Task 34 - Advanced Fuel Cells for Transportation Workshop, Vienna, Austria.
- Bodner M, Hacker V. Degradation of polymer electrolyte fuel cells accelerated by membrane defects. 2015. 3<sup>rd</sup> international workshop on degradation issues of fuel cells and electrolysers, Fira, Greece.

- Hacker V, Schenk A, Bodner M. Carbon support corrosion and membrane degradation. 2015. 8<sup>th</sup> International Summer School on Advanced Studies of Polymer Electrolyte Fuel Cells, Yokohama, Japan.
- 2014 Hacker V, Weinberger S, Bodner M. Advanced Fuel Cell Diagnostics. 2014. IEA AFC, Annex 22 Meeting, Seoul, Republic of Korea.
- 2013 Hacker V, Hofer A, Bodner M, Grimmer C, Schenk A. Pt-free Direct Ethanol Fuel Cells. 2013. 8<sup>th</sup> A3PS Conference Eco-Mobility 2013, Wien, Austria.
- 2012 Stadlhofer A, Bodner M, Schröttner H, Hacker V. Pt-free catalysts for alkaline direct ethanol membrane electrode assemblies. 2012. 222<sup>nd</sup> ECS Meeting, Honolulu, Hawaii, United States.

#### 15.5. Conference Contributions

- 2017 Bodner M, Marius B, Rami M, Schenk A, Hacker V. Local Degradation Effects in Polymer Electrolyte Fuel Cells. 2017. Abstract from 7<sup>TH</sup> INTERNATIONAL CONFERENCE on FUNDAMENTALS AND DEVELOPMENT OF FUEL CELLS, Stuttgart, Germany.
- 2016 Bodner M, Schenk A, Marius B, Rami M, Hacker V. Air Starvation Accelerated Stress Tests in Polymer Electrolyte Fuel Cells. 2016. Abstract from Pacific Rim Meeting on Electrochemical and Solid-State Science 2016, Honolulu, United States.
- Hacker V, Schenk A, Bodner M. Carbon support corrosion and membrane degradation. 2016. Abstract from 9th International Summer School on Advanced Studies of Polymer Electrolyte Fuel Cells, Graz, Austria.

Schenk A, Grimmer C, Bodner M, Cermenek B, Hacker V. DAFC, DBFC, HPEM and AFC. 2016. Abstract from 9<sup>th</sup> International Summer School on Advanced Studies of Polymer Electrolyte Fuel Cells, Graz, Austria.

Bodner M, Rami M, Marius B, Schenk A, Hacker V. Determining Membrane Degradation in Polymer Electrolyte Fuel Cells by Effluent Water Analysis. 2016. Abstract from Pacific Rim Meeting on Electrochemical and Solid-State Science 2016, Honolulu, United States.

Schenk A, Gamper S, Grimmer C, Pichler BE, Bodner M, Weinberger S et al. Development of Low Cost High-Temperature Polymer Electrolyte Fuel Cell Membrane-Electrode-Assemblies for Combined Heat and Power Plants in Single Family Homes. 2016. Abstract from Pacific Rim Meeting on Electrochemical and Solid-State Science 2016, Honolulu, United States.

Schopp P, Bodner M, Nestl S, Hacker V. Layout of an Advanced Polymer Electrolyte Fuel Cell Stack for Material Testing. 2016. Abstract from 2<sup>nd</sup> International Workshop on Hydrogen and Fuel Cells, Graz, Austria.

Bodner M, Cermenek B, Rami M, Schenk A, Hacker V. MEMBRANE DEGRADATION MITIGATION BY THE PRESENCE OF PLATINUM ELECTROCATALYST. 2016. Abstract from 2<sup>nd</sup> International Workshop on Hydrogen and Fuel Cells, Graz, Austria.

Rami M, Bodner M, Hacker V. Optimization of Alkali Fusion of Nafion®. 2016. Abstract from 2<sup>nd</sup> International Workshop on Hydrogen and Fuel Cells, Graz, Austria.

Schenk A, Gamper S, Grimmer C, Bodner M, Weinberger S, Hacker V. Phosphoric Acid Tolerant Oxygen Reduction Reaction Catalysts for High-Temperature Polymer Electrolyte Fuel Cells. 2016. Abstract from Pacific Rim Meeting on Electrochemical and Solid-State Science 2016,

Honolulu, United States.

Schenk A, Hammer B, Bodner M, Cermenek B, Hacker V. The Austrian participation in the IEA Technology Collaboration Program on Advanced Fuel Cells. 2016. Abstract from 2nd International Workshop on Hydrogen and Fuel Cells, Graz, Austria.

2015 Hacker V, Schenk A, Bodner M. Carbon support corrosion and membrane degradation. In *Advanced Studies on Polymer Electrolyte Fuel Cells*. Graz: Verlag der Technischen Universität Graz. 2015. p. 91-101.

Bodner M, Hacker V. Investigation of Degradation in Polymer Electrolyte Fuel Cells. In 11. Minisymposium der Verfahrenstechnik. Wien: 2015. p. 103-106.

2014 Bodner M, Hacker V. Localisation of Pinholes in Polymer Electrolyte Membrane Fuel Cells. In 10. Minisymposium Verfahrenstechnik Proceedings. Wien: 2014. p. 87-90.

Bodner M, Hacker V. Pinhole Localisation in Polymer Electrolyte Membrane Fuel Cells. In *Advanced Studies of Polymer Electrolyte Fuel Cells 7<sup>th</sup> International Summer School*. Verlag der Technischen Universität Graz: 2014. p. 149-150.

2013 Bodner M, Hofer A, Hacker V. Investigation of active and passive alkaline direct ethanol fuel cells. In *Advanced Studies of Polymer Electrolyte Fuel Cells 6<sup>th</sup> International Summer School*. Verlag der Technischen Universität Graz: 2013. p. 135-136.

2012 Stadlhofer A, Bodner M, Schröttner H, Hacker V. Pt-Free Catalysts for Alkaline Direct Ethanol Membrane Electrode Assemblies. In *ECS Meeting*. .2012. p. 1328-1328.

2011 Bodner M, Stadlhofer A, Hacker V. Investigation of a Ni-based electrocatalyst for alkaline direct ethanol fuel cells. In

Advanced Studies of Polymer Electrolyte Fuel Cells 4<sup>th</sup> International Summer School. Verlag der Technischen Universität Graz. 2011. p. 85-86.

## 15.6. Poster

- 2016 Bodner M, Rami M, Marius B, Schenk A, Hacker V. Determining Membrane Degradation in Polymer Electrolyte Fuel Cells by Effluent Water Analysis. 2016. Poster session presented at Pacific Rim Meeting on Electrochemical and Solid-State Science 2016, Honolulu, United States.
- Bodner M, Cermenek B, Rami M, Schenk A, Hacker V. MEMBRANE DEGRADATION MITIGATION BY THE PRESENCE OF PLATINUM ELECTROCATALYST. 2016. Poster session presented at 2<sup>nd</sup> International Workshop on Hydrogen and Fuel Cells, Graz, Austria.
- Schenk A, Gamper S, Grimmer C, Bodner M, Weinberger S, Hacker V. Phosphoric Acid Tolerant Oxygen Reduction Reaction Catalysts for High-Temperature Polymer Electrolyte Fuel Cells Catalyst Activity and Durability for Hydrogen and Reformate Acidic Fuel Cells. 2016. Poster session presented at Pacific Rim Meeting on Electrochemical and Solid-State Science 2016, Honolulu, United States.
- Schenk A, Hammer B, Bodner M, Cermenek B, Hacker V. The Austrian Participation in the IEA Technology Collaboration Program on Advanced Fuel Cells. 2016. Poster session presented at 2<sup>nd</sup> International Workshop on Hydrogen and Fuel Cells, Graz, Austria.
- Schopp P, Bodner M, Nestl S, Hacker V. Layout of an Advanced Polymer Electrolyte Fuel Cell Stack for Material Testing. 2016. Poster session presented at 2<sup>nd</sup> International Workshop on Hydrogen and Fuel Cells, Graz, Austria.

- Rami M, Bodner M, Hacker V. Optimization of Alkali Fusion of Nafion®. 2016. Poster session presented at 2<sup>nd</sup> International Workshop on Hydrogen and Fuel Cells, Graz, Austria.
- 2015 Bodner M, Hacker V. Investigation of Degradation in Polymer Electrolyte Fuel Cells. 2015. Poster session presented at 11. Minisymposium der Verfahrenstechnik, Wien, Austria.
- 2014 Bodner M, Hacker V. Localisation of Pinholes in Polymer Electrolyte Membrane Fuel Cells. 2014. Poster session presented at 10. Minisymposium Verfahrenstechnik, Wien, Austria.
- Bodner M, Weinberger S, Hacker V. Pinhole Detection in Polymer Electrolyte Membrane Fuel Cells. 2014. Poster session presented at International Workshop on PEMFC Stack and Stack Component Testing, Stuttgart, Germany.
- Bodner M, Hacker V. Pinhole Localisation in Polymer Electrolyte Membrane Fuel Cells. 2014. Poster session presented at Advanced Studies of Polymer Electrolyte Fuel Cells 7<sup>th</sup> International Summer School, Graz, Austria.
- Weinberger S, Gebetsroither F, Bodner M, Hacker V. Spatial Current and Temperature Measurements within an Air Cooled Polymer Electrolyte Fuel Cell Stack. 2014. Poster session presented at International Workshop on PEMFC Stack and Stack Component Testing, Stuttgart, Germany.
- 2013 Stadlhofer A, Bodner M, Schenk A, Hacker V. Au-Ni bimetallic catalysts for the EOR in alkaline media. 2013. Poster session presented at 6<sup>th</sup> PBFC, International Conference on Polymer Batteries and Fuel Cells, Ulm, Germany.
- Stadlhofer A, Bodner M, Schenk A, Hacker V. Development of Pt-free anode catalysts for alkaline direct ethanol fuel

cells. 2013. Poster session presented at 9. Minisymposium der Verfahrenstechnik, Leoben, Austria.

Bodner M, Hofer A, Hacker V. Investigation of active and passive alkaline direct ethanol fuel cells. 2013. Poster session presented at 6th International Summer School On Advanced Studies of Polymer Electrolyte Fuel Cells, Yokohama Japan.

Hofer A, Bodner M, Hacker V. Materials for DEFCs. 2013. Poster session presented at Workshop on Polymer Ion Exchange Membranes, Bad Zwischenahn, Germany.

Bodner M, Hofer A, Hacker V. Optimization of the flow field for an alkaline direct ethanol fuel cell. 2013. Poster session presented at 15. Österreichische Chemietage 2013, Graz, Austria.

2012 Stadlhofer A, Bodner M, Cermenek B, Schenk A, Hacker V. Neue Materialien für die alkalische Direkt-Ethanol-Brennstoffzelle. 2012. Poster session presented at 7<sup>th</sup> A3PS Conference - ECO-MOBILITY 2012, Wien, Austria.

2011 Bodner M, Stadlhofer A, Hacker V. Investigation of a Ni-based electrocatalyst for alkaline direct ethanol fuel cells. 2011. Poster session presented at 4<sup>th</sup> International Summer School on Advanced Studies of Polymer Electrolyte Fuel Cells, Yokohama Japan.

Stadlhofer A, Bodner M, Hacker V. Ni-based electrocatalysts for alkaline direct ethanol fuel cells. 2011. Poster session presented at 62<sup>nd</sup> Annual Meeting of the International Society of Electrochemistry, Niigata, Japan.

Stadlhofer A, Bodner M, Hacker V. The Ethanol Oxidation Reaction in Alkaline Direct Alcohol Fuel Cells. 2011. Poster session presented at EICOON Workshop and School - Nanomaterial Issues in Electrochemical Energy Conversion: Fuel Cells, Batteries, Supercapacitors, Helsinki, Finland.

## 16. Selected Peer Reviewed Publications

### 16.1. H<sub>2</sub> Generation from Alkaline Electrolyzer.

*Bodner M, Hofer A, Hacker V. H<sub>2</sub> generation from alkaline electrolyzer. Wiley Interdiscip Rev Energy Environ 2015;4:365–81.*

*Contribution:*

Recent advances in catalyst and membrane development for alkaline electrolyzers are discussed. This work was partially completed in collaboration with Dr. Astrid Hofer, who provided the basic structure and Prof. Viktor Hacker, who advised in all aspects.

The review paper describes the reactions, taking place in alkaline electrolyzers and provides a detailed discussion of the limiting parameters. It also contains a detailed summary of available electrocatalysts and electrolytes as well as recent developments in the respective areas. Commercial aspects and existing systems were also included.



# H<sub>2</sub> generation from alkaline electrolyzer

Merit Bodner,\* Astrid Hofer and Viktor Hacker

Water electrolysis is a promising approach to hydrogen production from renewable energy sources. Even though it is not necessarily environmentally friendly and a large number of possible feedstocks for hydrogen production include fossil resources such as coal, natural gas, and mineral oil, but also biomass, water, and components such as ethanol, methane, or ammonia can be used for hydrogen production. Also, a large variety of different energy sources can be used for hydrogen production. The combination of hydrogen production with renewable energy systems, such as photovoltaics, hydropower, or wind energy is very suitable though. Many innovative processes have been subject to intense research and some have already reached high efficiencies. Alkaline water electrolyzers with anion-conducting membranes hold many advantages in comparison to other systems. As cheaper, non-noble metals are stable in alkaline media, the relatively low cost of the electrode materials is one of the main advantages of alkaline systems over electrolyzers using proton-conducting electrolytes. Therefore, the main part of published literature on alkaline electrolysis describes electrodes based on low cost materials such as nickel for both anode and cathode. Yet still alkaline water electrolyzers have to compete against other forms of hydrogen production, such as steam reforming of natural gas. Even though many studies expect water electrolysis to become economically viable on a long-term basis, conventional hydrogen production is still hard to under-price. © 2014 John Wiley & Sons, Ltd.

#### How to cite this article:

*WIREs Energy Environ* 2015, 4:365–381. doi: 10.1002/wene.150

## INTRODUCTION

Due to the increasing global energy demand, novel supply strategies have to be developed in order to avoid a vast increase in CO<sub>2</sub> emissions. Many new approaches have been subject to intense research.

Hydrogen is considered one of the future key energy carriers in all of today's energy prognoses and its importance for the future energy system has been discussed in numerous publications over many years.<sup>1–5</sup> Hydrogen does not occur in nature in its molecular form and is usually bound in water or hydrocarbons. As both water and hydrocarbon are very abundant on earth, the limitation on possible feedstocks will not be a restriction. Possible feedstocks for hydrogen production include fossil resources such

as coal, natural gas, and mineral oil as well as biomass, water, and components such as ethanol, methane, or ammonia. Also, a large variety of different energy sources can be used for hydrogen production.

Up to now, as much as 96% of the world hydrogen production is based on fossil fuels and conventional energy sources, 48% of that being from natural gas via steam reforming, 30% from naphtha reforming, and 18% from coal gasification. These processes are high in emission. Therefore, in order for hydrogen to become a sustainable energy carrier, production cannot rely on those feedstocks.<sup>6</sup>

Hydrogen production has to satisfy three major requirements in order to fulfil its role in the future:

- it has to follow sustainable pathways
- use abundant and renewable feedstocks
- the produced hydrogen is required to be of high purity, as impurities are harmful for most applications, such as fuel cells.

\*Corresponding author: merit.bodner@tugraz.at

Institute of Chemical Engineering and Environmental Technology, Graz University of Technology, Graz, Austria

Conflict of interest: The authors have declared no conflicts of interest for this article.

Only when both the feedstock for the process and the energy source for the electrical power input are renewable, hydrogen can be regarded as sustainable.

The possibilities for a sustainable hydrogen production are given. Many routes, based on renewable feedstocks are known. For example, hydrogen can derive from biomass processing, biological or solar thermal water splitting, and water electrolysis using renewable primary energy sources.

Today, natural gas is the most common feedstock for hydrogen production,<sup>3,7</sup> but methane can also derive from biomass gasification. Furthermore, other compounds, such as bioethanol, can be converted by steam reforming too.

Hydrogen can also be produced by biological conversion of biomass or water with microorganisms. This so-called bio-hydrogen production includes photolytic reactions. The energy of light is used to produce hydrogen with photosynthetic microbes such as algae and cyanobacteria.<sup>8,9</sup> Thermochemical conversion for hydrogen production can be applied with various raw materials, yet the process requires either extremely high energy inputs or the yield of hydrogen in the gas mixture is low.

Fermentation methods are also an option for hydrogen production.<sup>7,9</sup>

Yet for the usage in most of the common applications, such as fuel cells or for synthesis, hydrogen has to reach a purity of 99.3–99.8% or more. This can be achieved either by complex and expensive purification steps, or simpler, by methods producing hydrogen at an already high purity, such as water electrolysis.<sup>10</sup> Water electrolyzers mostly use conventional energy sources, but the usage of renewable energy is of great interest.

Also, hydrogen can be stored without the self-discharge many batteries exhibit. Electrolysis is very suitable to produce hydrogen from surplus energy of renewable energy sources, such as hydropower, photovoltaics, and wind energy.<sup>6</sup> The perspective for the implementation of hydrogen production systems using renewable power sources is considered positive.<sup>11</sup> Hydrogen can be stored in a variety of different forms. It can be stored gaseous at increased pressure, liquid at very low temperatures, or in metal hydrides. The stored hydrogen can then either be used in a fuel cell to produce electricity in order to meet changing load demands or can be transported and further used, e.g., in hydrogen-powered vehicles for transportation.<sup>6</sup>

The combination of a photovoltaic module with an alkaline water electrolyzer (AWE) has been examined, as this technology of hydrogen production has no CO<sub>2</sub> emission.<sup>10</sup> This system would be especially suitable for off-grid power supply.<sup>6</sup>

Wind power is the most rapidly growing renewable energy sector and large plants have already been installed all over the world. Wind-powered electrolysis has the potential to become the first economically viable technology to produce large amounts of renewable hydrogen in the near future.<sup>6</sup> Yet commercially available electrolyzers are usually designed for stationary on-grid operation and are easily damaged by intermittent operation.<sup>12</sup> But still, hydrogen was produced efficiently and with a satisfying purity and oxygen content below 0.2%.<sup>6</sup>

The solar thermal electrochemical photo (STEP) process is an attempt to use the full solar spectrum (visible and thermal) for water electrolysis. This is a hybrid thermal and electrochemical photo process in which the sub-bandgap and the excess super-bandgap heat are used to heat the electrolysis chamber, lowering the energy required to split water. Higher temperatures decrease the water splitting potential and simultaneously decrease the kinetic overpotential losses. Therefore, the charge transfer is favored. The STEP process is intrinsically more efficient than other solar energy-powered conversion processes and an economically viable process for the hydrogen generation via electrolytic water splitting.<sup>13</sup>

## CLASSIFICATION

A multitude of different setups for electrolysis cells were introduced. And as for fuel cells, the classification system was swamped with new inventions. Electrolysis cells used to be divided into three types. Alkaline electrolysis cells use liquid electrolytes such as sodium or potassium hydroxides. Acidic electrolysis cells are usually equipped with proton-conducting polymer electrolyte membranes. The third option is solid oxide electrolyte cells, converting water steam electrolysis at high temperatures.

With new inventions and the development of novel materials, electrolysis systems can now be classified by different methods.

### Classification by Operation Condition

Different electrolysis systems require different operation conditions, which then again influence the electrical efficiency strongly.<sup>14</sup> Temperature and pressure have to be adapted to each type of cell. A differentiation between low (70–80°C), intermediate (150–200°C), and high (700–1000°C) temperature cells as well as low- and high-pressure systems is possible.<sup>15,16</sup>

## Classification by Substrate

Electrolysis cells usually use water, but other substrates are also possible. The usage of ammonia, methanol, urea, or even black liquor,<sup>17,18</sup> a byproduct of the paper industries, is possible and subject to intense research.

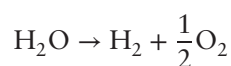
## Classification by Electrolyte

The electrolyte is one of the most common properties chosen to describe the electrolysis cell. It can be distinguished between the pH of the electrolyte (alkaline and acid) or the electrolyte's state (liquid electrolyte, polymer electrolyte, or solid oxide electrolyte). Polymer electrolyte membranes used to be based on acidic polymers only, but with the rise of anion-exchange membranes (AEMs) in past years, membranes are no longer solely proton-exchange membranes (PEMs).<sup>19</sup>

Because of the great amount of innovations in the field of AWEs and its promising features, this review will focus on alkaline electrolysis.

## FUNDAMENTALS OF ALKALINE ELECTROLYSIS

The biggest advantages of alkaline electrolysis systems are their robustness, their long lifetime and the lower costs due to cheaper electrode materials. Independent of the electrolyte, the water splitting reaction is endothermic and gives hydrogen and oxygen.



This general formula consists of a cathode (hydrogen evolution reaction, HER) and an anode reaction (oxygen evolution reaction, OER) (Figure 1). During the reaction, gas bubbles are formed on the cathode and anode surface, containing hydrogen and oxygen, respectively. The bubbles are detached from the surface at a certain size.<sup>20</sup>

The formation of a gas phase results in several negative phenomena in the electrolysis system. The electrode surface is blocked by gas bubbles and the electron transfer between electrode and electrolyte is hindered. Bubbles increase the resistance of the electrolyte and damage the electrode surface.<sup>20,21</sup>

The drawback of AWEs is the low maximum power density achieved with liquid electrolytes.<sup>21</sup> This limitation is caused by the negative effect of bubble formation. As bubble formation is inevitable in electrolysis cells, materials and configurations have to be adapted and optimized. Several methods have been applied to avoid the negative effects. Application

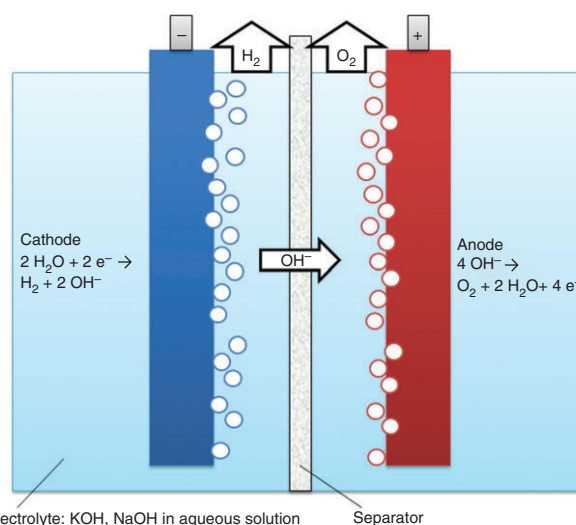
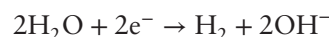


**FIGURE 1** | Scheme of an alkaline water electrolysis cell.

of centrifugal fields, super gravity fields, magnetic fields, ultrasound, and microwave treatments results in a more complex system setup, yet do not improve the efficiency significantly.<sup>21</sup> A very promising method to improve the performance of the electrolysis cells is the implementation of an AEM and a zero gap configuration, respectively. Operation with an AEM would additionally avoid further negative effects of liquid electrolytes.

## Hydrogen evolution reaction

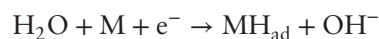
Within alkaline media, the HER proceeds via the formula



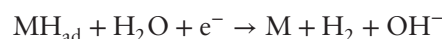
with a standard electrode potential of  $E^0 = -0.828$  V versus SHE.<sup>22</sup>

The HER can be divided into two consecutive steps as follows.

The water dissociation (Volmer step)



is followed by the hydrogen emission. This happens either via the Heyrovsky step



or the Tafel step



The Tafel and the Heyrovsky steps proceed in parallel and competitively, differentiated by chemical

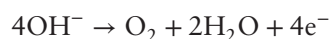
(Tafel) and electrochemical (Heyrovsky) desorption.<sup>23</sup> The reaction rate of the first step is usually small. As a consequence, diffusion phenomena on the cathode can be neglected.<sup>24</sup> The reaction rate of the HER is strongly dependent on the strength of the metal–hydrogen bond and the catalyst surface morphology. Depending on the catalyst system, the hydrogen from the substrate is adsorbed (e.g. on Pt-based catalysts) or absorbed (e.g. on Ni-based catalysts) and is emitted as molecular hydrogen H<sub>2</sub> via complex intermediate steps.

Therefore, the rate-determining step (rds) depends on the catalyst. For most materials, the rds is the Volmer step, whereas the hydrogen desorption was identified as the rds for Ni–Fe–P catalysts.<sup>25</sup>

Hydrogen evolution is not limited by diffusion due to the high population of participating molecules in alkaline water solution.<sup>22</sup> Yet the reaction rate of the HER in acidic media is higher by 2–3 orders of magnitude than in alkaline environment.<sup>26</sup>

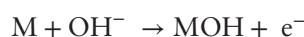
## Oxygen Evolution Reaction

The overall OER in alkaline media proceeds via the formula

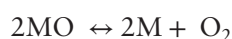
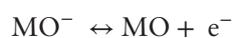
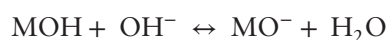


at  $E^0 = 0.401$  V versus SHE.<sup>27</sup>

The steps of the OER in alkaline media have been proposed by Yeager in 1974 with a reported reaction order of 1 and are:



A different mechanism was proposed by Kubiszal and Budniok, who used a nickel matrix with embedded Mo/Si particles.<sup>28</sup>



The rds depends on the applied potential.<sup>28</sup>

Due to the complex reaction pathway, the anode reaction is the major cause for high overpotentials in water electrolysis cells. The onset potential of the OER is generally higher than 1.4 V, due to overpotentials of over 150 mV. Overpotentials of 0.4 V are common.<sup>27</sup>

The kinetics of the OER is slow. The reaction follows a complex multistep mechanism via four electrons and, in acidic cells, four proton-transfer steps and four OH<sup>−</sup> transfer steps in alkaline media, respectively. The reaction paths include multiple high-energy intermediates. Catalyst development is still subject of active research. The overpotential highly depends on the anode material, the electrode surface, and the temperature.<sup>29</sup>

## COMPONENTS

### Electrodes

The relatively low cost of the electrode materials is one of the main advantages of alkaline systems over electrolyzers using proton-conducting electrolytes. Therefore, the main part of published literature on alkaline electrolysis describes electrodes based on low-cost materials such as nickel for both anode and cathode.

The exact kinetics of both the HER and the OER, or any other anode reaction with different substrates, strongly depend on the electrode material. But nevertheless it can be stated that on most electrode surfaces, the overpotential of the HER is very small compared to that of the OER. The anode reaction is much more strongly inhibited. The OER's overpotential is in most cases the limiting factor and usually the most inefficient part of alkaline systems.<sup>29</sup> The performance of the catalysts depends not only on the chosen catalyst materials, but also on many other factors such as the support material, pretreatment, and the resulting microstructure and morphology.

Many catalysts for alkaline water electrolysis are adapted from catalysts used for the chlor-alkali electrolysis.<sup>29,30</sup> But due to the reduced corrosiveness of the produced oxygen compared to chlorine, Ni-based electrodes and cell chambers are possible for both electrode departments instead of titanium in chlor-alkali electrolyzers.<sup>30</sup>

### Cathode

Numerous publications<sup>26,31–33</sup> are available on the characteristics of the HER on platinum catalysts, as it is the most active electrode material. But due to the high cost of Pt, steel and nickel usually have been the cathode materials of choice.<sup>22</sup>

Yet the cathode catalyst is still subject to active research and the novel catalyst systems can be divided into three groups as follows:

- group (i): metals with improved microstructure and surface area
- group (ii): metal alloys
- group (iii): hydrogen storage alloys

Much work has been dedicated to the improvement of stability and activity of Ni-based electrodes. This enhancement can be achieved by coating or co-depositing a more active or more stable material such as cobalt,<sup>34</sup> aluminium,<sup>35–37</sup> or iron<sup>38,39</sup> and incorporation of additional elements such as sulphur<sup>40–44</sup> with the aim to improve the surface microstructure to gain group (i) catalysts. As the HER mainly involves surface processes, the electrocatalytic activity can vastly be improved by adaption of the surface composition and microstructure.<sup>45</sup> The HER in alkaline media is, in contrast to acidic systems, very sensitive concerning the surface structure.<sup>26</sup>

Group (ii) includes catalysts designed after the strategy based on the hydrogen bond strength.<sup>22</sup> Relating to the volcano curve for elemental metals,<sup>46</sup> it appears comprehensible to combine hypo-d-electron metals with hyper-d-electron metals, e.g., Ni–Mo,<sup>21,47–50</sup> Co–Mo, Ni–Cr,<sup>47</sup> or Ni–W<sup>51,52</sup> catalysts, in order to optimize the hydrogen bond strength. Adaption of the d-band structure by designing Ni–nitrogen complexes as performed for HER catalysts is so far only observed for acidic applications.<sup>53</sup>

Group (iii) hydrogen storage alloys are another type of effective electrocatalysts for the cathode. Hydrogen is absorbed during HER and can be released on demand to protect the electrode surface from damage.<sup>54</sup>

Of course these groups cannot be separated clearly and the enhancing effect of alloying Mo to Ni is mainly ascribed to an increased surface area rather than synergetic effects.<sup>55</sup>

### Platinum Group-Based Catalysts

Acidic water electrolyzers and fuel cells usually use platinum-based electrodes such as Pt/C or polycrystalline Pt. In alkaline media, the kinetics of the HER are orders of magnitude slower than in acidic media. This is due to a shorter distance between platinum and the adsorbed hydrogen in alkaline media, indicating a stronger bond. Therefore, the Heyrovsky step is the rds in alkaline electrolyzers, whereas the HER in acidic media simply follows the Nernstian hydrogen diffusion overpotential relationship.<sup>31</sup>

The catalytically active area can be enlarged by using supported platinum catalysts. This approach is very common for PEM fuel cells. In proton-exchange electrolysis cells, both Pt/C and Pt/WC have been used. Compared to bulk Pt, an increase in activity has been achieved for both catalysts, yet no synergetic effect between catalyst metal and support material was reported.<sup>32</sup> In alkaline media, a platinum catalyst was improved by its deposition on a Ni/C substrate. Yet the Ni/C substrate alone already showed improved activity for the HER.<sup>33</sup>

Palladium shows a significant catalytic activity for the HER in alkaline media. As cathode material, different palladium salts were deposited on gold surface, forming Pd islands. The strong interaction between Au and Pd decreases the adsorption energy of hydrogen and thereby enhanced the catalytic activity, whereas a plain Au surface exhibits large overpotentials. The islands deposited when using PdCl<sub>2</sub> turned out to be smaller, thinner and showed a pronounced step decoration, resulting in an increased activity.<sup>56</sup>

### Group (i) Catalysts

Mild steel is another traditional cathode material. In order to improve the catalytic activity, different types of additives can be added. Elezovic et al. used molybdenum to increase the surface roughness with increased content. Fe–Mo alloys on a mild steel substrate have been shown to achieve low HER overpotentials with Mo contents of 59.3 at.%.<sup>57</sup>

In a similar study, Rosalbino et al. further used rare earth metals as additive for a Fe–Mo electrode. Fe<sub>75</sub>Mo<sub>20</sub>MM<sub>5</sub> (MM = mischmetal, 50.2 at.% Ce, 26.3 at.% La, 17.5 at.% Nd, and 6.0 at.% Pr) exhibited a lower Tafel slope and higher exchange current density than the Fe<sub>80</sub>Mo<sub>20</sub> alloy used for comparison. The improvement of the catalyst derives from a synergetic effect between the different alloy phases.<sup>58</sup>

Many catalysts lose their activity after a few cycles of operation due to surface contamination. To avoid the loss of active sites, phosphorous is used as amorphism causing additive. Amorphous alloys, such as Fe–P, Fe–P–Pt, or Fe–P–Ce, have interesting mechanical, magnetic, and electrical properties. Furthermore, the corrosion stability in alkaline media for medium-term operation is given. Especially high activities have been observed on Fe<sub>94</sub>P<sub>4</sub>Pt<sub>2</sub> and Fe<sub>94</sub>P<sub>4</sub>Ce<sub>2</sub> electrodes. This is ascribed to geometric surface effects, but also to the synergetic effects between Fe and P<sub>2</sub>Pt, P<sub>2</sub>Pt<sub>5</sub>, FePt, and especially FeCe phases.<sup>45</sup>

In order to develop novel, inexpensive and highly stable electrode materials, current research is mainly focusing on nonplatinum group metals.<sup>47</sup> Among the non-noble metals, Ni is the most active pure

metal toward the HER in AWEs. Furthermore, the dissolution of Ni is slow, making nickel one of the most stable non-noble metals in alkaline media and a promising material for a large-scale production.<sup>35</sup>

To improve the activity, i.e., decrease the overpotential for the HER of pure nickel catalysts, the surface area has to be increased. Ni nanoparticles show an optimized surface morphology, showing low overpotential and high exchange current densities.<sup>59</sup>

In their study, Zeng and Zhang used polished Ni electrodes. It was proven that a rougher surface reduces the overpotential. Whilst the apparent activity was improved, Ni–Co electrodes did show no increased intrinsic activity compared to the Ni electrodes. It was concluded, that the improvement of the apparent activity is only attributed to the increased surface area.<sup>60</sup>

Coating with graphene oxide has been shown to increase the catalytic activity of the Ni electrode.<sup>61</sup>

#### Group (ii) Catalysts

HER catalysts based on Raney-Ni doped with elements such as Fe, Cr, Mo, Sn, or Co, but also rare earth metals or sulphides have been shown to suppress the overpotential, compared to pure Ni electrodes. Again, the morphology determines the activity. It is suggested, that the formation of Ni hydrides by hydrogen adsorption during the HER improves the stability by inhibiting passivation of the catalyst surface. The best long-term performance was achieved with 70% Raney-Ni 7000, 10% Carbonyl Fe, 10% Carbonyl Ni, and 10% polytetrafluoroethylene (PTFE); PTFE being required as binder.<sup>47</sup>

With the aim to generate catalysts with higher active surfaces, Ni–Al alloys were prepared by Kjartansdóttir et al. The aluminium was then etched, resulting in a large surface area. Compared to polished Ni, the catalyst with the highest surface area exhibited a drastically decreased overpotential toward the HER.<sup>35</sup> Ni–W electrodes have shown an improved intrinsic activity toward the HER, because of synergistic effects between a metal with internally paired d-electrons (Ni) and an alloying element with partially or half-filled d-orbitals and less electronegativity (W) than the host metal. This effect improves the catalytic activity due to the modified electron density at the nickel surface.<sup>51</sup>

#### Group (iii) Catalysts

Another issue the AWE faces is the deactivation of the catalyst during power interruption. This is due to the depolarized state of the electrodes during periods of power interruption. Reversed currents cause corrosion and a severe change of electrode composition and structure. Therefore, hydrogen storage alloys

have been implemented in HER electrodes. Hydrogen is adsorbed during operation and can be released during power interruption. Hydrogen is then consumed at the cathode, protecting the electrode from being corroded and thereby improving the time stability during intermitted electrolysis.<sup>54</sup>

Ti<sub>2</sub>Ni is one type of hydrogen storage alloy that has been implemented in AWEs. As cathode material, Ti<sub>2</sub>Ni particles were mixed with carbonyl Ni powder and polyvinyl alcohol as binder. The mixture was then poured into Ni foam as substrate and coated with a Ni–Mo alloy. The electrode exhibits excellent resistance against power interruption and anodic oxidation. Besides the Volmer reaction, the hydrogen diffusion, the Heyrovsky and the Tafel reaction, a fifth step, the hydride formation, is now also taking place at the cathode. The HER although is mainly determined by the Ni–Mo coating on the electrode surface.<sup>12</sup>

Hu also prepared an electrode material containing MmNi<sub>3,3</sub>Co<sub>0,75</sub>Mn<sub>0,4</sub>Al<sub>0,27</sub> as hydrogen storage alloy in Ni-foam substrate with a Ni–Mo coating. Compared to the Ti<sub>2</sub>Ni-based cathode, this electrode exhibited an even better stability in times of power interruption. The catalytic activity was again shown to mainly depend on the molybdenum content in the electrode coating.<sup>54</sup>

In Table 1, a list of published cathode catalyst systems for the alkaline HER is provided. Comparison of the catalysts based on the published performance is difficult, as detailed data on the measuring technique are not given or various techniques are applied. Operation conditions, such as the temperature, often differ vastly and different types and concentrations of electrolyte are used. As all this influences the electrolyzer greatly, a direct comparison is not possible.

Alkali metals such as Na, K, and Li also influence the HER mechanism strongly;<sup>26</sup> therefore, the electrolyte affects the measurement.

#### Anode

Due to the high overpotential required for the OER, the potential for the anodic oxygen evolution is positive, independent of the used electrocatalyst. This causes the surface of all materials to be covered by an oxide layer. Furthermore, the high overpotentials at the anode give rise to corrosion of the electrocatalyst and the support material.<sup>29</sup> This is one major obstacle prevailing when improving the lifetime of a catalyst.

For future implementation of novel electrocatalysts, the material must show a sufficient activity toward the OER and long-term stability, especially under the harsh conditions of an AWE. Furthermore, catalysts consisting of cheap, commercially available

**TABLE 1** | Comparison of HER Catalysts

Electrode	Performance	Conditions	References
Pt/C	0.6 mA cm <sup>-2</sup> exchange current density	0.1 M KOH, thin film	Ref 31
Polished Ni	422 mV overpotential at 75 A cm <sup>-2</sup>	0.5 M KOH, SCE, 3.14 mm <sup>2</sup> disk electrode	Ref 60
Co/C	1.1 × 10 <sup>-2</sup> mA cm <sup>-2</sup> exchange current	0.1 M NaOH w/o ME nanoflakes	Ref 34
Ni <sub>1</sub> Co <sub>9</sub> /C	9.1 × 10 <sup>-3</sup> mA cm <sup>-2</sup> exchange current	0.1 M NaOH w/o ME nanoflakes	Ref 34
Raney Ni	100 mV overpotential at 500 mA cm <sup>-2</sup>	28 wt% KOH, 80°C	Ref 47
Ni–Cr Raney	80 mV overpotential at 500 mA cm <sup>-2</sup>	28 wt% KOH, 80°C	Ref 47
Ni <sub>64</sub> W <sub>36</sub>	1.6 × 10 <sup>-6</sup> mA cm <sup>-2</sup> exchange current density	0.1 M NaOH	Ref 51
MmNi <sub>3,3</sub> Co <sub>0,75</sub> Mn <sub>0,4</sub> Al <sub>0,27</sub>	88 mV overpotential at 200 mA cm <sup>-2</sup>	Ni foam substrate and Ni–Mo coating, 30 wt% KOH	Ref 54
LaNi <sub>4,9</sub> Si <sub>0,1</sub>	84 mV overpotential at 200 mA cm <sup>-2</sup>	Ni foam substrate and Ni–Mo coating, 30 wt% KOH	Ref 54
Ti <sub>2</sub> Ni	60 mV overpotential at 200 mA cm <sup>-2</sup>	Ni foam substrate and Ni–Mo coating, 30 wt% KOH	Refs 12 and 54
Ni <sub>60</sub> Mo <sub>40</sub>	29 mA cm <sup>-2</sup> 59 mV overpotential at 250 mA cm <sup>-2</sup>	30 wt% KOH, 70°C, nanocrystalline fcc, mechanical alloyed	Ref 62
Ni–S	39.2 mA cm <sup>-2</sup> 90 mV overpotential at 150 mA cm <sup>-2</sup>	28 wt% NaOH, electrodeposited, thiourea	Ref 40
Fe–Mo	20.4 × 10 <sup>3</sup> mA cm <sup>-2</sup>	Fe(20%)–Mo(60%), 1 M NaOH, 25°C	Ref 57
Ni–(Ebonex–Ru)	597 mA cm <sup>-2</sup> 156 mV at 100 mA cm <sup>-2</sup>	Ni–Ti <sub>4</sub> O <sub>7</sub> –Ru, 1 M NaOH at 25°C	Ref 63
Pd/Au	NA	Pd/Au(111)	Ref 56
Ni–Sn	NA	Alloy coating deposited on Ni mesh	Ref 64
Ni–S–Co	70 mV at 150 mA cm <sup>-2</sup>	80°C, electrodeposition	Ref 41
Ni <sub>3</sub> Al	1.9 mA cm <sup>-2</sup>	6 M KOH	Ref 36
Ni <sub>3</sub> Al–Mo	13 mA cm <sup>-2</sup>	6 M KOH	Ref 37
Ni–S–Mn	97.5 mA cm <sup>-2</sup>	30% KOH, amorphous alloy	Ref 43
Ni <sub>81</sub> P <sub>16</sub> C <sub>3</sub>	2.11 mA cm <sup>-2</sup> 125.4 mV at 250 mA cm <sup>-2</sup>	1 M NaOH, 25°C	Ref 39
Ni <sub>62</sub> Fe <sub>35</sub> C <sub>3</sub>	24.5 mA cm <sup>-2</sup> 112.6 mV at 250 mA cm <sup>-2</sup>	1 M NaOH, 25°C	Ref 65
Ni–Co	29 mA cm <sup>-2</sup>	0.5 M NaOH, 25°C, electrodeposited	Ref 66
Fe <sub>94</sub> P <sub>4</sub> Ce <sub>2</sub>	0.075 mA cm <sup>-2</sup>	1 M NaOH, 25°C	Ref 45

materials are favored and the preparation methods should be simple, flexible, and easily upscalable to industrial size. An ideal catalyst would further be usable in other applications.<sup>67</sup>

### Metal-Based Catalysts

Ir-, Pt-, Rh-, and Pd-based electrodes have shown similar activity. Yet none outperformed Ni-based electrodes.<sup>29</sup>

Highly porous Raney-Ni, doped with Fe was used as gas diffusion electrode. By adding Co<sub>3</sub>O<sub>4</sub> powder and carbonyl Fe/Ni, an essentially stable behavior over weeks of testing was achieved.<sup>67</sup>

When implementing metal oxide electrodes, Ru has shown the highest performance, whilst Co

and Fe have been shown the least active. The poor performance of Co and Fe oxides might be due to their solubility in alkaline media.<sup>68</sup>

The usage of precious metal alloys with nickel did not significantly decrease the overpotential of the OER. Furthermore, the electrode was largely covered by a nickel oxide film after long-term electrolysis. The precious metal oxides were dissolved in alkaline media.<sup>29</sup>

### Oxide-Based Catalysts

PtO has shown a very low activity. When CoOOH was added though, the activity was improved significantly. Further experiments have shown that PtO functions as support only and can be substituted.

$M^{2+\delta}O^{\delta}(OH)_{2-\delta}/Pt(111)$ -based catalysts can be considered purely mono-functional. The reaction rate is driven by the strength of the interaction between two oxidic species. The rds is the recombination, not the adsorption. Therefore, too strong interactions can stabilize the reaction intermediates, poisoning the surface and decreasing the OER activity. Nickel has shown optimal interaction strength and is therefore the most suitable catalyst.<sup>69</sup>

Pyrochlore oxides with the general formula  $A_2[B_{2-x}A_x]O_{7-y}$  give a low Tafel slope and have been reported to show good activities toward the OER, due to their oxygen deficiency.  $Pb_2[Ru_{1.67}Pb_{0.33}]O_{6.5}$  has displayed very low overpotential toward the OER and reasonable long-term stability. Other promising pyrochlore oxides are  $Pb_2(Ir_{1.67}Pb_{0.33})O_{6.5}$  and  $Nd_3IrO_7$ .<sup>29</sup>

Furthermore, multiple spinel cobalt oxides have been subject to a considerable number of studies.  $Co_3O_4$ -based anode catalysts possess a high activity toward the catalysis of the OER, a high stability even in strong alkaline media, low costs, electrical conductivity, and good availability. Implementing nickel, lithium, or copper in a binary  $M_xCo_{3-x}O_4$  type oxide was found to increase the activity. The implementation of lithium has shown the most suitable results, leading toward more negative anodic peak positions with increasing Li content. Among a variety of other Li-doped cobalt oxides with different lithium contents,  $Li_{0.21}Co_{2.79}O_4$  has the highest electrical conductivity and activity toward the OER.<sup>70</sup>

### Improvement of the Catalyst Surface

Besides the catalyst composition, the morphology also influences OER strongly. Due to faster reaction kinetics, the effect of bubble formation on the electrode surface is especially severe on electrodes with a high catalytic activity. Bubble overpotential can be even higher than the OERs activation overpotential. To decrease the overpotential of the OER, the detachment of the formed bubbles has to be improved. So far, research has been focusing on methods such as the application of magnetic or ultrasonic fields, super gravity, or microgravity. The characteristics of the formed bubbles can also be influenced by the catalyst morphology though. Ahn et al. have prepared four nickel catalysts of different morphologies. Flat, smooth, cauliflower-like, and needle-like catalysts have been compared. A larger surface roughness improves the catalyst activity and increases the hydrophilicity, benefiting the bubble detachment. Therefore, catalysts with hierarchical morphologies are favorable for the water electrolysis cell.<sup>71</sup>

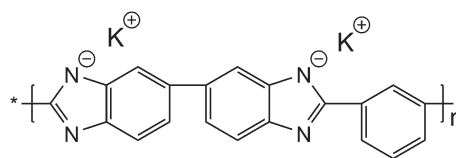


FIGURE 2 | KOH doped polybenzimidazole.

### Electrolyte

Many AWEs use liquid electrolytes such as KOH. This causes a variety of complications in applications. Leakage and carbonation are major issues with liquid alkaline electrolytes. Furthermore, bubble formation is inevitable in electrolysis cells, yet causes damage to the electrode surfaces and increases the electron transfer resistance. These are some of the major obstacles for the AWE.

Among other more or less successful methods to avoid the negative effects of bubble formation, such as the implementation of a magnetic, ultrasonic, or super gravity field,<sup>72</sup> the zero gap configuration was developed, using alkali-doped separators or solid electrolytes instead of liquid electrolytes. The electrodes are attached to the separator,<sup>30</sup> thereby avoiding damage due to bubble formation.

### Separators and Electrolyte-Doped Membranes

The main requirements for the separator are gas separation, electric isolation, and high chemical and thermal stability. The separator material alone is not ion conducting. Ion-exchange capacity is achieved by alkali doping. As the wettability directly affects the resistance of the separator, the structure of the material is of high importance.<sup>73</sup> The separator is usually porous; inorganic materials such as asbestos and other ceramics had often been used,<sup>16</sup> but more recent research has mainly focused on organic separators. Electrolyte-doped membranes or ion-solvating polymers are polymers with no ionic group attached to the backbone but have electronegative centers where the potassium salts attach.<sup>74</sup> For example, PTFE,<sup>75</sup> low-density polyethylene (LDPE)-based membranes<sup>76</sup> and polybenzimidazole (PBI) (Figure 2)<sup>77</sup> doped with an anion-exchange phase, aqueous KOH or any other alkali salt solutions have been applied in AWEs.

### Anion-Conductive Polymer Electrolytes

With the development of proton-conducting membranes, the possibilities widened for acidic water electrolysis cells. Therefore, zero gap configurations were implemented in acidic systems earlier than in alkaline cells. In polymer electrolytes, such as PEMs, the ionic group is bound to the polymer backbone.<sup>78,79</sup> Usually, no further additives are necessary.

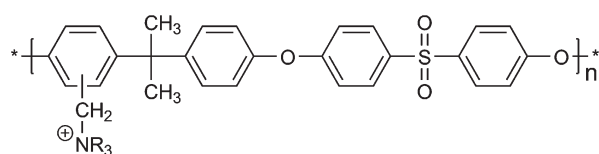


**FIGURE 3** | Quaternary ammonium polysulfone membrane.

Yet when using acidic electrolytes, cationic impurities, that are common in the feed water, tend to bind to the proton-exchanging moiety, reducing the conductivity.<sup>19</sup>

Analog to the PEMs, anion-conducting polymer electrolytes have been subject to intense research lately. They cannot only be used in electrolysis cells, but in other applications as well. A large variety of different membranes can be used and even more AEMs are still to be investigated for usage in AWEs. Commercial membranes such as the A201 from Tokuyama Corp.<sup>19</sup> or Selemion AMV from Asahi Glass Co. Ltd.<sup>61</sup> have already been successfully applied in AWEs.

Yet other, noncommercial polymer electrolytes such as LDPE-based membranes with UV-induced grafted vinyl benzyl chloride (VBC) functional groups,<sup>80</sup> quaternary ammonia (QA)-modified poly VBC membranes (qPVB/Cl),<sup>81</sup> polysulfone functionalized with quaternary ammonium groups (QAPS) (Figure 3),<sup>48</sup> and polyethylenetetrafluoroethylene

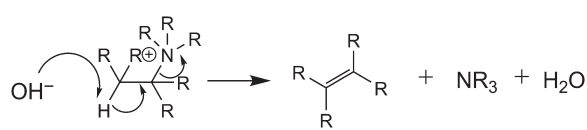


**FIGURE 4** | Hoffman elimination.

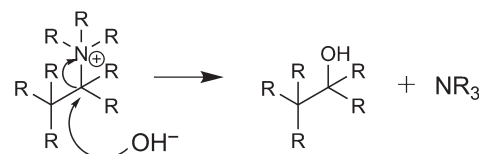


**FIGURE 5** | Nucleophilic attack.

(ETFE)-based polymers functionalized with QA<sup>82</sup> have been used for small-scale tests as well. Ionomers, typically alike the polymer electrolytes used as membrane, but also others such as QPDTB, a polymethacrylate-based copolymer of three monomers with QA moieties,<sup>83</sup> need to be added to the electrodes as binders. Some examples for alkaline electrolytes used in electrolyzers are listed in Table 2. Yet still, electrolyte has often to be added, as the conductivity may not be sufficient.

AEM water electrolyzers have been reported to show lower performance than PEM electrolyzers. This is due to the higher membrane resistance (up to three

**TABLE 2** | Comparison of Different AEMs for Alkaline Electrolysis Cells

Membrane	Conductivity	Current density	Cathode	Anode	High frequency resistance	Thickness	References
Zero gap diaphragm with 30 wt% KOH	$54.3 \times 10^{-2} / (\Omega \text{cm})$ at 25°C <sup>a</sup>	470 mA cm <sup>-2</sup> at 1.8 V, 50°C	Mo/Raney Ni	Co <sub>3</sub> O <sub>4</sub> /Raney Ni	NA	NA	Refs 19, <sup>a</sup> 84
Tokuyama A201	0.04 S cm <sup>-1</sup> at 23°C <sup>b</sup>	399 mA cm <sup>-2</sup> at 1.8 V, 50°C	Pt black	IrO <sub>2</sub>	0.23 Ω cm <sup>2</sup> at 2.0 V, 50°C	28 μm	Refs 19, <sup>b</sup> 85
Selemion AMV	$2.52 \times 10^{-1} \text{ S cm}^{-1}$	90 mA/cm <sup>-2</sup> at 2.0 V, 30°C	Ni/Zn/S coated Ni foam	Graphene oxide-coated NiO	NA	120 μm	Ref 61
QAPS	$>10^{-2} \text{ S cm}^{-1}$	0.4 A/cm <sup>-2</sup> at 1.8–1.85 V, 70°C	Ni–Mo	Ni–Fe	NA	70 μm	Ref 48
qPVB/Cl	$2.7 \times 10^{-2} \text{ S cm}^{-1}$ at 60°C	250 mA cm <sup>-2</sup> at 2.24 V, 55°C	Ni nano powder	Cu <sub>0.7</sub> Co <sub>2.3</sub> O <sub>4</sub>	0.37 Ω cm <sup>2</sup> at 60°C	70 μm	Ref 81
QA-ETFE <sup>c</sup> , QPDTB ionomer	138.7 mS cm <sup>-1c</sup> (ionomer: 0.059 S cm <sup>-1</sup> at 50°C)	100 mA cm <sup>-2</sup> at 1.9 V, 22°C	Ni nanopowder	Cu <sub>0.7</sub> Co <sub>2.3</sub> O <sub>4</sub>	0.85 Ω cm <sup>2</sup> at 22°C full MEA resistance	88.4 μm <sup>c</sup>	Refs 83, <sup>c</sup> 82
LDPE-g-VBC	17 mS cm <sup>-1</sup> at 60°C	300 mA cm <sup>-2</sup> at 2.1 V, 45°C <sup>**</sup>	NA	NA	0.3–0.43 Ω cm <sup>2</sup> at 45°C	NA	Ref 80

<sup>\*\*</sup> Data was taken from a diagram, since the values were not stated within the text.

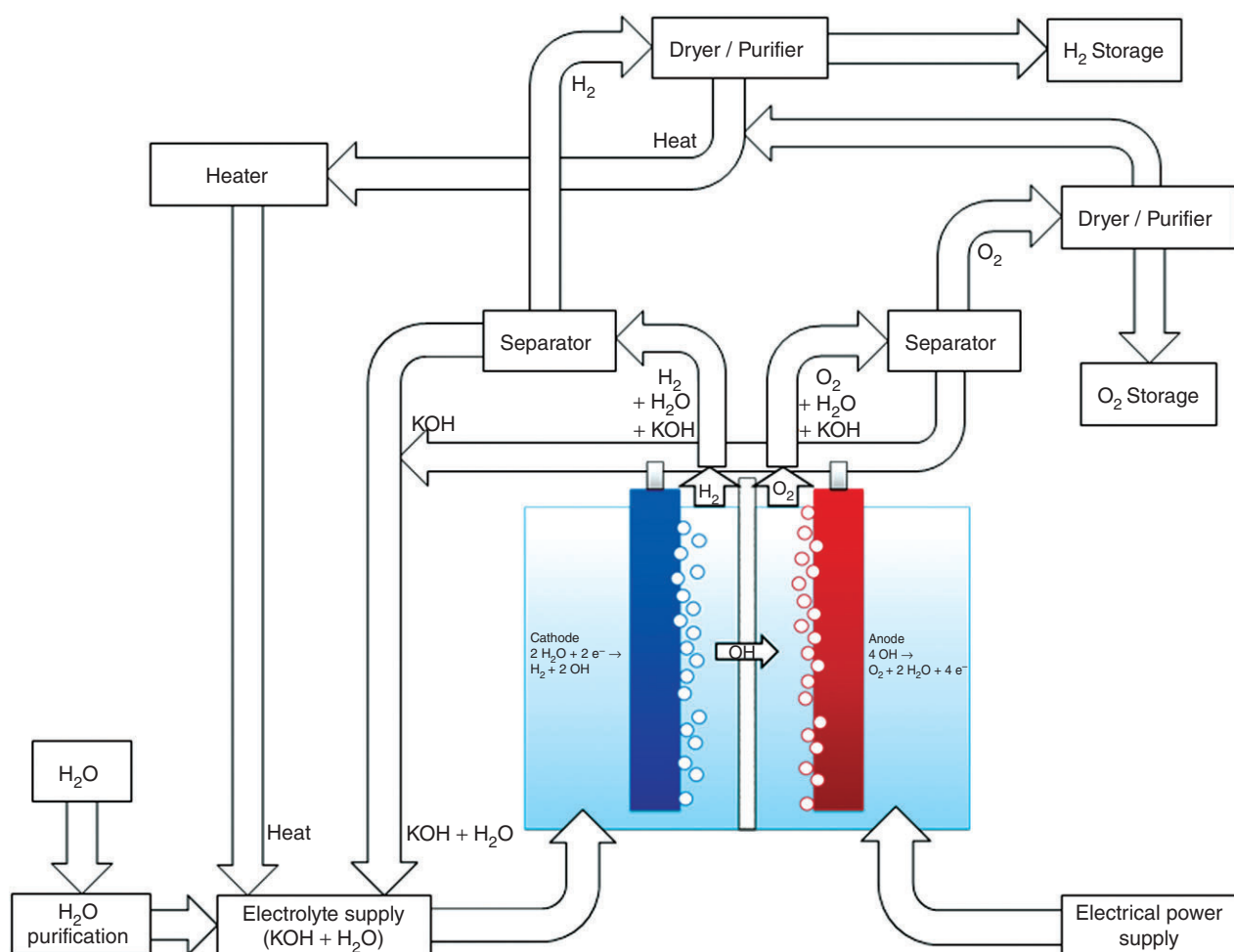


**FIGURE 6** | Illustration of an alkaline water electrolyzer system.

times higher values were reported), slower hydroxide transport compared to protons and possibly lower catalyst utilization. The latter is reported to be due to the different structures of Nafion and alkaline polymer electrolytes.

In order to lower the membrane resistance and improve the ion conductivity, a higher density of ionic groups can be implemented within the membrane, yet this leads to poor flexibility and mechanical stability.<sup>19,29</sup>

Some of the reported AEMs already achieve passable values for conductivity, but lifetime is an issue and has not reached a satisfying value yet. Hydroxide ions are nucleophiles and can degrade AEMs via two mechanisms. If a hydrogen atom is bonded to the  $\beta$ -carbon, Hoffman elimination (Figure 4) occurs and either the vinyl group remains attached to the polymer with the tertiary amine released, or an alkene is released with the tertiary amine as fixed group. Alternatively, without a hydrogen atom at the  $\beta$ -carbon, the nitrogen center is attacked by the nucleophile,

resulting in the loss of an alkene group and a neutral tertiary amine group fixed to the polymer (Figure 5). Either way, a nucleophilic attack results in the loss of anion-exchange groups and therefore reduced ion conductivity. As the Hoffman elimination is the more rapid reaction, one way to minimize degradation can be avoiding a hydrogen atom at the  $\beta$ -carbon.<sup>19,29</sup>

### Solid Oxide Electrolyte

Besides the low-temperature electrolyzers, requiring liquid water for ion conductivity, high-temperature electrolyzers are possible as well. High temperatures result in high catalytic activities due to reduced overpotentials. This allows operation at higher reaction rates and the electrolyte conductivity depends on the temperature. Other than in alkaline electrolytes, in solid oxide electrolysis cells (SOECs) the  $O^{2-}$  moiety operates as ionic species, with yttria-stabilized zirconia as most common electrolyte material.<sup>86,87</sup>

Among the SOECs, a few proton-conducting materials, or solid acids, exist. They usually consist

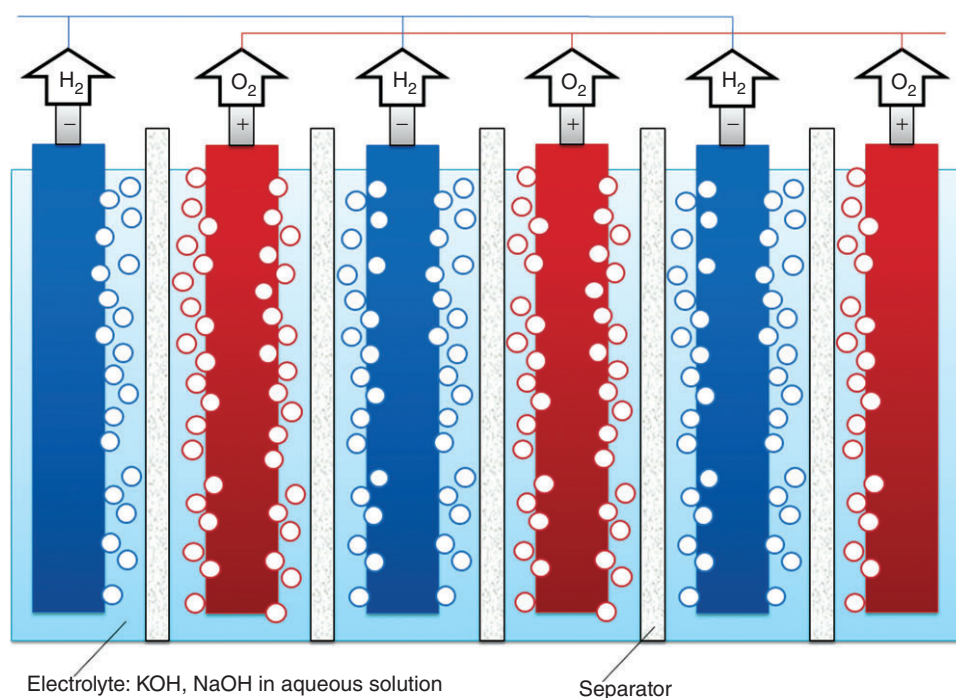


**FIGURE 7** | Unipolar configuration of a water electrolyzer.

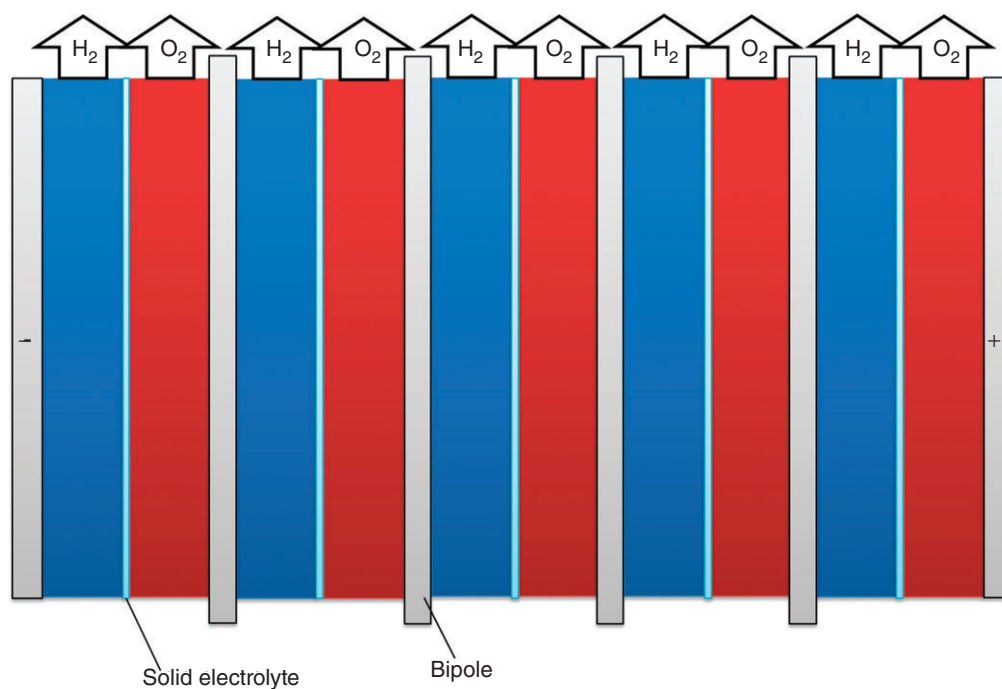


**FIGURE 8** | Bipolar configuration of a water electrolyzer.

out of an alkali metal (or NH<sub>4</sub>) and tetrahedral oxyanion chains, that are linked via hydrogen bonds and recently have gained attention for the use in acidic high-temperature electrolyzers.<sup>88</sup>

Yet solid acids and solid oxides are crystalline materials and therefore show poor mechanical

properties. This has to be overcome by methods such as incorporating the solid electrolyte into a composite membrane. SOECs are in an early stage of development and materials developed for the solid oxide fuel cell cannot be used for these systems. Therefore, solid electrolytes are subject to ongoing and extensive

**TABLE 3** | Basic Parameters of Commercially Available Alkaline Electrolyzers

Company	Type	Electrolyte	Working Temp. (°C)	Postulated Performance	Capacity	Service Life	References
NEL Hydrogen	NEL A 150–485	25% KOH	80	3.8–4.4 kWh Nm <sup>-3</sup> H <sub>2</sub>	50–485 Nm <sup>3</sup> H <sub>2</sub> /h	30–40 years	Ref 91
Hydrog(e)nic	HySTAT 10–60	30% KOH	70 <sup>a</sup>	4.9–5.4 kWh Nm <sup>-3</sup> at full load	4–60 Nm <sup>3</sup> H <sub>2</sub> /h	50.000 h	Refs 95, <sup>a</sup> 84
Uralhim mash	FV-180–500	NA	85–90	NA	172–536 m <sup>3</sup> H <sub>2</sub> /h	25.000 h/10 years <sup>b</sup>	Ref 96, <sup>b</sup> 84
Teledyne	Titan HMXT 50–200	NA	NA	NA	2.8–11.2 Nm <sup>3</sup> H <sub>2</sub> /h	25 + years	Ref 97
	Titan EC 500–750	NA	NA	NA	20–40 Nm <sup>3</sup> H <sub>2</sub> /h	25 + years	
	Titan EL 1000–1400	NA	NA	NA	56–80 Nm <sup>3</sup> H <sub>2</sub> /h	NA	
McPhy	Baby McPhy	NA	NA	2.8 kW max. consumption	400 Nlt/h	NA	Ref 98
	Mclyzer 3–30 bar	NA	NA	7.4–63 kW max. consumption	3–60 Nm <sup>3</sup> H <sub>2</sub> /h	NA	
IHT	Type 20-S-556	NA	NA	4.3–4.6 kWh Nm <sup>-3</sup> H <sub>2</sub>	27–760 Nm <sup>3</sup> H <sub>2</sub> /h	10–15 years	Ref 92

**TABLE 4** | Hydrogen Prices, Germany 2012

	Alkaline (€/kg)	PEM (€/kg)
Mainstream grid (100% load)	3.2	4.1
Mainstream grid (balancing service)	2.7	3.5
Renewable energy sources (off-grid)	5.0	7.6

research, yet no commercial electrolyte is so far available that is customized for the use in a water electrolyzer and their durability is still insufficient.<sup>86,88,89</sup>

## COMMERCIAL ALKALINE WATER ELECTROLYSIS SYSTEMS

Alkaline electrolysis has been known for over 200 years.<sup>90</sup> Electrolyzers are a mature technology and able to produce large quantities of hydrogen. The first commercial system was installed by NEL Hydrogen, formerly Norsk Hydro from Norway in 1927 to produce pure hydrogen via electrolysis for the Haber-Bosch ammonia fertilizer process.<sup>91</sup> Yet soon, the production was extended to various industrial applications and plants were installed exceeding capacities of 20.000 Nm<sup>3</sup> H<sub>2</sub>/h.<sup>91,92</sup> Alkaline electrolyzers are cheap in production and achieve a high

lifetime, whilst most other types of electrolyzers mainly struggle with long-term stability.

### System Setup

Due to the highly corrosive environment in alkaline electrolyzers, only a limited number of materials can be used within the system. Metal sheets, e.g., from nickel or stainless steel, or plastics such as acrylic materials, PTFE or Plexiglas can be used.<sup>21,93,94</sup> The full electrolysis process is illustrated in Figure 6.

The electrolysis cell can be built using either a unipolar or bipolar configuration. When built with a unipolar layout (Figure 7), all positive electrodes, and all negative electrodes respectively, are coupled in parallel. The electrodes are all submerged in one electrolyte bath. The total voltage is the same as that applied to the single cell. This configuration is simple to build, yet holds rather large Ohmic losses. The bipolar configuration (Figure 8), however, usually uses a zero-gap configuration and each electrode except the end plates is used as both anode and cathode, respectively. The electrodes are coupled in series and the overall voltage is the sum of the voltages of the individual cells. Therefore, this type of electrolyzer is operated at high voltages and low current densities. This is undesirable, as the current density determines the rate of hydrogen production and bipolar modules are usually connected in parallel

to increase the current. Bipolar electrolysis systems show lower Ohmic losses than unipolar systems, yet leakage is a more severe issue, resulting in a more complex design.<sup>21,93</sup>

The bipolar layout is also commonly used for PEM electrolysis cells.<sup>78</sup>

### Available AWEs

Alkaline water electrolysis has been established for a long time. Multiple different AWEs are commercially available and in operation worldwide. The basic parameters for some examples are listed in Table 3.

Only limited information is accessible on the layout, used materials and operation conditions commercially available electrolyzers use. Even though asbestos has been banned within the EU since 1999, an exception was made for installed electrolysis units until 2015<sup>99</sup> and it is reported, that in some electrolyzers, asbestos is still used as separator. As electrode material, typically nickel foams or stainless steel are used.<sup>84</sup>

Conventional AWEs typically reach energy efficiencies of 73–83%.<sup>100</sup> The costs of hydrogen produced in Germany in 2012 either with an alkaline or a PEM electrolyzer from mainstream grid power supply in comparison to hydrogen from a balancing scenario, using excessive energy to operate the electrolyzer or a renewable generator within an off-grid scenario are listed in Table 4. Hydrogen from the steam methane reforming process can be produced with costs of about 1.8€/kg.<sup>101</sup> It is indicated, that half of the costs of the alkaline electrolyzer derive from the stack because of the large and heavy components, but also because the costs have not yet been fully driven down by mass production. It is expected for the price to decrease to about 66% of its current value by 2030.<sup>101</sup>

## CONCLUSION

AWEs are a mature technology and have reached a commercial state long ago. Yet they are a perfect example of how novel scientific innovations take time to reach commercial applications. Many commercial systems are available, yet most of them still use separators and catalysts developed centuries ago.

Due to the rise of renewable energy sources and the therefore fluctuating grid, the need for an efficient possibility to store excess energy has awakened and a newly found interest in water electrolysis has risen. Therefore, numerous new approaches are being investigated.

For both anode and cathode electrocatalysts, many new approaches have been proposed so far, showing a large increase in both activity and long-term stability. By applying novel preparation methods, the surface area was enlarged and thereby, the total metal loading was reduced without loss of activity.

For the combination of electrolysis systems with renewable energy sources, the stability of the catalyst during periods of power interruption is of high importance. Therefore, hydrogen storage alloys as cathode electrocatalysts appear especially suitable.

Proton-conducting membrane electrolyzers were the first step toward a lighter and simpler system, as solid electrolytes hold many advantages compared to liquid electrolytes. Yet, despite the fact that PEM electrolyzers are close to reaching commercialization, acidic systems hold severe drawbacks, like the lack of a cheap electrocatalyst.

For alkaline electrolyzers, the usage of anion-conducting membranes is a promising approach to make these cells smaller and lighter, but also to avoid KOH leakage.

## REFERENCES

1. Züttel A, Borgschulte A, Schlapbach L. *Hydrogen As a Future Energy Carrier*. Weinheim: Wiley-VCH Verlag GmbH & Co. KGaA; 2008.
2. S Dunn, Hydrogen futures: toward a sustainable energy system, *Int J Hydrogen Energ*, 2002, 27, 235–264.
3. Turner JA. Sustainable hydrogen production. *Science* 2004, 305:972–974.
4. Turner JA. A Realizable Renewable Energy Future. *Science* 1999, 285:687–689.
5. Dincer I. Green methods for hydrogen production. *Int J Hydrogen Energ* 2012, 37:1954–1971.
6. Gandía L, Oroz R, Ursúa A. Renewable hydrogen production: performance of an alkaline water electrolyzer working under emulated wind conditions. *Energy Fuel* 2007, 21:1699–1706.
7. Holladay JD, Hu J, King DL, Wang Y. An overview of hydrogen production technologies. *Catal Today* 2009, 139:244–260.
8. McKinlay J, Harwood C. Photobiological production of hydrogen gas as a biofuel. *Curr Opin Biotechnol* 2010, 21:244–251.
9. Show K-Y, Lee D-J, Chang J-S. Bioreactor and process design for biohydrogen production. *Bioresour Technol* 2011, 102:8524–8533.
10. Dukic A, Firak M. Hydrogen production using alkaline electrolyzer and photovoltaic (PV) module. *Int J Hydrogen Energ* 2011, 36:7799–7806.

11. Da Silva EP, Marin Neto AJ, Ferreira PFP, Camargo JC, Apolinário FR, Pinto CS. Analysis of hydrogen production from combined photovoltaics, wind energy and secondary hydroelectricity supply in Brazil. *Sol Energ* 2005, 78:670–677.
12. Hu W, Lee J. Electrocatalytic properties of Ti<sub>2</sub>Ni/Ni-Mo composite electrodes for hydrogen evolution reaction. *Int J Hydrogen Energ* 1998, 23:253–257.
13. Licht S, Chitayat O, Bergmann H, Dick A, Ayub H, Ghosh S. Efficient STEP (solar thermal electrochemical photo) production of hydrogen—an economic assessment. *Int J Hydrogen Energ* 2010, 35:10867–10882.
14. Mazloomi SK, Sulaiman N. Influencing factors of water electrolysis electrical efficiency. *Renew Sustain Energy Rev* 2012, 16:4257–4263.
15. Ganley JC. High temperature and pressure alkaline electrolysis. *Int J Hydrogen Energ* 2009, 34:3604–3611.
16. Hauch A, Ebbesen S. Highly efficient high temperature electrolysis. *J Mater Chem* 2008, 18:2331.
17. Ghatak HR. Electrolysis of black liquor for hydrogen production: some initial findings. *Int J Hydrogen Energ* 2006, 31:934–938.
18. Ghatak H, Kumar S, Kundu P. Electrode processes in black liquor electrolysis and their significance for hydrogen production. *Int J Hydrogen Energ* 2008, 33:2904–2911.
19. Leng Y, Chen G, Mendoza AJ, Tighe TB, Hickner MA, Wang C-Y. Solid-state water electrolysis with an alkaline membrane. *J Am Chem Soc* 2012, 134:9054–9057.
20. Zeng K, Zhang D. Recent progress in alkaline water electrolysis for hydrogen production and applications. *Prog Energy Combust Sci* 2010, 36:307–326.
21. Marini S, Salvi P, Nelli P, Pesenti R, Villa M, Berrettoni M, Zangari G, Kiros Y. Advanced alkaline water electrolysis. *Electrochim Acta* 2012, 82:384–391.
22. Trasatti S. Hydrogen evolution. In: Garce J, ed. *Encyclopedia of Electrochemical Power Sources*, vol. II. 1st ed. Amsterdam: Elsevier B.V.; 2009, 41–48.
23. Kibria M, Mridha M, Khan A. Electrochemical studies of a nickel electrode for the hydrogen evolution reaction. *Int J Hydrogen Energ* 1995, 20:435–440.
24. De Giz M, Tremiliosi-Filho G, Gonzalez ER. Mechanistic study of the hydrogen evolution reaction on Ni-Co-Zn electrodes. *Electrochim Acta* 1994, 39:1775–1779.
25. De Giz MJ, Tremiliosi-Filho G, Gonzalez ER, Srinivasan S, Appleby AJ. The hydrogen evolution reaction on amorphous nickel and cobalt alloys. *Int J Hydrogen Energ* 1995, 20:423–427.
26. Subbaraman R, Tripkovic D, Strmcnik D, Chang K-C, Uchimura M, Paulikas AP, Stamenkovic V, Markovic NM. Enhancing hydrogen evolution activity in water splitting by tailoring Li<sup>+</sup>-Ni(OH)<sub>2</sub>-Pt interfaces. *Science* 2011, 334:1256–1260.
27. S Trasatti, Oxygen evolution, in *Encyclopedia of electrochemical power sources*, II, 1st, J Garce. Amsterdam: Elsevier B.V., 2009, 49–55.
28. Kubisztal J, Budniok A. Study of the oxygen evolution reaction on nickel-based composite coatings in alkaline media. *Int J Hydrogen Energ* 2008, 33:4488–4494.
29. Pletcher D, Li X. Prospects for alkaline zero gap water electrolyzers for hydrogen production. *Int J Hydrogen Energ* 2011, 36:15089–15104.
30. Manabe A, Kashiwase M, Hashimoto T, Hayashida T, Kato A, Hirao K, Shimomura I, Nagashima I. Basic study of alkaline water electrolysis. *Electrochim Acta* 2013, 100:249–256.
31. Sheng W, Gasteiger HA, Shao-Horn Y. Hydrogen oxidation and evolution reaction kinetics on platinum: acid vs alkaline electrolytes. *J Electrochem Soc* 2010, 157:B1529.
32. Liu Y, Mustain WE. Evaluation of tungsten carbide as the electrocatalyst support for platinum hydrogen evolution/oxidation catalysts. *Int J Hydrogen Energ* 2012, 37:8929–8938.
33. Solmaz R, Gündoğdu A, Döner A, Kardaş G. The Ni-deposited carbon felt as substrate for preparation of Pt-modified electrocatalysts: application for alkaline water electrolysis. *Int J Hydrogen Energ* 2012, 37:8917–8922.
34. Baranton S, Coutanceau C. Nickel cobalt hydroxide nanoflakes as catalysts for the hydrogen evolution reaction. *Appl Catal B-Environ* 2013, 136–137:1–8.
35. Kjartansdóttir C, Nielsen L, Møller P. Development of durable and efficient electrodes for large-scale alkaline water electrolysis. *Int J Hydrogen Energ* 2013, 38:8221–8231.
36. Dong H, Lei T, He Y, Xu N, Huang B, Liu CT. Electrochemical performance of porous Ni<sub>3</sub>Al electrodes for hydrogen evolution reaction. *Int J Hydrogen Energ* 2011, 36:12112–12120.
37. Wu L, He Y, Lei T, Nan B, Xu N, Zou J, Huang B, Liu CT. Characterization of the porous Ni<sub>3</sub>Al-Mo electrodes during hydrogen generation from alkaline water electrolysis. *Energy* 2013, 63:216–224.
38. Song LJ, Meng HM. Effect of carbon content on Ni-Fe-C electrodes for hydrogen evolution reaction in seawater. *Int J Hydrogen Energ* 2010, 35:10060–10066.
39. Shervedani R, Madram AR. Electrocatalytic activities of nanocomposite Ni<sub>81</sub>P<sub>16</sub>C<sub>3</sub> electrode for hydrogen evolution reaction in alkaline solution by electrochemical impedance spectroscopy. *Int J Hydrogen Energ* 2008, 33:2468–2476.
40. Han Q, Liu K, Chen J, Wei X. A study on the electrodeposited Ni-S alloys as hydrogen evolution reaction cathodes. *Int J Hydrogen Energ* 2003, 28:1207–1212.

41. Han Q. Study of amorphous Ni–S–Co alloy used as hydrogen evolution reaction cathode in alkaline medium. *Int J Hydrogen Energ* 2004, 29:243–248.
42. Yuan T, Li R-D, Zhou K. Electrocatalytic properties of Ni–S–Co coating electrode for hydrogen evolution in alkaline medium. *Trans Nonferrous Met Soc China* 2007, 17:762–765.
43. Shan Z, Liu Y, Chen Z, Warrender G, Tian J. Amorphous Ni–S–Mn alloy as hydrogen evolution reaction cathode in alkaline medium. *Int J Hydrogen Energ* 2008, 33:28–33.
44. Vandenborre H, Vermeiren P, Leysen R. Hydrogen evolution at nickel sulphide cathodes in alkaline medium. *Electrochim Acta* 1984, 29:297–301.
45. Sequeira CAC, Santos DMF, Brito PSD. Electrocatalytic activity of simple and modified Fe–P electrodeposits for hydrogen evolution from alkaline media. *Energy* 2011, 36:847–853.
46. Trasatti S. Work function, electronegativity, and electrochemical behavior of metals. *Electroanal Chem Interfacial Electrochem* 1972, 39:163–184.
47. Marini S, Salvi P, Nelli P, Pesenti R, Villa M, Kirov Y. Stable and inexpensive electrodes for the hydrogen evolution reaction. *Int J Hydrogen Energ* 2013, 38:11484–11495.
48. Xiao L, Zhang S, Pan J, Yang C, He M, Zhuang L, Lu J. First implementation of alkaline polymer electrolyte water electrolysis working only with pure water. *Energy Environ Sci* 2012, 5:7869.
49. Jaksic JM, Vojnovic M, Krstajic NV. Kinetic analysis of hydrogen evolution at Ni–Mo alloy electrodes. *Electrochim Acta* 2000, 45:4151–4158.
50. Lačnjevac UČ, Jović BM, Jović VD, Krstajic NV. Determination of kinetic parameters for the hydrogen evolution reaction on the electrodeposited Ni–MoO<sub>2</sub> composite coating in alkaline solution. *J Electroanal Chem* 2012, 677–680:31–40.
51. Oliver-Tolentino M. Electrochemical behavior of Ni<sub>x</sub>W<sub>1-x</sub> materials as catalyst for hydrogen evolution reaction in alkaline media. *J Alloys Compd* 2012, 536:245–249.
52. Wang M, Wang Z, Guo Z, Li Z. The enhanced electrocatalytic activity and stability of NiW films electrodeposited under super gravity field for hydrogen evolution reaction. *Int J Hydrogen Energ* 2011, 36:3305–3312.
53. Dalla Corte DA, Torres C, Correa PDS, Rieder ES, Malfatti CDF. The hydrogen evolution reaction on nickel-polyaniline composite electrodes. *Int J Hydrogen Energ* 2012, 37:3025–3032.
54. Hu W. Electrocatalytic properties of new electrocatalysts for hydrogen evolution in alkaline water electrolysis. *Int J Hydrogen Energ* 2000, 25:111–118.
55. Krstajic NV, Jovic V, Gajickrstajic L, Jovic B, Antozzi A, Martelli G. Electrodeposition of Ni–Mo alloy coatings and their characterization as cathodes for hydrogen evolution in sodium hydroxide solution. *Int J Hydrogen Energ* 2008, 33:3676–3687.
56. Smiljanić M, Srejić I, Grgur B, Rakočević Z, Štrbac S. Catalysis of hydrogen evolution on different Pd/Au(111) nanostructures in alkaline solution. *Electrochim Acta* 2013, 88:589–596.
57. Elezović NR, Jović VD, Krstajic NV. Kinetics of the hydrogen evolution reaction on Fe–Mo film deposited on mild steel support in alkaline solution. *Electrochim Acta* 2005, 50:5594–5601.
58. Rosalbino F, Macciò D, Saccone A, Angelini E, Delfino S. Fe–Mo–R (R = rare earth metal) crystalline alloys as a cathode material for hydrogen evolution reaction in alkaline solution. *Int J Hydrogen Energ* 2011, 36:1965–1973.
59. Pătru A, Antitomaso P, Sellin R. Size and strain dependent activity of Ni nano and micro particles for hydrogen evolution reaction. *Int J Hydrogen Energ* 2013, 38:11695–11708.
60. Zeng K, Zhang D. Evaluating the effect of surface modifications on Ni based electrodes for alkaline water electrolysis. *Fuel* 2014, 116:692–698.
61. Seetharaman S, Balaji R, Ramya K, Dhathathreyan KS, Velan M. Graphene oxide modified non-noble metal electrode for alkaline anion exchange membrane water electrolyzers. *Int J Hydrogen Energ* 2013, 38:14934–14942.
62. Huot JY, Trudeau ML, Schulz R. Low hydrogen overpotential nanocrystalline Ni–Mo cathodes for alkaline water electrolysis. *J Electrochem Soc* 1991, 138:1316–1321.
63. Lačnjevac UČ, Jović BM, Jović VD, Radmilović VR, Krstajic NV. Kinetics of the hydrogen evolution reaction on Ni-(Ebonex-supported Ru) composite coatings in alkaline solution. *Int J Hydrogen Energ* 2013, 38:10178–10190.
64. Jović BM, Lačnjevac UČ, Krstajic NV, Jović VD. Ni–Sn coatings as cathodes for hydrogen evolution in alkaline solutions. *Electrochim Acta* 2013, 114: 813–818.
65. Shervedani RK, Madram AR. Kinetics of hydrogen evolution reaction on nanocrystalline electrodeposited Ni<sub>62</sub>Fe<sub>35</sub>C<sub>3</sub> cathode in alkaline solution by electrochemical impedance spectroscopy. *Electrochim Acta* 2007, 53:426–433.
66. Correia A, Machado S, Avaca L. Studies of the hydrogen evolution reaction on smooth Co and electrodeposited Ni–Co ultramicroelectrodes. *Electrochim Commun* 1999, 1:600–604.
67. Marini S, Salvi P, Nelli P, Pesenti R, Villa M, Kirov Y. Oxygen evolution in alkali with gas diffusion electrodes. *Int J Hydrogen Energ* 2013, 38:11496–11506.
68. Miles MH, Huang YH, Srinivasan S. The oxygen electrode reaction in alkaline solutions on oxide electrodes

- prepared by the thermal decomposition method. *J Electrochem Soc* 1978, 125:1931–1934.
69. Subbaraman R, Tripkovic D, Chang K-C, Strmcnik D, Paulikas AP, Hirunsit P, Chan M, Greeley J, Stamenkovic V, Markovic NM. Trends in activity for the water electrolyser reactions on 3d M(Ni,Co,Fe,Mn) hydr(oxy)oxide catalysts. *Nat Mater* 2012, 11:550–557.
  70. Wu X, Scott K. A Li-doped  $\text{Co}_3\text{O}_4$  oxygen evolution catalyst for non-precious metal alkaline anion exchange membrane water electrolyzers. *Int J Hydrogen Energ* 2013, 38:3123–3129.
  71. Ahn SH, Choi I, Park H-Y, Hwang SJ, Yoo SJ, Cho E, Kim H-J, Henkensmeier D, Nam SW, Kim S-K, et al. Effect of morphology of electrodeposited Ni catalysts on the behavior of bubbles generated during the oxygen evolution reaction in alkaline water electrolysis. *Chem Commun (Camb)* 2013, 49:9323–9325.
  72. Wang M, Wang Z, Gong X, Guo Z. The intensification technologies to water electrolysis for hydrogen production—a review. *Renew Sustain Energy Rev* 2014, 29:573–588.
  73. Rosa VM, Santos MBF, Da Silva EP. New materials for water electrolysis diaphragms. *Int J Hydrogen Energ* 1995, 20:697–700.
  74. Merle G, Wessling M, Nijmeijer K. Anion exchange membranes for alkaline fuel cells: A review. *J Membr Sci* 2011, 377:1–35.
  75. Wu X, Scott K, Xie F, Alford N. A reversible water electrolyser with porous PTFE based  $\text{OH}^-$  conductive membrane as energy storage cells. *J Power Sources* 2014, 246:225–231.
  76. Hnát J, Paidar M, Schauer J. Polymer anion-selective membranes for electrolytic splitting of water, part II: enhancement of ionic conductivity and performance under conditions of alkaline water electrolysis. *J Appl Electrochem* 2012, 42:545–554.
  77. Aili D, Hansen MK, Renzaho RF, Li Q, Christensen E, Jensen JO, Bjerrum NJ. Heterogeneous anion conducting membranes based on linear and crosslinked KOH doped polybenzimidazole for alkaline water electrolysis. *J Membr Sci* 2013, 447:424–432.
  78. Millet P, Ngameni R, Grigoriev SA, Fateev VN. Scientific and engineering issues related to PEM technology: Water electrolyzers, fuel cells and unitized regenerative systems. *Int J Hydrogen Energ* 2011, 36:4156–4163.
  79. Carmo M, Fritz DL, Mergel J, Stolten D. A comprehensive review on PEM water electrolysis. *Int J Hydrogen Energ* 2013, 38:4901–4934.
  80. Faraj M, Boccia M, Miller H. New LDPE based anion-exchange membranes for alkaline solid polymeric electrolyte water electrolysis. *Int J Hydrogen Energ* 2012, 37:14992–15002.
  81. Cao Y, Wu X, Scott K. A quaternary ammonium grafted poly vinyl benzyl chloride membrane for alkaline anion exchange membrane water electrolyzers with no-noble-metal catalysts. *Int J Hydrogen Energ* 2012, 37:9524–9528.
  82. Cheng H, Scott K, Lovell KV, Horsfall JA, Waring SC. Evaluation of new ion exchange membranes for direct borohydride fuel cells. *J Membr Sci* 2007, 288:168–174.
  83. Wu X, Scott K. A polymethacrylate-based quaternary ammonium  $\text{OH}^-$  ionomer binder for non-precious metal alkaline anion exchange membrane water electrolyzers. *J Power Sources* 2012, 214:124–129.
  84. Millet P, Grigoriev S. Water electrolysis technologies. In: Gandia LM, Arzamendi G, Dieguez PM, eds. *Renewable Hydrogen Technologies: Production, Purification, Storage, Applications and Safety*. Amsterdam: Elsevier; 2013, 19–41.
  85. Duan Q, Ge S, Wang C-Y. Water uptake, ionic conductivity and swelling properties of anion-exchange membrane. *J Power Sources* 2013, 243:773–778.
  86. Ni M, Leung M, Leung D. Technological development of hydrogen production by solid oxide electrolyzer cell (SOEC). *Int J Hydrogen Energ* 2008, 33:2337–2354.
  87. Yu B, Zhang W, Xu J, Chen J, Luo X, Stephan K. Preparation and electrochemical behavior of dense YSZ film for SOEC. *Int J Hydrogen Energ* 2012, 37:12074–12080.
  88. Goñi-Urtiaga A, Presvytes D, Scott K. Solid acids as electrolyte materials for proton exchange membrane (PEM) electrolysis: review. *Int J Hydrogen Energ* 2012, 37:3358–3372.
  89. Manage MN, Hodgson D, Milligan N, Simons SJR, Brett DJL. A techno-economic appraisal of hydrogen generation and the case for solid oxide electrolyzer cells. *Int J Hydrogen Energ* 2011, 36:5782–5796.
  90. Trasatti S. Water electrolysis: who first? *J Electroanal Chem* 1999, 476:90–91.
  91. NEL Hydrogen AS. 2014. Available at: <http://www.nel-hydrogen.com>. (Accessed June 26, 2014).
  92. IHT Industrie Haute Technology S.A. 2014. Available at: <http://www.iht.ch>. (Accessed June 26, 2014).
  93. Santos DMF, Sequeira CAC, Figueiredo JL. Hydrogen production by alkaline water electrolysis. *Quim Nova* 2013, 36:1176–1193.
  94. Olivares-Ramírez JM, Campos-Cornelio ML, Uribe Godínez J, Borja-Arco E, Castellanos RH. Studies on the hydrogen evolution reaction on different stainless steels. *Int J Hydrogen Energ* 2007, 32:3170–3173.
  95. Hydrogenics Corporation. 2014. Available at: <http://www.hydrogenics.com>. (Accessed June 26, 2014).
  96. OAO Uralkhimash. 2014. Available at: <http://www.ekb.ru>. (Accessed June 26, 2014).
  97. Teledyne Technologies Incorporated. 2014. Available at: <http://www.teledyne.com>. (Accessed June 26, 2014).
  98. McPhy Energy S.A. 2014. Available at: <http://www.mcphy.com>. (Accessed June 26, 2014).

99. Otero J, Sese J, Michaus I, Santa Maria M, Guelbenzu E, Irusta S, Carrilero I, Arruebo M. Sulphonated polyether ether ketone diaphragms used in commercial scale alkaline water electrolysis. *J Power Sources* 2014, 247:967–974.
100. Mori M, Mržljak T, Drobnič B, Sekavčnik M. Integral characteristics of hydrogen production in alkaline electrolyzers. *Stroj Vestn-J Mech E* 2013, 10: 585–594.
101. Bertuccioli L, Chan A, Hart D, Lehner F, Madden B, and Standen E. Fuel cells and hydrogen joint undertaking. Development of Water Electrolysis in the European Union Final Report, 2014.

## 16.2. The Effect of Platinum Electrocatalyst on Membrane Degradation in Polymer Electrolyte Fuel Cells.

*Bodner M, Cermenek B, Rami M, Hacker V. **The Effect of Platinum Electrocatalyst on Membrane Degradation in Polymer Electrolyte Fuel Cells.** Membranes (Basel) 2015;5:888–902.*

### *Contribution:*

The effect of platinum on membrane degradation was investigated by a combined mechanical and chemical accelerated stress tests. Dipl.-Ing. Bernd Cermenek conducted the ex-situ membrane characterisation and Mija Rami, BSc determined the fluoride emission rate. Both contributed descriptions of their experiments to the manuscript. Prof. Viktor Hacker advised in all aspects.

An accelerated stress test was developed in order to simultaneously induce chemical and mechanical membrane degradation by OCV hold conditions and humidity cycling. A full membrane electrode assembly was tested. For comparison and in order to determine the influence of the platinum electrocatalyst on membrane degradation, a membrane without electrodes underwent the identical procedure.

In the absence of platinum, the membrane exhibited a more severe degradation rate.

Article

## The Effect of Platinum Electrocatalyst on Membrane Degradation in Polymer Electrolyte Fuel Cells

Merit Bodner \*, Bernd Cermenek \*, Mija Rami and Viktor Hacker

Institute of Chemical Engineering and Environmental Technology, NAWI Graz,  
Graz University of Technology, Inffeldgasse 25C, Graz 8010, Austria;  
E-Mails: mija.rami@tugraz.at (M.R.); viktor.hacker@tugraz.at (V.H.)

\* Author to whom correspondence should be addressed; E-Mails: merit.bodner@tugraz.at (M.B.); bernd.cermenek@tugraz.at (B.C.); Tel.: fjfjhjf43-(316)-873-8786 (M.B.); +43-(316)-873-8788 (B.C.); Fax: +43-(316)-873-8782 (M.B. & B.C.).

Academic Editor: Bruno Scrosati

Received: 30 September 2015 / Accepted: 1 December 2015 / Published: 8 December 2015

---

**Abstract:** Membrane degradation is a severe factor limiting the lifetime of polymer electrolyte fuel cells. Therefore, obtaining a deeper knowledge is fundamental in order to establish fuel cells as competitive product. A segmented single cell was operated under open circuit voltage with alternating relative humidity. The influence of the catalyst layer on membrane degradation was evaluated by measuring a membrane without electrodes and a membrane-electrode-assembly under identical conditions. After 100 h of accelerated stress testing the proton conductivity of membrane samples near the anode and cathode was investigated by means of *ex situ* electrochemical impedance spectroscopy. The membrane sample near the cathode inlet exhibited twofold lower membrane resistance and a resulting twofold higher proton conductivity than the membrane sample near the anode inlet. The results from the fluoride ion analysis have shown that the presence of platinum reduces the fluoride emission rate; which supports conclusions drawn from the literature.

**Keywords:** polymer electrolyte fuel cell; membrane degradation; fluoride emission rate; segmented cell; OCV conditions; relative humidity cycling; membrane resistance; proton conductivity

---

## 1. Introduction

Polymer electrolyte fuel cells are a promising approach to realise a sustainable power supply due to their high efficiency and flexibility. However, the lifetime and thus the commercialisation of fuel cells are still limited by degradation effects of both the electrodes and the membrane.

The mechanism of Nafion<sup>®</sup> degradation has been well described previously [1–3]. Membrane degradation is accelerated under open circuit voltage (OCV) conditions. This is due to the correlation between the fluoride emission rate and hydrogen crossover [4]. Oxygen crossover has a similar effect, but the permeability of oxygen is lower than that of hydrogen [5]. The ionomer decomposes with the degradation front starting on the cathode side. Thereby, hydrogen crossover leads towards mixed potentials and thus a reduced open circuit voltage. Once the cathode ionomer has been consumed, both the hydrogen crossover and the fluoride emission rate reach plateaus until the anode ionomer starts to decompose [5].

Hydrogen peroxide formation has long been considered to be a major contributor to membrane degradation. Other than carbon corrosion, which is provoked by high potentials [6], it has been reported that the formation of hydrogen peroxide is favoured at anodic potential. Perfluorinated sulfonic acid (PFSA) membranes are fairly stable even in concentrated H<sub>2</sub>O<sub>2</sub> solutions; yet degrade in the presence of metallic contaminations such as iron, aluminium, copper and titanium due to the formation of harmful radical in the presence of these metals [7,8]. Nafion electrolyte has been reported to only decompose in the presence of platinum electrocatalyst, hydrogen and oxygen in a setup with similar conditions as in a fuel cell [9]. On the other hand, Pt has also been reported to reduce the negative effect of hydrogen peroxide formation by decomposing it without the formation of harmful radicals [10]. Thus, *ex situ* experiments [9,10] and experiments with platinum implemented in the membrane [11] have shown that platinum electrocatalyst both enables and counteracts membrane degradation. In this work, the effect of the platinum electrocatalyst on the fuel cell operation was determined in a single cell setup.

## 2. Results

### 2.1. Accelerated Stress Test

During 100 h of open circuit voltage and relative humidity (rH) cycling as accelerated stress test (AST), the voltage was recorded (Figure 1). No significant decrease over a time period of 100 h was noted. When switching to a relative humidity of 0%, a short period of increased OCV was recorded, followed by a slow decline. When switching back to a relative humidity of 80%, a similar but less pronounced effect was noted.

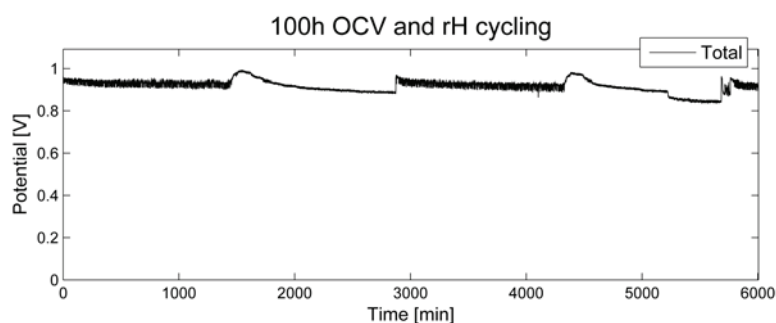


**Figure 1.** Open circuit voltage for 100 h of relative humidity cycling.

2.2. Electrochemical Characteristics of the Membrane-Electrode-Assembly

Electrochemical characterisation at the beginning of lifetime (BoL) and at the end of lifetime (EoL) shows an improvement of the fuel cell properties in most aspects (Table 1). The membrane-electrode-assembly (MEA) shows an increase of power density (Figure 2), reduced hydrogen crossover and increased active cathode catalyst surface area. After 100 h of OCV conditions and relative humidity cycling, the membrane resistance is only slightly increased by approximately 0.54%. This is an indication for minor membrane degradation.

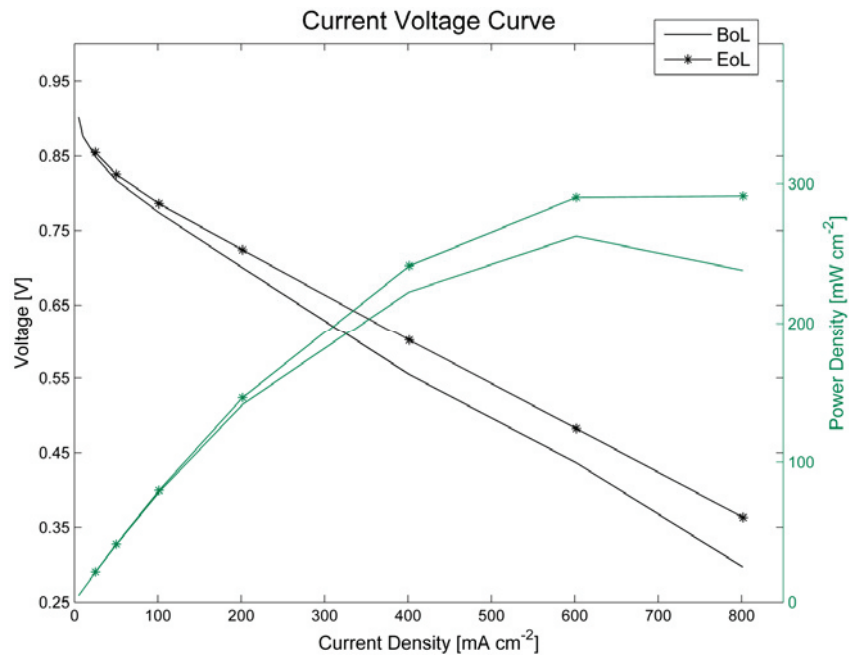


**Figure 2.** Polarisation curve of a single cell before (BoL) and after (EoL) 100 h at OCV and under humidity cycling.

**Table 1.** Electrochemical characteristics of a single cell before (BoL) and after (EoL) 100 h at OCV and under humidity cycling.

Electrochemical Parameter	Before (BoL)	After (EoL)
Power density (mW cm <sup>-2</sup> )	262.66	291.28
Membrane resistance (mΩ)	9.28	9.32
Hydrogen crossover current density (mA cm <sup>-2</sup> )	0.510	0.451
Active surface area (m <sup>2</sup> g <sup>-1</sup> )	31.031	41.852

Most notably is, however, the strong increase of active catalyst surface area on the cathode side. The spatially resolved current shows a rather homogeneous distribution (Figure 3). Thus, this effect appears not to depend on local conditions near either electrode. This might be due to hydrogen, crossing over from the anode to the cathode. The presence of hydrogen on the cathode results in a chemical reduction of the cathode catalyst, thus increasing the active catalyst surface area. The uniform increase might be due to the thick membrane used in these experiments, possibly leading to a more homogeneous crossover. This can be explained by the effect of crossover on membrane degradation. A thinner membrane allows more hydrogen crossover which then locally accelerates membrane degradation in

areas of higher hydrogen partial pressure, inducing a gradient in membrane thickness and thus a gradient in crossover.

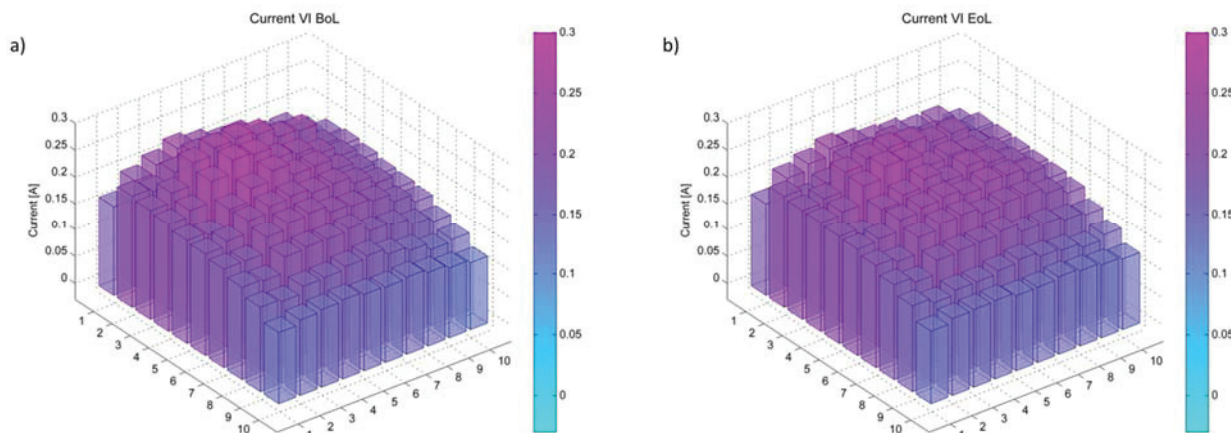


**Figure 3.** Local current at a total current of 20 A spatially resolved for a single cell (a) before (BoL) and (b) after (EoL) 100 h at OCV and under humidity cycling.

In general, electrochemical characterisation has shown an improvement of the fuel cell parameters after 100 h of humidity cycling under OCV conditions.

### 2.3. Effect of the Electrodes on the Polymer Electrolyte Degradation

#### 2.3.1. Change of Membrane Resistance

Figure 4b depicts after 100 h of AST that the measured resistance  $R_{tot}$  of NAFION<sup>®</sup> XL (A) near the anode inlet is only slightly higher and the measured resistance  $R_{tot}$  of NAFION<sup>®</sup> XL (C) near the cathode inlet is lower than measured resistance  $R_{tot}$  of NAFION<sup>®</sup> XL (R) used as reference (Table 2). The measured resistance  $R_{tot}$  denotes the sum of the inverse conductivity from respective NAFION<sup>®</sup> XL membrane ( $\sigma_{membrane} = 1/R_{membrane}$ ) and ultra-pure water ( $\sigma_{UPW} = 1/R_{UPW}$ ), respectively.

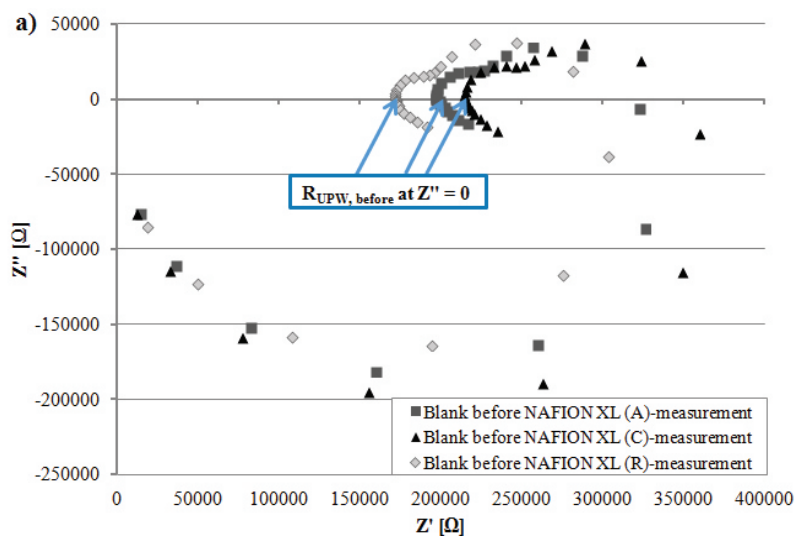


**Figure 4.** Cont.

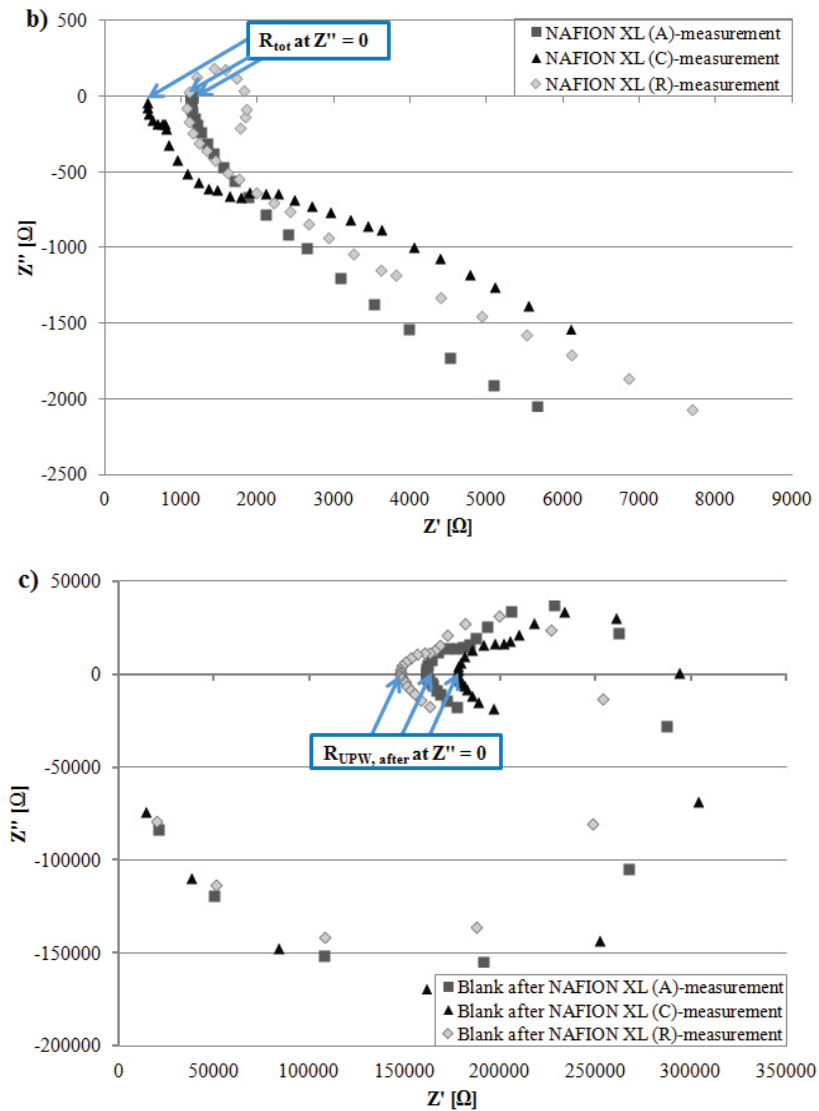


**Figure 4.** Comparison of (a) resistance from ultra-pure water ( $\sim 18 \text{ M}\Omega\cdot\text{cm}$ )  $R_{UPW}$ , before (b) measured resistance  $R_{tot}$  from NAFION<sup>®</sup> XL (A), (C) and (R) (c) resistance from ultra-pure water  $R_{UPW}$ , after.

**Table 2.** Determined measured parameters of NAFION<sup>®</sup> XL (A = anode inlet), (C = cathode inlet) and (R = reference); ultra-pure water (UPW), width of membrane (W), thickness of membrane (T), distance between the inner sense electrodes (d), resistivity of membrane ( $\rho$ ), in-plane proton conductivity of membrane ( $\sigma$ ).

Sample	$R_{tot}$ ( $\Omega$ )	$R_{UPW}$ , before ( $\Omega$ )	$R_{UPW}$ , after ( $\Omega$ )	$R_{mem.}$ ( $\Omega$ )	W (cm)	T (cm)	d (cm)	$\rho$ ( $\Omega\cdot\text{cm}$ )	$\sigma$ ( $\text{mS}\cdot\text{cm}^{-1}$ )
NAFION XL (A)	1150	197837	161176	1158	1.0	0.0131	0.425	36	28.06
NAFION XL (R)	1098	172042	147256	1106	1.0	0.0131	0.425	34	29.33
NAFION XL (C)	557	214935	177533	558	1.0	0.0133	0.425	17	57.23

The real membrane resistance  $R_{membrane}$  of samples (A), (C) and (R) corrected with the resistance of ultra-pure water after every EIS measurement (Equation (2)) is matched in Figure 5. It is evident that

the real membrane resistance  $R_{\text{membrane}}$  of membrane sample (A) increases by approximately 5% and of membrane sample (C) decreases by approximately 49% compared to reference sample (R).

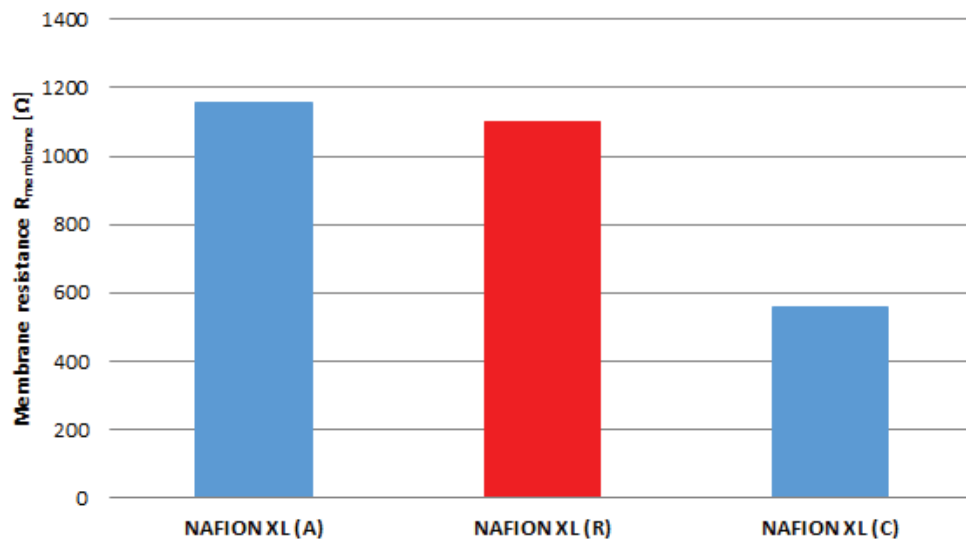


**Figure 5.** Membrane resistance (*ex-situ*) for the reference (R) and for samples near the anode inlet (A) and cathode inlet (C) after 100 h of AST.

The obtained results from Figure 5 are related to the results of Figure 6. The in-plane proton conductivity of membrane samples (A) and (C) exhibits a decrease of approximately 5% as well as an increase of approximately 49% in comparison with reference sample (R).

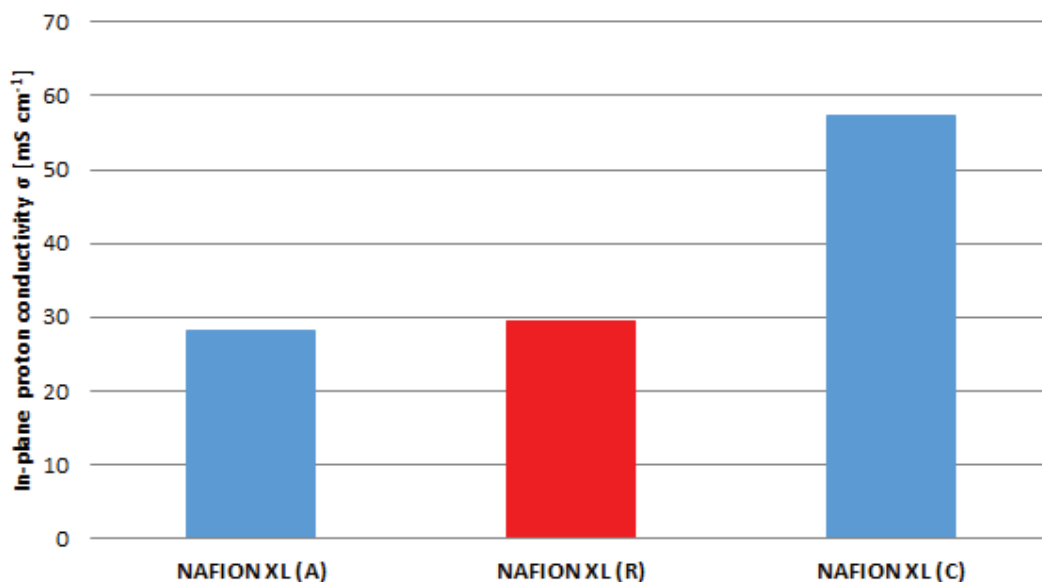


**Figure 6.** Proton conductivity (*ex-situ*) for the reference (R) and for samples near the anode inlet (A) and cathode inlet (C) after 100 h of AST.

The membrane sample near the anode inlet (A) indicates a higher degradation rate than the membrane sample near the cathode inlet (C) after 100 h of AST. The determined measured parameters of all membrane samples are once more summarised in Table 2.

2.3.2. Fluoride Emission Rate

Even though the fluoride concentration is low in all four samples, the fluoride emission rate (FER) (Figure 7) is clearly higher for the membrane without electrodes than for the MEA by a factor of 1.6 and 3.2 on the anode and cathode, respectively. Before adding total ionic strength adjustment buffer II (TISAB II), the pH was in the range of 5.45 to 5.68 for all samples and apparently independent of the fluoride concentration, always slightly higher on the cathode side.

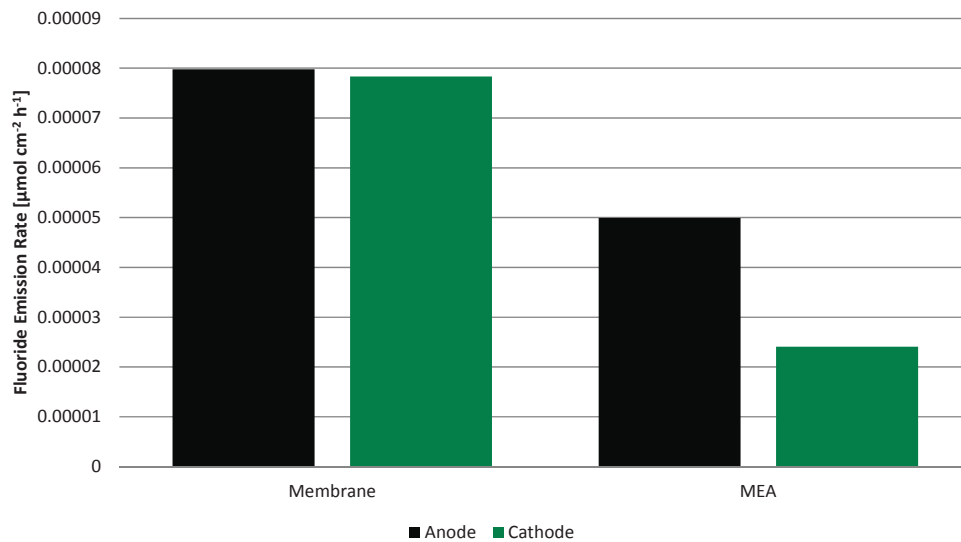


**Figure 7.** Fluoride emission rate during 100 h operation on anode and cathode side for the membrane alone and for the MEA.

2.3.3. Off-Gas Analysis

The off-gas analysis (Figure 8) shows a rather steady oxygen partial pressure during the 100 h of OCV operation. The hydrogen content is also steady during humidity cycling for the membrane (Figure 8a); however it increased during operation of the membrane-electrode-assembly and furthermore changes with humidity cycling (Figure 8b).

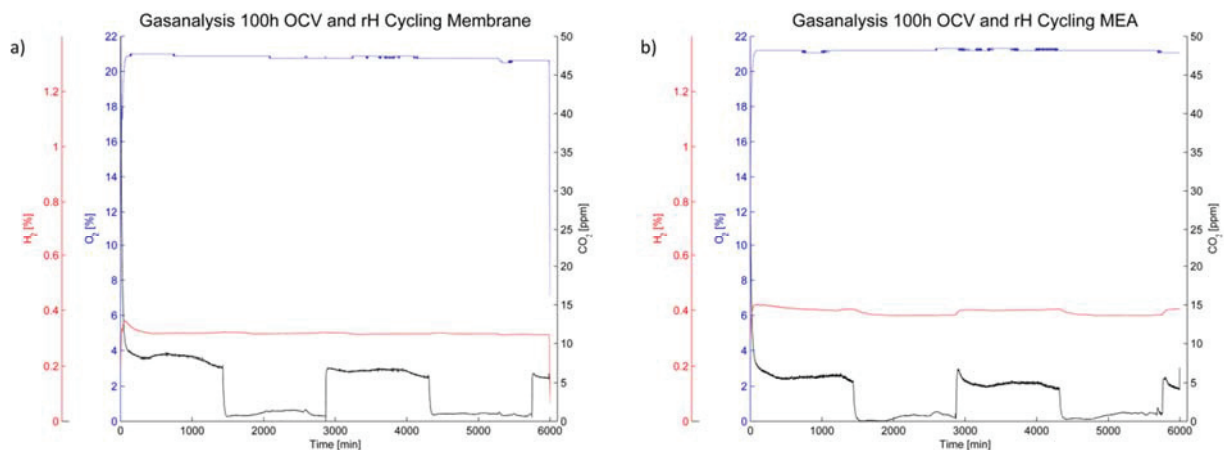


**Figure 8.** Gas analysis of the cathode off-gas for (a) the membrane without electrodes and (b) the membrane-electrode-assembly.

The CO<sub>2</sub> content is, while rather low in general, dependent on the relative humidity in the cell. A higher carbon emission rate was noted under humid conditions for both the membrane without electrodes and the MEA. However, the level of CO<sub>2</sub> in the cathode off-gas was higher for the membrane without electrodes than for the MEA (Figure 8).

### 3. Discussion

In Table 3, results at various conditions and with different materials are shown. Compared to the literature [1,4,5,7,12,13], the fluoride emission rate is low in all cases. More fluoride is released from the membrane without electrodes. This is rather unexpected compared to other findings [4]. However, a deceleration of membrane decomposition in the presence of platinum has been reported previously [10,11]. There, it is assumed that Pt catalyses the decomposition of H<sub>2</sub>O<sub>2</sub> formed in case of gas crossover without the formation of harmful radicals.

**Table 3.** Comparison of the fluoride emission rate at different conditions.

Current	Temperature	Relative Humidity (%)	Total Duration	Membrane	Conditions	FER	Reference
0 (A)	65 (°C)	0–80 (%), 24 (h) interval	100 (h)	Nafion® XL	H <sub>2</sub> /synth. Air	$1.58 \cdot 10^{-4}$ ( $\mu\text{mol} \cdot \text{cm}^{-2} \cdot \text{h}^{-1}$ )	this work
0 (A)	65 (°C)	0–80 (%), 24 (h) interval	100 (h)	Nafion® XL MEA	H <sub>2</sub> /synth. Air	$7.40 \cdot 10^{-5}$ ( $\mu\text{mol} \cdot \text{cm}^{-2} \cdot \text{h}^{-1}$ )	this work
0 (A)	95 (°C)	50 (%)	200 (h)	PFSA-type MEA	H <sub>2</sub> /synth. Air	$1 \cdot 10^{-5.5} - 1 \cdot 10^{-4.5}$ ( $\text{gF} \cdot \text{cm}^{-2} \cdot \text{h}^{-1}$ )*	[1]
0 (A)	90 (°C)	30 (%)	NA	Nafion 117	H <sub>2</sub> /O <sub>2</sub>	0.05 ( $\mu\text{mol} \cdot \text{cm}^{-2} \cdot \text{h}^{-1}$ )	[4]
0 (A)	90 (°C)	30 (%)	NA	Nafion 117, anode only	H <sub>2</sub> /O <sub>2</sub>	2.5 ( $\mu\text{mol} \cdot \text{cm}^{-2} \cdot \text{h}^{-1}$ )	[4]
0 (A)	90 (°C)	30 (%)	NA	Nafion 117, cathode only	H <sub>2</sub> /O <sub>2</sub>	2.5 ( $\mu\text{mol} \cdot \text{cm}^{-2} \cdot \text{h}^{-1}$ )	[4]
0 (A)	90 (°C)	75 (%)	900 (h)	Gore PRIMEA® 5510 CCM	H <sub>2</sub> /synth. Air	0–7.00 ( $\mu\text{mol} \cdot \text{cm}^{-2} \cdot \text{h}^{-1}$ )*	[5]
300 ( $\text{mA} \cdot \text{cm}^{-2}$ )	75 (°C)	0–100 (%), 10 (min) interval	441 (h)	Ion Power® NR 212 MEA	H <sub>2</sub> /synth. Air	0.01–0.225 ( $\mu\text{mol} \cdot \text{cm}^{-2} \cdot \text{h}^{-1}$ ) *	[12]
10 ( $\text{mA} \cdot \text{cm}^{-2}$ )	70 (°C)	0–100 (%), 10/40 (min) interval	625 (h) *	Gore™ 57 CCM	H <sub>2</sub> /synth. Air	0.1–6.9 ( $\mu\text{mol} \cdot \text{h}^{-1}$ ) *	[13]

Note: \* Taken from plot.

The performance of the fuel cell is ascending, despite of a minor increase of the membrane resistance. The improved electrochemical properties of the MEA after 100 h of AST might be due to the chemical reduction of Pt-oxides in the cathode catalyst by hydrogen, crossing over from the anode. Due to the relatively thick membrane, the crossover is homogeneous, since thinner membranes exhibit a higher hydrogen crossover, leading to a gradient in membrane degradation and thus a gradient in crossover.

After switching to dry operating conditions, the partial pressures of the reactant gases increase and the open circuit voltage surges. During relative humidity cycling, a slightly increased level of hydrogen was noted in the cathode off gas for the MEA. The level also increases at humid conditions for the MEA, whilst it remains unchanged for the membrane without electrodes.

The permeability of membranes towards gases is a function of temperature and humidity [14]. This might cause the fluctuating hydrogen crossover in the MEA experiment, but should be identical for both setups. Thus, the more likely reason is that this effect is somehow caused by the manufacturing process. Since both membrane and MEA were used as received, the latter cannot be precluded. Other than the membrane, the MEA had to undergo hot-pressing. This could have led to thermal degradation of the polymer electrolyte or a morphological change [3].

Additionally, the CO<sub>2</sub> content in the cathode off-gas is, while rather low in comparison with the literature [15], clearly dependent on the relative gas humidity. This is expected to be caused by carbon corrosion of the carbon backing layer and catalyst support at high relative humidity. However, the carbon content is even higher in case of the membrane without electrodes and thus without carbon support materials. In this case, carbon may only be derived from two sources—the graphitic flow plates or the carbon from the proton conductive polymer. However, the carbon oxidation of graphitic bipolar plates is potential dependent and thus provoked by the positive potential at the air electrode [6]. Graphite oxidation is therefore only expected when using a membrane-electrode-assembly, since no voltage was recorded without the presence of platinum electrocatalyst. Thus, membrane degradation is left as source of the higher amount of carbon dioxide in the cathode off-gas.

The ex-situ EIS measurements show that NAFION<sup>®</sup> XL sample (C) near the cathode inlet after 100 h of AST exhibits lower membrane resistance as well as higher in-plane proton conductivity than a NAFION<sup>®</sup> XL sample (A) near the anode inlet after 100 h of AST and a reference sample (R) without stress, respectively. The better performance of NAFION<sup>®</sup> XL sample (C) compared to the other membrane samples is probably due to the higher water content. As the cathode gas flow is higher, more water is transported into the cathode department and might accumulate near the inlet, leading to a gradient in proton conductivity. This assertion can be explained by means of the random network model as well as the cluster network model [16].

#### 4. Conclusions

From the fluoride emission rate and the carbon dioxide release, it can be concluded that the presence of platinum electrocatalyst in the fuel cell reduces membrane degradation significantly. This is despite the higher hydrogen crossover in the MEA, which is apparently caused by the manufacturing process. Gas crossover is known to accelerate hydrogen peroxide formation. In the presence of platinum electrocatalyst, however, H<sub>2</sub>O<sub>2</sub> appears to be decomposed without forming harmful radicals in a fuel cell setup as well as it has been reported in an ex-situ setup.

Hydrogen passing through the membrane is also responsible for the increased performance density and the homogeneous current distribution after 100 h of AST testing.

## 5. Experimental Section

A Nafion<sup>®</sup> XL supported membrane without electrodes was implemented in a 25 cm<sup>2</sup> single cell with single serpentine flow fields on both sides and a segmented cathode. A S++ device for spatially resolved measurement of the current in 100 segments and of the temperature in 25 segments was used.

A membrane-electrode-assembly from IRD fuel cells A/S was used with an identical membrane and a catalyst loading of 0.2 mg·cm<sup>-2</sup> on the anode and 0.4 mg·cm<sup>-2</sup> on the cathode, respectively. The MEA was implemented in the same single cell as the membrane, underwent electrochemical characterisation and was operated under identical conditions. Both membrane and MEA underwent 100 h of AST testing. Afterwards, the cell with electrodes was again electrochemically characterised.

Effluent water was collected on both sides and the off-gas was analysed on the cathode side in both setups. Electrochemical characterisation, effluent water and off-gas analysis were performed as described previously [15].

### 5.1. Accelerated Stress Test

As an accelerated stress test (Figure 9), the cell was kept under OCV conditions at atmospheric pressure and was operated in pseudo-counter flow. One side, noted as anode, was fed with hydrogen (5.0) at a flow rate of 86.8 mL·min<sup>-1</sup> and the other side, noted as cathode, was fed with synthetic air (5.0) at a flow rate of 275.3 mL·min<sup>-1</sup>. This represents a stoichiometry of 1.5 and 2.0 at a hypothetical current density of 0.3 A·cm<sup>-2</sup> at anode and cathode, respectively. The temperature was held at 65 °C and the relative humidity was switched between 80% and 0% every 24 h for 100 h. Thereby, a combination of chemical and mechanical membrane degradation was induced. A hold at open circuit potential accelerates chemical membrane degradation [5], while relative humidity cycling causes swelling and shrinkage of the membrane, thus inducing mechanical stress [12]. Combining mechanical and chemical stressors have been shown to have overlapping effects, resulting in a severe reduction of durability for example for an MEA being operated under normal operation conditions accompanied by relative humidity cycling [17].

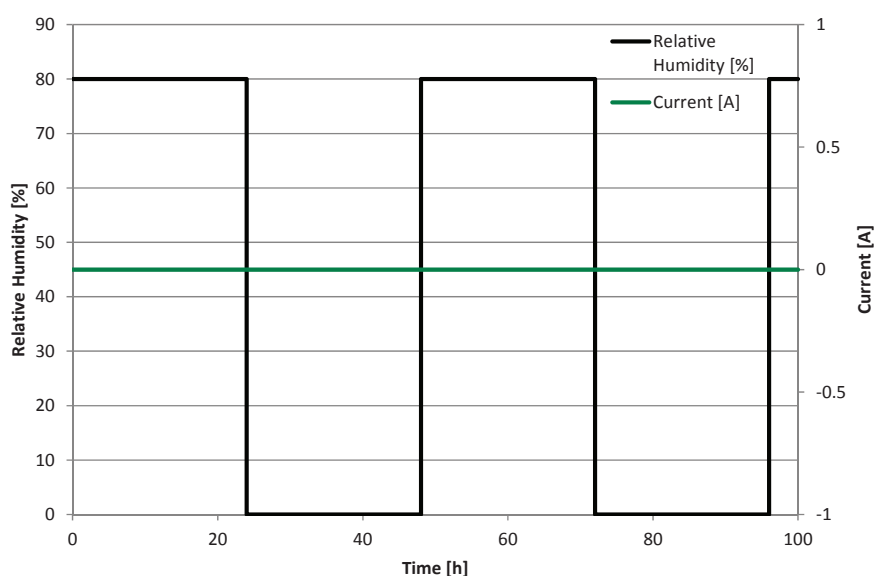


Figure 9. Accelerated Stress Test.

Gases were humidified using bubblers with monitoring of the relative humidity in the heated cathode feed line using a SHT75 temperature and humidity sensor from Sensirion AG. It was evident, that the relative humidity declined rapidly after switching to dry operation and increased rapidly after switching back to humidified operation. Here, “rapidly” means in a time range of approximately 10 min.

## 5.2. Determination of Fluoride Ion Using Fluoride Ion Selective Electrode

The Fluoride Ion Selective Electrode ( $F^-$ -ISE) is considered to be the simplest and most reliable technique to determine the concentration of fluoride ions in a solution [18]. Measurements with a  $F^-$ -ISE are rapid (the response time being of order of  $10^{-2}$  s to 2 min), non-destructive, easy and requiring simple equipment [19]. In this work the concentration of fluoride ions in fuel cell effluent water was measured by means of direct potentiometry using a  $F^-$ -ISE.

### 5.2.1. Apparatus

An Orion 5-Star pH/ISE/DO/conductivity meter was used to measure the potential of the Thermo Scientific Orion® 9609BNWP Fluoride Combination Ion Selective Electrode at room temperature.

### 5.2.2. Reagents

Chemicals of analytical grade were used without further purification. Series of standard solutions (conc.  $F^-$  ion; 0.02, 0.2 ppm) were prepared by suitable dilution of 2 ppm  $F^-$  with Total Ionic Strength Adjustment Buffer II standard. Samples have been prepared using TISAB II solution, which provides a constant background ionic strength, decomplexes fluoride ions and adjusts the solution pH between 5.0 and 5.5 [20]. All solutions were prepared from water which had been both deionized and distilled. Thermo Scientific Orion® 9609BNWP Fluoride Combination Ion Selective Electrode was filled with Optimum Results A™ ISE filling solution from Thermo Scientific Orion.

### 5.2.3. Measurement Procedure

Fluoride Combination Ion Selective Electrode was calibrated using three standard solutions; conc.  $F^-$  ion 0.02, 0.2 and 2.0 ppm. After obtaining an electrode slope value between  $-54$  and  $-60$  mV the concentration of fluoride ions in given samples has been measured. Samples were prepared by mixing the fuel cell effluent water and TISAB II in a ratio of one to one. The concentration of fluoride ions in the sample was read directly from the device display. After every measurement the electrode was rinsed thoroughly with water and calibrated anew. In the time between measurements the electrode was stored in the standard solution with the lowest concentration of fluoride ion.

## 5.3. Determination of in-Plane Proton Conductivity of NAFION® XL Membrane Using Electrochemical Impedance Spectroscopy

The membrane resistance of three pieces of NAFION® XL (A, C, R) was determined by means of electrochemical impedance spectroscopy (EIS) using a Conductivity Clamp (Bekktech BT110 LLC, Scribner Associates, Southern Pines, NC, USA) to calculate the in-plane proton conductivity of each

membrane. The denotations A, C and R in bracket mean pieces of membrane from near the anode inlet, cathode inlet and a piece of an untreated membrane used as reference.

For the test procedure, two pieces of the NAFION<sup>®</sup> XL membrane after AST were cut out at sizes of 2.5 × 1.0 cm with a scalpel from the anode inlet and cathode inlet, respectively. Further, the respective membrane sample was incorporated in the BT110 Conductivity Clamp which was connected with a GAMRY Instruments INTERFACE 1000 Potentiostat/Galvanostat/ZRA in a four-electrode arrangement. The BT-110 Conductivity Clamp including membrane was hung in a heated surface-grinding cell filled with ultra-pure water (~18 MΩ·cm) and parameters were adjusted in GAMRY software program for EIS measurements.

Generally, following measuring process was realised for every membrane sample:

- before: 5 EIS measurements of ultra-pure water (without membrane)
- 5 EIS measurements of respective NAFION<sup>®</sup> XL membrane
- after: 5 EIS measurements of ultra-pure water (without membrane)

All EIS measurements were carried out at 65 °C in potentiostatic mode and 5 points per decade were recorded. Before the EIS measurements were started, the open circuit potential (OCP) was measured for 50 s. A sinusoidal alternating current (AC) voltage of 50 mV (rms) was applied on the electrochemical system (BT110 Conductivity Clamp including membrane) in a frequency range of 0.1–100,000 Hz and the sinusoidal AC current was measured resulting the impedance  $Z$  of the membrane. From the resulting Nyquist-diagram, the frequency-independent measured resistance  $R_{tot}$  of respective membrane was read in high frequency range (HFR) at the measurement point which was sliced with the  $x$ -axis corresponding to the real part of impedance  $Z'$  at imaginary part of impedance  $Z''$  equals zero ( $y$ -axis) (Figure 4). The value of the measured resistance  $R_{tot}$  was used to assign the real membrane resistance  $R_{membrane}$  of respective NAFION<sup>®</sup> XL. The charge transport ( $H^+$ ) occurs not only through the membrane, but also via the electrolyte (~18 MΩ·cm water). Therefore, the electrolyte resistance  $R_{UPW, after}$  should be considered for the calculation of proton conductivity of respective membrane (Equation (1)) [21,22].

$$\frac{1}{R_{tot}} = \frac{1}{R_{membrane}} + \frac{1}{R_{UPW, after}} \quad (1)$$

The membrane resistance  $R_{membrane}$  is specified in Equation (2) [21,22].

$$R_{membrane} = \frac{1}{\frac{1}{R_{tot}} - \frac{1}{R_{UPW, after}}} \quad (2)$$

For the determination of in-plane proton conductivity, the thickness  $T$  of the respective NAFION<sup>®</sup> XL membrane in wet state was measured by a micrometer screw (10-fold determination) after measurement process. Equation (3) shows how the in-plane proton conductivity of respective membrane was calculated [21,22].

$$\sigma_{membrane} = \frac{d}{R_{membrane} \cdot T \cdot W} \quad (3)$$

The meaning of parameters from Equation (3) was already described in Table 2 (Section 2.3.1).

## Acknowledgments

The research leading to these results received funding from the European Community's 7th Framework Programme for the Fuel Cells and Hydrogen Joint Technology Initiative, Grant Agreement No. 621216.

## Author Contributions

Merit Bodner conducted the single cell measurements for the membrane and the membrane-electrode-assembly including *in situ* characterisation, analysed the resulting data, gave advice regarding the effluent water analysis and contributed to the writing process.

Bernd Cermenek performed the *ex situ* membrane characterisation, analysed the resulting data and contributed to the writing process.

Mija Rami, was responsible for the effluent water analysis and contributed to the writing process.

Viktor Hacker contributed his experience, supervised the project and gave advice on all aspects of the conducted work.

## Conflicts of Interest

The authors declare no conflict of interest.

## Abbreviations

AST	accelerated stress test
BoL	beginning of lifetime
EIS	electrochemical impedance spectroscopy
EoL	end of lifetime
FER	fluoride emission rate
F <sup>-</sup> -ISE	fluoride ion selective electrode
MEA	membrane-electrode-assembly
OCP	open circuit potential
OCV	open circuit voltage
PFSA	perfluorinated sulfonic acid
rH	relative humidity
TISAB	total ionic strength adjustment buffer
UPW	ultra-pure water

## References

1. Coms, F.D. The chemistry of fuel cell membrane chemical degradation. *ECS Trans.* **2008**, *16*, 235–255.
2. Collier, A.; Wang, H.; Ziyuan, X.; Zhang, J.; Wilkinson, D. Degradation of polymer electrolyte membranes. *Int. J. Hydrog. Energy* **2006**, *31*, 1838–1854.

3. Samms, S.R. Thermal stability of Nafion<sup>®</sup> in simulated fuel cell environments. *J. Electrochem. Soc.* **1996**, *143*, 1498–1504.
4. Mittal, V.O.; Russell-Kunz, H.; Fenton, J.M. Is H<sub>2</sub>O<sub>2</sub> Involved in the membrane degradation mechanism in PEMFC? *Electrochem. Solid-State Lett.* **2006**, *9*, A299–A302.
5. Kundu, S.; Fowler, M.W.; Simon, L.C.; Abouatallah, R.; Beydokhti, N. Degradation analysis and modeling of reinforced catalyst coated membranes operated under OCV conditions. *J. Power Sources* **2008**, *183*, 619–628.
6. Heinzl, A.; Mahlendorf, F.; Jansen, C. Fuel cells—Proton-exchange membrane fuel cells bipolar plates. *Encycl. Electrochem. Power Sources* **2009**, doi:10.1016/b978-044452745-5.00226-4.
7. Aarhaug, T.A.; Svensson, A.M. Degradation rates of PEM fuel cells running at open circuit voltage. *ECS Trans.* **2006**, *3*, 775–780.
8. Li, H.; Tsay, K.; Wang, H.; Shen, J.; Wu, S.; Zhang, J.; Jiab, N.; Wesselb, S.; Abouatallah, R.; Joosc, N.; *et al.* Durability of PEM fuel cell cathode in the presence of Fe<sup>3+</sup> and Al<sup>3+</sup>. *J. Power Sources* **2010**, *195*, 8089–8093.
9. Aoki, M.; Uchida, H.; Watanabe, M. Novel evaluation method for degradation rate of polymer electrolytes in fuel cells. *Electrochem. Commun.* **2005**, *7*, 1434–1438.
10. Aoki, M.; Uchida, H.; Watanabe, M. Decomposition mechanism of perfluorosulfonic acid electrolyte in polymer electrolyte fuel cells. *Electrochem. Commun.* **2006**, *8*, 1509–1513.
11. Macauley, N.; Wong, K.H.; Watson, M.; Kjeang, E. Favorable effect of in-situ generated platinum in the membrane on fuel cell membrane durability. *J. Power Sources* **2015**, *299*, 139–148.
12. Vengatesan, S.; Fowler, M.W.; Yuan, X.-Z.; Wang, H. Diagnosis of MEA degradation under accelerated relative humidity cycling. *J. Power Sources* **2011**, *196*, 5045–5052.
13. Panha, K.; Fowler, M.; Yuan, X.-Z.; Wang, H. Accelerated durability testing via reactants relative humidity cycling on PEM fuel cells. *Appl. Energy* **2012**, *93*, 90–97.
14. Catalano, J.; Myezwa, T.; de Angelis, M.G.; Baschetti, M.G.; Sarti, G.C. The effect of relative humidity on the gas permeability and swelling in PFSI membranes. *Int. J. Hydrog. Energy* **2012**, *37*, 6308–6316.
15. Bodner, M.; Hochenauer, C.; Hacker, V. Effect of pinhole location on degradation in polymer electrolyte fuel cells. *J. Power Sources* **2015**, *295*, 336–348.
16. Smitha, B.; Sridhar, S.; Khan, A.A. Solid polymer electrolyte membranes for fuel cell applications—A review. *J. Membr. Sci.* **2005**, *259*, 10–26.
17. Gittleman, C.S.; Coms, F.D.; Lai, Y. Membrane durability. *Polym. Electrolyte Fuel Cell Degrad.* **2012**, doi:10.1016/b978-0-12-386936-4.10002-8.
18. Sunitha, V.; Reddy, B.M. Determination of fluoride concentration in ground water by ion selective electrode. *Int. J. Curr. Res. Aca Rev.* **2014**, *2*, 159–166.
19. Alcacer, L.; Barbosa, M.R.; Almeida, R.A.; Marzagao, M.F. On the preparation of ion-selective electrodes. *Rev. Port. Quím.* **1973**, *15*, 192–200.
20. Pakalns, P. Non-ionic detergent as a complexing agent in the determination of fluoride with the fluoride electrode. *Microchim. Acta* **1983**, *79*, 29–35.

21. Dedmond, E.; Cooper, K. Application Note—Effect of Solution Conductivity on in-Plane Membrane Conductivity Measurement. Available online: <http://www.scribner.com/files/knowledgebase> (accessed on 25 September 2015).
22. Ranacher, C.; Resel, R.; Moni, P.; Cermenek, B.; Hacker, V.; Coclite, A.M. Layered nanostructures in proton conductive polymers obtained by initiated chemical vapor deposition. *Macromolecules* **2015**, *48*, 6177–6185.

© 2015 by the authors; licensee MDPI, Basel, Switzerland. This article is an open access article distributed under the terms and conditions of the Creative Commons Attribution license (<http://creativecommons.org/licenses/by/4.0/>).

### 16.3. Effect of Pinhole Location on Degradation in Polymer Electrolyte Fuel Cells.

*Bodner M, Hochenauer C, Hacker V. **Effect of pinhole location on degradation in polymer electrolyte fuel cells.** J Power Sources 2015;295:336–48.*

#### *Contribution:*

The effect of membrane defects in different areas of the membrane electrode assembly on fuel cell operation and the thereby induced component degradation was investigated. X-ray computed tomography measurements were provided by Prof. Christoph Hochenauer. Prof. Viktor Hacker advised in all aspects.

A membrane electrode assembly was characterised in a segmented single cell and underwent a short period of load cycling with constant gas supply, inducing anode starvation. The fuel cell was disassembled and defects were introduced by perforation of the MEA. After reassembly, the single cell underwent the identical procedure.

Small defects have proven not to affect the fuel cell operation significantly. However, pinholes near the anode inlet have affected the operation characteristics as well as the behaviour during starvation to the negative. This is mainly due to temperature effects.



# Effect of pinhole location on degradation in polymer electrolyte fuel cells



Merit Bodner<sup>a,\*</sup>, Christoph Hochenauer<sup>b</sup>, Viktor Hacker<sup>a</sup>

<sup>a</sup> Graz University of Technology, Institute of Chemical Engineering and Environmental Technology, NAWI Graz, Inffeldgasse 25/C, 8010 Graz, Austria

<sup>b</sup> Graz University of Technology, Institute of Thermal Engineering, Inffeldgasse 25/B, 8010 Graz, Austria

## HIGHLIGHTS

- Degradation in a fuel cell with various pinholes was investigated.
- Mild defects may result in a temporarily improved performance.
- A correlation between carbon corrosion and hydrogen crossover was evident.
- Defects near the anode inlet have the strongest influence on degradation.
- Fuel starvation resulted in a more severe voltage drop with a perforated membrane.

## ARTICLE INFO

### Article history:

Received 3 June 2015  
Received in revised form  
3 July 2015  
Accepted 7 July 2015  
Available online xxx

### Keywords:

Polymer electrolyte fuel cell  
Pinholes  
Electrode degradation  
Segmented cell  
Carbon corrosion  
Fluoride emission rate  
Fuel cell operation characteristics

## ABSTRACT

This work analyses the impact of the location of pinholes in polymer electrolyte fuel cells on the degradation of the electrodes. Defects with a diameter of 0.45 mm were created in a 25 cm<sup>2</sup> membrane electrode assembly (MEA) of a fuel cell. The MEA was operated and characterised using a segmented single cell. The effects of the pinholes on degradation were measured and evaluated. Defects affected the fuel cell behaviour during periods of hydrogen starvation, thus accelerating the degradation process of the carbon support as well as the loss of active platinum catalyst surface area. Furthermore, the effects of the induced pinholes on membrane degradation and performance decay were determined.

Pinholes close to the anode inlet in general have shown a more severe effect on the fuel cell operation parameters, such as open circuit voltage, performance, membrane resistance and hydrogen crossover, than pinholes at any other locations. Also, electrode degradation was accelerated. These effects were mainly due to locally increased temperatures.

© 2015 Elsevier B.V. All rights reserved.

## 1. Introduction

The polymer electrolyte fuel cell produces power at high efficiencies and is, therefore, of interest both for use in automotive applications [1,2] and combined heat and power units in residential applications [3]. However, commercial systems do not fully live up to the expectations with regard to operational lifetime yet. The aim for mobile applications is 5.000 h and 40.000–80.000 h for stationary applications [4].

Limitations in lifetimes are mainly caused by the degradation of

the membrane electrode assembly (MEA). The degradation of the membrane has a different effect on the fuel cell operation than degradation of the electrodes. In order to improve durability, it is necessary to gain a profound understanding of each failure mode.

Pinholes and areas of membrane thinning both result in a localised increase in hydrogen crossover and are, therefore, expected to lead to further degradation in a similar way. Both defects may derive from membrane degradation under undesirable operation conditions, such as operation under conditions of open circuit potential (OCV) or low humidity. Pinholes and cracks can, furthermore, be introduced to the membrane by mechanical stressors either within the fuel cell, during membrane manufacturing, or during implementation in the fuel cell. Such defects, therefore, cannot be avoided completely and their effects should be investigated.

\* Corresponding author.

E-mail addresses: [merit.bodner@tugraz.at](mailto:merit.bodner@tugraz.at) (M. Bodner), [christoph.hochenauer@tugraz.at](mailto:christoph.hochenauer@tugraz.at) (C. Hochenauer), [viktor.hacker@tugraz.at](mailto:viktor.hacker@tugraz.at) (V. Hacker).

Pinholes are the subject of intense research, which has mostly been conducted using accelerated stress tests that provoke specific defective modes [5–7]. However, only few studies have been conducted that evaluate the effects of pinholes on different operation parameters or further degradation processes [8–10], and none of the cited studies have taken the effects of pinhole locations on the observed results into account.

This research evaluates the effects of pre-existing defects at different locations in the membrane on the behaviour of the fuel cell during normal and critical operation modes and on further degradation processes of the electrodes and the membrane. Pinholes were created in the membrane electrode assembly at various locations. A single cell setup with a segmented cathode was used for in-situ characterisation.

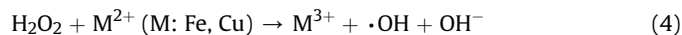
## 2. Degradation in polymer electrolyte fuel cells

Pinholes in the fuel cell membrane are formed by material inhomogeneities, mechanical stress and degradation. The local operation conditions around the pinholes change in comparison to normal operation. The direct chemical oxidation of hydrogen with oxygen leads to a temperature increase at the affected area. Furthermore, the formation of water is affected locally due to the direct oxidation, thus causing a higher humidification at the location of increased crossover. Additionally, the direct consumption of the reactant gases can lead to local starvation conditions further down the channels, thus affecting the electrode corrosion process and induce the formation of hydrogen peroxide in case of oxygen starvation. Hydrogen peroxide is known to be formed by incomplete oxygen reduction [11]. This affects both electrode corrosion and membrane degradation.

### 2.1. Membrane degradation

#### 2.1.1. Causes for membrane degradation

Membrane degradation is triggered by hydrogen peroxide formation, which is favoured at OCV conditions.  $\text{H}_2\text{O}_2$  can be detected within the drain water [12,13]. It decomposes to hydroxyl radicals in the presence of metal ions such as  $\text{Fe}^{3+}$  and  $\text{Cu}^{2+}$  (Equations (1)–(5)) [14].



The degradation of the perfluorosulfonic acid (PFSA) backbone of the membrane, but also of the ionomer within the electrode is quantified by measuring the fluoride content in the effluent water. Fluoride ions are emitted in form of HF and therefore, the fluoride ion emission is directly linked to the pH value of the exhaust water.

The fluoride emission rate (FER) is used to determine the decomposition of the electrolyte. However, the C–F bond is thermodynamically stable and  $\text{F}^-$  cannot be abstracted by the OH radical, formed by the homolytic cleavage of the O–O bond of hydrogen peroxide. Instead, the abstraction of a hydrogen atom by the OH radical is favoured [15].

$\text{H}\cdot$  is formed by the abstraction of a hydrogen atom from molecular  $\text{H}_2$  by  $\cdot\text{OH}$  and aggressive towards the C–F bonds in PFSA.  $\text{H}\cdot$  is able to induce damage of the polymer backbone, which is

consistent with the accelerated fluoride release over time and in dependence of hydrogen crossover exhibited in chemical degradation studies of PFSA based membranes [15].

The membrane degradation is accelerated at OCV conditions, since hydrogen is not consumed and  $\text{H}\cdot$  can be formed in larger quantities. The fluoride emission rate increases with low humidity, a higher partial pressure of oxygen on the cathode, high temperature and most importantly high hydrogen pressure. Due to the high boiling point of hydrogen peroxide (150 °C) compared to water, high temperatures are thought to result in a higher  $\text{H}_2\text{O}_2$  concentration, thus accelerating the degradation. Chemical degradation is the most severe among the degradation phenomena and it results in membrane thinning and pinhole formation, leading to increased hydrogen crossover, further accelerating degradation [13].

The FER is not always clearly associable with the degree of membrane degradation. Decreasing rates have been reported, despite operation at harmful conditions. The emission of fluorine in form of C–F compounds is possible and cannot be detected by common fluoride detection methods. Therefore, FER detection is not always an accurate method for quantification of membrane degradation [16].

#### 2.1.2. Effect of membrane degradation on the fuel cell operation

The effect of pinholes on the OCV depends on their size. A rather small pinhole with a diameter of 0.7 mm has shown close to no impact on the open circuit potential, whilst a larger pinhole with a diameter of 1.2 mm resulted in an immediate reduction of the potential [10]. At high current densities, a perforated MEA has exhibited a serious decrease in performance and strong voltage fluctuation. However, the effect was smaller at low current densities [9].

The increased hydrogen crossover results in elevated hydrogen diffusion current. The distribution of the crossed over hydrogen was visualised by spatial resolution [8]. Not only the affected area exhibits an increased hydrogen diffusion current, but also the surrounding segments.

With the C–S bond being the weakest in the polymer electrolyte, sulphur can be released as  $\text{SO}_2$  or  $\text{SO}_3$ , the latter via a hydrogen peroxide triggered sulfonyl radical mechanism. This also contributes to the main chain scission, increases the membrane resistance due to the loss of proton conducting species and further accelerates the degradation of the PFSA backbone [15,17].

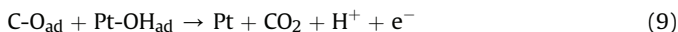
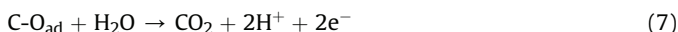
### 2.2. Electrode

The process of electrode degradation is divided into carbon corrosion and catalyst degradation. Both influence each other and affect the electrochemical surface area (ECSA) by decreasing the catalytically active area.

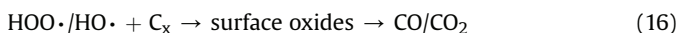
#### 2.2.1. Degradation of the carbon support

The rate of the corrosion of the carbon support is determined by the  $\text{CO}_2$  content of the off-gas. Carbon nanoparticles undergo severe degradation at potentials that exceed 1 V. The  $\text{CO}_2$  concentration is increased even more in the presence of platinum; however, a direct correlation between  $\text{CO}_2$  evolution and platinum loading, in a sense that platinum catalyses the carbon oxidation, has not been found due to the limited area of the carbon/platinum interface [18].

The proposed mechanism of carbon corrosion follows a two-step reaction pathway (Equations (6) and (7)), that consists of a carbon oxidation step, followed by a water-gas shift reaction. The second reaction (Equation (7)) is the rate determining step. In the presence of a catalyst, it follows an alternative platinum catalysed pathway (Equations (8) and (9)) [18].



Another proposed mechanism for carbon corrosion is the catalysis of the reaction of oxygen and water, which yields highly reactive OH and OOH radicals (Equations (10)–(15)) that attack carbon, form surface oxide groups, then decompose into gaseous CO and CO<sub>2</sub> compounds (Equation (16)) at increased temperatures [19].



The fundamental role that water takes during carbon corrosion is evident in either case. High humidity levels as well as high temperatures, a low pH, large Pt/carbon interface, high oxygen concentrations and high potentials all accelerate carbon corrosion [20,21]. At potentials above 1.0 V, carbon is released as CO<sub>2</sub>, while CO is formed at electrode potentials exceeding 1.2 V [22].

During periods of fuel starvation, all hydrogen fed to the fuel cell is oxidised near the anode inlet. To maintain the current, the carbon support is oxidised instead, according to Equations (6), (8) and (9). Operation of the fuel cell at an anode stoichiometry below 1.0 induces a gradient in the current density, the overall potential, and the anode potential. The potential gradient, in particular, results in uneven degradation. At local anode potentials above 1.23 V, electrolysis occurs in accordance with Equation (17). The products of both carbon oxidation as well as electrolysis, CO<sub>2</sub> and O<sub>2</sub>, respectively, can be detected in the anode off-gas [23].



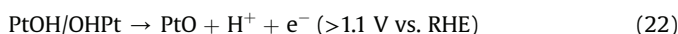
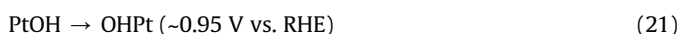
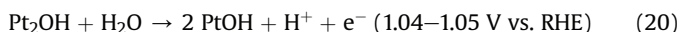
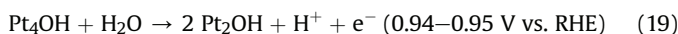
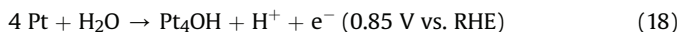
The rate of degradation of the carbon support correlates with the extent of the electrolysis, but can be reduced by pre-treatment of the carbon support [24,25].

### 2.2.2. Degradation of the platinum catalyst

Platinum degradation is caused by particle agglomeration and growth, dissolution and redistribution, and blockage of the active catalyst area by poisoning. Both particle agglomeration and redistribution are preceded by platinum dissolution, which has been reported to occur under standard conditions and at remarkable rates at intermediate potentials [26], whereas at higher potentials, exceeding 1.1 V, a protective layer is formed. Dissolution of platinum predominantly occurs on the cathode side, and is strongly affected by operational conditions [20,27].

The oxidation of platinum (Equations (18) and (20)) depends on the potential and results in the formation of PtOH at 1.05 V vs. the reversible hydrogen electrode (RHE). Depending on the time, and at

anodic potentials above 0.95 V vs. RHE, the irreversible formation of OHPt occurs by place exchange (Equation (21)). The more stable species are characterised by a lower positive reduction potential. Above 1.1 V vs. RHE, platinum is further oxidised to PtO (Equation (22)) [28,29].



Agglomeration is considered the most dominant mechanism of catalyst degradation. By agglomeration of nanoparticles into larger particles, the high surface energy and thus the electrochemical surface area are reduced. The smaller particles dissolve and are subsequently reduced on larger particles. This process of coupled transport of electrically charged species is the main reason for particle growth and is referred to as Ostwald ripening [20].

The underlying mechanism and the position of the redeposition of dissolved platinum strongly depend on the gas concentration and crossover of both hydrogen and oxygen.

The local concentration of Pt ions in the cathode catalyst layer is higher with less hydrogen crossover. Thus, it is assumed that hydrogen chemically reduces platinum oxides, resulting in less Pt ion formation, since this predominantly follows the platinum oxide pathway. The platinum particle growth and the relative loss of active platinum surface area have been shown to increase with decreasing crossover [30].

When platinum is dissolved in an acidic environment and at high potentials, the ions are transported through the membrane. Since platinum ions are easily reduced, they are possibly stabilised by chloride stemming from contaminations or fluoride from membrane degradation, and form anionic complexes. In the absence of hydrogen in the anode department, the platinum ions are reduced on the anode catalyst surface. In the presence of hydrogen in the polymer electrolyte membrane, metallic aggregates are formed. The position of platinum particles depends on the hydrogen concentration and is also affected by the presence of oxygen in the cathode department [31]. The agglomerates formed within the membrane are reported to be in a range of 10–100 nm, whereas those within the electrocatalyst range from 2 to 5 nm [32].

## 3. Experimental

The fuel cell was operated at 65 °C with humidified gas on the anode and cathode with a relative humidity of 80% on both sides. For humidification, gas bubblers were used. During normal operation, hydrogen and synthetic air were fed at a stoichiometry of 1.5 and 3, respectively. The increased load during the starvation periods lowered the stoichiometry to 0.9 on the anode and 1.8 on the cathode, respectively. In order to prevent hydrogen from being drawn back into the fuel cell from the off-gas during fuel starvation, check valves were installed directly at the fuel cell outlet. To avoid a pressure difference, the valves were installed at both the anode and cathode. The cracking pressure of the check valves was noted and validated as  $2.33 \cdot 10^{-2}$  bar.

### 3.1. Segmented single cell setup

An in-house designed rectangular 25 cm<sup>2</sup> single cell with a 4-

fold serpentine flow field on both sides and with a segmented cathode was used for in-situ characterisation. The current for each of the 30 segments was measured separately using shunt resistors. The MEA was a pre-commercial catalyst coated Nafion type membrane with a thickness of 18  $\mu\text{m}$  and a platinum catalyst loading of 0.4  $\text{mg cm}^{-2}$  on both the anode and cathode. Sigracet GDL 24 BC carbon coated carbon paper with 5wt% PTFE was used as a backing layer.

The MEA was assembled and conditioned for 8 h. Afterwards, it was characterised and the single cell was disassembled. The MEA was perforated from the cathode to the anode side with pinholes using a 0.45 mm needle. This diameter was carefully chosen, considering two key aspects: enabling an observable effect of the introduced defect on the fuel cell operation, without disabling the latter. Pinholes in the same order of magnitude were introduced and characterised before, as well as reported to have been formed during normal cell aging [10,33–35]. The areas of perforation can be seen in Fig. 1.

The cell was reassembled and again characterised. A single pinhole represents a damage of 0.16  $\text{mm}^2$  or 0.006% of the surface area of a cell.

The characterisation, except the starvation interval, was conducted twice and all experiments were repeated for a full characterisation, yielding four values for each electrochemical property that could be used to determine the standard deviation.

### 3.2. Electrochemical characterisation

The fuel cell was electrochemically characterised using polarisation curves, electrochemical impedance spectroscopy and hydrogen diffusion measurements [36] using an IM6 potentiostat with a PP240 power potentiostat, both from ZAHNER Elektrik for a current up to  $\pm 40$  A.

Cyclic voltammetry measurements were conducted to determine the loss of active surface area. Carbon corrosion was enforced by load cycling induced starvation. The operation conditions used are summarised in Table 1.

### 3.3. Starvation interval

The load was cycled five times during the characterisation procedure in order to provoke carbon corrosion. The gas flow was held stable during the entire measurement, set to satisfy the hydrogen consumption at 400  $\text{mA cm}^{-2}$ , resulting in hydrogen starvation during the intervals of increased current density. Thereby, the influence of the implemented defects on electrode degradation could be evaluated. To enable gas analysis, nitrogen was added to the anode gas flow.

The current density was held at 400  $\text{mA cm}^{-2}$  for 3 min, followed by a starvation interval at 666  $\text{mA cm}^{-2}$  for 10 s. The potential response was obtained. The conditions are listed in Table 1.

### 3.4. Off-gas analysis

The off-gas on either the anode or the cathode side was analysed with an online gas analyser (ABB) during the fuel cell operation. The content of CO and  $\text{CO}_2$  was analysed with two Uras 14 units set for different concentration ranges; hydrogen, with a Caldos 17 unit; and oxygen, with a Magnos 106 unit. The amount of hydrogen in the cathode off-gas and oxygen in the anode off-gas respectively, are indicators for increased gas crossover due to membrane defects, but potentially also for electrolysis, which might occur at high potentials. The  $\text{CO}_2$  content in the off-gas of both electrodes correlates with the degree of carbon corrosion.

### 3.5. Effluent water analysis

The off-gas, that did not undergo gas analysis, passed through a condensation trap. The condensed water was mixed with TISAB II, as received from Thermo Scientific, at a ratio of 50:50 and analysed in regards of fluoride ion content with a 9609BNWP fluoride ion selective electrode from Thermo Scientific. The fluoride emission rate was calculated.

### 3.6. Computed tomography

A sample of MEA with a pinhole at position 4 was analysed at the University of Applied Sciences Upper Austria – Research and Development Ltd., Research group Computed Tomography, using computed tomography (CT) to determine the local structure. After the perforation, the MEA was implemented in the single cell and characterised at operational temperature. For the CT-analysis, a voxel length of 1.5  $\mu\text{m}$  was used on a 2.2  $\text{mm}^2$  sample.

## 4. Results and discussion

### 4.1. Fuel cell characteristics

#### 4.1.1. Open circuit voltage

The open circuit voltage was noted before and after each characterisation. The OCV decreased with each pinhole. However, the extent of the decrease was small (Table 2). A more detailed view of the decrease shows that the loss is the highest for pinholes near the cathode inlet.

The decrease per pinhole was the highest after the perforation of pinhole 6, near the cathode inlet. A loss of open circuit potential of 17.4 mV compared to the initial potential was noticed. The effect of the additional pinhole 7 directly at the cathode inlet results in a further decrease of approximately 11.8 mV.

The potential decay is however fairly small considered the damage in all cases.

#### 4.1.2. Fuel cell performance

The power density shows, that up to two pinholes caused no, or

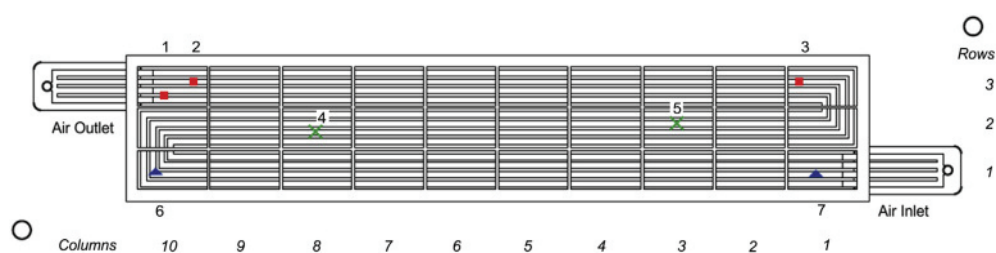


Fig. 1. Locations of pinholes created by MEA perforation of the 25  $\text{cm}^2$  segmented cell, with ■ the first set of pinholes (1–3) near anode inlet, × second set of pinholes (4,5) in the middle section, and ▲ third set of pinholes (6,7) near the cathode inlet.

**Table 1**  
Operation conditions.

	Load (range) [mA cm <sup>-2</sup> ]	Set potential (range) [V]	Gases Anode/Cathode
Conditioning	400	–	H <sub>2</sub> /Air
Cyclic Voltammetry	–	0.06–0.70	H <sub>2</sub> /N <sub>2</sub>
Starvation Cycling	400–666	–	H <sub>2</sub> in N <sub>2</sub> (1.15:1)/Air
Polarisation	0–800	–	H <sub>2</sub> /Air
Electrochemical Impedance Spectroscopy	200	–	H <sub>2</sub> /Air
Hydrogen Diffusion Measurement	–	0.43	H <sub>2</sub> /N <sub>2</sub>

**Table 2**  
Results from the electrochemical characterisation.

Pinhole location	0	1	1, 2	1, 2, 3	4	4, 5	6	6, 7
OCV [V]	0.934	0.933	0.925	0.914	0.909	0.902	0.928	0.915
± Standard deviation [V]	9.01 × 10 <sup>-3</sup>	6.22 × 10 <sup>-3</sup>	6.76 × 10 <sup>-3</sup>	8.91 × 10 <sup>-3</sup>	2.09 × 10 <sup>-3</sup>	3.44 × 10 <sup>-3</sup>	3.94 × 10 <sup>-3</sup>	1.88 × 10 <sup>-3</sup>
Decrease [%]	–	0.034	–0.898	–1.222	–1.161	–0.749	–1.525	–1.165
Power Density [mW cm <sup>-2</sup> ]	278.9	285.4	284.6	266.0	264.0	262.3	287.6	286.2
± Standard Deviation [mW cm <sup>-2</sup> ]	7.224	9.843	2.488	8.315	8.175	10.471	4.629	5.784
Decrease [%]	–	2.000	–0.216	–6.510	–2.320	–0.676	3.815	–1.008
Membrane Resistance [Ω]	1.60 × 10 <sup>-2</sup>	1.62 × 10 <sup>-2</sup>	1.57 × 10 <sup>-2</sup>	1.58 × 10 <sup>-2</sup>	1.61 × 10 <sup>-2</sup>	1.62 × 10 <sup>-2</sup>	1.55 × 10 <sup>-2</sup>	1.54 × 10 <sup>-2</sup>
± Standard Deviation [Ω]	2.6 × 10 <sup>-4</sup>	7.65 × 10 <sup>-4</sup>	2.87 × 10 <sup>-4</sup>	1.31 × 10 <sup>-4</sup>	4.50 × 10 <sup>-5</sup>	1.24 × 10 <sup>-4</sup>	2.02 × 10 <sup>-4</sup>	9.90 × 10 <sup>-5</sup>
Decrease [%]	–	1.584	–2.989	0.619	1.305	0.496	–3.655	–1.627
Current Density H <sub>2</sub> Diffusion [mA cm <sup>-2</sup> ]	7.087	6.415	7.703	7.140	8.477	9.478	8.254	8.888
± Standard Deviation [mA cm <sup>-2</sup> ]	0.959	0.909	0.376	0.949	0.950	0.895	0.856	0.628
Decrease [%]	–	–10.27	21.02	–7.46	22.59	12.53	30.09	12.95
Active Catalyst Surface Area [m <sup>2</sup> g <sup>-1</sup> ]	45.42	44.29	40.29	31.07	32.44	28.66	45.44	45.19
± Standard Deviation [m <sup>2</sup> g <sup>-1</sup> ]	2.749	0.603	1.753	3.057	5.093	4.725	0.454	1.934
Decrease [%]	–	–2.22	–9.01	–22.59	–7.26	–11.75	–1.11	–0.58

just a minor performance decay (Table 2 and Fig. 2, 1). Moreover, even an increase of the power density is visible for the first pinholes in the inlet and in the outlet regions, respectively. A maximum gain of 17.5 mW cm<sup>-2</sup> was reported for pinhole 6. This is most likely due to an increased temperature by chemical oxidation of hydrogen, thereby improving the local reaction kinetics.

For the pinhole near the anode inlet (positions 1 to 3), this phenomenon is confirmed by the current distribution measurement (Fig. 2, 2). The current is increased locally at the affected segment after the first perforation. After additional perforation steps, the local current density however decreases. While the perforation of the membrane at position 2 does not provoke vast overall performance decay, the most severe effect is observed for pinhole 3 near the anode inlet with a performance decrease of 27.5 mW cm<sup>-2</sup>. A locally decreased current in the affected segments is however not visible. Additional perforation steps in the middle section reduce the performance further, however to a smaller extent.

For the pinhole near the cathode inlet, a similar local effect can be observed (Figs. 2 and 3) and the additional perforation does not result in a significantly decreased performance (Table 2).

#### 4.1.3. Gas crossover and carbon corrosion during operation

The off-gas was analysed during characterisation. During operation, hydrogen and oxygen were consumed, resulting in fluctuating net flow rates. Thus, the time the gases remained in the gas analyser varied and no quantifications of the crossed over gases and carbon emission could be made.

Gas analysis (Table 3) has shown an elevated level of hydrogen in the cathode off-gas for most measurements. A clear increase of the crossover during fuel cell operation in dependence of the implementation of pinholes was only evident for pinholes near the anode inlet.

The oxygen concentration in the anode off-gas was rather low for most measurements. Nevertheless, it was elevated for pinholes near the middle section and for the pinhole at position 3 near the

anode inlet. This is in correlation with the decrease of the performance density (Table 2) for pinholes in this area. In the middle section, performance decay and an increased oxygen concentration were recorded; both however did not reach excessive levels. The oxygen content was low for the pinhole near the cathode inlet at position 6. This is also consistent with the performance.

Since the polarisation curves were recorded galvanostatically, it is evident that the cell potential is strongly affected by oxygen at the anode. This particular effect is however less strong for the operation at low current densities and under open circuit potential than at higher current densities. This can be attributed to the decreasing anode pressure at higher loads, thus encouraging crossover from the cathode.

For pinholes near the anode inlet, an increase of carbon corrosion with the implementation of each pinhole was evident. At the middle section however, the carbon content slightly decreased. Near the cathode outlet the carbon emission was rather stable. Since the second characterisation with a pinhole directly at position 7 had to be aborted due to excessive oxygen crossover, the carbon emission for this particular pinhole is unknown.

A correlation between gas crossover and carbon corrosion was only evident for pinholes near the anode inlet and the therefore increased hydrogen content in the cathode off-gas. It can be concluded that, as the positive effect of the locally increased temperature is overshadowed by the negative effects of the increased crossover, the carbon corrosion begins.

#### 4.1.4. Membrane resistance

A clear trend of the effect of a pinhole on the membrane resistance is not evident for the area close to the anode inlet (Table 2). However, a slight decrease of the membrane resistance is reported for pinholes near the cathode inlet. This is most likely caused by an improved humidification after a longer period of operation. This is further accelerated by the increased water production deriving from the direct reaction of the crossed over reactants. Water is less likely to be removed near the anode outlet due to the lower flow

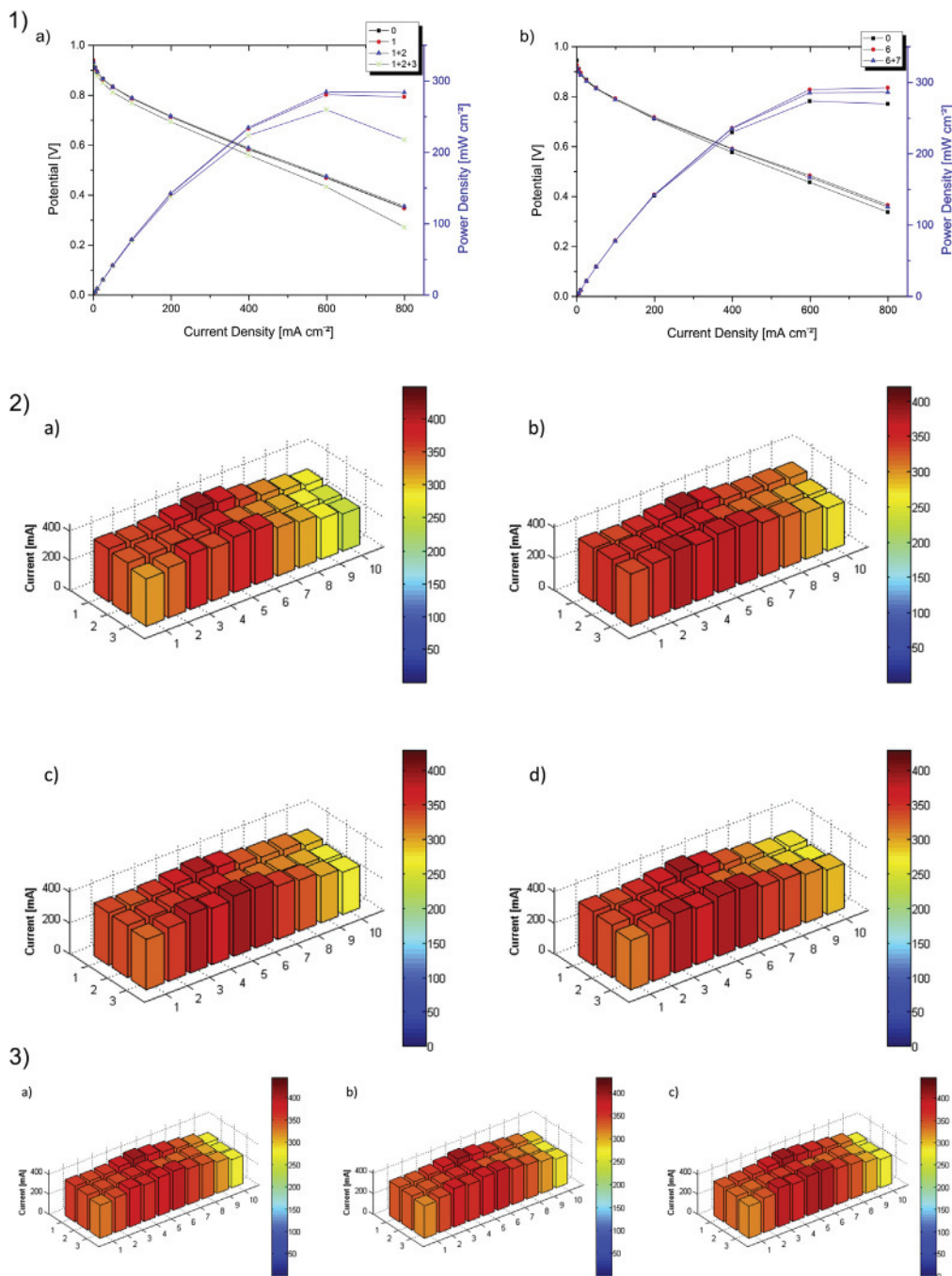


**Fig. 2.** Polarisation Curves 1) a) with no pinhole and with pinholes at locations 1, 1 and 2 and 1 to 3, b) with no pinhole and with pinholes at the locations 6 and 6 and 7, and current distribution at 400 mA cm<sup>-2</sup> 2) a) without pinholes, b) after the first perforation at the anode inlet (row 3/column 10, position 1), c) after the second perforation of the same segment (position 2) and d) after the additional perforation (row 3/column 1, position 3), 3) a) without pinholes, b) after the first perforation (row 1/column 10, position 6) and c) after the additional perforation (row 1/column 1, position 7) at the cathode inlet.

rate of the anode gas stream. Therefore, water being produced in the area near the anode outlet/cathode inlet remains in the fuel cell for a longer period of time.

In the middle section, the resistance was slightly increased. A vaster effect is to be expected for pinholes in areas of excessive oxygen crossover, since this leads to hydrogen peroxide formation at the anode. Therefore, the accelerated degradation at the middle section could be due to the longer dwell time of oxygen within the fuel cell for pinholes not located directly at the anode outlet.

#### 4.1.5. Hydrogen diffusion experiments

The hydrogen diffusion is characterised electrochemically. A relatively high initial hydrogen crossover was evident for all experiments. This appears to be a characteristic of the membrane that was used. The current increased with the implementation of pinholes, yet the standard deviation is rather high for hydrogen diffusion experiments in all cases. However, trends for the effect of the pinholes are still evident (Table 2).

After the implementation of the first pinhole, a decrease of hydrogen diffusion current was recorded. The current rises after

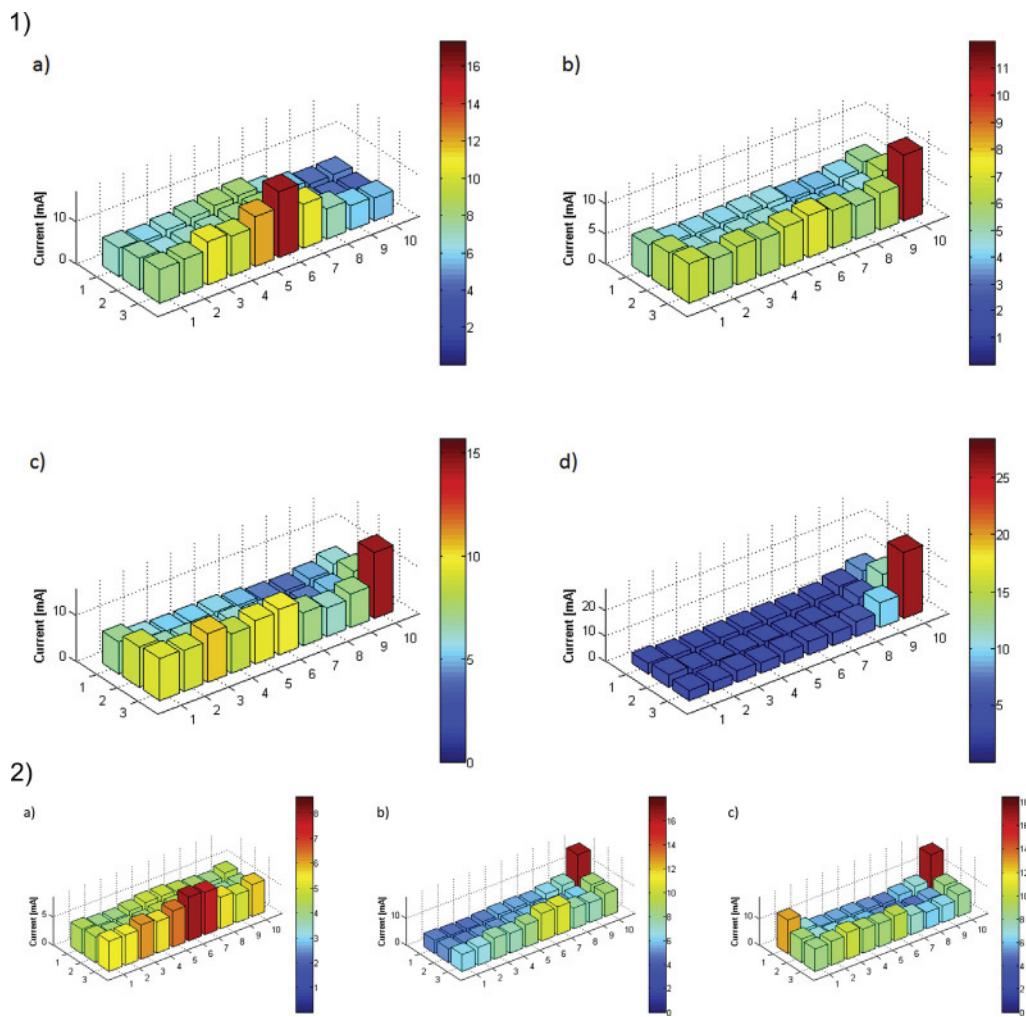


**Fig. 3.** Hydrogen diffusion current distribution 1) a) without pinholes, b) after the first perforation at the anode inlet (row 3/column 10, position 1), c) after the second perforation of the same segment (position 2) and d) after the additional perforation (row 3/column 1, position 3), 2) a) without pinholes, b) after the first perforation at position 6 (row 1/column 10) and c) after the additional perforation (row 1/column 1, position 7) at the cathode inlet.

**Table 3**

Hydrogen content in the cathode flow, oxygen content in the anode flow and summarised carbon emission for both anode and cathode during polarisation measurement in dependence of the pinhole location, all normalised for the lowest value.

Pinhole location	0	1	1, 2	1, 2, 3	4	4, 5	6	6, 7
H <sub>2</sub> Crossover in cathode off-gas	3.26	4.07	4.18	4.23	1.03	1.00	3.96	3.94
O <sub>2</sub> Crossover in anode off-gas	1.42	1.87	1.00	9.21	8.08	3.78	1.10	–
Carbon Corrosion	4.41	7.41	8.58	18.90	14.82	11.45	4.04	1.00

implementation of the second pinhole, but slightly decreases for the third pinhole.

This is due to a vast amount of hydrogen, crossing over from the anode to the cathode being immediately purged from the fuel cell by the cathode nitrogen flow during measurement. This is confirmed by the cathode off-gas analysis (Table 4). Therefore, the hydrogen diffusion current appears lower, since a large amount of crossed over hydrogen is not oxidized within the fuel cell.

The spatial distribution of the hydrogen diffusion current for the pinholes near the anode inlet has shown, that the current is almost only increased at the segment directly at the anode inlet, whilst the current in the rest of the segments remains low (Fig. 3, please note the different scales).

The current of the segments surrounding the pinhole is increased (Fig. 3, 1). This could be due to hydrogen, crossing over to the cathode and being distributed there. This is however unlikely

**Table 4**

Hydrogen content in the cathode off-gas stream during hydrogen diffusion measurements in dependence of the pinhole location, all normalised for the lowest value.

Pinhole location	0	1	1, 2	1, 2, 3	4	4, 5	6	6, 7
H <sub>2</sub> Crossover in cathode Off-gas diffusion measurement	1.00	3.48	20.56	26.63	6.47	1.24	1.03	1.00

considering the higher cathode gas flow. Alternatively, this may derive from membrane thinning of the area surrounding the pinhole, coupled with hydrogen crossing over to parallel channels.

The sections in the middle and close to the cathode inlet show an increase of the current density with an increasing number of defects, as is shown in Table 2. The second pinhole however has a smaller impact than the first pinhole in both cases.

The pinhole near the cathode inlet does not lead to increased hydrogen content in the off-gas (Table 4), whilst the hydrogen diffusion current is clearly raised at the affected segments (Fig. 3, 2). Therefore, for the pinhole at the cathode inlet, all crossed over hydrogen is directly oxidised at the cathode catalyst surface. Also a slight increase of the current at the surrounding segments is visible. It is evident, that the crossed over hydrogen does not only follow the flow pattern, but is also crossing over to parallel channels, leading to an increase of the current at all surrounding segments.

The effect of the second pinhole at position 7 is smaller than that of the pinhole at position 6 in both the overall current and the local current.

#### 4.1.6. Active catalyst surface area

An increased hydrogen diffusion current results in a shift of the cyclic voltammetry curve towards higher currents. This may alter the results of the active surface area, making them incomparable when the curve is tilted, since the capacitive current does not reach a steady level. However, all obtained results were considered valid since the capacitive current did reach a stable value in all cases.

Table 2 shows a decrease in the active surface area with each implemented pinhole. The decay is vast for the perforation step of the second and especially the third pinhole at the anode inlet and the pinholes 4 and 5 in the middle section of the MEA. At the cathode inlet region, however, the loss of surface area was small, even after the implementation of a pinhole directly in the segment at the cathode inlet.

The vast decrease in the active catalyst surface area after implementation of the pinholes at the positions 2 to 5 was due to a strong local increase in the temperature at areas of increased hydrogen crossover, namely the anode inlet. The hydrogen crossing over from the anode was directly oxidised by oxygen at the cathode catalyst, resulting in an area of increased temperature. This accelerated the local degradation of the platinum catalyst. Platinum was dissolved at a higher rate and reduced by the hydrogen present, leading to Ostwald ripening and reduction of the platinum within the electrolyte, thus resulting in a decrease of the cathode's active catalyst surface area near the anode inlet.

#### 4.2. Starvation

Carbon corrosion was intensified by load cycling induced fuel starvation. By analysis of the off-gas, the carbon emission was evaluated.

##### 4.2.1. Voltage drop during fuel starvation

When pinholes were created at the anode inlet area, the voltage dropped rapidly with each starvation cycle and reached a state of cell reversal in most cases (Fig. 4, 1). When pinholes were introduced in the middle section, however, a similar but weaker effect was observed (Fig. 4, 2), whereas pinholes near the anode outlet had an even smaller effect on the voltage drop (Fig. 4, 3).

The impact of the first pinhole near the anode inlet on the current of the segments was insignificant. When a second hole was introduced, the resulting hydrogen starvation led to a strong reduction in the current in the segments along the channels. The third pinhole further strengthened this gradient (Fig. 5, 1).

Pinholes created in the middle section also resulted in a gradual

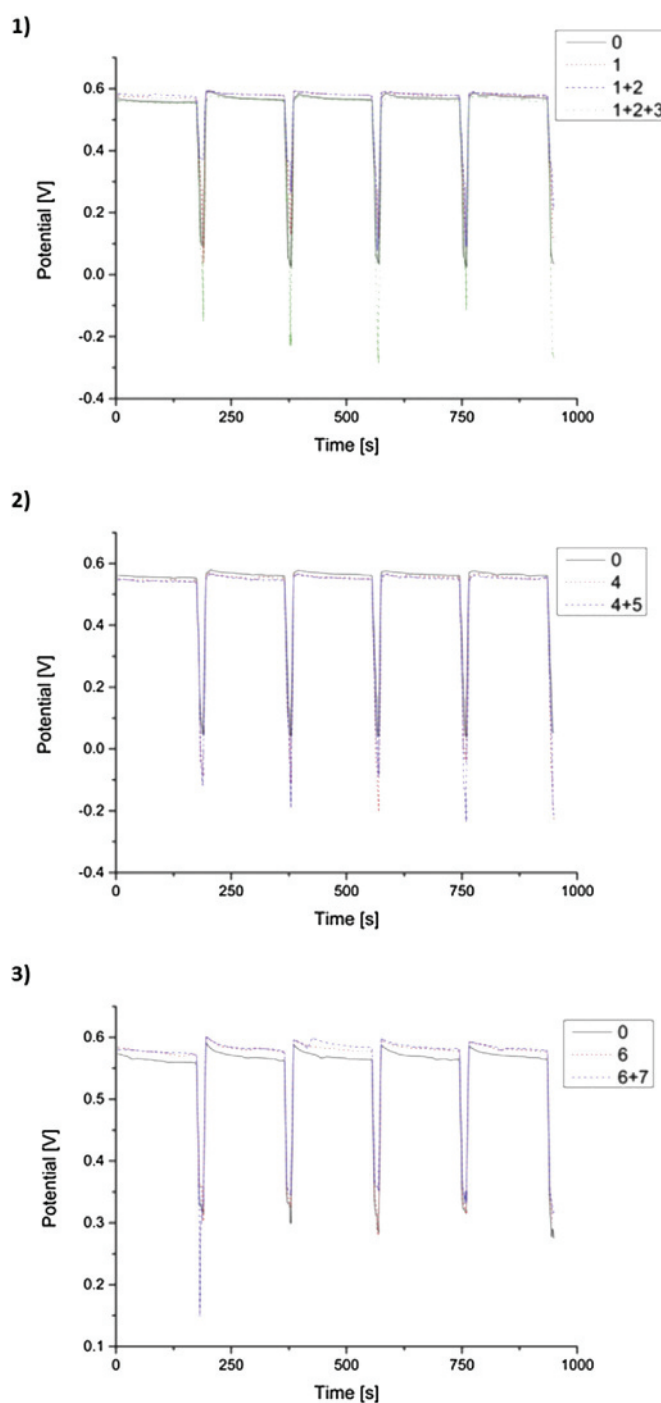
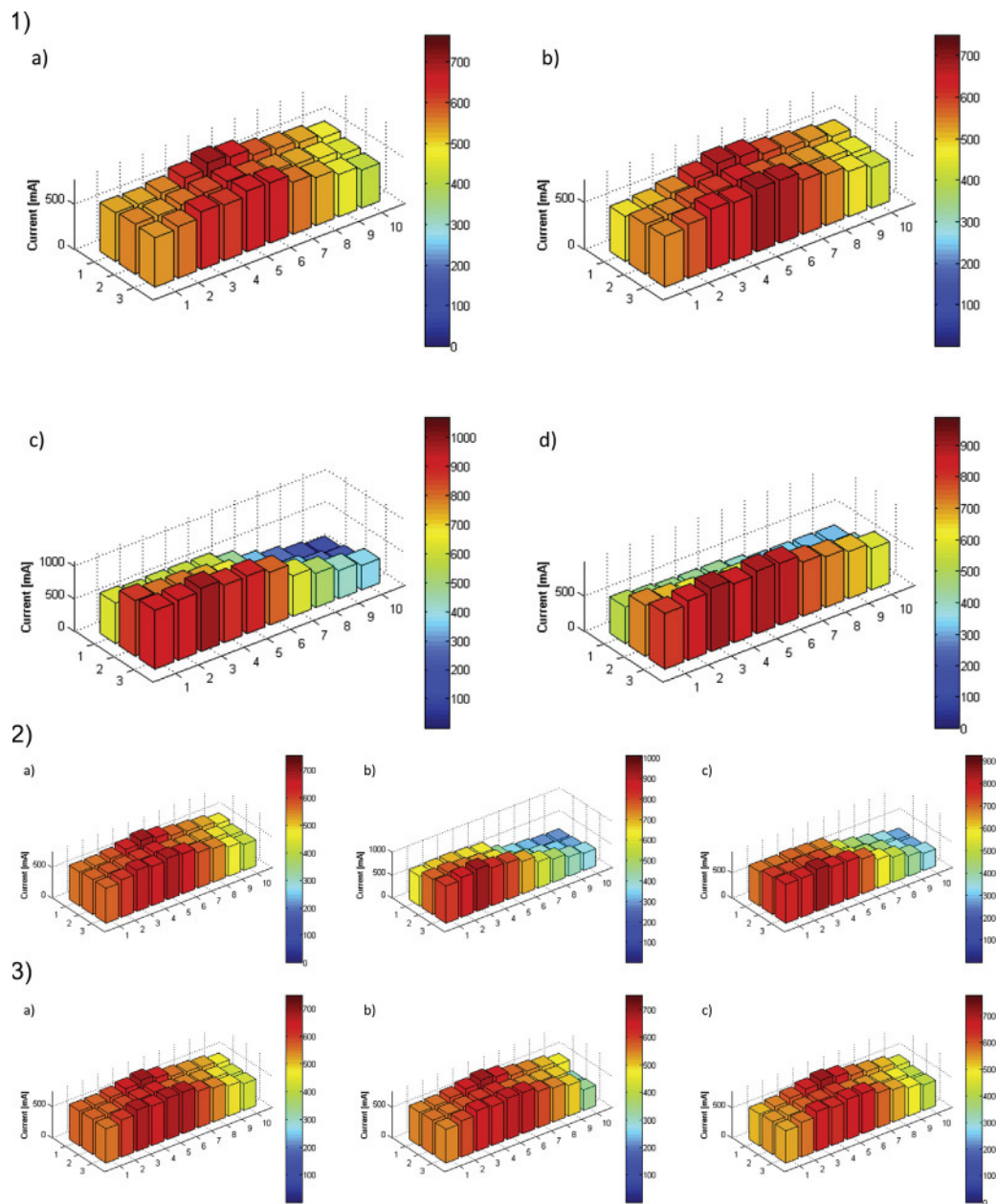


Fig. 4. Potential over five starvation cycles for 1) the reference MEA and the MEA with pinholes at the positions 1, 1 and 2, and 1, 2 and 3, 2) reference MEA and the MEA with pinholes at the positions 4 and 4 and 5, 3) the reference MEA and the MEA with pinholes at the positions 6 and 6 and 7.

current distribution, however, the effect was less severe (Fig. 5, 2), whilst only a minor effect on the current distribution was noted when defects were introduced near the cathode inlet (Fig. 5, 3).

Pinholes introduced near the anode inlet intensified fuel starvation effects, because hydrogen was oxidised immediately. This had no or only a minor effect during normal operation since a slight surplus was present. Hydrogen was oxidised either electrochemically or directly after crossing over to the cathode, and thus induced a strong pressure drop.



**Fig. 5.** Current distribution during fuel starvation 1) a) without pinholes, b) after the first perforation at the anode inlet (row 3/column 10, position 1), c) after the second perforation of the same segment (position 2) and d) after the additional perforation (row 3/column 1, position 3), 2) a) without pinholes, b) after the first perforation at position 4 (row 2/column 8) and c) after the additional perforation at position 5 (row 2/column 3) at the cathode inlet and 3) a) without pinholes, b) after the first perforation at position 6 (row 1/column 10) and c) after the additional perforation (row 1/column 1, position 7) at the cathode inlet.

#### 4.2.2. Gas crossover during starvation

The starvation cycles were clearly represented in the off-gas analyses (Fig. 6). The high amount of hydrogen detected in the anode off-gas analysis during the measurement was considered to be caused by the dead volume in the gas analysis unit and the low gas flow on the anode (Fig. 6, a and b). The peak width was also attributed to the gas flow rate. A high flow rate resulted in narrow peaks, as was observable in the cathode off-gas, whilst the anode off-gas exhibited wider peaks. During fuel starvation, hydrogen was completely consumed, resulting in an anode pressure drop, thus increasing the oxygen crossover. However, due to the higher cathode gas flow, the total oxygen crossover increased not only during the periods of fuel starvation, but also over the entire measurement (Fig. 6, b).

Traces of hydrogen could be detected in the cathode off-gas throughout the entire measurement period. During the starvation cycles prior to the first perforation, the hydrogen content was clearly reduced during the starvation period (Fig. 6, c). After perforation, however, the partial pressure of hydrogen in the cathode off-gas clearly increased during the starvation period, causing a more severe cell reversal (Fig. 6, d and Fig. 4, 1).

The traces of oxygen and hydrogen detected in the anode and the cathode off-gas, respectively, hinted towards gas cross-over. However, it is also possible for hydrogen and oxygen to be formed via electrolysis during the starvation periods. The anode potential may have risen to above 1.23 V locally, inducing electrochemical oxygen formation from water. This was not necessarily visible in the overall potential, but is unlikely, since the cell

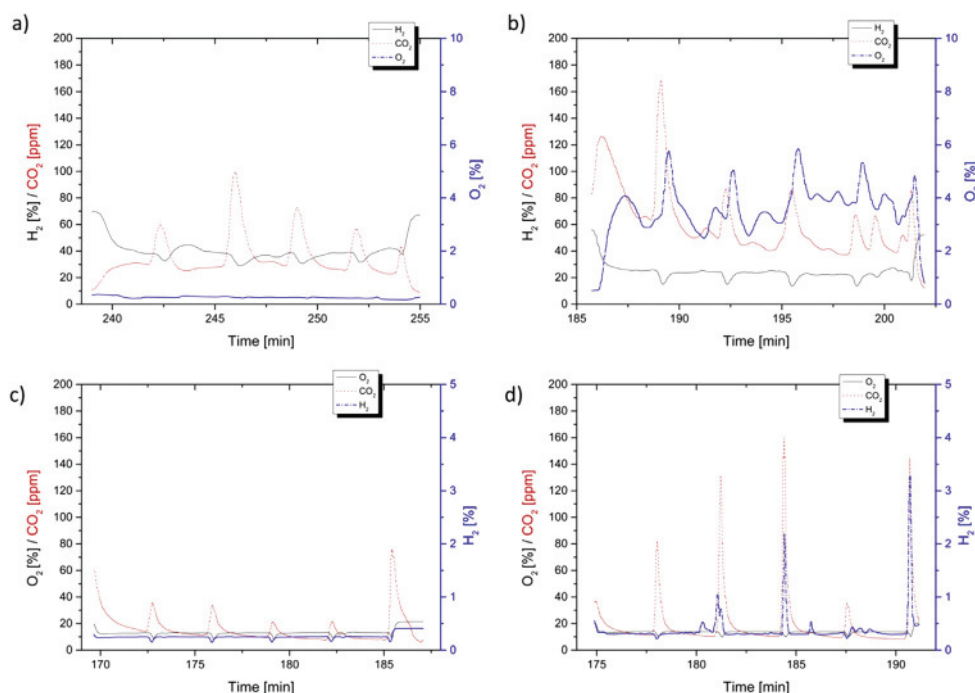


**Fig. 6.** Gas analysis of the anode off-gas with a) no pinhole, b) pinholes in the positions 1, 2 and 3 and the cathode off-gas with c) no pinhole and d) pinholes in the positions 1, 2 and 3.

potential reversal never exceeded  $-0.3$  V. Electrolysis was, therefore, highly improbable.

The introduction of a pinhole near the anode inlet caused increased hydrogen crossover and, therefore, a more severe fuel starvation. This is shown in Table 5 for the first three pinholes; however, neither clear verification nor contradiction of this process could be concluded for the middle section and the anode outlet. This is most likely due to the consumption of the crossed over hydrogen, which, therefore, was not measurable in the off gases. The crossed over hydrogen was immediately carried out for pinholes near the cathode outlet and, therefore, was not oxidised at the cathode catalyst.

The oxygen crossover to the anode flow is shown in Table 5. Due to an excessively high amount of oxygen in the hydrogen flow, the fuel starvation experiments conducted with the membrane electrode assembly that had a pinhole directly at the cathode inlet (position 7) had to be aborted.

A sharp increase of oxygen content in the anode off-gas was visible when pinholes were created in the positions 3 and 4. These represented the area close to the anode inlet. The pinhole at position 5 did not further increase the crossover, and even resulted in a decrease. This finding was unexpected, but can be potentially explained either by the existence of higher local temperatures, which resulted in a reduction of the size of the existing holes, or by the formation of liquid water from the direct oxidation of hydrogen, blocking the pinhole. When water is formed near the cathode inlet, it has to pass through the entire fuel cell, whilst it is removed

immediately when formed near the cathode outlet.

#### 4.2.3. Carbon emission

Whilst the carbon emission showed a stable rate for the first few pinholes, a sharp increase was visible after the perforation of the third hole and was also high when pinholes were introduced in the middle section (Table 5). When pinholes were created only in the anode outlet region, a small carbon emission rate was recorded. However, no data for the anode gas was available for the pinhole at position 7, since this experiment could not be completed due to safety issues. Therefore, the carbon emission appeared lower than it presumably would have been in this region.

The carbon emission rate correlated with the degree of cell reversal during starvation.

On average, the carbon emission rate was higher on the anode side. This is consistent with what has been reported in the literature, since the anode potential rises and carbon oxidation occurs [23].

#### 4.3. Fluoride emission

A connection between the location of pinholes and the fluoride emission rate is not evident and the fluoride content is stable in almost all samples. Compared to the initial fluoride emission, the overall fluoride content in the waste water decreased over time for the experiment in all cases (Fig. 7, 1).

Only for pinholes near the anode inlet and the middle section,

**Table 5**

Hydrogen content in the cathode flow, oxygen content in the anode flow and summarised carbon emission for both the anode and cathode during starvation, depending on the pinhole location, all normalised for the lowest value.

Pinhole location	0	1	1, 2	1, 2, 3	4	4, 5	6	6, 7
H <sub>2</sub> Crossover in Cathode Off-Gas Starvation	1.14	1.29	1.60	1.58	1.00	1.02	1.17	1.12
O <sub>2</sub> Crossover in Anode Off-Gas Starvation	1.30	1.48	1.18	24.10	20.43	3.20	1.00	–
Carbon Emission	3.25	3.12	3.29	6.15	7.02	4.32	1.82	1.00

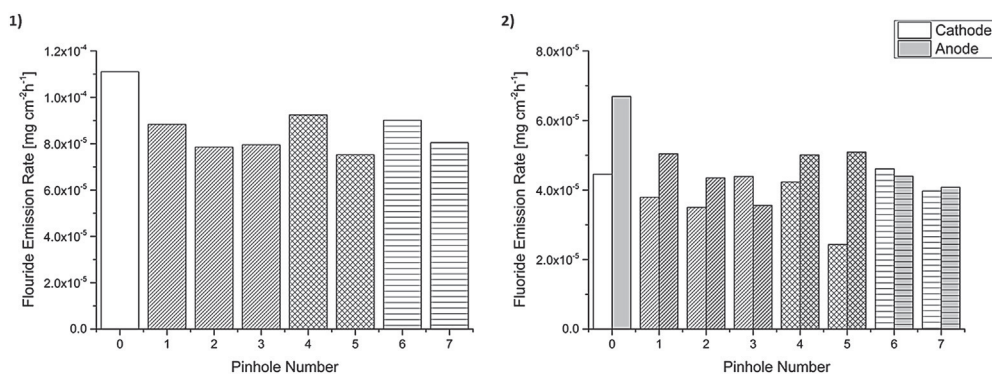


Fig. 7. Fluoride emission rate 1) without pinholes and for the pinholes near the anode inlet (1–3), in the middle section (4, 5) and near the cathode inlet (6, 7) and 2) different fluoride emission rates without pinholes and for the pinholes near the anode inlet (1–3), in the middle section (4, 5) and near the cathode inlet (6, 7) for anode and cathode.

increasing fluoride content was reported in the cathode waste water (Fig. 7, 2). However, in this case the amount of collected waste water was initially lower than usual, thus resulting in an extraordinarily low fluoride emission rate for the measurement prior to the first perforation.

Ignoring this value, the fluoride emission rate is decreasing over the time in all experiments, following a similar pattern. Therefore, the degradation pathway of the membrane backbone leading to HF formation appears not to be affected by pinholes and their location to a measurable extent at the set operation conditions. Measuring the total fluoride content appears advisable for future measurements, since membrane degradation is expected to be affected by gas crossover and raised temperatures.

#### 4.4. Computed tomography

The upper image was recorded in-plane, whilst the lower image in Fig. 8 shows the top down view on the perforated sample of the MEA.

Taken from the obtained pictures, the pinhole has a diameter of approximately  $200 \mu\text{m}$  at the most narrow and approximately  $450 \mu\text{m}$  at the widest point (taken from Fig. 8, upper image). Thus, the pinhole does get deformed. However, since the initial diameter is still persistent in plane of the membrane, it seems, that not the high temperature and the mechanical stress caused the deformation, but rather that it already occurred during perforation.

#### 4.5. Discussion

The effect of a pinhole on the various operation parameters strongly varies with its location, but is not the same for all fuel cell parameters. Defects near the cathode inlet have exhibited a less severe effect on the different degradation phenomena than pinholes in the middle section or near the anode inlet. The results of the effect of the different pinhole locations on the electrochemical parameters of a fuel cell are summarised in Table 6, whilst the non-electrochemical characteristics can be found in Table 7.

Pinholes near the cathode inlet only affected the OCV significantly. This effect could also derive from the higher stoichiometry on the cathode side and the even higher flow rate since air and not pure oxygen is used, though. In general, the immediate effect of pinholes on the OCV has been proven to be rather low, as was expected from the literature [10].

Performance decay was the highest at the anode inlet. However, for some results, even an improvement was exhibited at first, until a critical point was reached. For the anode inlet, the critical step was the perforation of the membrane at position 3. Since this

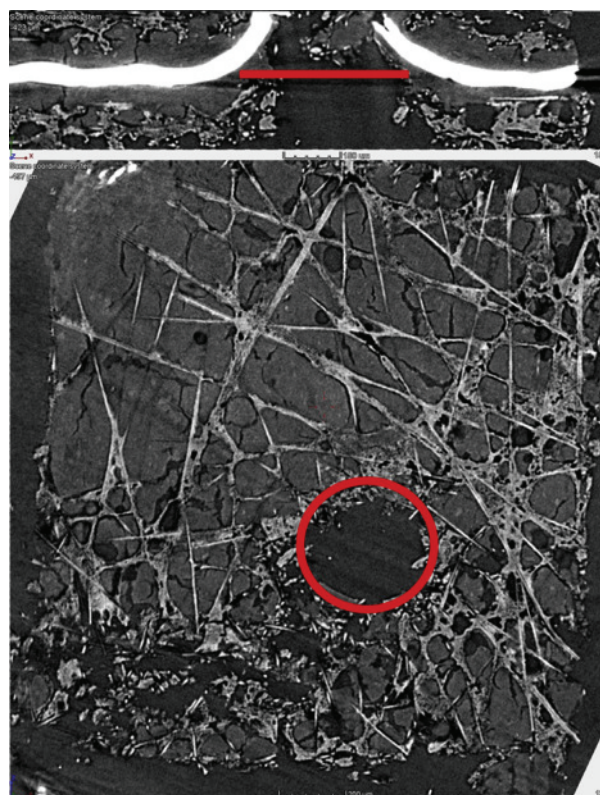


Fig. 8. Computed tomography of a pinhole at position 4.

particular pinhole did not show in the spatial visualisation of the current density during the hydrogen diffusion measurement (Fig. 3 d), it is likely that the reduced performance is not directly related to the additional perforation step and more to the growth of the pinholes at the positions 1 and 2 during the ongoing operation.

A decreasing membrane resistance for pinholes near the cathode inlet is an indicator for an improvement of the humidification after a longer period of operation. Water within the membrane is crucial for the proton conductivity. Thus, the increased water production due to reactant crossover will lead to a reduced membrane resistance. Near the middle section however, a slight increase of the resistance was evident. This is an indicator for membrane degradation. However, the information, which can be drawn from the fluoride emission rate, is vague. To obtain a deeper understanding of this process, it is advisable to measure the total fluorine emission in the future.

**Table 6**  
Summary of the effects of the pinhole location on different electrochemical characteristics.

	Anode inlet	Middle section	Cathode inlet
OCV	Mild decrease	Mild decrease	Stronger, but still mild decrease
Power density	Gain to intermediate loss	mild decrease	Gain to mild loss
Membrane resistance	Mildly alternating results	Mild increase	Mild decrease
H <sub>2</sub> diffusion current	Strongly alternating results	Vast increase	Vast increase
Loss of ECSA	Low to vast loss	Intermediate to vast loss	Low loss
Voltage drop during starvation	Cell reversal	Cell reversal	No cell reversal

**Table 7**  
Summary of the effect of the pinhole location on different non-electrochemical characteristics.

	Anode inlet	Middle section	Cathode inlet
H <sub>2</sub> crossover in cathode Off-gas diffusion measurement	Increasing from low to high content	Intermediate to low content	Low content
H <sub>2</sub> crossover in cathode Off-Gas	Increasing content	Low content	Stable intermediate content
O <sub>2</sub> crossover in anode Off-gas	Low content, sudden increase to high content	High content, decrease to low content	Low content
Carbon corrosion	Increasing high emission	High emission	Decreasing low emission
H <sub>2</sub> content in the cathode Off-gas during starvation	Increasing, but low H <sub>2</sub> content	Increasing, but low H <sub>2</sub> content	Low H <sub>2</sub> content
O <sub>2</sub> content in the anode off-gas during starvation	Low O <sub>2</sub> content, sudden increase to high content	High O <sub>2</sub> content, drop to low content	Low O <sub>2</sub> content
Carbon corrosion	Low to intermediate carbon corrosion	Intermediate to low carbon corrosion	Low carbon corrosion
Fluoride emission	Decreasing low emission	Decreasing low emission	Decreasing low emission

A high standard deviation was persistent in all hydrogen diffusion measurements. Temperature and humidity influence this parameter strongly and excessive amounts of hydrogen are purged out of the fuel cell in the cathode off-gas if the defects are located near the anode inlet. The hydrogen diffusion current can therefore not be used as a reliable indicator for membrane defects and an additional gas analysis is necessary.

The loss of active catalyst surface area was most severe when pinholes were created near the anode inlet and in the middle section. Platinum catalyst dissolution, agglomeration and redistribution are mainly driven by increased temperatures, which is consistent with the previously drawn conclusions [27]. Temperatures are expected to be increased near the defective area to an extent, at which they can have a significant impact on the fuel cell operation [33]. Another driving force is the loss of carbon support. Alike the loss of catalyst surface area, the carbon emission rate was the highest near the anode inlet and the middle section. A correlation between degradation and cell reversal during periods of fuel starvation was evident. However, since excessive carbon corrosion is reported at potentials exceeding 1 V [18], a value that never appeared in the overall cell potential, the local conditions might have been more diverse than assumed initially. However, since at potentials exceeding 1.2 V, CO is formed and can be detected in the cathode outlet [22], a potential above 1.23 V, as would be necessary for the formation of O<sub>2</sub> via electrolysis appears highly unlikely, since no CO was detected in the off-gas at any time. The formation of PtO at potentials above 1.1 V [29] is however plausible. The loss of active surface area and the potential drop during starvation correlate.

A connection between performance loss and oxygen detected in the anode gas stream was evident. This was however the strongest near the anode inlet and the middle section. After the implementation of the pinhole at position 7, the experiment had to be aborted due to too high oxygen content in the anode off-gas. An effect of this defect on the fuel cell operation was not confirmed by the mild performance decay reported in a previous measurement with a pinhole at the same location. The conclusion, which can be drawn from these results however is that, to a certain extent,

performance decay can be used as an indicator for oxygen crossover and vice-versa.

A correlation of hydrogen crossover and carbon corrosion was noticed. A connection with oxygen crossover and electrode degradation was however not evident.

## 5. Conclusion

The effect of pinholes at various locations on the degradation of the membrane has been investigated. Furthermore, the fuel cell was characterised and the impact of the induced defects on the chosen parameter was observed.

During the operation of a defective fuel cell, multiple different effects overlap. The crossover of hydrogen and oxygen, temperature and current distribution, as well as the humidity do interact, but a clear correlation was not always evident.

It can be concluded, that the effect which pinholes have on the fuel cell operation is the strongest near the anode inlet and the middle section. The higher hydrogen partial pressure results in an increase of the local temperatures for defects in this area. The unevenly increased temperature temporarily leads towards improved operation parameters, but a sudden drop occurs after a critical point is reached and the positive effect of the elevated temperature is exceeded by the negative effects of the defects, such as carbon corrosion and performance decay. Therefore, excessive crossover has to be avoided.

Many of the results support the conclusion that one of the major effects of membrane defects on fuel cell characteristics under operation conditions is an uneven temperature distribution rather than an increased membrane degradation rate due to hydrogen peroxide formation. The temperature is increased locally near the area of perforation. This accelerates the processes of carbon corrosion and platinum electrocatalyst agglomeration.

Contrary to what was expected, the increase of carbon corrosion was even stronger affected by the potential than by high local temperatures. The carbon oxidation rate is driven by cell reversal during starvation due to the rising anode potential. When pinholes were introduced near the cathode inlet, a small effect on fuel

starvation was observed, while pinholes introduced in the middle section showed an intermediate effect, and pinholes near the anode inlet induced a larger cell potential drop, resulting in a higher carbon emission rate. The cell reversal is also correlated to the loss of the cathode's active platinum surface area. Near the anode inlet, pinholes clearly contribute to the degradation rate of the carbon support and the Pt catalyst.

Under the chosen conditions, defects near the anode inlet show a significant acceleration of further degradation, whilst defects near the cathode inlet have only a small effect.

### Acknowledgement

The research leading to these results has received funding from the European Community's 7th Framework Programme for the Fuel Cells and Hydrogen Joint Technology Initiative, Grant Agreement no 621216.

Also, the authors would like to thank Dietmar Salaberger (Upper Austria University of Applied Sciences) for the CT Scans.

### References

- [1] G. Cipriani, V. Di Dio, F. Genduso, D. La Cascia, R. Liga, R. Miceli, et al., Perspective on hydrogen energy carrier and its automotive applications, *Int. J. Hydrogen Energy* (2014) 1–13.
- [2] M. Bodner, A. Hofer, V. Hacker, H<sub>2</sub> generation from alkaline electrolyzer, *Wiley Interdiscip. Rev. Energy Environ.* 4 (2015) 365–381.
- [3] M. Gandiglio, A. Lanzini, M. Santarelli, P. Leone, Design and optimization of a proton exchange membrane fuel cell CHP system for residential use, *Energy Build.* 69 (2014) 381–393.
- [4] O.Z. Sharaf, M.F. Orhan, An overview of fuel cell technology: fundamentals and applications, *Renew. Sustain Energy Rev.* 32 (2014) 810–853.
- [5] S. Zhang, X. Yuan, H. Wang, W. Merida, H. Zhu, J. Shen, et al., A review of accelerated stress tests of MEA durability in PEM fuel cells, *Int. J. Hydrog. Energy* 34 (2009) 388–404.
- [6] S. Kundu, M.W. Fowler, L.C. Simon, R. Abouattallah, N. Beydokhti, Degradation analysis and modeling of reinforced catalyst coated membranes operated under OCV conditions, *J. Power Sources* 183 (2008) 619–628.
- [7] K. Panha, M. Fowler, X.-Z. Yuan, H. Wang, Accelerated durability testing via reactants relative humidity cycling on PEM fuel cells, *Appl. Energy* 93 (2012) 90–97.
- [8] T.V. Reshetenko, G. Bender, K. Bethune, R. Rocheleau, Application of a segmented cell setup to detect pinhole and catalyst loading defects in proton exchange membrane fuel cells, *Electrochim Acta* 76 (2012) 16–25.
- [9] Y.-H. Cho, H.-S. Park, J.-H. Kim, Y.-H. Cho, S. Won Cha, Y.-E. Sung, The operation characteristics of MEAs with pinholes for polymer electrolyte membrane fuel cells, *Electrochim Acta* 11 (2008) B153.
- [10] B.T. Huang, Y. Chatillon, C. Bonnet, F. Lapique, S. Leclerc, M. Hinaje, et al., Experimental investigation of pinhole effect on MEA/cell aging in PEMFC, *Int. J. Hydrogen Energy* 38 (2013) 543–550.
- [11] A. Pozio, R.F. Silva, M. De Francesco, L. Giorgi, Nafion degradation in PEFCs from end plate iron contamination, *Electrochim Acta* 48 (2003) 1543–1549.
- [12] V.O. Mittal, H. Russell Kunz, J.M. Fenton, Is H<sub>2</sub>O<sub>2</sub> involved in the membrane degradation mechanism in PEMFC? *Electrochim Solid State Lett.* 9 (2006) A299.
- [13] M. Inaba, T. Kinumoto, M. Kiriake, R. Umabayashi, A. Tasaka, Z. Ogumi, Gas crossover and membrane degradation in polymer electrolyte fuel cells, *Electrochim Acta* 51 (2006) 5746–5753.
- [14] A.B. LaConti, M. Hamdan, R.C. McDonald, Mechanisms of membrane degradation, in: W. Vielstich, A. Lamm, H.A. Gasteiger (Eds.), *Handb. Fuel Cells Fundam. Technol. Appl.* 3, John Wiley & Sons, Inc, Chichester, Sussex, 2003, pp. 647–662.
- [15] F.D. Coms, The chemistry of fuel cell membrane chemical degradation, *ECS, ECS Trans.* 16 (2008) 235–255.
- [16] T. Aarhaug, A. Svensson, Degradation rates of PEM fuel cells running at open circuit voltage, *ECS Trans.* 3 (2006) 775–780.
- [17] S. Samms, S. Wasmus, R. Savinell, Thermal stability of nafion® in simulated fuel cell environments, *J. Electrochem ...* 143 (1996) 1498–1504.
- [18] N. Linse, L. Gubler, G.G. Scherer, A. Wokaun, The effect of platinum on carbon corrosion behavior in polymer electrolyte fuel cells, *Electrochim Acta* 56 (2011) 7541–7549.
- [19] M. Cai, M.S. Ruthkosky, B. Merzougui, S. Swathirajan, M.P. Balogh, S.H. Oh, Investigation of thermal and electrochemical degradation of fuel cell catalysts, *J. Power Sources* 160 (2006) 977–986.
- [20] S. Zhang, X.-Z. Yuan, J.N.C. Hin, H. Wang, K.A. Friedrich, M. Schulze, A review of platinum-based catalyst layer degradation in proton exchange membrane fuel cells, *J. Power Sources* 194 (2009) 588–600.
- [21] W.R. Baumgartner, P. Parz, S.D. Fraser, E. Wallnöfer, V. Hacker, Polarization study of a PEMFC with four reference electrodes at hydrogen starvation conditions, *J. Power Sources* 182 (2008) 413–421.
- [22] J. Kim, J. Lee, Y. Tak, Relationship between carbon corrosion and positive electrode potential in a proton-exchange membrane fuel cell during start/stop operation, *J. Power Sources* 192 (2009) 674–678.
- [23] D. Liang, Q. Shen, M. Hou, Z. Shao, B. Yi, Study of the cell reversal process of large area proton exchange membrane fuel cells under fuel starvation, *J. Power Sources* 194 (2009) 847–853.
- [24] Y. Takagi, S. Okada, Y. Sato, Characteristics of electrode potential behavior and degradation under hydrogen-starved operation in PEFC, in: 208th ECS Meet, 2005, p. 550.
- [25] Y. Takagi, Y. Sato, Z. Wang, Effect of anode catalyst support on degradation of MEA caused by hydrogen starvation operation in PEFC, in: 210th ECS Meet, 2006, p. 2.
- [26] X. Yu, S. Ye, Recent advances in activity and durability enhancement of Pt/C catalytic cathode in PEMFC, *J. Power Sources* 172 (2007) 133–144.
- [27] R.L. Borup, J.R. Davey, F.H. Garzon, D.L. Wood, Inbody M a. PEM fuel cell electrocatalyst durability measurements, *J. Power Sources* 163 (2006) 76–81.
- [28] H. Angerstein-Kozłowska, B.E. Conway, W.B.A. Sharp, The realcondition of electrochemically oxidised platinum surfaces, *Electroanal. Chem. Interfacial Electrochem* 43 (1973) 9–36.
- [29] Y. Shao-Horn, W.C. Sheng, S. Chen, P.J. Ferreira, E.F. Holby, D. Morgan, Instability of supported platinum nanoparticles in low-temperature fuel cells, *Top. Catal.* 46 (2007) 285–305.
- [30] T.T.H. Cheng, E. Rogers, A.P. Young, S. Ye, V. Colbow, S. Wessel, Effects of crossover hydrogen on platinum dissolution and agglomeration, *J. Power Sources* 196 (2011) 7985–7988.
- [31] K. Yasuda, A. Taniguchi, T. Akita, T. Ioroi, Z. Siroma, Platinum dissolution and deposition in the polymer electrolyte membrane of a PEM fuel cell as studied by potential cycling, *Phys. Chem. Chem. Phys.* 8 (2006) 746–752.
- [32] T. Akita, A. Taniguchi, J. Maekawa, Z. Siroma, K. Tanaka, M. Kohyama, et al., Analytical TEM study of Pt particle deposition in the proton-exchange membrane of a membrane-electrode-assembly, *J. Power Sources* 159 (2006) 461–467.
- [33] S. Kreitmeyer, P. Lerch, A. Wokaun, F.N. Buchi, Local degradation at membrane defects in polymer electrolyte fuel cells, *J. Electrochem Soc.* 160 (2013) F456–F463.
- [34] G. De Moor, C. Bas, N. Charvin, E. Moukheiber, F. Niepceon, N. Breilly, et al., Understanding membrane failure in PEMFC: comparison of diagnostic tools at different observation scales, *Fuel Cells* 12 (2012) 356–364.
- [35] C. Lim, L. Ghassemzadeh, F. Van Hove, M. Lauritzen, J. Kolodziej, G.G. Wang, et al., Membrane degradation during combined chemical and mechanical accelerated stress testing of polymer electrolyte fuel cells, *J. Power Sources* 257 (2014) 102–110.
- [36] C. Grimmer, S. Nestl, J. Senn, V. Hacker, Selective real-time quantification of hydrogen within mixtures of gases via an electrochemical method, *Int. J. Hydrogen Energy* 40 (2015) 2055–2061.

#### 16.4. Air Starvation induced Degradation in Polymer Electrolyte Fuel Cells.

*Bodner M, Schenk A, Salaberger D, Rami M, Hochenauer C, Hacker V. **Air Starvation induced Degradation in Polymer Electrolyte Fuel Cells.** Fuel Cells 2017;17:18–26.*

##### *Contribution:*

The cathode gas flow rate was cycled to induce air starvation in a polymer electrolyte fuel cell. Dr. Alexander Schenk contributed to the writing process. Mija Rami, BSc determined the fluoride emission rate and contributed to the respective part. Dipl.-Ing. Dietmar Salaberger and Prof. Christoph Hochenauer provided X-ray computed tomography measurements and contributed to the respective part. Prof. Viktor Hacker advised in all aspects.

Two different tests were conducted. By cycling the cathode gas flow rate, oxygen starvation was induced. In the respective tests, the duration of the starvation interval was varied. The off-gas composition, fluoride emission rate and electrochemical parameters were monitored. Short cathode supply interruption exhibited a positive effect on the fuel cell performance. Extensive cycling, however, resulted in highly uneven operation conditions and thus locally accelerated degradation rates.



# Air Starvation Induced Degradation in Polymer Electrolyte Fuel Cells

M. Bodner<sup>1\*</sup>, A. Schenk<sup>1</sup>, D. Salaberger<sup>2</sup>, M. Rami<sup>1</sup>, C. Hochenauer<sup>3</sup>, V. Hacker<sup>1</sup>

<sup>1</sup> Graz University of Technology, Institute of Chemical Engineering and Environmental Technology, NAWI Graz, Inffeldgasse 25/C, 8010 Graz, Austria

<sup>2</sup> University of Applied Sciences, Wels Campus, Stelzhamerstrasse 23, 4600 Wels, Austria

<sup>3</sup> Graz University of Technology, Institute of Thermal Engineering, Inffeldgasse 25/B, 8010 Graz, Austria

Received: August 03, 2016; accepted January 13, 2017; published online ■■■

## Abstract

While hydrogen starvation in fuel cells is intensely investigated and strategies for avoidance have been developed, almost no data are available for other unexpected events, such as malfunction of the air supply. In this study we induce oxygen starvation in a manner closer to failure in real systems than commonly applied accelerated stress tests.

By cycling the cathode gas flow, two accelerated stress tests were introduced; simulating short periods of air starvation with duration of either 10 or 60 seconds. Short cathode under-supply does not lead to fuel cell failure. Air starvation results in a voltage drop and hydrogen evolution. This is accompanied by the reduction of platinum oxides in the respective areas, which leads to an improvement of the active catalyst

surface area. After extensive cycling, degradation becomes the dominant effect. X-ray computed tomography is used to visualize the change of the catalyst particle size and distribution in dependence on the location in the fuel cell. Throughout the experiments, a total voltage decay rate of  $1.427 \text{ mV h}^{-1}$ , a total fluoride emission rate of  $0.0031 \mu\text{mol h}^{-1} \text{ cm}^{-2}$  and severe current and temperature gradients during starvation were observed, leading to an inhomogeneous agglomeration of the platinum electrocatalyst.

**Keywords:** Accelerated Stress Test, Air Starvation, Degradation, Hydrogen Evolution Reaction, Platinum Agglomeration, Polymer Electrolyte Fuel Cell, X-ray Computed Tomography

## 1 Introduction

Polymer electrolyte fuel cells (PEMFCs) convert hydrogen into water and electricity at high efficiencies and are therefore considered fundamental for a sustainable future [1–3]. However, different types of degradation, such as decomposition of the membrane, oxidation of the electrode support or loss of catalyst surface area and their effect on fuel cell operation [4], are still under investigation in order to prolong the operational life.

### 1.1 Fuel Cell Degradation

Membrane durability is limited by chemical and mechanical degradation. In the case of chemical degradation, hydroxyl or peroxy radicals can attack residual terminal H-groups at the end group site. This initiates further decomposition, leading to the release of HF, which can be detected in the fuel cell effluent water. Improvement of the chemical structure of the polymer electrolyte has significantly reduced the fluoride

emission rate (FER), as the number of reactive end groups has been reduced. The radical formation depends on the presence of both hydrogen and oxygen at the same site and thus is a function of gas crossover. Mechanical failure, e.g., formation of cracks or pinholes, on the other hand is caused by non-uniform contact pressure, high differential gas pressure or stresses due to changing temperature or humidity. The membrane's resistivity towards the formation of cracks or pinholes has however been improved significantly by reinforcing the membrane [5].

Within the fuel cell electrodes, the platinum catalyst, carbon support, and the Teflon binder can undergo degradation. This is driven by increased temperature and potential.

One of the major degradation issues is the dissolution of platinum and thus loss thereof. At potentials above  $0.85 \text{ V}$  versus the reversible hydrogen electrode (RHE) and  $80^\circ\text{C}$ , how-

[\*] Corresponding author, [merit.bodner@tugraz.at](mailto:merit.bodner@tugraz.at)

ever, an oxide film is formed on the catalyst surface, reducing the dissolution rate beyond expectation. This indicates the formation of a protective layer atop of the metal surface. This is also confirmed by surface X-ray scattering. Platinum oxides can, other than platinum lost due to dissolution, be reactivated by reduction during potential cycling. This then again enables dissolution of platinum, which is then either lost or redeposited into larger particles, lowering the surface energy and resulting in a decreased active catalyst surface area [5].

When the carbon is oxidized, the electrode loses the hydrophobic character as carbon surface oxides are formed. In the presence of platinum, carbon can also be further oxidized to carbon dioxide, which is then inevitably lost resulting in a loss of electric conductivity within the electrode. Degradation of the polytetrafluoroethylene (PTFE) binder also results in a decreased hydrophobicity and thus worsening the water transport mechanism [5]. Flooding can then lead to reactant starvation on both anode and cathode and thus depolarizing the fuel cell [6, 7].

### 1.2 Accelerated Stress Tests

Amongst the various harmful operation conditions, some are avoidable after identification, yet others are too intrinsic for sustainable operation, such as dead end operation, that strategies for degradation mitigation are required [7–9]. Either way, obtaining a fundamental understanding of the respective mechanism is necessary. This is mostly done by material testing. However, in order to understand real life degradation of fuel cells, accelerated stress tests (ASTs), which are simulating real failure modes, are necessary.

A fast adaptability of the gas flows is essential for operation in automotive applications with alternating and hardly predictable load conditions. Since hydrogen is fed at a lower stoichiometry to ascertain high fuel efficiency, anode starvation is an issue [10, 11]. For stationary applications, however, the fuel cell can be operated in a steady load point, benefiting the lifetime. Critical events, such as hydrogen starvation [12], have been intensely investigated and widely understood. Therefore, less obvious events, such as malfunctioning of the air supply, are now of interest [13, 14].

### 1.3 Air Starvation

During normal operation in a polymer electrolyte fuel cell, the hydrogen oxidation reaction (HOR) and the oxygen reduction reaction (ORR) take place on the anode and the cathode according to Eq. (1) and Eq. (2), respectively. At low oxygen stoichiometry, the current is limited by the oxygen reduction reaction. If the current exceeds said value, the cathode potential drops sharply and the cell voltage decreases. At very low cathode potentials, a second electrochemical process, the hydrogen evolution reaction (HER) or proton reduction reaction (PRR) occurs (Eq. (3)). Protons are reduced to molecular hydrogen at the cathode, which can be detected in the off-gas. The current density thus increases again with decreasing

potential, leading to a so-called “comma shaped” polarization curve in the respective areas [15].



As there is still oxygen supplied to the areas near the cathode inlet, a gradient is induced. The current density decreases from the air inlet towards the outlet and the comma shape becomes more pronounced [15]. This is due to the different reactions, taking place in the different compartments. At a low cathode stoichiometry, voltage oscillations occur during galvanostatic operation, caused by the low inlet flux. Also, the cathode active layer temperature increases at the air inlet, leading to an accelerated membrane electrode assembly (MEA) degradation in this area [13]. An increased temperature induces platinum agglomeration [16]. This temperature gradient is even more pronounced, since a reduction of temperature has been noted in the middle of the fuel cell and near the cathode outlet by Dou et al. [17]. They speculate that this is attributed to the proton reduction reaction, taking place in the areas of decreasing temperature.

Oxygen starvation (OS) was, to our knowledge, so far only induced by either a steady low air flow [17–19] or load cycling at steady air flow [13]. Especially during load cycling, multiple effects overlap. The hydrogen stoichiometry has to either be extraordinarily high, or anode starvation effects contribute to the fuel cell behavior. Therefore, an AST in which the cathode stoichiometry was cycled by changing cathode flow rates is proposed in this work, portraying cathode supply malfunction more realistically and minimizing overlapping effects.

## 2 Experimental

A square 25 cm<sup>2</sup> single cell with an MEA for stationary applications (IRD A/S, Odense, Denmark) and an S++ current scan shunt device (S++ Simulation Services, Murnau-Westried, Germany) with 10×10 segments for current and 5×5 segments for temperature measurement was used for fuel cell operation. The fuel cell was operated in pseudo-co-flow with a single channel flow pattern and identical flow plates on both anode and cathode (Figure 1).

The temperature of the fuel cell was maintained at 65 °C and no back pressure was applied. The anode was supplied with pure hydrogen and the cathode with synthetic air, respectively. Both gases were fed with a relative humidity of 80%.

### 2.1 Electrochemical Characterization

The performance was determined from polarization curves, the membrane resistance by electrochemical impedance spec-

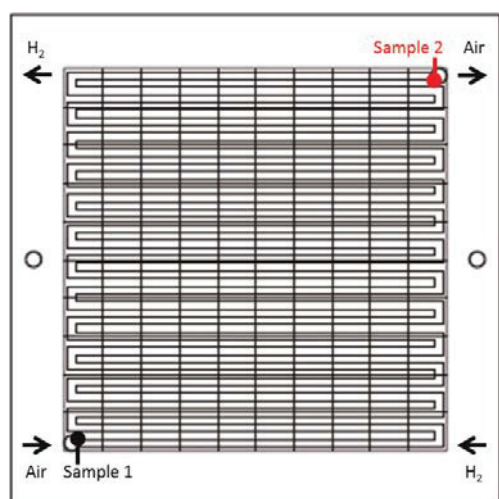


Fig. 1 Cathode flow plate of the segmented single cell with  $10 \times 10$  segments for current measurement and the samples taken for X-ray computed tomography measurements.

troscopy, the hydrogen diffusion current by linear sweep voltammetry and the cathode electrochemical surface area by cyclic voltammetry. All measurements were performed at the beginning (BoT) as well as at the end of testing (EoT) and conducted as has been reported previously [4,20] using a IM6 potentiostat with an additional PP240 load (both ZAHNER-elektrik GmbH & Co. KG, Kronach, Germany).

## 2.2 Accelerated Stress Test Development

The anode stoichiometry was held at 1.5 at a current density of  $0.5 \text{ A cm}^{-2}$ . Two different testing protocols were conducted. At first, the cathode stoichiometry was held at 2 for 3,590 s, followed by 10 s with a reduced stoichiometry of 0.9. In a second test, the same MEA was held at a stoichiometry of 2 for 3,540 s and at 0.9 for 60 s, respectively (Figure 2). Check valves prevent gases from being drawn back into the fuel cell during fluctuating pressures caused by starvation [4]. One full accelerated stress test consisted of 100 cycles or 100 h of testing. Both ASTs were performed consecutively with the same membrane electrode assembly. In between testing, the cell was purged with nitrogen on both anode and cathode until the

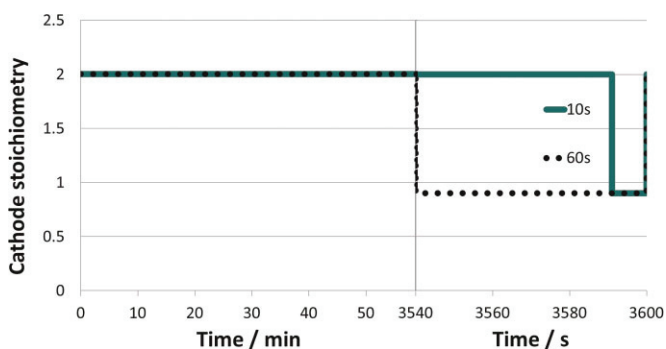


Fig. 2 ASTs with 10 and 60 seconds of air starvation each cycle.

voltage dropped to zero. The fuel cell was then stored at room temperature under nitrogen atmosphere overnight. The entire procedure was repeated with a pristine membrane electrode assembly for verification.

## 2.3 Fluoride Emission Rate

The effluent water was collected for further analysis [20,21]. A fluoride ion selective electrode (ISE) (9609BNWP from Thermo Fisher Scientific, Waltham, MA USA) was used to detect fluoride ions. With knowledge of the total amount of effluent water, the fluoride emission rate was determined.

## 2.4 Off-Gas Analysis

The anode and cathode off-gases were analyzed, as described previously [4,22], in a continuous gas analyzer (ABB Automation Products GmbH). The content of CO and CO<sub>2</sub> is analyzed with an Uras 14, hydrogen with a Caldos 17 and oxygen with a Magnos 106 unit. Yet, due to large gas volumes in the detectors and alternating flow rates, data should only be used comparative as a reliable quantification is not possible. The carbon corrosion and the hydrogen formation can, however be detected by measuring the content of carbon oxides and hydrogen in the off-gas.

## 2.5 Computed Tomography

Two samples with a diameter of 2 mm were characterized using X-ray micro computed tomography (X $\mu$ CT), from the areas indicated in Figure 1.

The X-ray computed tomography scans were performed at a laboratory  $\mu$ CT device Nanotom 180NF (GE phoenix | X-ray, Wunstorf, Germany). Since a matrix detector (Hamamatsu  $2,300 \times 2,300$  pixels) was used, the system worked in cone beam geometry [23]. The voxel size was set to  $1.3 \mu\text{m}$  edge length, which lead to a scan volume of  $(2.6 \text{ mm})^3$ .

The X-ray source parameters voltage (U) and current (I) were optimized for the material system to achieve optimal contrast and resolution. The integration time of 1,000 ms and 1,700 projections lead to a total scan time of 170 minutes.

## 3 Results and Discussion

### 3.1 Cathode Stoichiometry Cycling

The average voltage decay rate was  $0.309 \text{ mV h}^{-1}$  for the accelerated stress test with a starvation period of 10 s. For the 60 s of starvation AST the decay rate was  $2.682 \text{ mV h}^{-1}$  giving an overall voltage decay rate of  $1.427 \text{ mV h}^{-1}$  over the testing time of 200 h and both accelerated stress tests.

During the AST with starvation intervals of 10 s voltage drops were only noted occasionally (Figure 3a), whereas the voltage dropped to zero and below during almost every starvation interval in the accelerated stress test with 60 s of air starvation (Figure 3b). During the short starvation interval, the

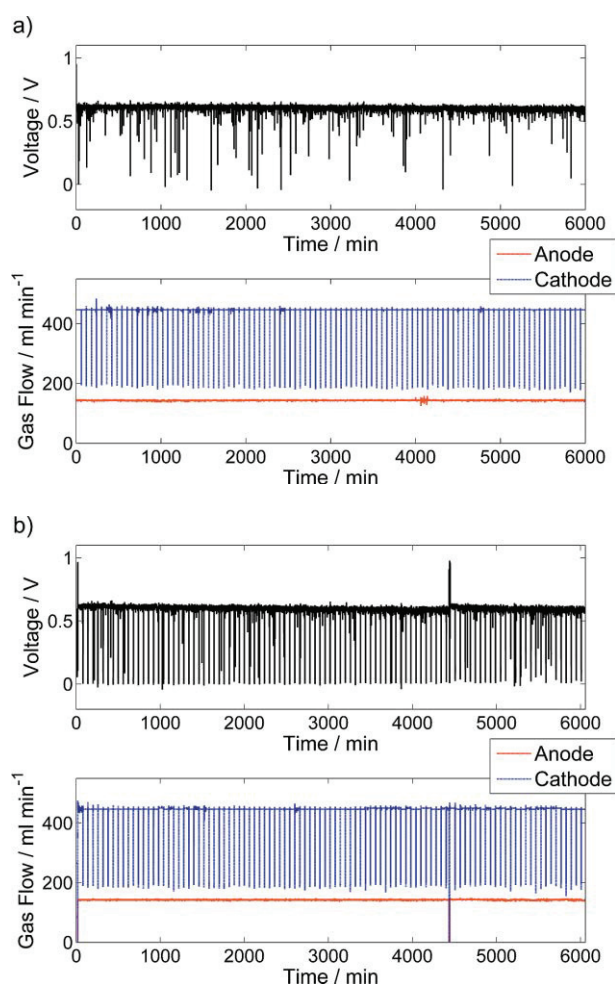


Fig. 3 Voltage and gas flow rates for 10 seconds starvation AST (a) and for 60 seconds starvation AST (b); for 100 hours each.

air present in the gas-phase within the fuel cell and the gas lining is sufficient to provide additional oxygen, thus sustaining the fuel cell voltage. A slight fluctuation of the mass flow controllers and the back pressure due to droplet formation cannot be avoided completely, resulting in the observed infrequent voltage behavior. In case of the longer air starvation periods, the voltage decreases during the 60 s of reduced air flow until all oxygen is consumed and a maximum gradient of current and temperature distribution is noted. The voltage reaches a steady minimum, slightly below zero.

The current distribution during starvation intervals of 10 s (Figure 4a) and 60 s (Figure 5a) show how the gradient is enforced with a longer duration of starvation. The same trend can be seen in the temperature distribution for the 10 s AST (Figure 4b) and the 60 s AST (Figure 5b).

For both accelerated stress tests, the pattern and the gradient between the highest and the lowest value barely change between the first and the last air starvation cycle (Figures 4 and 5). Only for the 10 s test, the temperature distribution shows a more distinguished front of increased temperature near the cathode inlet and along the flow channel for the last cycle.

### 3.2 Electrochemical Parameters

The mean values of the electrochemical parameters are listed in Table 1. After the 100 cycles with 10 s of cathode starvation, an improved performance is noted. After refreshment under nitrogen atmosphere on both sides and additional 100 cycles with 60 s of cathode starvation, the performance declined. The electrochemical surface area of the cathode catalyst follows a similar pattern (Figure 6a and b).

During OS, not only protons, but also platinum oxides are reduced on the cathode and thus the active cathode catalyst surface area and performance are increased. However, with continuous cycling, degradation exceeds the positive effect and thus both values decline.

The membrane resistance and hydrogen diffusion current both decline or remain more or less stable over time. For the fuel cell operation, this represents a benefit.

### 3.3 Membrane Degradation

The fluoride emission rate is an indicator for membrane degradation and used to determine the chemical decomposition of the polymer electrolyte.

The results (Figure 7) show that the amount of fluoride emitted is higher on the anode than on the cathode for both accelerated stress tests. The fluoride emission rate declines with time. Thus, the amount of fluoride detected in the effluent water from the AST with 60 s of cathode starvation is with a total of  $0.0026 \mu\text{mol h}^{-1} \text{cm}^{-2}$  lower than for the AST with 10 s of starvation with  $0.0037 \mu\text{mol h}^{-1} \text{cm}^{-2}$ , giving an average fluoride emission rate of  $0.0031 \mu\text{mol h}^{-1} \text{cm}^{-2}$ . This is within the range of reported fluoride emission rates [20].

### 3.4 Electrode Degradation

The primary factors, used to determine the electrode degradation, are carbon corrosion of the electrode support and loss of active electrocatalyst surface area. The latter is predominantly caused by agglomeration of the platinum nanoparticles.

#### 3.4.1 Carbon Corrosion

The data from the gas analyses are shown in Figure 8 for both (a and c) anode and (b and d) cathode during the 100 cycles of the AST with (a and b) the 10 and (b and c) the 60 s of

Table 1 Electrochemical characteristics before and after cathode stoichiometry cycling.

	10s Cycle		60s Cycle	
	BoT	EoT	BoT	EoT
Power Density / $\text{mW cm}^{-2}$	293.2	322.1	318.7	316.8
Membrane Resistance / $\text{m}\Omega$	8.771	8.807	8.541	8.839
Hydrogen Diffusion Current / $\text{mA cm}^{-2}$	0.909	0.764	0.755	0.675
Cathode Electrochemical Surface Area / $\text{m}^2 \text{g}^{-1}$	42.46	46.62	46.06	44.13

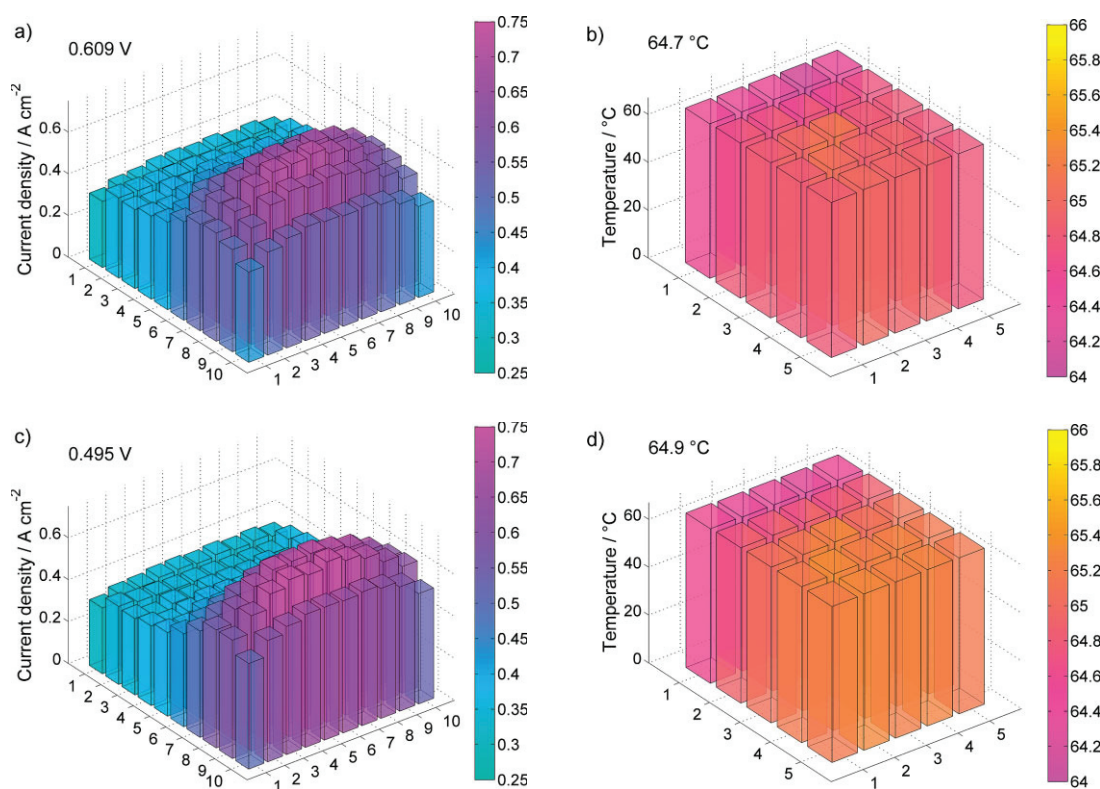


Fig. 4 Current (a and c) and temperature (b and d) distribution of the single cell during the first (a and b) and the 100th (c and d) 10 seconds OS interval.

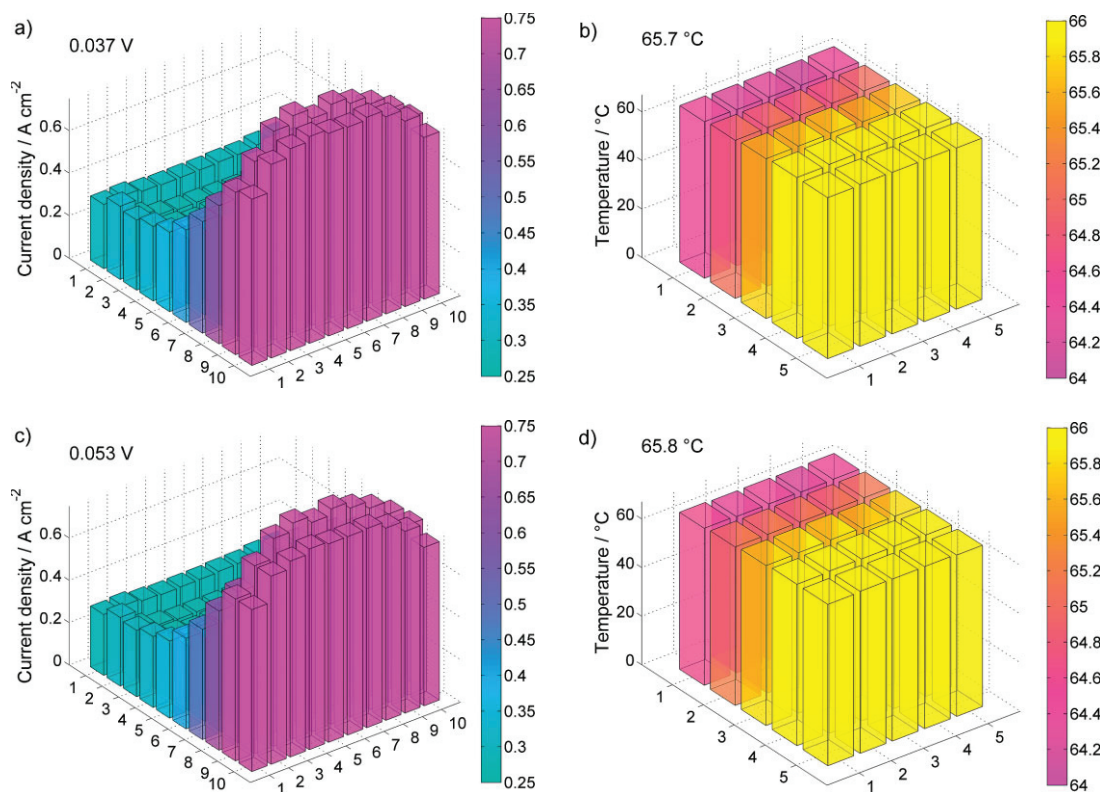


Fig. 5 Current (a and c) and temperature (b and d) distribution of the single cell during the first (a and b) and the 100th (c and d) 60 seconds OS interval.

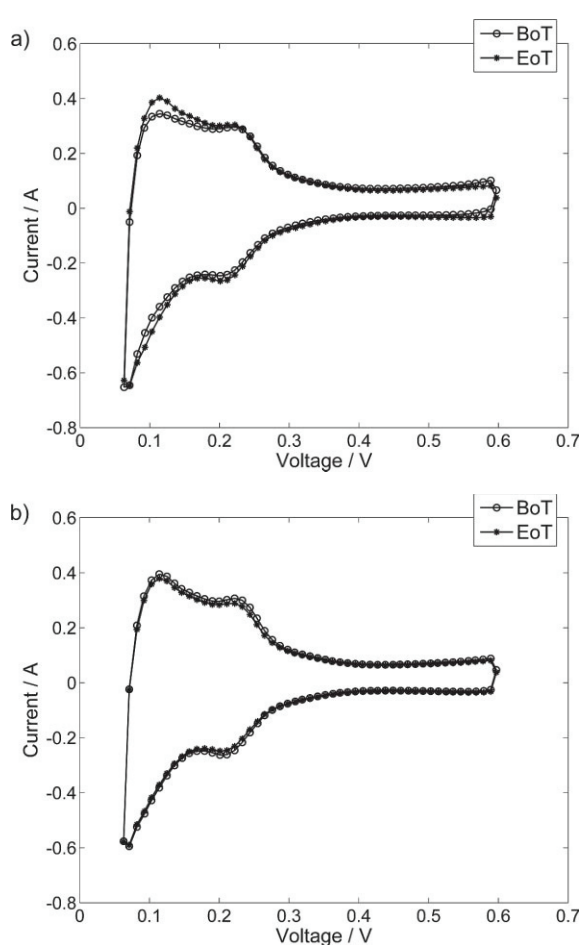


Fig. 6 Cyclic voltammety at the beginning and the end of testing for the 10 seconds AST (a) and the 60 seconds AST (b).

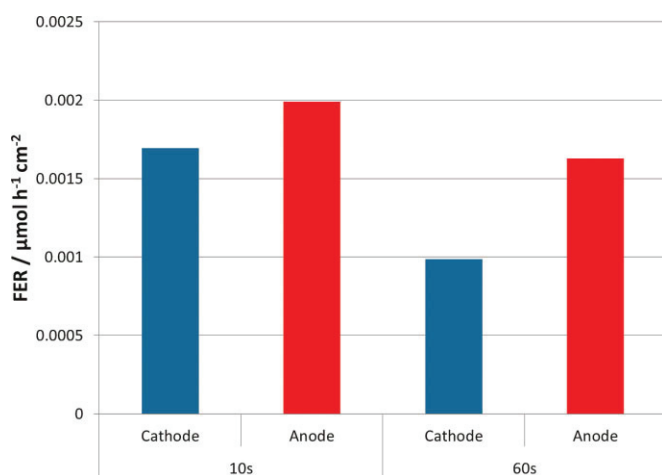


Fig. 7 Fluoride emission rates for both ASTs for anode and cathode.

air starvation. Typically, higher carbon content was registered in the exhaust of the anode side due to the generally higher cathode gas flow. The lower carbon content in the cathode exhaust is not only a result of the higher flow rate that is used, it is also assigned to the composition of air. As air consists of

79% nitrogen the gaseous (carbonaceous) degradation products are diluted in the exhaust stream. Same is also expected to be the reason for the relatively high oxygen content on the anode. This is, however, steady during operation and thus not affected by the accelerated stress test. In the cathode off-gas however, hydrogen peaks were observed, correlating with the voltage drops during 10 s of stoichiometry cycling. This is due to the PRR, taking place on the cathode in areas of air starvation.

In case of the 60 s starvation interval accelerated stress test, more hydrogen was detected in the cathode off-gas. This is in clear correlation to the potential drop and therefore in agreement with the outcome expected from what has been reported by Zamel et al. [15]. Despite the lack of oxygen, the current did not decrease during starvation periods, thus a reduction reaction other than that of oxygen had to take place. The detection of hydrogen in the cathode off-gas during air starvation and that the hydrogen diffusion current is not increased (Table 1), as this would indicate crossover, allows assuming that protons are reduced near the cathode outlet instead of oxygen.

### 3.4.2 Pt Agglomeration

During normal operation, the current and temperature distribution is compared before and after the respective ASTs (Figure 9a–d). It is shown that the current decreases in the area closer to the cathode inlet and increases near the outlet. This trend is, however, less pronounced than one would expect. The temperature distribution shows a similar, yet not identical pattern. In previous experiments, similar ASTs were conducted in which the cathode supply was shut off completely in some cases [22]. There, the effect on the electrochemical parameters was less severe, however the gradient was more distinguished.

Both anode and cathode show similar rates of Pt electrocatalyst agglomeration during air starvation cycling in Figure 10a, which represents the results of the computed tomography of sample 1 (as seen in Figure 1) that was taken near the cathode inlet. The cross-section of the membrane electrode assembly reveals areas without platinum as well as areas with larger particles/agglomerates on both sides. In contrast, Figure 10b shows the results of sample 2 (as seen in Figure 1), which was taken near the cathode outlet of the very same membrane electrode assembly. There, as indicated with arrows in Figure 10, the cathode shows a more homogeneous Pt electrocatalyst film and almost no areas of thinning. In this sample, the anode shows a similar if not more inhomogeneous catalyst distribution compared to the anode in the sample from near the cathode inlet. Thus, platinum agglomerates on the cathode side are more frequent near the air inlet. Near the air outlet, agglomeration is inhibited on the cathode by the presence of hydrogen, formed in the areas of oxygen starvation. A change in structure of the electrode support material was not clearly evident from the computed tomography scans.

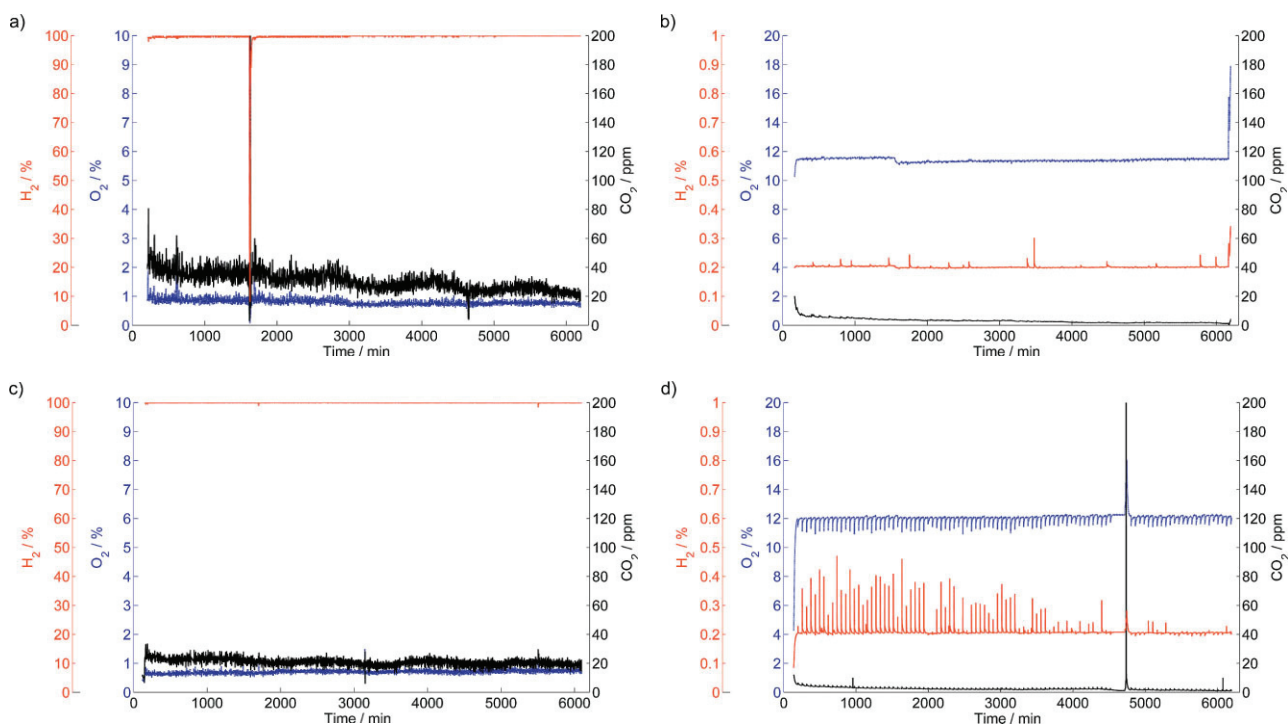


Fig. 8 Gas analysis of the 100 cycles of the 10 seconds starvation AST of the anode (a) and the cathode (b) off-gas and the 100 cycles of the 60 seconds starvation AST of the anode (c) and the cathode (d) off-gas.

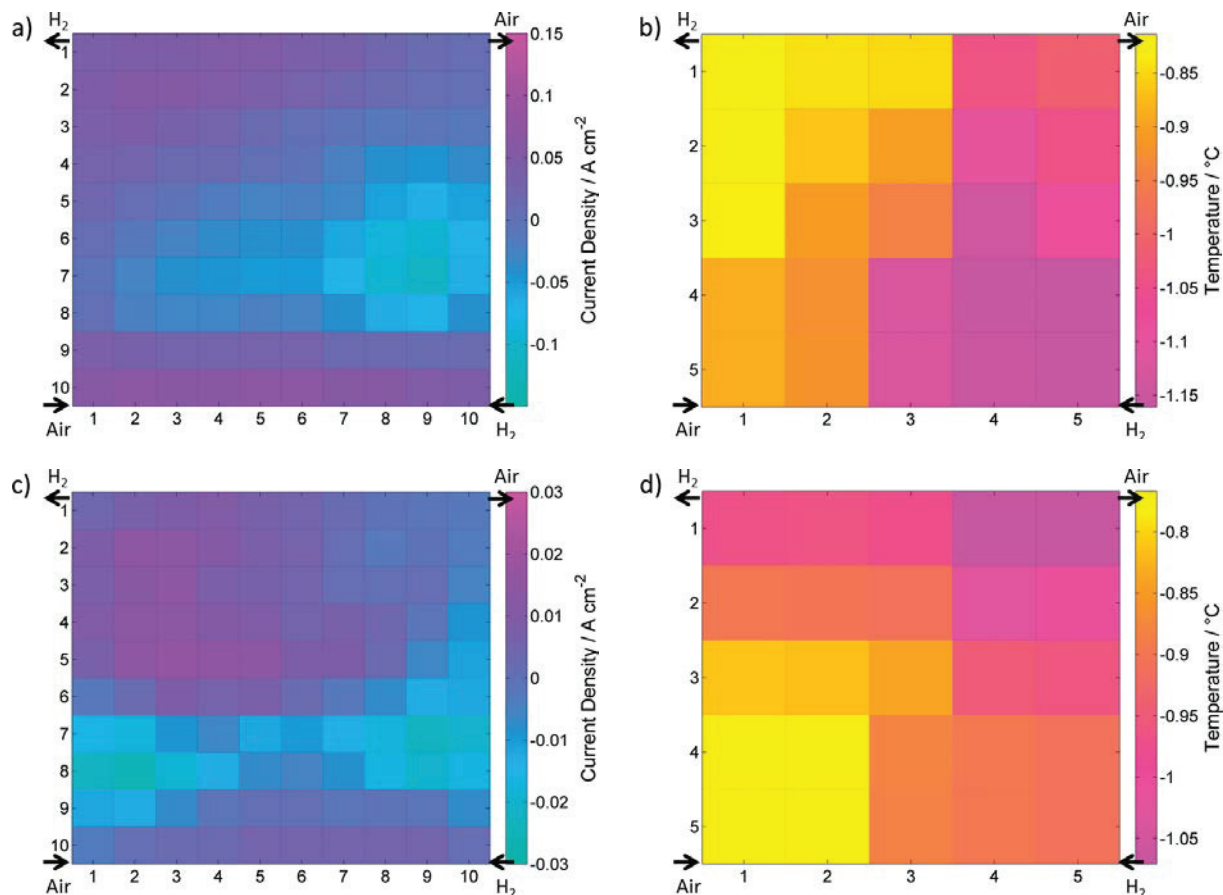


Fig. 9 Local current (a and c) and temperature (b and d) changes during normal operation before and after the 10 seconds AST (a and b) and the 60 seconds AST (c and d).

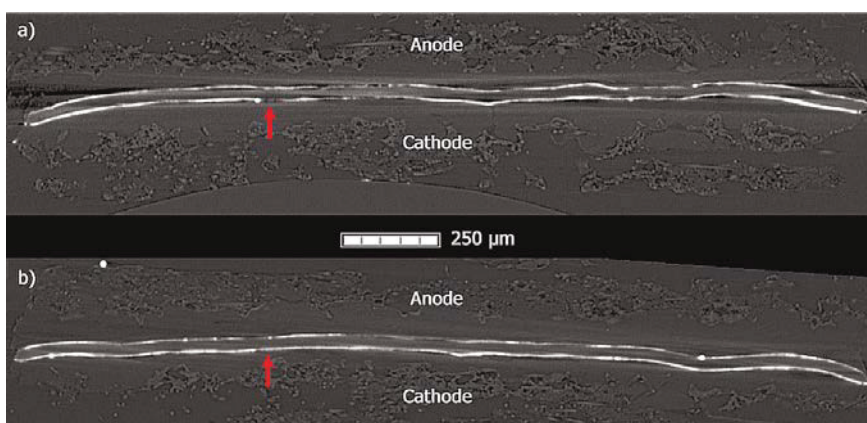


Fig. 10 Cross sectional computed tomography image of (a) sample 1 near the cathode inlet and (b) sample 2 near the cathode outlet.

## 4 Conclusion

It has been shown that short intervals of oxygen starvation on the cathode do not necessarily lead to fuel cell failure. Even an improvement of power density and cathode active catalyst surface area was noted *via* electrochemical characterization after 100 cycles with air undersupply duration of 10 s. In comparison to previous results [22], the effect of the longer starvation duration on the electrochemical parameters was more pronounced. Yet, the change in local current density was not as distinguished as after short starvation with lower cathode stoichiometries.

When the cathode was depleted of oxygen, the potential dropped, protons were reduced and hydrogen was formed, as proven by cathode off-gas analysis. Typically, the switch from oxygen reduction to proton reduction/hydrogen evolution reaction takes place in the areas of lower temperatures during air starvation [17]. Due to the different reactions taking place in different areas of the membrane electrode assembly, a temperature gradient is induced with the maximum temperature close to the cathode inlet.

Also, platinum oxides are reduced at low potentials and thus available to catalyze the oxygen reduction reaction during normal operation. This is in agreement with literature [15, 22] and expected as a result of this study.

Computed tomography has shown that the structure of the platinum catalyst layer differs significantly along the air flow channels after both ASTs had been conducted. This phenomenon is assigned to the induced temperature gradient that was visualized by the segmented single cell during starvation, showing peak values near the air inlet, but it is also assigned to the reductive conditions in areas of oxygen depletion. An accelerated dissolution and redeposition rate of platinum due to platinum oxide reduction [5] was not confirmed by the experiments, but could have been less significant compared to the electrocatalyst agglomeration due to the discussed temperature gradients and thus not distinguishable.

It is shown that the gradient induced by air starvation and the potential cycling on the cathode result in a change of cata-

lyst structure. This might not cause severe degradation initially, but does result in uneven operation conditions and thus locally accelerated degradation.

## Acknowledgment

The research leading to these results has received funding from the European Union's Seventh Framework Programme (FP7/2007–2013) for the Fuel Cells and Hydrogen Joint Technology Initiative under grant agreement n° 621216.

## Abbreviations

AST	Accelerated stress test
BoT	Beginning of testing
EoT	End of testing
FER	Fluoride emission rate
HER	Hydrogen evolution reaction
HOR	Hydrogen oxidation reaction
ISE	Ion selective electrode
MEA	Membrane electrode assembly
ORR	Oxygen reduction reaction
OS	Oxygen starvation
PRR	Proton reduction reaction
PTFE	Polytetrafluoroethylene
RHE	Reversible hydrogen electrode
X $\mu$ CT	X-ray micro computed tomography

## References

- [1] G. Cipriani, V. Di Dio, F. Genduso, D. La Cascia, R. Liga, R. Miceli, G. Ricco Galluzzo, *Int. J. Hydrogen Energy* **2014**, *39*, 8482.
- [2] M. Gandiglio, A. Lanzini, M. Santarelli, P. Leone, *Energy Build.* **2014**, *69*, 381.
- [3] L. Carrette, K. A. Friedrich, U. Stimming, *Fuel Cells* **2001**, *1*, 5.

- [4] M. Bodner, C. Hochenauer, V. Hacker, *J. Power Sources* **2015**, *295*, 336.
- [5] F. A. de Bruijn, V. A. T. Dam, G. J. M. Janssen, *Fuel Cells* **2008**, *8*, 3.
- [6] R. Schweiss, *Fuel Cells* **2016**, *16*, 100.
- [7] B. Chen, J. Wang, T. Yang, Y. Cai, M. Pan, Z. Tu, C. Zhang, S. H. Chan, Y. Yu, *Energy Convers. Manag.* **2016**, *119*, 60.
- [8] B. Chen, W. Ke, M. Luo, J. Wang, Z. Tu, M. Pan, H. Zhang, X. Liu, W. Liu, *Energy* **2015**, *91*, 799.
- [9] B. Chen, J. Wang, T. Yang, Y. Cai, C. Zhang, S. H. Chan, Y. Yu, Z. Tu, *Energy* **2016**, *106*, 54.
- [10] S.ENZ, T. A. Dao, M. Messerschmidt, J. Scholta, *J. Power Sources* **2015**, *274*, 521.
- [11] P. Pei, H. Chen, *Appl. Energy* **2014**, *125*, 60.
- [12] S. Zhang, X. Yuan, H. Wang, W. Merida, H. Zhu, J. Shen, S. Wu, J. Zhang, *Int. J. Hydrogen Energy* **2009**, *34*, 388.
- [13] M. Gerard, J.-P. Poirot-Crouvezier, D. Hissel, M.-C. Pera, *Int. J. Hydrogen Energy* **2010**, *35*, 12295.
- [14] Y. X. Wang, D. J. Xuan, Y. B. Kim, *Int. J. Hydrogen Energy* **2013**, *38*, 13381.
- [15] N. Zamel, R. Hanke-Rauschenbach, S. Kirsch, A. Bhattarai, D. Gerteisen, *Int. J. Hydrogen Energy* **2013**, *38*, 15318.
- [16] R. L. Borup, J. R. Davey, F. H. Garzon, D. L. Wood, M. A. Inbody, *J. Power Sources* **2006**, *163*, 76.
- [17] M. Dou, M. Hou, D. Liang, Q. Shen, H. Zhang, W. Lu, Z. Shao, B. Yi, *J. Power Sources* **2011**, *196*, 2759.
- [18] A. Taniguchi, T. Akita, K. Yasuda, Y. Miyazaki, *Int. J. Hydrogen Energy* **2008**, *33*, 2323.
- [19] Z. Liu, L. Yang, Z. Mao, W. Zhuge, Y. Zhang, L. Wang, *J. Power Sources* **2006**, *157*, 166.
- [20] M. Bodner, B. Cermenek, M. Rami, V. Hacker, *Membranes* **2015**, *5*, 888.
- [21] M. Bodner, M. Rami, B. Marius, A. Schenk, V. Hacker, *ECS Trans.* **2016**, *75*, 703.
- [22] M. Bodner, A. Schenk, B. Marius, M. Rami, V. Hacker, *ECS Trans.* **2016**, *75*, 769.
- [23] E. N. Landis, D. T. Keane, *Mater. Charact.* **2010**, *61*, 1305.